# Strongly coupled, low noise dc-SQUID amplifiers

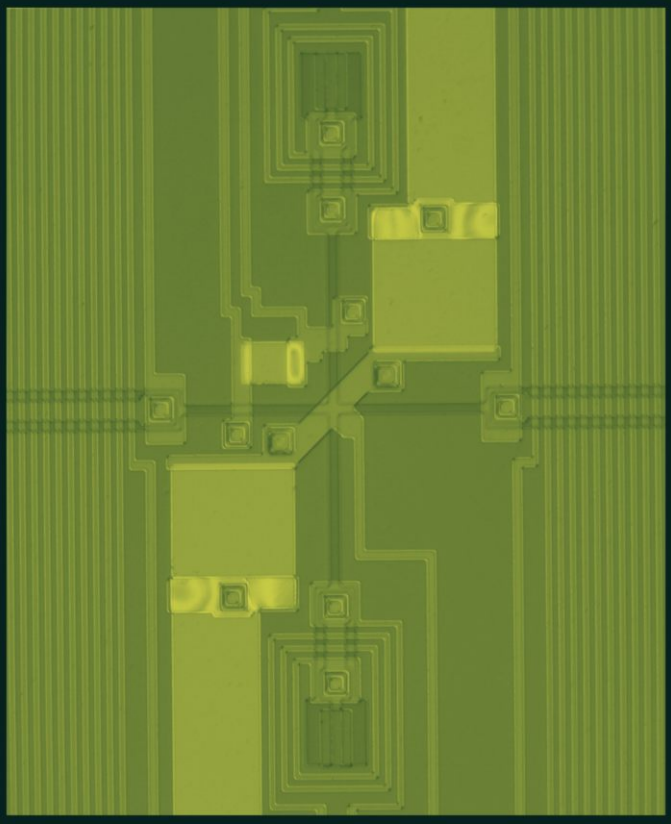

Johannes Pleikies

**Ph.D. committee**

| | | |
|---|---|---|
| Chairman and secretary | | |
| | Prof. Dr. G. van der Steenhoven | University of Twente |
| Supervisor | | |
| | Prof. Dr. H. Rogalla | University of Twente |
| Assistent supervisor | | |
| | Dr. Ir. J. Flokstra | University of Twente |
| Members | | |
| | Prof. Dr. Ir. H. Hilgenkamp | University of Twente |
| | Prof. Dr. P. J. Kelly | University of Twente |
| | Prof. Dr. Ir. B. Nauta | University of Twente |
| | Prof. Dr. G. Frossati | Leiden University |
| | Dr. H. G. Meyer | IPHT Jena, Germany |

**Front cover:** Photograph of a dc-SQUID with a parallel washer configuration. See Fig. 5.9 on page 120 for details.

**Back cover:** Circles of constant equivalent input noise temperature of an amplifier in the complex space of the normalized input impedance. See Fig. 2.3 on page 28 for details.

The work described in this thesis has been mainly performed in the Low Temperature division of the Department of Applied Physics at the University of Twente, P.O. Box 217, 7500 AE Enschede, The Netherlands. Parts of the work were performed at the Kamerlingh Onnes Laboratory at the Leiden University, P.O. Box 9504, 2300 RA Leiden, The Netherlands. Financial support has been partly provided by the "Stichting voor Technische Wetenschappen" (STW).

J. Pleikies
"Strongly coupled, low noise dc-SQUID amplifiers"
Ph.D. Thesis, University of Twente, Enschede, The Netherlands.

ISBN: 978-90-365-2832-0

Printed by Ipskamp Drukkers B.V., Enschede, The Netherlands

# STRONGLY COUPLED, LOW NOISE DC-SQUID AMPLIFIERS

PROEFSCHRIFT

ter verkrijging van
de graad van doctor aan de Universiteit Twente,
op gezag van de rector magnificus,
prof. dr. H. Brinksma,
volgens besluit van het College voor Promoties
in het openbaar te verdedigen
op woensdag 10 Juni 2009 om 16.45 uur

door

Johannes Pleikies

geboren op 13 april 1980
te Erfurt, Duitsland

Dit proefschrift is goedgekeurd door:
Prof. Dr. H. Rogalla (promotor)
Dr. Ir. J. Flokstra (assistent-promotor)

*In memory of my grandfather*

# Contents

# Chapter 1

# Introduction

## 1.1 Motivation and overview of the thesis

The dc Superconducting Quantum Interference Device (dc-SQUID) is one of the most sensitive magnetic field sensors available [1–3]. Since its first discovery in 1964 by Jaklevic et al. [4], SQUID magnetometers were employed in many applications. They can be used to measure biomagnetic signals originating from the activity of the heart or the brain [5–7], for the non-destructive testing of aircraft wheels [8] or archaeological research [9]. SQUIDs are utilized to investigate magnetic properties of materials [10], also including spatial information on the sample of interest [11]. Furthermore, SQUIDs can be used to measure nuclear magnetic resonance [12] as well as for sensitive thermometry [13–15].

By means of a coupling coil, the SQUID can be transformed into an amplifier for electrical currents. The properties of this *SQUID amplifier* are even more promising, see for example reference [16] or chapter 8 in reference [3]. The minimum sensitivity that can be reached in a measurement is predicted to be quantum limited [16–18] and some experiments on dc-SQUIDs or related devices approach this limit [19, 20]. Possible applications of SQUID amplifiers are for example voltmeters [21], metrology [22, 23], the readout of cryogenic particle detectors [24, 25] or the detection of gravitational waves [26–29].

The developed sensors presented in chapter 5 are intended for the utilization in the first spherical resonant mass gravitational wave antenna MiniGRAIL [28–33]. Here, a 1.4 ton heavy sphere is cooled to temperatures below 1 K. A passing gravitational wave will slightly change the dimensions of the sphere. Using a capacitive transducer, this vibration is read out by a SQUID amplifier. To feasibly detect gravitational waves, displacements of the order of $10^{-21}$ m have to be measured. Therefore, minimum noise SQUIDs are required.

This thesis covers topics related to the design and operation of minimum noise SQUID amplifiers. In this introduction chapter, we will give an overview of the basics of superconducting electronics, the theory of dc-SQUID sensors and some general related aspects.

In chapter 2, we investigate requirements and optimization criteria for practical SQUID amplifier based systems with different connected input circuits. In our analysis, we include the flux-locked loop operation, that is often used in practice. We discuss typical effects that occur in measurements and that can be used for characterizing the SQUID as well as its

readout system. The investigated influence of the properties of the SQUID are used to define optimization criteria for a low noise readout of basic input circuits.

In chapter 3, we numerically investigate the optimized design and operation dc-SQUIDs with respect to the results obtained in chapter 2. Based on a circuit simulator, we developed a feasible system for numerically characterizing SQUIDs. This is used to investigate the properties of typical SQUIDs over a variety of parameters. Compared to other published work on standard dc-SQUIDs, we give a very broad overview, especially on aspects related to the interaction of the SQUID with a coupled input circuit. In the second part of chapter 3 we investigate the properties of SQUIDs with an integrated coil. We numerically investigate the behavior of a simplified model of such SQUIDs. The results are used to give some guidelines for the operation and design of such sensors [15, 34]. In the final part of chapter 3 we present a numerical experiment of a standard SQUID strongly coupled to a capacitive input circuit. This appears to have many parallels to the SQUID with a long integrated coil, the results are used to verify the assumptions underlying the analysis of chapter 2.

The sensitivity of SQUIDs can be further improved by cooling. In chapter 4, we investigate a limit one typically faces here—the hot-electron effect. We present measurements on its influence in *PdAu* thin-film resistors. The same type of resistor was employed in our SQUID designs. We show experiments on the influence of this hot-electron effect and compare them to existing theories. Furthermore, we experimentally and numerically investigate the suppression of the hot-electron effect by means of passive cooling.

The final chapter 5 shows measurements on our developed SQUIDs for an optimized readout of MiniGRAIL [34–36]. We describe the design, modeling and experiments of the developed sensors. Here, many aspects of the preceding parts of the thesis are applied and evaluated. From the comparison of experimental and numerical results, we conclude that the performance of SQUIDs with an integrated coil is more controllable and predictable than is usually assumed.

## 1.2 Basics of superconducting electronics

### 1.2.1 Superconductivity

Superconductivity was first discovered by Kamerlingh Onnes in 1911. To his surprise, the electrical resistance of mercury vanished after cooling it in a bath of liquid *He*. This effect was later found for a variety of pure metals, alloys and ceramics with different critical temperatures $T_C$. Below these temperatures the superconducting state is reached. In this thesis we concentrate on low-$T_C$ superconducting electronics. The SQUIDs that will be presented in chapter 5 are based on *Nb* and are operated at temperatures of 4.2 K and below.

The theory of superconductivity can be found in textbooks on the subject [37]. At this point we will only name the most important effects. The general properties of low-$T_C$ superconductors were explained in 1957 by Bardeen, Cooper and Schrieffer in the BCS theory [38]. In the superconducting state, pairs of electrons form so-called *Cooper pairs* caused by a strong interaction of the electrons with phonons, which represent vibrations of the lattice. The resistance vanishes because of this strong interaction between the carriers of the electrical current and the lattice.

Cooper pairs are Boson particles, which means that the condensate of all Cooper pairs in a superconductor can be represented by a single quantum mechanical wave function

$\bar{\Psi}(r) = \left|\bar{\Psi}(r)\right| e^{j\phi(r)}$. The bar $\bar{}$ above variables indicates complex quantities. The square of the absolute value of this wave function $\left|\bar{\Psi}(r)\right|^2$ is proportional to the density of Cooper pairs at one particular point $r$ in the superconductor.

In 1933 Meissner and Ochsenfeld found another unique property of superconducting materials. If the superconductor is put into a magnetic field, currents start to flow which expel the field from the inner part of the superconductor. Connected to this effect, all currents sent through a superconductor of sufficient thickness are also expelled to a finite outer layer of the conductor. This Meissner-Ochsenfeld effect is related to the phase $\phi(r)$ of the quantum mechanical wave function via the flux quantization.

### 1.2.2 Flux quantization

The argument of the quantum mechanical wave function $e^{j\phi(r)}$ is single-valued at any point in the superconductor. Accordingly, a closed line integral over the phase gradient in the superconductor $\oint \nabla\phi(r)\,\mathrm{d}r$ can only take values of $2\pi n$, $n$ being an integer.

$$2\pi n = \oint \nabla\phi(r)\,\mathrm{d}r \tag{1.1}$$

The gradient of the phase of the wave function in a superconductor $\nabla\phi(r)$ is expressed by the sum of two terms, one proportional to the current density of the Cooper pairs and one proportional to the magnetic vector potential $A_P$. In the inner parts of a thick enough superconductor, no current is running. Therefore, the phase gradient $\nabla\phi(r)$ can be expressed as $\nabla\phi(r) = 2eA_P(r)/h$ [39]. Here, $e = 1.60{\cdot}10^{-19}$ C is the elementary charge, $h = 6.63{\cdot}10^{-34}$ J s is Planck's constant. Integrating the phase gradient over the inner parts of a closed superconducting ring and using Stoke's theorem leads to:

$$2\pi n = \oint \nabla\phi(r)\,\mathrm{d}r = 2\pi\frac{2e}{h}\oint A_P(r)\,\mathrm{d}r = 2\pi\frac{2e}{h}\iint B\,\mathrm{d}A = 2\pi\frac{2e}{h}\Phi_T \tag{1.2}$$

Here, $B$ is the magnetic flux density in a surface $A$ bounded by the integration path. The total magnetic flux through the ring $\Phi_T$ can now be expressed as an external flux $\Phi_E$ and a self-generated flux $LI$ originating from the current $I$ in the ring and its inductance $L$. The flux quantization condition reads:

$$n\frac{h}{2e} = n\Phi_0 = \frac{\Phi_0}{2\pi}\oint \nabla\phi(r)\,\mathrm{d}r = \Phi_E + LI = \Phi_T \tag{1.3}$$

The total flux $\Phi_T$ through a closed superconducting loop can therefore only take integer values of the magnetic flux quantum $\Phi_0 = 2.07{\cdot}10^{-15}$ Wb. This flux quantization condition was formally derived by London on a phenomenological basis in 1950, before the publication of the BCS theory. In his theory, he introduced the London penetration depth $\lambda_L$ [37, 39, 40]. This parameter determines how far currents and magnetic fields can penetrate a superconductor.

The Meissner-Ochsenfeld effect is in fact originating in the flux quantization. If the external flux through a closed superconducting ring with $n$ enclosed flux quanta is changed by $\mathrm{d}\Phi_E$, Eqn. (1.3) is maintained by a compensating current $I = -\mathrm{d}\Phi_E/L$ in the ring.

For calculations on the behavior of superconducting electronics, the phase change $\varphi_L$ over

an inductance $L$ is needed. According to Eqn. (1.3), this quantity can be expressed as:

$$\varphi_L = \frac{2\pi}{\Phi_0}\Phi_T = \frac{2\pi}{\Phi_0}\Phi_E + \frac{2\pi}{\Phi_0}LI \tag{1.4}$$

### 1.2.3 Josephson effect

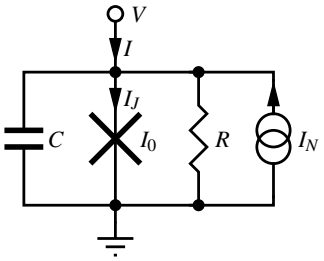


**Figure 1.1:** The RCSJ model of a Josephson junction.

In 1962, Brian Josephson predicted that a supercurrent can tunnel through a thin isolating barrier between two superconductors. This *Josephson effect* is based on the diffusion of the wavefunction of the Cooper pairs from the two superconducting electrodes into the isolator, where they can interact [41]. The behavior of the theoretical *Josephson junction* is described by the two Josephson equations [41]:

$$I_J = I_0 \sin(\varphi) \tag{1.5}$$

$$V = \frac{\Phi_0}{2\pi}\frac{\mathrm{d}\varphi}{\mathrm{d}t} \tag{1.6}$$

Here, $I_J$ is the current through the ideal Josephson junction, $\varphi$ is the phase difference between the phases of the wavefunction $\phi$ of the two adjacent superconductors, $V$ is the voltage across the Josephson junction and $t$ is the time. $I_0$ is the *critical current* of the Josephson junction, which is a function of the geometry, materials, the temperature and the magnetic field [39, 40, 42]. The Josephson junction is in schematics typically symbolized by a cross as shown in Fig. 1.1.

Suppose that the phase difference across a Josephson junction performs a change from $\varphi$ to $\varphi + 2\pi n$ as a result of an arbitrary dynamical process involving a changing bias current $I_J$. According to Eqn. (1.5), $I_J$ has to be the same in the beginning and the end of the process. If one integrates the voltage across the Josephson junction, Eqn. (1.6), from the beginning to the end of the process, one gets $\int V\,\mathrm{d}t = n\,\Phi_0$. This represents an induced voltage due to the change in magnetic flux of $n$ flux quanta in any superconducting loop connected to the Josephson junction. Accordingly, Josephson junctions can be seen as controllable gates for flux quanta.

Based on the same argument, a measured mean voltage $\langle V \rangle$ across a Josephson junction must be caused by a train of induced flux quanta. The average frequency of this process, the *Josephson frequency*, $f_J$ reads:

$$f_J = \frac{\langle V \rangle}{\Phi_0} = 483\ \frac{\mathrm{MHz}}{\mu\mathrm{V}}\ \langle V \rangle \tag{1.7}$$

Note that the flux quantization condition Eqn. (1.3) is not fulfilled anymore, because a part of the total phase in the superconducting loop is now caused by the Josephson junction. Still, the total phase change around a superconducting loop is quantized to integer multiples of $2\pi$, see Eqn. (1.1). This forms in combination with the Josephson Eqns. (1.5)–(1.6) and the phase drop over inductances, see Eqn. (1.4), the basis to calculate the behavior of superconducting circuits involving Josephson equations.

### 1.2.4 RCSJ model of a Josephson junction

In practice, Eqns. (1.5) and (1.6) only sufficiently model the dynamics of a Josephson junction in the quasi-static case. The complete dynamics of many Josephson junctions are well explained by the resistively capacitively shunted junction (RCSJ) model [40, 43, 44], which is shown in Fig. 1.1. Here, a capacitance $C$ and a resistance $R$ are connected in parallel to the ideal Josephson junction. This models the electrostatic capacitance between the two superconducting electrodes and the direct tunneling of electrons in the voltage state, respectively. In practice, the resistance $R$ is often determined by a comparably small externally connected resistor. This is also the case throughout this thesis. The RCSJ model is only valid for point-like Josephson junctions with a *gap voltage* $V_G \gg I_0 R$ [40]. $I_0 R$ is the *characteristic voltage* of the Josephson junction. These requirements are fulfilled throughout this thesis.

Figure 1.1 also contains a noise current source $I_N$ which models the thermal Nyquist noise of the effective resistance $R$ with a noise power spectral density (PSD) of $4k_B T/R$. Here, $k_B = 1.38{\cdot}10^{-23}$ J/K is the Boltzmann constant and $T$ is the temperature. Such a frequency independent noise PSD is called "white". The noise parameter

$$\Gamma = \frac{2\pi k_B T}{I_0 \Phi_0} \tag{1.8}$$

relates the Josephson coupling energy to the thermal energy [40]. For low-$T_C$ Josephson junctions, its value is typically in the order of $10^{-2}$. In this regime, there is no serious influence on the general functioning of the Josephson junction.

The resulting nonlinear differential equation reads with Eqns. (1.5)–(1.6) [40, 43, 44]:

$$C\frac{\mathrm{d}V}{\mathrm{d}t} + \frac{V}{R} + I_0 \sin(\varphi) = I + I_N \tag{1.9}$$

$$\frac{\Phi_0 C}{2\pi}\frac{\mathrm{d}^2\varphi}{\mathrm{d}t^2} + \frac{\Phi_0}{2\pi R}\frac{\mathrm{d}\varphi}{\mathrm{d}t} + I_0 \sin(\varphi) = I + I_N \tag{1.10}$$

Using the *Stewart-McCumber parameter* $\beta_C$ [43, 44] and normalizing the currents to $I_0$, these expressions read:

$$\frac{\beta_C}{(2\pi I_0 R/\Phi_0)^2}\frac{\mathrm{d}^2\varphi}{\mathrm{d}t^2} + \frac{1}{2\pi I_0 R/\Phi_0}\frac{\mathrm{d}\varphi}{\mathrm{d}t} + \sin(\varphi) = i + i_N \tag{1.11}$$

$$\beta_C = 2\pi I_0 R^2 C \,/\, \Phi_0 \tag{1.12}$$

$$i = I/I_0 \qquad i_N = I_N/I_0$$

Figure 1.2 shows a simulation of a Josephson junction according to the RCSJ model. This simulation was done with *JSIM* [45] with noise extensions [46], whose use will be explained in more detail in chapter 3. Once the critical current of the Josephson junction is reached, it starts to oscillate. Figure 1.2(a) shows these voltage oscillations of the Josephson junction. Each voltage pulse shown here corresponds, as pointed out before, to one induced flux quantum. The *characteristic frequency* $I_0 R/\Phi_0$ describes, at least for $\beta_C \ll 1$, the timescale of any changes in the state of the Josephson junction. A normalized time would be according to Eqn. (1.11) expressed as $t\,2\pi I_0 R/\Phi_0$.

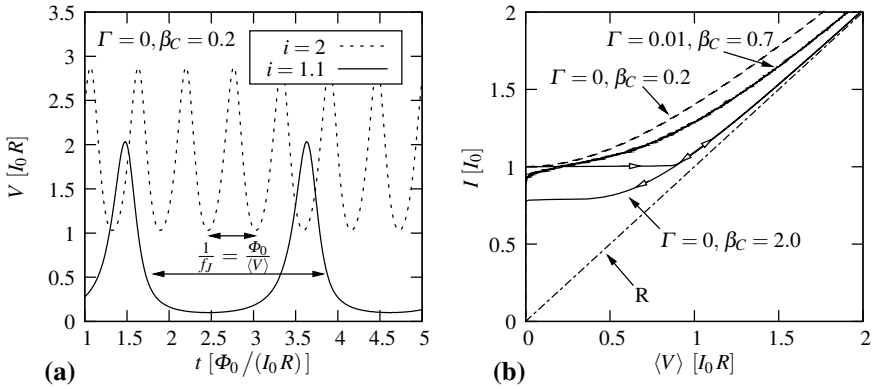


**Figure 1.2:** Simulation of the dynamics of Josephson junctions according to the RCSJ model. **(a)** Time dependent voltage of an underdamped Josephson junction at two different bias currents. **(b)** The mean (dc) current–voltage characteristics of Josephson junctions with varying $\beta_C$ and $\Gamma$ and of the shunt resistance. Each of the current–voltage characteristics was calculated in one simulation by sweeping the current $I$ up and down. This sweep was done very slow compared to the Josephson oscillations. The voltage $V$ was at the same time averaged by means of an attached low-pass filter.

In Fig. 1.2, we show simulated current–voltage characteristics for a few Josephson junctions. In case of a finite temperature, the voltage state is reached at currents smaller than the critical current $I_0$, as one can see for the current–voltage characteristics with $\Gamma > 0$. This is usually referred to as "noise rounding". At currents $I \gg I_0$, the Josephson junction has no influence on the dynamics anymore and behaves like the effective resistance $R$.

For values of the Stewart-McCumber parameter $\beta_C > 0.7$, the noise-free Josephson junction behaves hysteretic. This can be seen in Fig. 1.2(b) for the case $\beta_C = 2$. The junction is switching from the superconducting state to the voltage state at currents close to the critical current $I_0$ for all values of $\beta_C$, but for the switching back from the voltage state to the superconducting state, the current needs to be brought back to a value smaller than $I_0$ [43, 44]. The exact dynamic behavior is strongly dependent on the thermal noise $\Gamma$ in consequence of the random bias current [47]. Usually one refers to *overdamped* Josephson junctions for $\beta_C \ll 1$ and to *underdamped* Josephson junctions for $\beta_C \gg 1$.

The hysteresis is a potential source of noise and irregular behavior and thus has to be suppressed in most types of superconducting electronics, as in our case. As one can see from Eqn. (1.12), the hysteresis can be suppressed by decreasing the resistance $R$. As pointed out before, this can be achieved by connecting an external shunt resistor in parallel to the Josephson junction.

The advent of Josephson junctions opened a complete new branch of electronics. One obvious application of the Josephson effect is employed in SQUIDs: the application of the Josephson effect for magnetic field sensors. Since the discovery of SQUIDs in 1964 [4], several types of these sensors emerged. Besides the here treated dc-SQUID, another variant is given by the rf-SQUIDs, which are represented by a superconducting ring interrupted by one Josephson junction [2]. Further devices are for example the (double-)relaxation-oscillation SQUIDs ((D)ROS) [48–51], arrays of SQUIDs [52], microstrip SQUIDs [19], digital SQUIDs [53–55] or SQUIDs with additional positive feedback (APF) [56].

In this thesis we concentrate on the dc-SQUID because of its in practice almost unchal-

lenged sensitivity. Furthermore, with state of the art technologies and readout electronics, it is comparably stable to fabricate and easy to utilize. From here on, we often simply refer to the dc-SQUID as a "SQUID".

## 1.3 Dc-SQUID amplifiers

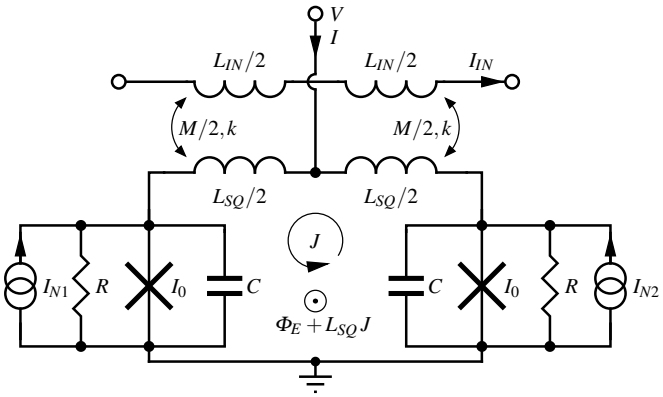


**Figure 1.3:** Basic schematic of a dc-SQUID amplifier

The basic schematic of a dc-SQUID is shown in Fig. 1.3. A superconducting ring with an inductance $L_{SQ}$ is interrupted by two Josephson junctions. Bias leads are connected between the two Josephson junctions. For simplicity, symmetric SQUID parameters are assumed throughout this thesis, so the parameters of the Josephson junction $R$, $C$ and $I_0$ are the same for both junctions. Furthermore, the SQUID inductance $L_{SQ}$ is distributed symmetrically over the two branches. The SQUID inductance is coupled to an input inductance $L_{IN}$ with a coupling factor $k$ and a mutual inductance $M = k\sqrt{L_{SQ}L_{IN}}$. This input inductance allows one to couple an electrical signal into the SQUID.

The currents through the two Josephson junctions can be completely described by a symmetrically split bias current $I$ and a circulating current $J$ running in the SQUID loop. The two coupled Josephson junctions now behave with Eqns. (1.4), (1.11) and Kirchhoff's laws according to the following, again normalized, system of nonlinear differential equations:

$$\begin{aligned}
\frac{\beta_C}{(2\pi I_0 R/\Phi_0)^2}\frac{\mathrm{d}^2\varphi_1}{\mathrm{d}t^2} + \frac{1}{2\pi I_0 R/\Phi_0}\frac{\mathrm{d}\varphi_1}{\mathrm{d}t} + \sin(\varphi_1) &= \frac{i}{2} + j + i_{N1} \\
\frac{\beta_C}{(2\pi I_0 R/\Phi_0)^2}\frac{\mathrm{d}^2\varphi_2}{\mathrm{d}t^2} + \frac{1}{2\pi I_0 R/\Phi_0}\frac{\mathrm{d}\varphi_2}{\mathrm{d}t} + \sin(\varphi_2) &= \frac{i}{2} - j + i_{N2} \qquad (1.13) \\
\frac{\varphi_2 - \varphi_1}{2\pi} = \frac{\Phi_E + L_{SQ}J}{\Phi_0} &= \frac{\Phi_E}{\Phi_0} + \frac{\beta_L}{2}j \\
\beta_L = \frac{2I_0 L_{SQ}}{\Phi_0} \qquad j &= \frac{J}{I_0} \qquad (1.14)
\end{aligned}$$

Here, we introduced the *screening parameter* $\beta_L$ [57] and the *external flux* $\Phi_E$, as shown in Fig. 1.3. Note that the total flux enclosed by the SQUID loop $\Phi_T$ is the external flux plus a self generated contribution: $\Phi_T = \Phi_E + L_{SQ}J$.

The system of nonlinear Eqns. (1.13) shows a complex dynamical behavior and is therefore usually solved numerically. This was done first by Tesche and Clarke [57, 58] in 1977, but also some other important literature on the dynamics of standard low-Tc dc-SQUID should be mentioned here [2, 40, 59–61].

### 1.3.1 Characteristics

Figure 1.4 shows a simulation of the mean characteristics of a SQUID. The calculations were done, like all simulations on SQUIDs in this thesis, using the already mentioned *JSIM* [45] with noise extensions [46]. Details can be found in chapter 3.

All characteristics are periodic regarding the applied flux, which means that any parameter of a SQUID at a flux $\Phi_E$ is identical at all values of external flux $\Phi_E + n\,\Phi_0$, $n$ being an integer. From here on, any external flux is usually given in the range $-0.5$ to $0.5\,\Phi_0$.

There exist more symmetries for the here assumed balanced SQUID. The voltage is symmetric relative to the $\Phi_E = 0$ axis, so $V(\Phi_E) = V(-\Phi_E)$, and the circulating current is point symmetric around $(\Phi_E, J) = (0,0)$, which means that $J(\Phi_E) = -J(-\Phi_E)$. Also these symmetries will be used throughout the thesis and therefore we often only give values of external flux in the range 0 to 0.5 $\Phi_0$.

The critical current $I_{0,SQ}$ of a SQUID, the current $I$ where the voltage state is the reached, depends on the applied flux. Its minimum is reached at $|\Phi_E| = 0.5\,\Phi_0$ and depends on $\beta_L$ and to some extent on $\Gamma$ via the already mentioned "noise rounding". In case of the SQUID shown in Fig. 1.4 with $\beta_L = 1$, the minimum critical current is $\approx 1\,I_0$. The maximum critical current is for all values of $\beta_L$ reached at $\Phi_E = 0$ and takes a value of $\approx 2\,I_0$. This corresponds to the critical current of the two parallel Josephson junctions. As mentioned before, the observed critical current of a SQUID is generally dependent on $\Gamma$.

In a configuration as shown in Fig. 1.3, the coupling inductance $L_{IN}$ is a possible source for external flux $\Phi_E = M\,I_{IN}$ and can therefore be used to readout a connected impedance. The SQUID amplifies a small change of the external flux into a small voltage. This is characterized by the *flux-to-voltage transfer function* $G_{V\Phi}$. The forward gain of the amplifier from the input current to the output voltage is $M\,G_{V\Phi}$. Another small-signal parameter $G_{VI}$

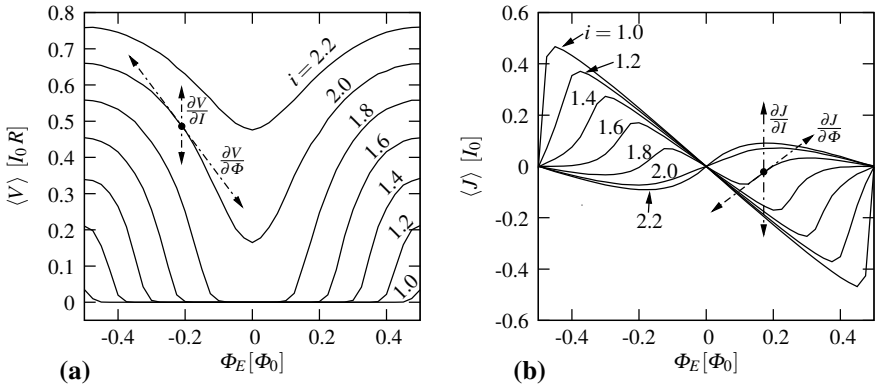


**Figure 1.4:** Simulation of the characteristics of voltage and circulating current of a SQUID with $\beta_L = 1$, $\Gamma = 0.01$ with changing bias current $I$. **(a)** Flux–voltage characteristics. **(b)** Flux–circulating current characteristics.

describes the *output resistance* of the SQUID, as seen from the bias terminals. In total there are four of these small-signal parameters, as indicated in Fig. 1.4. The two remaining ones can be of importance in case a load is connected to the coupling coil of the SQUID.

$$G_{V\Phi} = \frac{\partial V}{\partial \Phi_E} \qquad G_{J\Phi} = \frac{\partial J}{\partial \Phi_E} \tag{1.15}$$

$$G_{VI} = \frac{\partial V}{\partial I} \qquad G_{JI} = \frac{\partial J}{\partial I} \tag{1.16}$$

The *dynamic inductance* of the SQUID $1/G_{J\Phi}$ describes how the circulating current $J$ reacts on an applied external flux, thus how the effective input impedance seen from $L_{IN}$ is influenced by the SQUID. The *reverse transfer function* $G_{JI}$ characterizes the interaction between the input and the output of the amplifier. It describes how a small change of the bias current $I$ results in a small change of the circulating current $J$ which can have an influence on a connected input impedance. The influence of all these parameters will be studied in more detail in chapter 2.

### 1.3.2 Sensitivity

A simulation of the dynamics of a SQUID in the presence of thermal noise is shown in Fig. 1.5. Both Josephson junctions switch with the same average frequency, which corresponds to the Josephson frequency, see Eqn. (1.7). As one can see from the time series of the voltage of the two junctions and the circulating current in Fig. 1.5(a), there is a random variation of this frequency. This causes noise being "mixed down" from the Josephson frequency to a white noise spectrum at lower frequencies. This can be seen in Figs. 1.5(b) and (c), where we plotted the noise PSDs of the same time series.

The power spectral density $S_{xx}$, or the cross spectral density $S_{xy}$, are defined by the auto-correlation function $c_{xx}$, or cross-correlation function $c_{xy}$, respectively [62]:

$$c_{xy}(t') = \int_{-\infty}^{\infty} x(t)\, y(t+t')\, \mathrm{d}t \tag{1.17}$$

$$S_{xy}(\omega) = \int_{-\infty}^{\infty} c_{xy}(t')\, \mathrm{e}^{-\mathrm{j}\omega t'}\, \mathrm{d}t' \tag{1.18}$$

Here, $x(t)$ and $y(t)$ are two time series and $\omega = 2\pi f$ is the angular frequency. For $y(t) = x(t)$, these equations represent the auto-correlation $c_{xx}(t')$ and power spectral density $S_{xx}(\omega)$ of the time series $x(t)$.

The *additional noise* of the amplifier is determined by the noise on the output of the SQUID $S_{VV}$, the PSD of the voltage across the SQUID $V$. This contribution adds noise to the input signal of the amplifier. Together with the already introduced flux-to-voltage transfer function, $S_{VV}$ can be referred to an equivalently measured additional flux noise PSD:

$$S_{\Phi,VV} = \frac{S_{VV}}{{G_{V\Phi}}^2} \tag{1.19}$$

Another contribution, the *back-action noise* of the amplifier is determined by the noise on the circulating current in the SQUID $S_{JJ}$, which can drive currents through a connected input

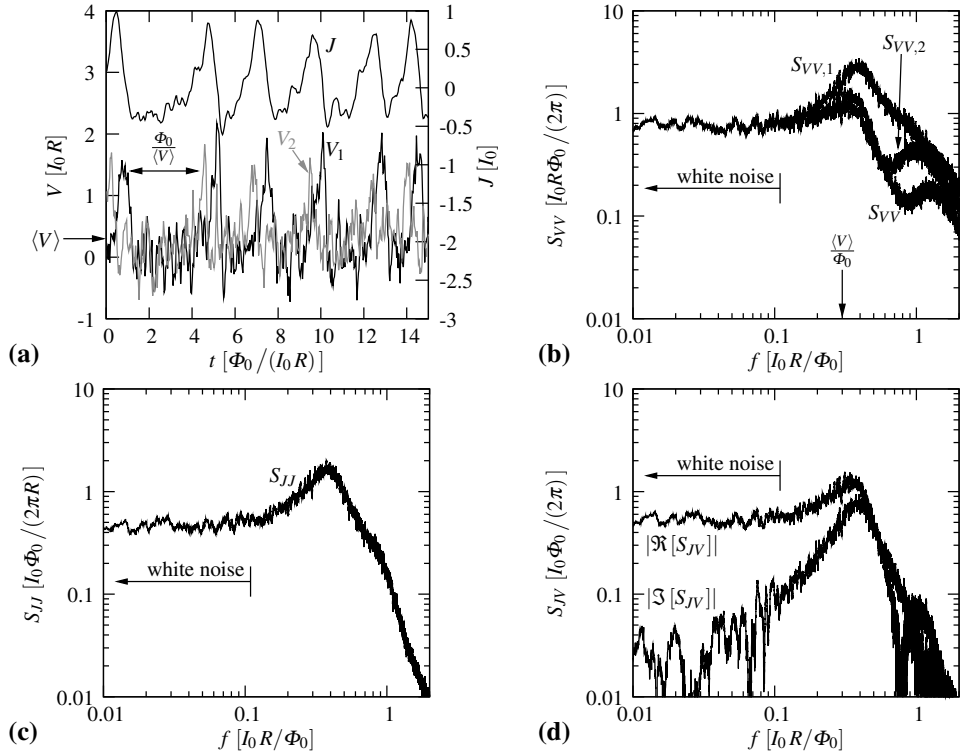


**Figure 1.5:** Simulation of the dynamics of a SQUID with $\beta_L = 1$, $\Gamma = 0.05$, $I = 1.7\,I_0$, $\Phi_E = 0.25\,\Phi_0$. The mean value of the voltage yielded $\langle V \rangle = 0.3\,I_0\,R$, which is indicated alongside with the average Josephson frequency or period, respectively.
**(a)** The time dependent voltage of both Josephson junctions $V_1$, $V_2$ and the circulating current $J$. **(b)** The calculated PSD of the voltage across the two junctions $V_1$,$V_2$ and the voltage across the SQUID $V$. For comparison, see figure 2.12 on page 53 in reference [2]. **(c)** The calculated PSD of the circulating current. **(d)** The calculated real part and imaginary part of the cross spectral density $S_{JV}$ between $J$ and $V$.

impedance. Its PSD is shown in Fig. 1.5(c).

There also exists a correlation between the additional and the back-action noise contributions, whose cross spectral density $S_{JV}$ is depicted in Fig. 1.5(d). At frequencies well below the Josephson frequency, the imaginary part of the correlation can be neglected [63], whereas the real part is white, it is independent of the frequency. The real correlation spectrum can be interpreted in a simple way as a generation of output voltages that are caused by an apparent external flux via the flux-to-voltage transfer. This apparent input signal is caused by the noise on the circulating current $J$ that is running through the SQUID inductance $L_{SQ}$ [63]. The imaginary part is directly caused by the changing phase over the inductance $L_{SQ}$ and the time dependent voltages of the Josephson junctions. This makes clear why the imaginary part of the cross spectral density $\Im\,[S_{JV}]$ is negligibly small at frequencies much smaller than the Josephson frequency.

Wide-spread parameters for comparing the noise performance are the so-called energy resolutions. They express the noise energy per bandwidth referred to the SQUID inductance

$L_{SQ}$. These quantities are related to experimental values by:

$$\varepsilon_{VV} = \frac{S_{\Phi,VV}}{2L_{SQ}} = \frac{S_{VV}}{2L_{SQ}{G_{V\Phi}}^2} \tag{1.20}$$

$$\varepsilon_{JJ} = \frac{S_{JJ}L_{SQ}}{2} \tag{1.21}$$

$$\varepsilon_{JV} = \frac{S_{JV}}{2G_{V\Phi}} \tag{1.22}$$

The *additional energy resolution* $\varepsilon_{VV}$ is also used to characterize magnetometers, whereas the other noise contributions are unimportant in this application of SQUIDs. Another important figure of merit, the *coupled energy resolution* $\varepsilon_{VV}/k^2 = S_{\Phi,VV}L_{IN}/(2M^2)$, should directly be mentioned here because of its special importance. It refers the additional noise of the SQUID to the input coil instead of the SQUID loop. This value can also be more easily determined in experiments because $L_{IN}$ and $M$ are directly accessible whereas $L_{SQ}$ is not.

In this thesis we concentrate on the higher audio frequency range to the intermediate frequency range, say $\approx 10^2$ to $10^7$ Hz. That means that the signal frequency is considered above $1/f$ noise contributions [2] and much below the Josephson frequency, which takes typical values of the order of $10^{10}$ to $10^{11}$ Hz. In this frequency range, the noise PSDs $S_{VV}$, $S_{JV}$ and the correlation spectrum $S_{JV}$ can be considered white and real [57, 63]. The small-signal parameters, Eqns. (1.15) and (1.16), are usually also assumed real and independent of the frequency. Only for the dynamic inductance of the SQUID $1/G_{J\Phi}$, a delay and thus an imaginary part is mentioned in literature [59, 64, 65]. This delay is, expressed in a simple way, caused by the shunt resistances connected in parallel to the SQUID inductance. The involved time constants are in the order of the period of the Josephson oscillations and can have an effect in some, especially high-frequency, applications. Nevertheless, experiments on SQUIDs show much larger time delays on the input of the SQUID [65, 66]. A possible explanation for this effect will be given in chapter 2.

The sensitivity of SQUID sensors was investigated in many publications, see for example [57–60, 63, 67]. Also in this thesis, see chapter 3, we will numerically characterize SQUIDs with the focus on their usage as an amplifier. Here, we will for simplicity only use the following pioneer approximation formulas from the work of Tesche and Clarke [57, 58, 63] which are given for the white noise region of an optimized SQUID $\beta_L = 1$ in the overdamped $\beta_C \ll 1$ and the low temperature $\Gamma \ll 1$ limit:

$$S_{\Phi,VV,TC} \approx \ 16k_BT{L_{SQ}}^2/R \tag{1.23}$$

$$\varepsilon_{VV,TC} \approx \ \ 8k_BTL_{SQ}\ /R \tag{1.24}$$

$$\varepsilon_{JJ,TC} \approx 5.5k_BTL_{SQ}\ /R \tag{1.25}$$

$$\varepsilon_{JV,TC} \approx \ \ 6k_BTL_{SQ}\ /R \tag{1.26}$$

For the flux-to-voltage transfer function $G_{V\Phi}$ of the optimized SQUID, Tesche and Clarke found the following approximate expression [57, 58]:

$$G_{V\Phi} \approx R/L_{SQ} \tag{1.27}$$

The output resistance of the SQUID $G_{VI}$ is typically approximated in an optimum working

point with $R/\sqrt{2}$. Typical values of the dynamic inductance $1/G_{J\Phi}$ are larger than the SQUID inductance, $|G_{J\Phi}|L_{SQ} \lesssim 1$ [59, 65]. Note that this small-signal parameter can be both negative and positive, depending on the working point. The reverse transfer function can take values of $|G_{JI}| \approx 0.1$ [68]. This parameter was also measured in an experiment [69].

As one can see from Eqns. (1.24) to (1.26), the sensitivity of a SQUID with optimum inductance $\beta_L = 1$ can be improved in two ways. The first is to increase the shunt resistance $R$. The limit here is given by the capacitance of the Josephson junctions $C$ because of the already mentioned hysteresis. Furthermore, the SQUID inductance $L_{SQ}$ will also possibly resonate within the working range with roughly the effective capacitance of both junctions $C/2$ [70, 71]. These limits will be treated in more detail in chapter 3.

According to reference [60], the best sensitivity of a SQUID is well approximated by the overdamped model for $\beta_C \lesssim 0.7$. In reference [67], the dc-SQUID was optimized in the intermediate damping limit, resulting in a minimum additional $\varepsilon_{VV,min}$ of $\approx 12\,k_B T\sqrt{L_{SQ}C}$ at $\beta_C \approx 1$ to 2 and $\beta_L \approx 1$ to 2. This is close to the approximation formula in the overdamped limit, see Eqn. (1.24), when the McCumber parameter $\beta_C$, see Eqn. (1.12), takes values close to 1. Because of the relatively small differences [67], we will usually ignore the intermediate damped limit for simplicity and assume overdamped Josephson junctions.

Another measure to improve the sensitivity of a SQUID is to decrease the temperature, see Eqns. (1.24) to (1.26). The first limitation here is given by the hot-electron effect [72, 73], which occurs typically at bath temperatures below 1 K. It leads to a saturation of the temperature of the electrons in the shunt resistors of a SQUID and thus also to a saturation of the thermal noise of the shunt resistors. This effect will be investigated closer in chapter 4.

The second limit here is of quantum mechanical origin. The best reachable sensitivity of the SQUID for a perfectly matched input impedance is, in terms of a minimum reachable equivalent input noise temperature $T_{N0}$, given by [59, 64, 74]:

$$T_{N0} = \frac{\pi f}{k_B |G_{V\Phi}|}\sqrt{S_{VV}\,S_{JJ} - {S_{JV}}^2} = \frac{2\pi f}{k_B}\varepsilon_0 \tag{1.28}$$

$$\varepsilon_0 = \sqrt{\varepsilon_{VV}\varepsilon_{JJ} - {\varepsilon_{JV}}^2} \gtrsim \hbar/2 \tag{1.29}$$

This minimum noise temperature is, in the limit of very low temperatures $T \to 0$, restricted by quantum mechanics. Numerical simulations on SQUIDs with noise variables $i_{N1}$, $i_{N2}$ that model the zero-point fluctuations at the Josephson frequency, suggest that the minimum value for $\varepsilon_0$ is $\hbar/2 = h/(4\pi)$ [16, 17]. This result is close to the fundamental noise temperature achievable with any linear, phase insensitive, amplifier [16, 17, 74, 75]. Accordingly, the SQUID seems to have the potential to reach the quantum limit.

The signal-to-noise ratio of SQUID amplifiers in the thermal noise limit will be discussed in more detail in chapters 2 and 3.

## 1.4 Practical SQUID systems

### 1.4.1 Practical SQUID designs

SQUIDs are usually fabricated using thin-film processes, for an overview see for example chapter 3 of reference [2]. The Josephson junctions are directly integrated on one chip with the SQUID inductance, which is usually made of a so-called *washer* structure [76], an

open superconducting thin-film structure which is shorted by the Josephson junction. The enclosed free area can be used for coupling an external signal flux. The SQUID designs treated in chapter 5 were fabricated at the foundry at the *IPHT Jena* in the "LTS SQUID" process [77]. Here, $Nb/Al_2O_3-Al/Nb$ SINS Josephson junctions are used and two layers of *Nb* are available to form superconducting structures.

For many applications of SQUID amplifiers, a good coupling to the object of interest is of importance. Thus, a high coupling factor $k$ between the input coil $L_{IN}$ and the SQUID inductance $L_{SQ}$, as shown in Fig. 1.3, is desirable. This can be effectively achieved by integrating the input coil on top of the washer structure. Introduced parasitic capacitances within the design can strongly influence the dynamics of the SQUID, see for example references [65, 78–84]. This will be investigated in more detail in chapters 3 and 5.

Furthermore, we want to name another typical design that we also employed, the *resistively shunted SQUID*. Here, the SQUID inductance $L_{SQ}$ is connected to a parallel resistance. This design has some interesting properties [85–87]. Besides possibly damping resonances, it also allows to improve the performance of sub-optimal SQUIDs with $\beta_L \gg 1$. Also this will be treated in more detail in chapters 3 and 5.

### 1.4.2 SQUID electronics

Good reviews on SQUID electronics can be found in reference [88] or in chapter 4 of reference [2]. Here, we will introduce concepts and effects important for our purpose. We concentrate on the nowadays widely spread *directly coupled SQUID electronics*, which we also used throughout the experiments in chapter 4 and 5. Because we do not have to deal with $1/f$ noise, we did not have to use modulation schemes [2].

For our case, as in most of the experiments, the SQUID electronics fulfill mainly two purposes. On the one hand, the response of the SQUID has to be linearized. On the other hand, the SQUID has to be read out without degrading the sensitivity. The measurements shown in chapter 4 and 5 were partly performed at bath temperatures below 1 K. This asks for special measures for a low noise readout of the SQUID by the room temperature electronics.

#### Sensitivity

If the SQUID is biased with a constant current, as assumed in the last section, the readout electronics need to measure small changes in the voltage response $V$ of the SQUID without adding significant noise. According to Eqns. (1.23) and (1.27), the voltage noise PSD at the output of an optimized SQUID is $\approx 16 k_B T R$. For practical low-$T_c$ SQUIDs this leads to levels in voltage noise that can be hard to measure without a degradation of the sensitivity. The simple schematic of such a configuration is shown in Fig. 1.6(a). Here, the SQUID electronics are modeled as a high impedance $|Z_{AMP}| \gg G_{VI}$ voltage amplifier with a gain $G_{AMP}$ and two noise sources. A voltage noise $V_{N,AMP}$ with a PSD $S_{VV,AMP}$ models additional noise whereas the current noise source $I_{N,AMP}$ with a PSD $S_{II,AMP}$ models back-action noise from the amplifier. Both contributions are referred to the input of the amplifier. The amplifier noise can be added to the SQUID output noise in the following way, where uncorrelated noise sources and a high input impedance of the amplifier $R_{AMP} \gg G_{VI}$ were assumed [88]:

$$S_{VV} = S_{VV}{}' + S_{VV,AMP} + {G_{VI}}^2 S_{II,AMP} \tag{1.30}$$

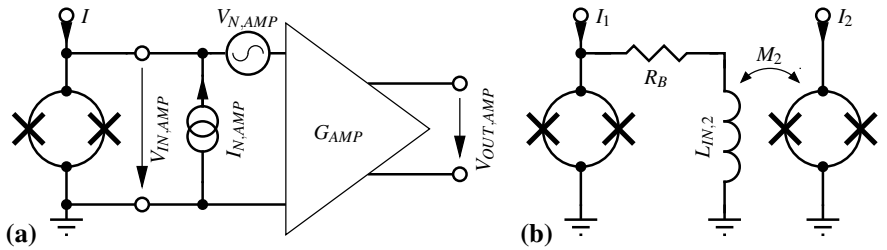


**Figure 1.6:** Schematics of **(a)** Directly coupled SQUID electronics including additional and back-action noise sources. **(b)** Two-stage SQUID setup.

Here, $S_{VV}{}'$ is the output voltage noise of the autonomous SQUID. Via the reverse transfer function $G_{JI}$ of the SQUID, the back-action and the correlation term can also have an influence:

$$\begin{aligned} S_{JJ} &= S_{JJ}{}' + G_{JI}{}^2\, S_{II,AMP} \\ S_{JV} &= S_{JV}{}' + G_{VI}\, G_{JI}\, S_{II,AMP} \end{aligned} \tag{1.31}$$

Here, $S_{JJ}{}'$ and $S_{JV}{}'$ are the back-action PSD and correlation spectral density of the autonomous SQUID, respectively. For a low noise operation, all the additional terms introduced by the readout electronics, should be minimized.

Optimized low noise room temperature SQUID electronics reach input voltage noise levels of $\sqrt{S_{VV,AMP}} \sim 0.3\ \mathrm{nV}/\sqrt{\mathrm{Hz}}$ [88], which is too high for measurements on typical SQUIDs, especially operated at temperatures below 4 K.

One way to solve this problem is a *two-stage SQUID setup* [2, 18, 89, 90], which is shown in Fig. 1.6(b). Here, the first stage SQUID, or sensor SQUID, is voltage biased via a small bias resistor $R_B \ll G_{VI,1}$ connected in parallel to the SQUID. This results in a working point of the SQUID at a voltage $\approx I_1 R_B$. A small flux change on the input of the first stage SQUID $\Delta\Phi_{E,1}$ causes a current $\approx \Delta\Phi_{E,1}\, G_{V\Phi,1}/G_{VI,1}$ in the output loop of the first stage. Here, $G_{V\Phi,1}$ and $G_{VI,1}$ represent the flux-to-voltage transfer and the output resistance of the first stage SQUID, respectively. If a loading of the first stage SQUID at the Josephson frequency is neglected, one can simply use the current-bias parameters of the SQUID as defined in the last section. The output current is then measured by a second SQUID via its coupling inductance $L_{IN,2}$. The total gain from the voltage of the first to the voltage of the second SQUID now reads:

$$G_{V1,V2} \approx \frac{M_2\, G_{V\Phi,2}}{G_{VI,1}} \tag{1.32}$$

Here, the input mutual inductance $M_2$ and flux-to-voltage transfer of the second stage SQUID were used. Under the condition $R_B \ll G_{VI,1}$ and the assumption that the bias resistor and the first stage SQUID are placed at the same bath temperature, the noise of the bias resistor can be neglected with respect to the voltage noise $\approx 16 k_B T R$ of the SQUID. Furthermore, back-action noise originating from the second stage SQUID can be neglected. The voltage noise at the output of the second stage then reads

$$S_{VV,2} \approx G_{V1,V2}{}^2\, S_{VV,1} + S_{VV,2}{}' \tag{1.33}$$

where the voltage noise PSD of the autonomous second stage SQUID $S_{VV,2}{}'$ was used. A

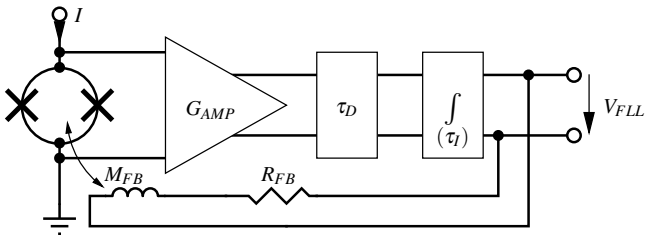


**Figure 1.7:** Simple schematic of a flux-locked loop electronics which consists of an amplifier with gain $G_{AMP}$, a delay element with time constant $\tau_D$ and an integrator with time constant $\tau_I$. A voltage offset can be adjusted in the electronics to set the working point.

high gain between the first and the second stage $G_{V1,V2}$ allows to eliminate the noise of the second stage and the following room temperature readout electronics. In case the gain $G_{V1,V2}$ is too high, filter inductances have to be placed in series with $L_{IN,2}$.

### Linearization of the SQUID response

The overall response of the SQUID can be linearized by negative feedback [91]. A schematic of a single pole *flux-locked loop* (FLL) setup is shown in Fig. 1.7. Small changes in voltage on the SQUID are measured, integrated and fed back to the SQUID via a mutual inductance with the SQUID $M_{FB}$. This leads to a constant flux point of the SQUID at small frequencies. In principle, the feedback can be directly applied via the coupling inductance of the SQUID $L_{IN}$. Nevertheless, in practice a separate feedback coil is typically used.

For an ideal FLL with a basic single-pole integrator, the output voltage of the FLL $V_{FLL}$ reads:

$$V_{FLL} = \Phi_E \frac{R_{FB}}{M_{FB}} \frac{1}{1+\mathrm{j}2\pi f \tau_{FLL}} \tag{1.34}$$

$$\tau_{FLL} = \left| \frac{R_{FB}}{M_{FB}} \frac{\tau_I}{G_{AMP} G_{V\Phi}} \right| \tag{1.35}$$

Here, $f$ is the frequency of the signal flux $\Phi_E$ in the SQUID, $G_{AMP}$ is the gain of the amplifier and possibly of a two-stage setup, $G_{V\Phi}$ is the flux-to-voltage transfer of the SQUID and $\tau_I$ is the time constant of the integrator. The overall time constant of the FLL $\tau_{FLL}$ determines the bandwidth.

Equation (1.35) is only valid for large time constants of the FLL $\tau_{FLL} \gg \tau_D$. Here, $\tau_D$ is the time constant associated with the delay element indicated in Fig. 1.7. If one tries to increase the bandwidth further, the frequency response changes and the FLL can become unstable [88]. The delay element models the time the signals need to travel between the SQUID and the room temperature electronics or the bandwidth of the open loop chain for example. The latter is influenced by the bandwidth of the readout amplifier or of a two-stage setup.

The influence of the FLL, as given in Eqn. (1.34), on the operation of a SQUID with a connected input impedance will be examined in more detail in chapter 2.

## 1.5 Readout of the first spherical gravitational wave antenna MiniGRAIL

SQUID amplifiers are interesting for a wide range of measurements. Besides their application as a magnetometer with an externally connected pickup-coil, there are several other types of measurements that can be conducted. There are many quantities that can be transformed into a weak electrical current which then can be measured by a SQUID amplifier. For example, the SQUID-based critical current comparators are extremely sensitive devices for measuring electrical signals. SQUIDs were used to perform noise thermometry, to read out thermal detectors for astronomy such as transition edge sensors or superconducting tunnel junctions and to perform measurements on qubits. An overview of possible applications can be found in reference [3].

In our case, the designated application is the readout of the first spherical resonant mass gravitational wave antenna *MiniGRAIL*, which is situated at Leiden University in the Netherlands. The quantity to determine here is thus an extremely small displacement. An overview on MiniGRAIL can be found in references [30–33].

The core of MiniGRAIL is a 1.4 ton heavy *CuAl* sphere with a diameter of 68 cm cooled down to cryogenic temperatures. The sphere has resonance modes with frequencies around 3 kHz and high quality factors of $\sim 10^6$. In case a gravitational wave is passing, some energy is coupled to the mass, whose different modes begin to resonate. This directly leads to the advantage of the spherical detector with respect to laser interferometers or resonant bar detectors. From the different resonant modes, the direction and polarization of a passing gravitational wave can be determined. To achieve this, the displacement of the surface of the sphere has to be measured at six points in a so-called *TIGA* configuration.

The high quality factor of the sphere keeps the influence of mechanical thermal noise low. A further measure to reduce mechanical noise is to lower the temperature. The intended temperature of the whole system of 20 mK is approached using an integrated dilution refrigerator. These extremely low temperatures need to be reached to be able to measure a low *strain sensitivity*, the relative displacement of the surface of the sphere compared to its diameter. The goal for the strain sensitivity is below $10^{-21}/\sqrt{\text{Hz}}$. The system is mechanically isolated from the environment by means of extreme mechanical damping of the sphere and its readout instruments.

The displacement of the surface of the sphere is in MiniGRAIL converted into an electrical signal using a capacitive transducer. The whole readout system is shown in Fig. 1.8. A displacement of the surface of the sphere is first mechanically amplified by two mass-spring systems, whereas the second mass forms a part of the capacitive transducer. This transducer has a capacitance of about $C_T \approx 5$ nF and is charged with up to 200 V. The capacitive transducer is a plate capacitor with a gap of tens of micrometers. A modulation of this gap generates a current that is coupled to the SQUID. A decoupling capacitance with values much bigger than $C_T$ prevents the transducer to discharge. The impedance matching of the high impedance of the capacitor to the much smaller inductive input impedance of the SQUID is achieved by a transformer. The electrical resonance frequency is close to the resonance frequencies of the different modes. The requirement of low dissipation is of course also valid for the electrical circuit.

Minimum experimental strain sensitivities at a temperature of 5 K were in the order of

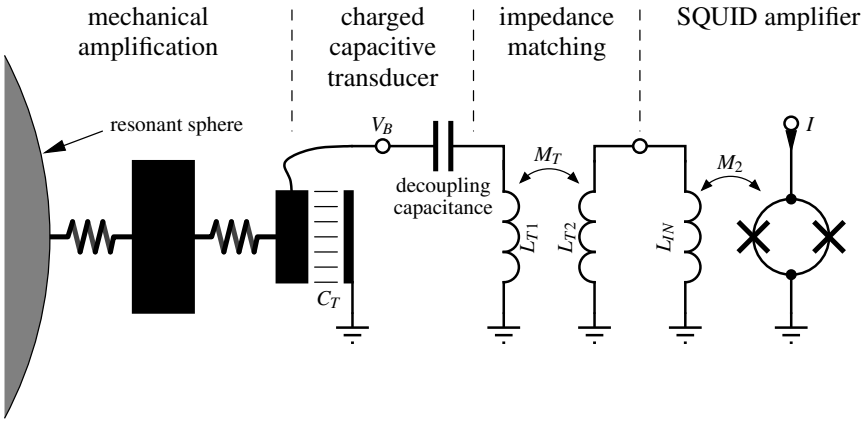


**Figure 1.8:** Simplified readout schematic of MiniGRAIL with the capacitive transducer $C_T$.

$10^{-20}/\sqrt{\text{Hz}}$ [33], which is sensitive enough for the detection of a gravitational wave signal originating from a supernova within our galaxy [31]. The corresponding displacement is $\sim 10^{-19}$ m [33]. The most dominant noise sources during this run were mainly mechanical thermal noise and the noise contribution of the SQUID amplifier. The improvement of the latter sets the focus of this thesis.

Although the topics of this thesis are mainly influenced by the requirements of the MiniGRAIL project, this work can be read in the general context of best possible SQUID measurements in the intermediate frequency range. In chapter 2, we deal with the question how SQUID systems behave with different connected input impedances. One of these impedances is a capacitance as in the case of MiniGRAIL. In chapter 3 we summarize, based on the results of chapter 2, the optimization of SQUIDs. The low bath temperatures of MiniGRAIL suggest an operation of the SQUID at these temperatures. Here, the already mentioned hot-electron effect is dominating on the sensitivity of the SQUID. In chapter 4, we describe experiments and calculations on the suppression of influences of the hot-electron effect. In the final chapter 5, we shows the design and characterization of SQUIDs for an optimized readout of MiniGRAIL.

# Chapter 2

# Low noise utilization of dc-SQUID amplifiers

For a practical low noise utilization of a SQUID amplifier, many effects have to be taken into account. First of all, the small-signal parameters of the SQUID, see Eqns. (1.15)–(1.16) on page 9, determine its effective input impedance as well as its gain. Secondly, its noise parameters, see Eqns. (1.20)–(1.22), influence the achievable signal-to-noise ratio. Thirdly, in practice the SQUID is usually linearized by means of a flux-locked loop, see section 1.4.2 on page 15, which should therefore be included in an analysis. The motivation for this chapter was to investigate the influence of all of these aspects on the practical performance of a SQUID based readout system for a general input circuit.

In section 2.1 we will introduce our basic assumptions regarding the SQUID dynamics. The SQUID dynamics can be influenced by the presence of a connected input circuit. We give a brief overview of studies in literature. Here, partly contradicting effects are postulated. We define our assumption for the following analysis.

In section 2.2, we show a small-signal analysis of the SQUID amplifier with a general input impedance connected to its input inductance. We incorporate the influence of the small-signal and noise parameters of the SQUID, the loading of the SQUID via a connected output circuit and a possible FLL operation. Parasitic mutual inductances that can be of importance in a practical measurement are included. Both the loading of the SQUID and the FLL operation can be modeled as feedback effects that on the one hand change the frequency response of the system and on the other hand shift noise contributions between the output and the input of the SQUID amplifier.

These feedback effects are investigated closer in section 2.3. Here, we especially focus on the input impedance of the amplifier and derive expressions for influences of a loading of the SQUID via an output circuit, the SQUID operated in FLL or a combination of both. The results give a possible explanation for measured resistive parts of the input impedance of SQUIDs operated in direct readout.

In the following section 2.4, we describe the achievable signal-to-noise of the system. It turns out that the feedback effects have no influence here. We derive the SQUID equivalent input noise temperature and express it in a general form which is independent of the connected input circuit. Based on this, we define three parameters of the SQUID that determine the

noise temperature with an arbitrary connected input impedance.

In the final section 2.5, we investigate the performance of three basic input circuits: a resistive, an inductive and a capacitive input circuit. For each of these cases, we derive expressions for the noise temperature as well as noise spectra in practical measurements. On the basis of this, we introduce a new technique to determine all noise parameters of a SQUID connected to a variable input inductance. For the resistive and capacitive input impedance, we introduce a way to characterize parasitic mutual inductances within the system. The influence of these parasitic elements on the stability of a capacitive input impedance is discussed. For the case of the capacitive input impedance, we derive an analytic expression for the achievable bandwidth.

## 2.1 SQUID dynamics in the presence of an input circuit

Before discussing the effects of the SQUID on a coupled input circuit, we want to give our basic assumptions about the opposite case. The input circuit can also influence the dynamics of the SQUID.

The schematic shown in Fig. 2.1 on page 22 shows our used model of a dc-SQUID coupled to a general input impedance $\bar{Z}_L$. The dynamics of the SQUID are determined at the Josephson frequency, see Eqn. (1.7) on page 4. Furthermore, the SQUID dynamics are dependent on the inductance of the SQUID $L_{SQ}$. In case $\bar{Z}_L$ represents an inductance, one can directly see that for small values of the coupled inductance and for high coupling factors $k$, the effective SQUID inductance is screened by the input circuit. In this case, the dynamics of the SQUID are changed. The same holds for the case that $\bar{Z}_L$ represents a resistive or capacitive input impedance. At the Josephson frequency, the effective SQUID inductance is screened by the input circuit.

There have been several groups of publications discussing the altered SQUID dynamics with a connected input impedance. Partly contradicting results were found. Here, we want to give a short overview before defining our assumptions regarding this effect.

The first group can be summarized in the two publications by Clarke et al. [64] and Danilov et al. [59]. They used a simple model of a SQUID just characterized by its low frequency parameters. An altered operation of the SQUID due to the presence of the input impedance is not treated.

The second group of publications by Tesche [74, 92] and Martinis et al. [93] analyzed the problem under the practical assumption that the effective SQUID inductance changes at a frequency much below the Josephson frequency. They treated this problem by splitting the equations of the SQUID into the nonlinear equations of a *reduced SQUID* with a lowered effective inductance at the Josephson frequency and a linear part accounting for the low frequency response of the SQUID. This will be treated in more detail in chapter 3. The derived results were not only that the SQUID dynamics change, also new features in the influence of noise of the SQUID at the measurement frequency were derived.

Nevertheless, in reference [93] from the second group of publications, the authors considered the case of “capacitive effects” within the SQUID design. The assumption for this case was that no currents are flowing through the connected input impedance $\bar{Z}_L$ at the Josephson frequency. This can be caused by a distributed capacitance between the input coil

and the SQUID inductance. For the case of "capacitive effects", the low frequency interaction of the SQUID with the connected input circuit follows the model as assumed in the first group of publications, only the exact small-signal and noise parameters are determined by the SQUID dynamics in the presence of intrinsic distributed capacitances.

A third group of publications, the papers by Folkner et al. [94] and by Carroll [68] states that the SQUID is influenced by the connected impedance but it does not necessarily introduce completely new effects. According to both publications [68, 94], the known small-signal parameters at low frequencies are sufficient to describe the effective input impedance and the gain of a SQUID amplifier, independent of the dominant mechanism at the Josephson frequency. In reference [68], also the influence of noise is treated. The results suggest that the same holds here. Most likely, there are no additional noise features at the measurement frequency.

Regarding these partly contradicting results, we conclude that the first group of publications is applicable. The analysis just has to be based on the correct small-signal and noise parameters of the SQUID. In this chapter, we will ignore what determines the SQUID dynamics: the SQUID can be a standard SQUID as introduced in section 1.3 on page 7, it could be influenced by intrinsic capacitances and it could possibly be loaded by connected external circuits at the Josephson frequency. Furthermore, we assume that it does not matter in which frequency range the effective SQUID inductance is undergoing a change. This can happen either above, below or at the measurement frequency.

In chapter 3, section 3.4, we will test this assumption by means of numerical experiments on SQUIDs with strongly coupled capacitive input circuits.

## 2.2 Small-signal description of the system

We performed a small-signal analysis of the SQUID amplifier and its readout system with a connected input circuit based on the schematic shown in Fig. 2.1. In the rest of this chapter we will, unless explicitly stated otherwise, use small-signal values around one working point. Because we wanted to study effects of the FLL, we include a feedback coil with mutual inductances $M_{FB,SQ}$ to the SQUID and $M_{FB,IN}$ to the input circuit. The latter is usually considered of parasitic origin. Furthermore, two complex impedances are connected to the SQUID. The input impedance $\bar{Z}_L = R_L + \mathrm{j}X_L$ is connected to the input coil of the SQUID, it resembles the measurement object of interest. The voltage source $V_L$ models a signal source which will be later used to model thermal noise originating from the real part of the input impedance of the SQUID $\Re[\bar{Z}_L]$. The impedance connected to the output of the SQUID $\bar{Z}_{OUT} = R_{OUT} + \mathrm{j}X_{OUT}$ resembles the input impedance of the next amplifier stage.

The small-signal parameters of the SQUID $G_{V\Phi}$, $G_{J\Phi}$, $G_{VI}$ and $G_{JI}$ are assumed to be known at low frequencies. We also assume known noise parameters $S_{VV}$, the power spectral density (PSD) of the voltage of the SQUID, $S_{JJ}$, the PSD of the circulating current in the SQUID, and $S_{JV}$, the correlation spectral density of $V_N$ and $J_N$. They correspond to the parameters of an autonomous SQUID as introduced in section 1.3. The SQUID inductance $L_{SQ}$ also represents the effective value at the measurement frequency.

The effect of a resistive part of the input impedance of the autonomous SQUID would be represented by a complex dynamic inductance $1/\bar{G}_{J\Phi}$. Here, time delays are basically

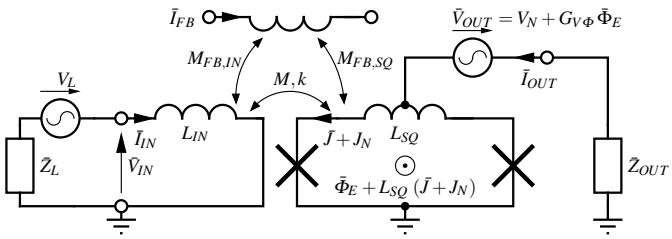


**Figure 2.1:** Schematics used for the small-signal analysis of the SQUID system with a connected input impedance $\bar{Z}_L$, a loading output impedance $\bar{Z}_{OUT}$ and a feedback coil for the FLL operation.

caused by the nonlinear inductive SQUID loop in combination with the shunt resistors. For this effect the time constant can only take positive and very small values in the order of the Josephson oscillations [59, 64, 65]. We will neglect this effect due to the the low measurement frequency $f$ compared to the Josephson frequency: $f \ll f_J$. We therefore assume $G_{J\Phi}$ to be real. We will come back to this issue below.

For completion, we directly want to point out that we performed the following calculation also including mutual inductances between the output circuit and the rest of the loops. For our low frequency case, the direct induction of voltages in the output loop can be neglected because of its rather small magnitude compared to voltages generated via the flux-to-voltage transfer function $G_{V\Phi}$. The mutual inductances between the output circuit and the SQUID loop $M_{OUT,SQ}$ and between the output circuit and the input circuit $M_{OUT,IN}$ couple magnetic flux from the output current $\bar{I}_{OUT}$ to the SQUID inductance $L_{SQ}$ and the input inductance $L_{IN}$, respectively. These mutual inductances can be included in the small-signal parameters of the SQUID:

$$G_{VI} = G'_{VI} + M_{OUT,SQ}\, G_{V\Phi} \tag{2.1}$$

$$G_{JI} = G'_{JI} + M_{OUT,SQ}\, G_{J\Phi} + M_{OUT,IN}/M \tag{2.2}$$

Here, the parameters with the apostrophe represent the values for the autonomous SQUID without the respective geometrical inductive coupling. The parasitic mutual inductances $M_{OUT,SQ}$ and $M_{OUT,IN}$ are not shown in Fig. 2.1 for simplicity.

The directions of the currents are chosen such that positive currents $\bar{J}$, $\bar{I}_{IN}$ and $\bar{I}_{FB}$ generate positive external flux $\bar{\Phi}_E$ through the SQUID loop, where we at the same time defined the mutual inductances $M$ and $M_{FB,SQ}$ to be positive. Accordingly, the total small-signal flux in the SQUID loop reads $\bar{\Phi}_E = M\,\bar{I}_{IN} + M_{FB,SQ}\,\bar{I}_{FB}$. The small-signal voltage measured on the output of the SQUID is $\bar{V}_{OUT} = V_N + G_{V\Phi}\,\bar{\Phi}_E$. The third mutual inductance $M_{FB,IN}$ can take positive and negative values, depending on the origin of the coupling. For a standard SQUID with one washer and both coils coupling to the same inductance, $M_{FB,IN}$ is typically positive. This can be changed for example by adding a small transformer between the input and the feedback loop [94]. Writing down the Kirchhoff law for the input and the output loop yields:

$$\begin{aligned} 0 = {} & -V_L + \mathrm{j}\omega M J_N + (\mathrm{j}\omega L_{IN} + \bar{Z}_L)\,\bar{I}_{IN} \\ & + \mathrm{j}\omega\,(M_{FB,IN} + M_{FB,SQ}\, G_{J\Phi} M)\,\bar{I}_{FB} + \mathrm{j}\omega M\, G_{JI}\,\bar{I}_{OUT} \end{aligned} \tag{2.3}$$

$$0 = V_N + G_{V\Phi} M\,\bar{I}_{IN} + G_{V\Phi} M_{FB,SQ}\,\bar{I}_{FB} + (G_{VI} + \bar{Z}_{OUT})\,\bar{I}_{OUT} \tag{2.4}$$

In this chapter we use the angular frequency $\omega = 2\pi f$. For the used voltages and currents see Fig. 2.1. In case the FLL is used, the negative feedback is applied such that the voltage across the output of the SQUID stays constant. Assuming a standard directly coupled FLL scheme [2] with a single-pole integrator, see Eqn. (1.34) on page 15, the following expressions for the feedback current can be used for the "direct readout" and the "flux-locked loop" (FLL) case:

Direct readout:

$$\bar{I}_{FB,\mathrm{DIR}} = 0 \tag{2.5}$$

Flux-locked loop:

$$\bar{I}_{FB,\mathrm{FLL}} = -\frac{M\bar{I}_{IN} + V_N/G_{V\Phi}}{M_{FB,SQ}\left(1 + \mathrm{j}\omega\,\tau_{FLL}\right)} \tag{2.6}$$

Here, $\tau_{FLL}$ is the time constant of the FLL, see Eqn. (1.34), which can only take positive real values. Combining Eqns. (2.3) to (2.6) allows to determine the input impedance of the SQUID $\bar{Z}_{IN}$ and the direct influence of the noise contributions on the input loop:

$$\bar{\Phi}_M = \bar{V}_{OUT}/G_{V\Phi} = M\bar{I}_{IN} + V_N/G_{V\Phi} \tag{2.7}$$

$$\bar{Z}_{IN} = \mathrm{j}\omega L_{IN}\left(1 + k^2 g_{J\Phi}\right) + \bar{Z}_{FB} \tag{2.8}$$

$$g_{J\Phi} = L_{SQ} G_{J\Phi} \tag{2.9}$$

$$\bar{V}_{IN} = \bar{Z}_{IN}\bar{I}_{IN} + \mathrm{j}\omega M J_N + \bar{Z}_{FB} V_N \big/ (G_{V\Phi} M) \tag{2.10}$$

$$\bar{I}_{IN} = \left(V_L - \bar{V}_{IN}\right)/\bar{Z}_L \tag{2.11}$$

The output signal can be considered as the measured flux in the SQUID $\bar{\Phi}_M$ in both the direct readout and the FLL case. It is only indirectly determined by the output voltage of the SQUID in direct readout and by the feedback current in FLL. Furthermore, we normalized the dynamic inductance of the SQUID to the SQUID inductance, see Eqn. (2.9).

The impedance $\bar{Z}_{FB}$, which was introduced in Eqns. (2.8) and (2.10), describes the influence of *feedback effects* originating from both the loading of the SQUID via the output circuit and from the negative feedback in FLL operation, or a combination of the two. The exact values of $\bar{Z}_{FB}$ will be given in the following section.

## 2.3 Influence of external circuits on the input loop

Both the loading of the SQUID via a connected output circuit and the influence of the FLL operation can be seen as *feedback effects*. Accordingly, both contributions are modeled by a virtual impedance $\bar{Z}_{FB}$ in Eqns. (2.8) and (2.10). As one can see from Eqn. (2.8), feedback causes a deviation of the input impedance from the purely imaginary input impedance of the autonomous SQUID $\mathrm{j}\omega L_{IN}\left(1 + k^2 g_{J\Phi}\right)$ [59]. Furthermore, it describes how the voltage noise $V_N$ at the output of the SQUID is fed back into the input circuit and acts as a back-action noise, see Eqn. (2.10).

To model the loading of the SQUID via the connected output circuit, we introduce the output time constant $\tau_{OUT}$:

$$\tau_{OUT} = \frac{X_{OUT}}{\omega\left(R_{OUT} + G_{VI}\right)} \tag{2.12}$$

This time constant $\tau_{OUT}$ can take positive and negative values. As one can see, it describes the phase shift between the output voltage of the SQUID $\bar{V}_{OUT}$ and the response current in the output loop $\bar{I}_{OUT}$ due to the imaginary load.

It is useful to norm the impedances to the geometric input inductance of the SQUID:

$$\begin{aligned} \bar{z}_{FB} &= \frac{\bar{Z}_{FB}}{\omega L_{IN}} = \frac{X_{FB}}{\omega L_{IN}} \left( \frac{R_{FB}}{X_{FB}} + \mathrm{j} \right) = \ell_{FB} \left( \omega \tau_{FB} + \mathrm{j} \right) \\ \bar{z}_{IN} &= \frac{\bar{Z}_{IN}}{\omega L_{IN}} = \mathrm{j} \left( 1 + k^2 g_{J\Phi} + \ell_{FB} \right) + \omega \tau_{FB} \ell_{FB} \end{aligned} \tag{2.13}$$

Here, we introduced the normed change in the input inductance of the SQUID $\ell_{FB}$ caused by the feedback effects. Furthermore, any change in effective input inductance is accompanied by the generation of a resistive part. This is characterized by a time constant $\tau_{FB}$ which is connected to the feedback mechanism. Combining Eqns. (2.3)–(2.11), these quantities read for either direct readout or FLL operation:

Direct readout: (2.14)

$$\begin{aligned} \ell_{FB,\mathrm{DIR}} &= -\frac{k^2 L_{SQ} G_{JI} G_{V\Phi}}{(R_{OUT} + G_{VI}) (1 + \omega^2 {\tau_{OUT}}^2)} \\ &\approx -\frac{k^2 L_{SQ} G_{JI} G_{V\Phi}}{R_{OUT} + G_{VI}} \\ \tau_{FB,\mathrm{DIR}} &= \tau_{OUT} \end{aligned}$$

Flux-locked loop: (2.15)

$$\begin{aligned} \ell_{FB,\mathrm{FLL}} &= -\frac{1}{1 + \omega^2 {\tau_{FLL}}^2} \left( k^2 g_{J\Phi} + \frac{k k_{FB,IN}}{k_{FB,SQ}} + \ell_{FB,\mathrm{DIR}} \omega^2 \tau_{FLL} \tau_{OUT} \right) \\ &\approx -k^2 g_{J\Phi} - \frac{k k_{FB,IN}}{k_{FB,SQ}} \\ \tau_{FB,\mathrm{FLL}} &= \tau_{FLL} \left( 1 + \frac{\ell_{FB,\mathrm{DIR}}}{\ell_{FB,\mathrm{FLL}}} \omega \tau_{FLL} (1 - \omega \tau_{OUT}) \right) \\ &\approx \tau_{FLL} \end{aligned}$$

The approximate expressions in Eqns. (2.14) and (2.15) are correct for $\omega \left| \tau_{FLL/OUT} \right| \ll 1$ and the fact that in a common SQUID setup usually $|\ell_{FB,\mathrm{DIR}} / \ell_{FB,\mathrm{FLL}}| \lesssim 1$ is valid. Note that, because in general $|\tau_{OUT}|$ determines the bandwidth in direct readout, the total time constant in FLL $\tau_{FLL}$ has to be chosen larger than $|\tau_{OUT}|$, see section 1.4.2 on page 13.

Looking at the different terms in Eqns. (2.14) and (2.15), one can see several effects that change the properties of the autonomous SQUID. These effects are caused by feedback from the output of the SQUID to the input via direct loading, via the FLL or a combination of both. The imaginary part of the output loop alters the input impedance of the SQUID via $G_{V\Phi}$ and $G_{JI}$ and generates a positive or negative real part, see Eqn. (2.14). In FLL, this effect is usually negligible, see Eqn. (2.15).

In Eqn. (2.15), one can see the dominant effects of the FLL. Here, the influence of the dynamic inductance of the SQUID $1/g_{J\Phi}$, which usually screens the geometric inductance $L_{IN}$, is canceled out [94]. Also in this case, a resistive component is generated by the time

constant of the FLL $\tau_{FLL}$. Furthermore, the (parasitic) coupling $k_{FB,IN}$ is directly altering the input inductance and generates resistive parts [94]. For a standard single-hole SQUID with $k_{FB,IN} > 0$, the generated resistance takes negative values. In section 2.5.1 we will describe one way to experimentally determine $k_{FB,IN}$. Note that applying the feedback directly via the input inductance $L_{IN}$ can simply be modeled by setting $k\,k_{FB,IN}/k_{FB,SQ} = 1$ in Eqns. (2.3)–(2.15). This results for $\omega\,\tau_{FLL} \ll 1$ in a total effective input impedance of the SQUID of only a negative resistive value and a very small inductive part.

The time constant of the feedback $\tau_{FB}$ is, besides changing the overall frequency response of the system, of special interest. In case a capacitive impedance is connected, a total negative resistance in the input loop can cause instabilities. This will be treated in section 2.5.3.

Resistive parts of the effective input impedance of the SQUID $\bar{z}_{IN}$ were studied in direct readout in references [65, 66] and compared to the already mentioned, and here neglected, theoretical time constant connected to a change in the circulating current of the autonomous SQUID [59, 65]. Here, time delays are basically caused by the nonlinear inductive SQUID loop in combination with the shunt resistors. The time constant of the autonomous SQUID can only take positive and very small values in the order of the Josephson oscillations.

The actually measured effects in references [65, 66] showed in both cases much larger time constants with positive and negative values. In both cases, the time constants were approximately proportional to the flux-to-voltage transfer $G_{V\Phi}$. Our treatment, see Eqns. (2.13)–(2.14), suggests a proportional dependency with $G_{V\Phi}$ and $\tau_{OUT}$. The time constant $\tau_{OUT}$, see Eqn. (2.12), typically takes in a practical setup much larger values than the timescale of the Josephson oscillations.

In case of employed *directly coupled SQUID electronics*, see Fig. 1.6 on page 14, $\bar{Z}_{OUT}$ can in practice be approximated by an input resistance of the amplifier connected in parallel to a parasitic capacitance $1/\bar{Z}_{OUT} = 1/R_{AMP} + \mathrm{j}\omega C_{AMP}$. This simplifies for $\omega\,R_{AMP}\,C_{AMP} \ll 1$ to $\bar{Z}_{OUT} \approx R_{AMP}\,(1 - \mathrm{j}\omega\,R_{AMP}C_{AMP})$. Using $R_{AMP} \gg G_{VI}$, this leads with Eqn. (2.12) to $\tau_{OUT} \approx -R_{AMP}C_{AMP}$.

In case the SQUID is used in a two-stage SQUID setup, which is also depicted in Fig. 1.6, it is biased via a small bias resistor $R_B$ in one loop with the input inductance of the second stage SQUID $L_{IN,2}$. This leads to $\tau_{OUT} \approx L_{IN,2}/\,(G_{VI} + R_B)$.

There is no precise description of the readout circuit of the SQUIDs measured in references [65, 66], but we believe that the measurements could be explained by this model. In general, one can say that a large reverse transfer function of the SQUID $|G_{JI}|$, a small loading output resistance $R_{OUT}$ and a large time constant of the output circuit $\tau_{OUT}$ increase effective input resistances. Also see Eqn. (2.2) for the influence of parasitic inductances within the SQUID system on $G_{JI}$. From our point of view, the model of a capacitive coupling between the output of the SQUID and the input coil, as presented in reference [65], does not hold for a SQUID with a reasonably symmetric coil layout and parasitic capacitances of the coil in the order of the capacitance of the Josephson junctions.

## 2.4 Equivalent input noise temperature

As pointed out before, in direct readout and FLL one can consider the output signal of the amplifier as the measured flux in the SQUID $\bar{\Phi}_M$. This signal can also be refered to the input loop. Combining Eqns. (2.7)–(2.11), the measured flux can be expressed in an equivalent

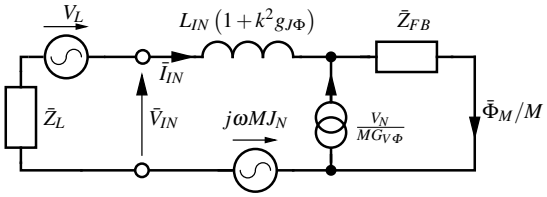


**Figure 2.2:** Schematic of the amplifier including feedback effects, represented by $\bar{Z}_{FB}$. The frequency response of the system as well as the influence of additional and back-action noise are modeled.

input voltage $\bar{V}_M$ that represents the sum of the actual input signal $V_L$ and a virtual input noise voltage which is caused by the readout system:

$$\begin{aligned}\bar{V}_M &= \frac{\bar{\Phi}_M\left(\mathrm{j}\omega L_{IN}\left(1+k^2 g_{J\Phi}\right)+\bar{Z}_{FB}+\bar{Z}_L\right)}{M} \\ &= \underbrace{V_L}_{\text{input signal}} + \underbrace{\frac{V_N\left(\mathrm{j}\omega L_{IN}\left(1+k^2 g_{J\Phi}\right)+\bar{Z}_{FB}+\bar{Z}_L\right)}{MG_{V\Phi}}}_{\text{additional noise}} \underbrace{-\mathrm{j}\omega M J_N - \frac{V_N \bar{Z}_{FB}}{M G_{V\Phi}}}_{\text{back-action noise}} \\ &= V_L + V_N \frac{\bar{Z}_L + \mathrm{j}\omega L_{IN}\left(1+k^2 g_{J\Phi}\right)}{MG_{V\Phi}} - \mathrm{j}\omega M J_N \end{aligned} \tag{2.16}$$

If the readout of the SQUID does not introduce further noise contributions, see Eqns. (1.30) and (1.31) on page 13, one can see from Eqn. (2.16) that feedback effects, which are represented by $\bar{Z}_{FB}$, do not alter the noise properties. This was also assumed in reference [64].

The feedback effects can be visualized in a schematic as shown in Fig. 2.2. Note how $\bar{Z}_{FB}$ affects both the total impedance of the input circuit as well as the influence of the output noise $V_N$. $\bar{Z}_{FB}$ still affects the transfer function between $V_L$ and $\bar{\Phi}_M$ but it does not alter the equivalent input voltage $\bar{V}_M$. Accordingly, feedback effects can drive additional noise into the input circuit without changing the signal-to-noise ratio.

The noise contribution of the amplifier can be described by an *equivalent input noise temperature* $T_N$. For this purpose, we first use the input voltage $V_L$ to introduce the Nyquist voltage noise of the resistance of the input circuit $R_L = \Re\left[\bar{Z}_L\right]$ with a PSD of $4k_B T R_L$. The uncorrelated noise contribution of the amplifier, which is part of the noise PSD $S_{V,M}$ of the equivalent input voltage $\bar{V}_M$, can now be expressed as an virtual change of the temperature of the input circuit from $T$ to $T+T_N$ [95]:

$$S_{V,M} = 4k_B(T+T_N)R_L \tag{2.17}$$

$$T_N = \frac{S_{V,M} - 4k_B T R_L}{4k_B R_L} \tag{2.18}$$

We call the equivalent input noise temperature $T_N$ from here on *noise temperature*. To calculate the PSD $S_{V,M}$ of the measured voltage $\bar{V}_M$, one also has to take the correlation between the additional and the back-action noise into account.

Suppose one has two correlated time series $x$ and $y$ with a PSD of $S_{xx}$ and $S_{yy}$, respectively. Their cross spectral density is given by $\bar{S}_{xy}$. For a definition of the spectral densities see Eqn. (1.18) on page 9. The two time series ($x$, $y$) are now in the frequency domain ($\tilde{x}$, $\tilde{y}$) first

multiplied by complex constants $\bar{A}$ and $\bar{B}$ and then added, $\tilde{w} = \bar{A}\,\tilde{x} + \bar{B}\,\tilde{y}$. The PSD $S_{ww}$ of the resulting signal $w$ is given by [95]:

$$S_{ww} = \left|\bar{A}\right|^2 S_{xx} + \left|\bar{B}\right|^2 S_{yy} + 2\,\Re\left[\bar{S}_{xy}\,\bar{A}\,\bar{B}^*\right] \tag{2.19}$$

Here, $^*$ notes the conjugate complex value. As discussed in section 1.3, especially see Fig. 1.5(d) on page 10, imaginary parts of the spectral density $S_{JV}$ of the two noise sources can be neglected at frequencies much smaller than the Josephson frequency. Combining Eqns. (2.16)–(2.19) leads to the following expression for the noise temperature $T_N$ of the SQUID:

$$\begin{aligned} T_N = \frac{1}{4\,k_B\,R_L}\Bigg\{ & S_{VV}\left|\frac{\bar{Z}_L + \mathrm{j}\omega\,L_{IN}\left(1 + k^2\,g_{J\Phi}\right)}{M\,G_{V\Phi}}\right|^2 + S_{JJ}\;\left|-\mathrm{j}\omega M\right|^2 \\ & + 2\,S_{JV}\,\Re\left[\mathrm{j}\omega M\left(\frac{\bar{Z}_L + \mathrm{j}\omega\,L_{IN}\left(1 + k^2\,g_{J\Phi}\right)}{M\,G_{V\Phi}}\right)\right]\Bigg\} \end{aligned} \tag{2.20}$$

As one can see from the respective terms, the correlation between $V_N$ and $J_N$ only has an influence if the two noises are added in-phase. Substituting the energy resolutions, Eqns. (1.20)–(1.22) from page 11, and normalizing the connected input impedance $\bar{Z}_L$, one gets:

$$\bar{z}_L = \frac{\bar{Z}_L}{\omega L_{IN}} = \frac{X_L}{\omega L_{IN}}\left(\frac{R_L}{X_L} + \mathrm{j}\right) = x_L\left(\omega\,\tau_L + \mathrm{j}\right) \tag{2.21}$$

$$\begin{aligned} T_N = \frac{1}{2\,k_B\,\tau_L\,x_L}\Bigg\{ & \frac{\varepsilon_{VV}}{k^2}\left(\left(1 + k^2\,g_{J\Phi} + x_L\right)^2 + \left(\omega\,\tau_L\,x_L\right)^2\right) \\ & + k^2\,\varepsilon_{JJ} - 2\,\varepsilon_{JV}\left(1 + k^2\,g_{J\Phi} + x_L\right)\Bigg\} \end{aligned} \tag{2.22}$$

The introduced parameters are the normalized input reactance $x_L$ and the corresponding time constant $\tau_L$. With some calculation, Eqn. (2.22) can be brought into the following form:

$$T_N = \frac{1}{2\,k_B\,\tau_L\,x_L}\Bigg\{ \underbrace{\frac{\varepsilon_{VV}}{k^2}\left(\left(x_L + 1 + k^2\,g_{J\Phi} - k^2\,\frac{\varepsilon_{JV}}{\varepsilon_{VV}}\right)^2 + \left(\omega\,\tau_L\,x_L\right)^2\right)}_{\text{additional noise}} + \underbrace{k^2\,\frac{{\varepsilon_0}^2}{\varepsilon_{VV}}}_{\text{back-action noise}}\Bigg\} \tag{2.23}$$

$$\varepsilon_0 = \sqrt{\varepsilon_{VV}\,\varepsilon_{JJ} - {\varepsilon_{JV}}^2} \tag{2.24}$$

Strictly speaking, the labels for the back-action and the additional noise shown here are only true for $\bar{z}_{FB} = 0$.

The noise temperature can now be minimized by first calculating $\partial T_N / \partial x_L = 0$ and solving for $x_L$, and afterwards performing the same steps for $\tau_L$. This results in a minimum achievable noise temperature $T_{N0}$ at an optimum normalized input impedance $\bar{z}_{L0} = \bar{Z}_{L0}/(\omega\,L_{IN})$:

$$T_{N0} = \frac{\omega\,\varepsilon_0}{k_B} \tag{2.25}$$

$$\bar{z}_{L0} = \frac{\bar{Z}_{L0}}{\omega\,L_{IN}} = \frac{k^2\,\varepsilon_0}{\varepsilon_{VV}} + \mathrm{j}\left(-1 - k^2\left(g_{J\Phi} - \frac{\varepsilon_{JV}}{\varepsilon_{VV}}\right)\right) = \omega\,\tau_{L0}\,x_{L0} + \mathrm{j}\,x_{L0} \tag{2.26}$$

This resembles the results obtained in literature [59, 64, 93]. $T_{N0}$ and $\varepsilon_0$ were already mentioned in the introduction, see Eqn. (1.28) on page 12. The general property of amplifiers, that the perfect noise matching does not have to coincide with a perfect impedance matching [95], also holds for SQUID amplifiers. Still, at least the imaginary part of the perfectly noise-matched input impedance is quite close to the conjugate complex value of the input impedance, as one can see from Eqn. (2.26). In case of a capacitive input impedance, there is a difference between the optimum noise frequency and the resonance frequency determined by $g_{J\Phi} - \varepsilon_{JV}/\varepsilon_{VV}$. This difference decreases for small coupling factors. Note that the minimum noise temperature is independent of the coupling factor. $\varepsilon_0$ can also be expressed as $\sqrt{(1-{\rho_{JV}}^2)\,\varepsilon_{VV}\varepsilon_{JJ}}$ where $\rho_{JV}$ is the statistical correlation coefficient between $V_N$ and $J_N$ with $|\rho_{JV}| \leq 1$.

To illustrate the properties of Eqn. (2.23) in a better way, it can be expressed in the following, for all types of amplifiers applicable [95], form:

$$\begin{aligned}\frac{T_N}{T_{N0}} &= 1 + \frac{\varepsilon_{VV}\,|\bar{z}_L - \bar{z}_{L0}|^2}{2\,k^2\,\varepsilon_0\,\omega\,x_L\,\tau_L} \\ &= 1 + \frac{\varepsilon_{VV}}{2\,k^2\,\varepsilon_0\,\omega\,x_L\,\tau_L}\left|\omega\,\tau_L x_L - k^2\,\frac{\varepsilon_0}{\varepsilon_{VV}} + \mathrm{j}\left(x_L + 1 + k^2\,g_{J\Phi} - k^2\,\frac{\varepsilon_{JV}}{\varepsilon_{VV}}\right)\right|^2 \\ &= 1 + \frac{\varepsilon_{VV}}{2\,\varepsilon_0}\,\frac{k^2}{\omega\,x_L\,\tau_L}\left|\frac{\omega\,\tau_L\,x_L}{k^2} - \frac{\varepsilon_0}{\varepsilon_{VV}} + \mathrm{j}\left(\frac{x_L+1}{k^2} + g_{J\Phi} - \frac{\varepsilon_{JV}}{\varepsilon_{VV}}\right)\right|^2 \end{aligned} \tag{2.27}$$

This equation describes circles of equivalent $T_N$ in the complex $\bar{z}_L/k^2 = \bar{Z}_L/(k^2\,\omega\,L_{IN})$ plane with $T_N$ dependent radii $\varepsilon_0\sqrt{{T_N}^2/{T_{N0}}^2 - 1}/\varepsilon_{VV}$ around the centers $k_B\,T_N/(\omega\,\varepsilon_{VV}) + \mathrm{j}\,x_{L0}/k^2$. Equation (2.27) is visualized in Fig. 2.3 for the standard SQUID approximation.

The analysis shown above emphasizes the importance of basically three parameters of the

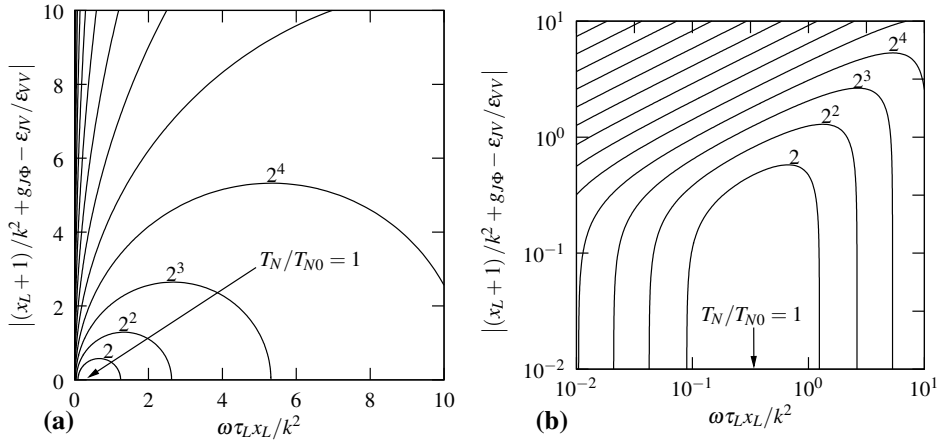


**Figure 2.3:** Noise temperature $T_N/T_{N0}$ in the complex $\bar{Z}_L/(k^2\,\omega\,L_{IN})$ plane, in **(a)** linear and **(b)** logarithmic scale, as defined in Eqn. (2.27). For the only needed parameter $\varepsilon_{VV}/\varepsilon_0$, the standard SQUID approximation $\varepsilon_{VV}/\varepsilon_0 \approx 3$ for an optimized SQUID was used, see Eqns. (1.24)–(1.26) on page 11. The shown circles are circles of equivalent noise temperature, the numbers indicated the multiples of $T_{N0} \approx 3\,T\,\omega\,L_{SQ}/R$. $x_{L0}$ was subtracted from the imaginary part. Note that this picture is independent of $k^2$ and feedback effects modeled by $\bar{Z}_{FB}$.

SQUID that one needs to know. These parameters will play a role in the following section. Besides the passive inductive properties $k^2$, $L_{IN}$ and $L_{SQ}$, the quantities of interest are:

- The additional energy resolution $\varepsilon_{VV}$ defines the increase in noise temperature for an unmatched input impedance $\bar{z}_L \neq \bar{z}_{L0}$.
- $\varepsilon_0$ defines the minimum reachable noise temperature for $\bar{z}_L = \bar{z}_{L0}$. Alternatively, the effective back-action noise term $\varepsilon_0{}^2/\varepsilon_{VV} = \varepsilon_{JJ} - \varepsilon_{JV}{}^2/\varepsilon_{VV}$ can be used.
- The term $g_{J\Phi} - \varepsilon_{JV}/\varepsilon_{VV}$ describes the difference between the optimum input reactance compared to the conjugate complex impedance of the geometric inductance of the SQUID $-\mathrm{j}\omega L_{IN}$.

The actual frequency dependent noise properties and the total frequency response are strongly dependent on the connected input input impedance $\bar{z}_L$. This will be investigated in more detail in the following section.

## 2.5 Readout of practical input impedances

In the last section, the noise temperature was determined. This parameter is of course not directly accessible in a typical measurement. Therefore, we calculated the actually measured flux noise. With Eqns. (2.13), (2.16), (2.17), (2.21) and (2.23) one can express the PSD $S_{\Phi,M}$ of the measured flux $\bar{\Phi}_M$ referred to the SQUID as:

$$S_{\Phi,M} = \frac{4k_B(T+T_N)x_L\tau_L M^2}{L_{IN}\left|\bar{z}_L + \bar{z}_{IN}\right|^2} \tag{2.28}$$

In this section, we want to analyze the noise temperature as well as the practical performance of a SQUID amplifier system with three basic input impedances, see Fig. 2.4.

As a practical note, we want to emphasize at this point that superconducting transformers can be used to match a given impedance to the noise-optimum impedance of the SQUID amplifier.

### 2.5.1 Resistance

Applying the results of the last section, we now connect a simple resistor to the SQUID system $\bar{z}_L = R_L/(\omega L_{IN}) = 1/(\omega\tau_R)$. Because there is no input reactance, the definition of the

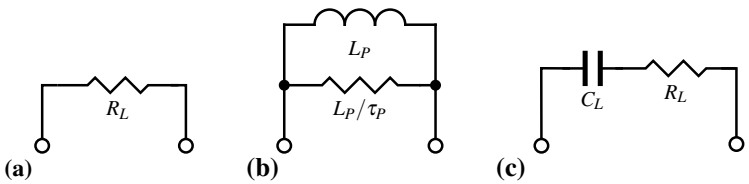


**Figure 2.4:** Schematic of the basic three input impedances investigated here. This includes **(a)** a resistance **(b)** an inductive input circuit, for example a pickup-coil, and **(c)** a lossy capacitive input circuit.

normalized input impedance, see Eqn. (2.21), now has to be adapted with $\omega\tau_L x_L = 1/(\omega\,\tau_R)$ in the limit $x_L \to 0$. Using this with Eqn. (2.23) leads to:

$$T_N = \frac{1}{2\,k_B\,\tau_R}\frac{\varepsilon_{VV}}{k^2}\left\{\underbrace{1+\omega^2\,{\tau_R}^2\left(1+k^2\,g_{J\Phi}-k^2\,\frac{\varepsilon_{JV}}{\varepsilon_{VV}}\right)^2}_{\text{additional noise}}+\underbrace{k^4\,\omega^2\,{\tau_R}^2\,\frac{{\varepsilon_0}^2}{{\varepsilon_{VV}}^2}}_{\text{back-action noise}}\right\} \tag{2.29}$$

At low frequencies, the noise temperature is determined by the *coupled energy resolution* $\varepsilon_{VV}/k^2$, there is no interaction between the SQUID and the input impedance.

At high frequencies $\omega\,\tau_R \gg 1$ the noise temperature scales with $\omega^2$ caused by both the additional and the back-action noise. The former is caused by the growing impedance mismatch from $\bar{z}_{L0}$ due to the missing input reactance. In other words, the input voltage $\bar{V}_L$ is low-pass filtered by the resistance and the input inductance of the SQUID. The latter is caused by the induced voltages in the input loop, which naturally increase with the frequency. The exact knee frequency between the low and high frequency limit is determined by another time constant $\tau_N$ that naturally depends on $\tau_R$, the back-action, and the optimum input reactance of the SQUID:

$$\begin{aligned} T_N &= \frac{1}{2\,k_B\,\tau_R}\frac{\varepsilon_{VV}}{k^2}\left(1+\omega^2\,{\tau_N}^2\right) \\ \tau_N &= \tau_R\sqrt{\left(1+k^2\,g_{J\Phi}-k^2\,\frac{\varepsilon_{JV}}{\varepsilon_{VV}}\right)^2+\left(k^2\,\frac{\varepsilon_0}{\varepsilon_{VV}}\right)^2} \end{aligned} \tag{2.30}$$

Note that the resistive input impedance is basically a short at the Josephson frequency. The altered SQUID dynamics should be therefore taken into account in all noise and small-signal parameters, see section 2.1.

The measured flux noise reads with Eqn. (2.28):

$$\begin{aligned} S_{\Phi,M} &= \frac{4\,k_B\,(T+T_N)\,x_L\,\tau_L\,M^2\,{L_{IN}}^{-1}}{\left|\bar{z}_L+\bar{z}_{IN}\right|^2} \\ &= \frac{4\,k_B\,T\,M^2\,{R_L}^{-1}+S_{\Phi,VV}\left(1+\omega^2\,{\tau_N}^2\right)}{\left|1+\omega^2\,\tau_R\,\tau_{FB}\,\ell_{FB}+\mathrm{j}\omega\,\tau_R\,(1+k^2 g_{J\Phi}+\ell_{FB})\right|^2} && (2.31) \\ &\approx \frac{4\,k_B\,T\,M^2\,{R_L}^{-1}+S_{\Phi,VV}\left(1+\omega^2\,{\tau_N}^2\right)}{1+\omega^2\,{\tau_R}^2\,(1+k^2\,g_{J\Phi}+\ell_{FB})^2} && (2.32) \end{aligned}$$

Here, we re-introduced the additional flux noise PSD $S_{\Phi,VV}$ of the SQUID. This noise is usually directly measured for an autonomous SQUID in FLL, see Eqn. (1.19) on page 9. For the approximate expression, we again used $\omega\,\tau_{FB} \ll 1$.

In FLL, the measured noise becomes with Eqn. (2.15), with negligible feedback via the output reactance and with $\omega\,\tau_{FLL} \ll 1$:

$$S_{\Phi,M,\mathrm{FLL}} \approx \frac{4\,k_B\,T\,M^2\,{R_L}^{-1}+S_{\Phi,VV}\left(1+\omega^2\,{\tau_N}^2\right)}{1+\omega^2\,{\tau_R}^2\left(1-k\,k_{FB,IN}\,{k_{FB,SQ}}^{-1}\right)^2} \tag{2.33}$$

One can see that the additional flux noise PSD $S_{\Phi,VV}$ is added to thermal noise of the resistance. At higher frequencies, back-action noise starts to contribute, the corner frequency

is characterized by $\tau_N$.

The sum of these noise contributions is low-pass filtered due to the resistive and inductive impedance in the input loop. The corner frequency of this low-pass filter is characterized by the time constant $\tau_R \left(1 - k\, k_{FB,IN}\, {k_{FB,SQ}}^{-1}\right)$, see the denominator in Eqn. (2.33). The additional factor originates in the effective change of the input inductance of the SQUID due to the FLL operation.

**Experimental possibilities**

The resistive input impedance obviously does not allow an operation at the minimum noise temperature. Nevertheless, it has some interesting properties. From the measured flux noise at low frequencies one can determine the temperature of the electron system in the resistor, if the mutual inductance $M$ and the input resistance are known. This will be used in chapter 4.

Furthermore, it can be useful regarding the characterization of SQUIDs. With a known mutual inductance $M$ and the known temperature, one can directly measure the value of the resistance from the measured flux noise at low frequencies. From the total frequency response of the system, one can get information about the inductances involved.

We will leave the small-signal analysis for a moment. Suppose, we have a SQUID with known $M$ and an attached input resistance $R_L$ that can be operated in direct readout and in FLL. If one modulates the feedback coil in direct readout with a known current at a frequency $\omega\,\tau_R \ll 1$, one can determine the mutual inductance $M_{FB,SQ}$ from the voltage oscillations of the SQUID with period $\Phi_0$. At these low frequencies the input of the SQUID is effectively open. If one now conducts the same measurement at a much higher frequency $\omega\tau_R \gg 1$, one measures a different value. At these high frequencies the input resistance is negligible compared to the effective input inductance of the SQUID $L_{IN}\left(1 + k^2\, g_{J\Phi} + \ell_{FB}\right)$ and thus flux is not only directly coupled to the SQUID, it is also coupled via $M_{FB,IN}$ and the input loop:

$$ {M_{FB,SQ}}' = M_{FB,SQ} - \frac{M\, M_{FB,IN}}{L_{IN}} = M_{FB,SQ}\left(1 - \frac{k\, k_{FB,IN}}{k_{FB,SQ}}\right) \qquad (\omega\tau_R \gg 1) \qquad (2.34) $$

Note that we chose $M$ and $M_{FB,SQ}$ to be positive. The $g_{J\Phi}$ terms make no difference for the high frequency measurement, because $\int g_{J\Phi}\, \mathrm{d}\Phi_E$ is zero if integrated over exactly one $\Phi_0$. This fits to the determination of the mutual inductance by comparing working points that differ by multiples of $\Phi_0$. The measured flux noise in FLL, Eqn. (2.33), now reads:

$$ S_{\Phi,M,\mathrm{FLL}} \approx \frac{4\, k_B\, T\, M^2\, {R_L}^{-1} + S_{\Phi,VV}\left(1 + \omega^2\, {\tau_N}^2\right)}{1 + \left(\omega\, L_{IN}\, {M_{FB,SQ}}'\, {M_{FB,SQ}}^{-1}\, {R_L}^{-1}\right)^2} \qquad (2.35) $$

If the resistance is now chosen small enough, the amplifier noise can be neglected over a wide frequency range. As said before, with the known temperature the exact value of $R_L$ can be derived from the measured $S_{\Phi,M,\mathrm{FLL}}$ at low frequencies. The corner frequency of the thermal noise contribution allows one to determine the geometric input inductance of the SQUID $L_{IN}$, where one has to use the ratio of the feedback mutual inductance at low and high frequencies ${M_{FB,SQ}}'/M_{FB,SQ}$, see the denominator in Eqn. (2.35). $M_{FB,IN}$ can now be easily determined from Eqn. (2.34). With the determined values of $L_{IN}$ and $M$, one can calculate the coupled energy resolution $\varepsilon_{VV}/k^2 = S_{\Phi,VV}\, L_{IN}/(2M^2)$.

There are other interesting properties of this measurement. First, if the coupling between feedback and input coil $M_{FB,IN}$ is mainly caused within the SQUID layout, this measurement can be used as a calibration measurement. In this case $M_{FB,IN}$ will not be changed when the input impedance is replaced. The comparison of the effective mutual feedback inductance at high frequencies $M_{FB,SQ}{}'$ to its small frequency value $M_{FB,SQ}$ gives an information about the sign of this coupling. If the mutual inductance is mainly caused by coupling to the same SQUID washer, $M_{FB,IN}$ will be positive, which caused $M_{FB,SQ}{}'$ to be smaller than the low frequency value $M_{FB,SQ}$. In this case the virtual resistance generated by the FLL, see Eqn. (2.15), will be negative and can cause instabilities with a capacitive impedance. This can be compensated by adding a small inductance in series to the input coil which is also coupled to the feedback current but with a negative sign [94]. This measure works if $M_{FB,SQ}{}'$ gets larger than the low frequency value $M_{FB,SQ}$. Note that this test can also be done with a connected and known capacitance.

In case the influence of the SQUID noise cannot be neglected, for example if the temperature $T$ is low, one can determine $S_{\Phi,VV}$ and $\tau_N$ via a fit of Eqn. (2.35). $\tau_N$ now gives some information about the back-action and the mismatch term. Still, this approach is not useful to determine the SQUID noise parameters because it is hard to distinguish between the back-action term and the term characterizing the shift in optimum input reactance.

### 2.5.2 Pickup coil

An interesting property of the pickup coil is that it mismatches the SQUID optimum input impedance $\bar{z}_{L0}$ because of the missing real part. In accordance to reference [59], we model a pickup coil as shown in Fig. 2.4(b). The pickup inductance $L_P$ is shunted by a resistance $L_P/\tau_P$ which models the thermal noise of an external source. $\tau_P$ can only take positive values. The resistance is chosen much larger than the impedance of the pickup loop in the interesting frequency range, thus $\omega\tau_P \ll 1$. The normalized input impedance can be expressed as:

$$\bar{z}_L = \bar{Z}_L \big/ (\omega L_{IN}) = m(\omega\,\tau_P + \mathrm{j}) \tag{2.36}$$

$$m = \frac{L_P}{L_{IN}} \tag{2.37}$$

Here, we defined the dimensionless inductance ratio $m$. Using this with Eqn. (2.27) leads to:

$$T_N = \frac{\omega\,\varepsilon_0}{k_B} + \frac{\varepsilon_{VV}}{2\,k^2\,k_B\,\tau_P\,m}\,|m(\omega\,\tau_P + \mathrm{j}) - \bar{z}_{L0}|^2 \tag{2.38}$$

For this input impedance it is useful to express the noise properties as an energy resolution $\varepsilon_P$ referred to the pickup coil. This is done by expressing the flux noise in the pickup coil via the equivalent voltage noise on the input, which is naturally represented by $T_N$. In combination with Eqn. (2.38) and the limit $\omega\tau_P \ll 1$, one gets:

$$\begin{aligned}\varepsilon_P &= \frac{4\,k_B\,T_N\,R_L}{2\,L_P\,\omega^2} = 2\,k_B\,T_N\,\tau_P = \frac{\varepsilon_{VV}}{k^2\,m}\,|\mathrm{j}\,m - \bar{z}_{L0}|^2 \\ &= \underbrace{\frac{\varepsilon_{VV}}{k^2\,m}\left(m + 1 + k^2\,g_{J\Phi} - k^2\,\frac{\varepsilon_{JV}}{\varepsilon_{VV}}\right)^2}_{\text{additional noise}} + \underbrace{\frac{k^2\,{\varepsilon_0}^2}{m\,\varepsilon_{VV}}}_{\text{back-action noise}}\end{aligned} \tag{2.39}$$

The minimum noise temperature is not reached because of the mismatch to the optimum input impedance $\bar{z}_{L0}$ due to the missing input resistance. The minimum $\varepsilon_P$ can again be calculated via $\partial\varepsilon_P/\partial m = 0$. This leads to a minimum energy resolution $\varepsilon_{P0}$ at the optimum inductance $m_0$:

$$m_0 = |\bar{z}_{L0}| = \sqrt{\left(1 + k^2 g_{J\Phi} - k^2\,\varepsilon_{JV}\,/\varepsilon_{VV}\right)^2 + \left(k^2\,\varepsilon_0\,/\varepsilon_{VV}\right)^2} \tag{2.40}$$

$$\varepsilon_{P0} = 2\left(m_0 + 1 + k^2\,g_{J\Phi} - k^2\varepsilon_{JV}\,/\varepsilon_{VV}\right)\varepsilon_{VV}/k^2 \tag{2.41}$$

This result is in agreement with literature [59, 64, 96]. Also in this case, the current noise $J_N$ and the correlation have to be taken into account to choose the perfect value for $L_P$.

The measured flux noise PSD reads with Eqn. (2.28) and $\omega\tau_P \ll 1$:

$$\begin{aligned} S_{\Phi,M} &= \frac{2\,\varepsilon_P\,m M^2}{L_{IN}\,|\mathrm{j}m + \bar{z}_{IN}|^2} = \frac{2\,\varepsilon_{VV}\,M^2}{k^2\,L_{IN}}\,\frac{|\mathrm{j}m - \bar{z}_{L0}|^2}{|\mathrm{j}m + \bar{z}_{IN}|^2} = S_{\Phi,VV}\,\frac{|\mathrm{j}m - \bar{z}_{L0}|^2}{|\mathrm{j}m + \bar{z}_{IN}|^2} \\ &= S_{\Phi,VV}\,\frac{\left|k^2\,\varepsilon_0/\varepsilon_{VV} + \mathrm{j}\left(m + 1 + k^2\,g_{J\Phi} - k^2\,\varepsilon_{JV}/\varepsilon_{VV}\right)\right|^2}{\left|\omega\,\tau_{FB}\,\ell_{FB} + \mathrm{j}\,\left(m + 1 + k^2\,g_{J\Phi} + \ell_{FB}\right)\right|^2} \end{aligned} \tag{2.42}$$

In FLL, the measured noise becomes with Eqn. (2.15) and with negligible feedback via the output reactance, $\omega\tau_{FLL} \ll 1$ and $\ell_{FB} \ll 1 + m$:

$$S_{\Phi,M,\mathrm{FLL}} = S_{\Phi,VV}\,\frac{\left(k^2\,\varepsilon_0/\varepsilon_{VV}\right)^2 + \left(m + 1 + k^2\,g_{J\Phi} - k^2\,\varepsilon_{JV}/\varepsilon_{VV}\right)^2}{\left(m + 1 - k\,k_{FB,IN}\,k_{FB,SQ}{}^{-1}\right)^2} \tag{2.43}$$

**Experimental possibilities**

The above results can be used for the correct dimensioning of an external pickup coil of a magnetometer. In practice, see Eqn. (2.40), this inductance is typically in the order of the input inductance of the SQUID. For an exact optimization, the back-action and the correlation terms are important [59, 64].

Also regarding the characterization of SQUIDs, there are some interesting properties. If one has a configuration with a small parasitic coupling between the feedback and the input coil $\left|k\,k_{FB,IN}\,k_{FB,SQ}{}^{-1}\right| \ll m + 1$ one gets:

$$\begin{aligned} S_{\Phi,M,\mathrm{FLL}} &= S_{\Phi,VV}\,\frac{\left(k^2\,\varepsilon_0/\varepsilon_{VV}\right)^2 + \left(m + 1 + k^2\,g_{J\Phi} - k^2\,\varepsilon_{JV}/\varepsilon_{VV}\right)^2}{(m+1)^2} \\ &= S_{\Phi,VV}\left(1 + 2k^2\,\frac{g_{J\Phi} - \varepsilon_{JV}/\varepsilon_{VV}}{m+1} + k^4\,\frac{(\varepsilon_0/\varepsilon_{VV})^2 + (g_{J\Phi} - \varepsilon_{JV}/\varepsilon_{VV})^2}{(m+1)^2}\right) \end{aligned} \tag{2.44}$$

This equation suggests a novel way to characterize the complete noise properties of a SQUID. A changeable pickup coil $L_P$ and thus a changeable $m$ allows to fit the three interesting noise parameters of the SQUID. This could for example be done by connecting the input inductance of an unbiased SQUID of the same kind with a variable external flux applied via its feedback coil. Of course, the screening of the SQUID inductance $L_{SQ}$ should be taken into account here, which can also change the SQUID parameters. Therefore, some minimum value of $m$ should be obtained.

Note that with a known coupling between the feedback and the input coil $M_{FB,IN}$, see the last section for the experimental determination, also Eqn. (2.43) could be used to fit the complete noise properties.

With a known capacitor in series to the changeable inductor, the measurement of $m$ is possible by measuring the resonance frequency. The flux noise $S_{\Phi,M,\mathrm{FLL}}$ far above the resonance corresponds to the case of a connected inductance. The exact properties of this configuration will be treated in the next section.

### 2.5.3 Capacitive input impedance

Now we will take a look at the most interesting input impedance, the capacitive impedance. From the results of section 2.4, one could see that the optimum input impedance for the SQUID $\bar{z}_{L0}$ has a negative imaginary part. Defining the passive resonance frequency $\omega_L$ between $L_{IN}$ and $C_L$ and the quality factor $Q_L$ of this resonance, the normalized input impedance reads with Fig. 2.4(c):

$$\bar{z}_L = \frac{\bar{Z}_L}{\omega L_{IN}} = \frac{\omega_L}{\omega Q_L} - \mathrm{j}\frac{{\omega_L}^2}{\omega^2} = x_L(\omega\tau_L + \mathrm{j}) \tag{2.45}$$

$$\omega_L = \frac{1}{\sqrt{L_{IN} C_L}} \qquad Q_L = \frac{1}{R_L}\sqrt{\frac{L_{IN}}{C_L}} \tag{2.46}$$

Note that for small dissipation $Q_L \gg 1$, the schematic shown in Fig. 2.4(c) can be replaced by a parallel connection of a capacitance and a resistance. Furthermore, the input impedance is basically a short at high frequencies and could change the behavior of the SQUID which should be taken into account in all noise and small-signal parameters, see section 2.1.

The noise temperature reads with Eqn. (2.23):

$$T_N = \frac{\varepsilon_{VV}\omega_L}{2k_B}\left\{ \underbrace{\frac{1}{k^2 Q_L} + \frac{Q_L}{k^2}\left(-\frac{\omega_L}{\omega} + \frac{\omega}{\omega_L}\left(1 + k^2 g_{J\Phi} - k^2\frac{\varepsilon_{JV}}{\varepsilon_{VV}}\right)\right)^2}_{\text{additional noise}} + \underbrace{k^2 Q_L\left(\frac{\omega}{\omega_L}\frac{\varepsilon_0}{\varepsilon_{VV}}\right)^2}_{\text{back-action noise}} \right\} \tag{2.47}$$

The global minimum of the noise temperature $T_{N0}$, see Eqn. (2.25), can be found by first setting the frequency dependent term of the additional noise to zero, which gives the optimum frequency $\omega_0$. This corresponds to $x_L = x_{L0}$. The optimum quality factor $Q_{L0}$ is found by minimizing the resulting expression.

$$T_{N0} = \frac{\omega_0 \varepsilon_0}{k_B} \tag{2.48}$$

$$\omega_0 = \omega_L\left(1 + k^2 g_{J\Phi} - k^2\frac{\varepsilon_{JV}}{\varepsilon_{VV}}\right)^{-1/2} \approx \omega_L \tag{2.49}$$

$$Q_{L0} = \frac{1}{k^2}\frac{\varepsilon_{VV}}{\varepsilon_0}\frac{\omega_L}{\omega_0} = \frac{1}{k^2}\frac{\varepsilon_{VV}}{\varepsilon_0}\sqrt{1 + k^2 g_{J\Phi} - k^2\frac{\varepsilon_{JV}}{\varepsilon_{VV}}} \approx \frac{3}{k^2} \tag{2.50}$$

Regarding our assumptions, this resembles the results from literature [59, 64, 96–98]. The given approximate expressions are based on the standard SQUID approximations, see Eqns. (1.24)–(1.26), with neglected shift in the optimum input reactance. Note that $T_{N0}$ is now fixed to one frequency and that it is independent of the coupling factor $k$. One interesting result is that if one wants to reach the minimum noise temperature with a high quality factor capacitor, the coupling factor should be chosen is much smaller than 1, see Eqn. (2.50). With perfect coupling $k = 1$, the optimum quality factor for a standard SQUID is $Q_{L0} \approx 3$.

In Fig. 2.5, a plot of Eqn. (2.47) is shown which illustrates the noise temperature for varying coupling $k$ and quality factor $Q_L$. From Fig. 2.5(a) one can see that for a high quality factor $Q_L \gg 1$ which is optimally matched with $k^2 \ll 1$, see Eqn. (2.50), the minimum noise temperature $T_{N0}$ is reached. Nevertheless, it is only read out efficiently over a very narrow bandwidth.

In case the ambient temperature of the input circuit and thus the noise temperature of interest is much higher than $T_{N0}$, this bandwidth can be extended by increasing the coupling factor [96], as illustrated in Fig. 2.5(b). This is typical for most audio frequency applications, if the SQUID and the input circuit are operated at the same temperature. With Eqns. (1.24)–(1.26) from page 11 and a SQUID with $L_{SQ} = 200$ pH and $R = 5\ \Omega$, the ratio $T_{N0}/T$ approximately reads $\omega_0 \cdot 10^{-10}$ s.

To determine the bandwidth, where the noise temperature $T_N$ is smaller than the temperature $T$ of the input circuit, Eqn. (2.47) can be brought into the following form:

$$T_N = \frac{\omega_L \varepsilon_{VV} Q_L}{2 k_B k^2} \left\{ \frac{1}{{Q_L}^2} - 2\left(1 + k^2 g_{J\Phi} - k^2 \frac{\varepsilon_{JV}}{\varepsilon_{VV}}\right) + \frac{{\omega_L}^2}{{\omega_M}^2}\left({\vartheta_M}^2 + 2\right) \right\} \tag{2.51}$$

$$\vartheta_M = \frac{\omega}{\omega_M} - \frac{\omega_M}{\omega} \qquad \omega_M = \omega_L \left\{ \left(k^2 \frac{\varepsilon_0}{\varepsilon_{VV}}\right)^2 + \left(1 + k^2 g_{J\Phi} - k^2 \frac{\varepsilon_{JV}}{\varepsilon_{VV}}\right)^2 \right\}^{-1/4} \tag{2.52}$$

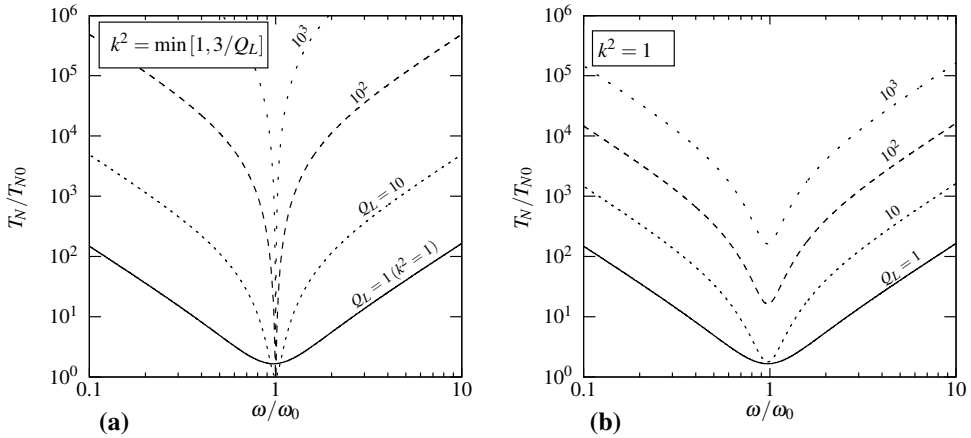


**Figure 2.5:** Noise temperature $T_N/T_{N0}$ versus frequency, according to Eqn. (2.47). The standard SQUID approximation ${Q_{L0}}^2 \approx 3/k^2$ was used and the frequency shift was neglected $\omega_0 \approx \omega_L$. **(a)** The noise temperature with varying $Q_L$ which was also set to $Q_{L0}$ by varying the coupling factor. Note that for $Q_L = 1$, $Q_{L0}$ and $T_{N0}$ cannot be reached because $k \leq 1$. **(b)** The same plot but with fixed perfect coupling $k^2 = 1$. The figure illustrates how a higher coupling factor $k^2 > 3/Q_L$ can increase the bandwidth at noise temperatures $T_N \gg T_{N0}$.

Here, the frequency $\omega_M$ of the minimum noise temperature at a non-optimum quality factor and the corresponding detuning $\vartheta_M$ were introduced.

The bandwidth $B$ with values of noise temperature $T_N \leq T$ and normalized to the ordinary frequency is now given by:

$$B = \frac{\omega_M}{2\pi}\,|\vartheta_M| = \frac{\omega_M}{2\pi}\sqrt{\frac{{\omega_M}^2}{{\omega_L}^2}\left\{\frac{2\,k_B\,T\,k^2}{\omega_L\,\varepsilon_{VV}\,Q_L} - \frac{1}{{Q_L}^2} + 2\left(1 + k^2\,g_{J\Phi} - k^2\frac{\varepsilon_{JV}}{\varepsilon_{VV}}\right)\right\} - 2} \quad (2.53)$$

The upper $f_{\mathrm{UPP}}$ and lower $f_{\mathrm{LOW}}$ frequencies, where $T_N = T$, are given by:

$$f_{\mathrm{LOW}} = \sqrt{\left(\frac{\omega_M}{2\pi}\right)^2 + \left(\frac{B}{2}\right)^2} - \frac{B}{2} \qquad f_{\mathrm{UPP}} = \sqrt{\left(\frac{\omega_M}{2\pi}\right)^2 + \left(\frac{B}{2}\right)^2} + \frac{B}{2} \quad (2.54)$$

These quite complicated expression give some idea about the influence of the different noise parameters. The larger part of the bandwidth is above $\omega_M$, see the logarithmic frequency scale in Fig. 2.5. From Eqn. (2.53), it becomes obvious that if one wants to reach a high bandwidth at a comparably high temperature $T/T_{N0} \gg 1$, a low coupled energy resolution $\varepsilon_{VV}/k^2$ is the most important parameter. The back-action and the shift in optimum input reactance are of secondary importance. In practice, these parameters can be neglected quite often, for example for $k^2 \ll 1$. In this case the bandwidth reads:

$$B \approx \frac{\omega_L}{2\pi}\sqrt{\frac{2\,k_B\,T\,k^2}{\omega_L\,\varepsilon_{VV}\,Q_L} - \frac{1}{{Q_L}^2}} \quad (2.55)$$

For a quality factor $Q_L = 10^6$, $k^2 = 0.5$, $\omega_L = 2\pi \cdot 3$ kHz and a standard SQUID with $L_{SQ} = 200$ pH and $R = 5\ \Omega$ the bandwidth yields $\approx 1.2$ kHz, see Eqn. (1.24) on page 11.

The measured flux noise PSD in an experiment yields with Eqns. (2.28) and (2.47):

$$\begin{aligned} S_{\Phi,M} &= \frac{1}{|\bar{z}_L + \bar{z}_{IN}|^2}\,\frac{4\,k_B\,(T + T_N)\,\omega_L M^2}{\omega^2\,Q_L\,L_{IN}} \\ &= \left|\frac{1}{Q_L} + \frac{\omega^2\,\tau_{FB}\,\ell_{FB}}{\omega_L} + \mathrm{j}\frac{\omega_L}{\omega_R}\left(\frac{\omega}{\omega_R} - \frac{\omega_R}{\omega}\right)\right|^{-2} \\ &\quad \cdot \left\{\frac{4\,k_B\,T\,M^2}{\omega_L\,Q_L\,L_{IN}} + S_{\Phi,VV}\left(\frac{1}{{Q_L}^2} + \left(\frac{\omega_L}{\omega_0}\right)^2\left(\frac{\omega}{\omega_0} - \frac{\omega_0}{\omega}\right)^2 + k^4\left(\frac{\omega}{\omega_L}\frac{\varepsilon_0}{\varepsilon_{VV}}\right)^2\right)\right\} \quad (2.56) \end{aligned}$$

$$\omega_R = \frac{\omega_L}{\sqrt{1 + k^2\,g_{J\Phi} + \ell_{FB}}} \quad (2.57)$$

Here, the actual resonance frequency $\omega_R$ of the system in a measurement with possible feedback effects is of importance. At this frequency, also the thermal noise term originating from the resistive part of the input circuit has the strongest influence. Equation (2.56) will be used for the verification of the assumptions of this chapter in a direct readout numerical experiment in chapter 3, section 3.4.

Note that at frequencies much above the effective bandwidth $\omega \gg 2\pi\,f_{\mathrm{UPP}}$ the SQUID is basically shortcut. Here, the measured flux noise is the same as in the case of the pickup loop with $m = 0$, see Eqns. (2.42)–(2.44). For the capacitive input impedance we did not

directly include an additional inductive part for simplicity, but this can be included easily by adapting the coupling factor $k^2 = M^2/(L_T L_{SQ})$. Here, $L_T$ is the total geometric inductance in the input circuit.

The measured flux noise at frequencies much below the effective bandwidth $\omega \ll 2\pi f_{\mathrm{LOW}}$ is with Eqn. (2.56) the additional flux noise PSD $S_{\Phi,VV}$. Accordingly, in this case the input of the SQUID is effectively open.

In FLL operation, the measured flux noise PSD yields:

$$S_{\Phi,M,\mathrm{FLL}} \approx \left\{ \left( \frac{1}{Q_L} - \frac{\omega^2 \tau_{FLL}}{\omega_L} \left( k^2 g_{J\Phi} + \frac{k k_{FB,IN}}{k_{FB,SQ}} \right) \right)^2 + \left( \frac{\omega_L}{\omega_R} \right)^2 \left( \frac{\omega}{\omega_R} - \frac{\omega_R}{\omega} \right)^2 \right\}^{-1} \cdot \left\{ \frac{4 k_B T M^2}{\omega_L Q_L L_{IN}} + S_{\Phi,VV} \left( \frac{1}{{Q_L}^2} + \left( \frac{\omega_L}{\omega_0} \right)^2 \left( \frac{\omega}{\omega_0} - \frac{\omega_0}{\omega} \right)^2 + k^4 \left( \frac{\omega}{\omega_L} \frac{\varepsilon_0}{\varepsilon_{VV}} \right)^2 \right) \right\} \tag{2.58}$$

$$\omega_R = \omega_L \left( 1 - \frac{k k_{FB,IN}}{k_{FB,SQ}} \right)^{-1/2} \tag{2.59}$$

### Stability

For a stable operation, the real part of the total impedance in the input loop $\Re\left[\bar{z}_L + \bar{z}_{IN}\right]$ has to be positive at its resonance frequency $\omega_R$. With Eqn. (2.15), this leads to the following stability criterion:

$$\frac{1}{Q_L} > -\frac{\omega_L \tau_{FB} \ell_{FB}}{1 + k^2 g_{J\Phi} + \ell_{FB}}$$

$$\text{Flux-locked loop: } \frac{1}{Q_L} \gtrapprox \omega_L \tau_{FLL} \left( k^2 g_{J\Phi} + \frac{k k_{FB,IN}}{k_{FB,SQ}} \right) \left( 1 - \frac{k k_{FB,IN}}{k_{FB,SQ}} \right)^{-1} \tag{2.60}$$

In case the quality factor is large, it is no easy task to fulfill this requirement. In case the FLL cannot be made very fast, attention has to be paid that the coupling between the feedback and the signal coil $k_{FB,IN}$ is negative and of large value compared to the term including $g_{J\Phi}$. As mentioned in section 2.5.1, this can be compensated by adding a small inductance in series to the input coil which is also coupled to the feedback current, only with a negative sign [94].

Another measure to generate this needed positive feedback should also be mentioned here—the “cold damping” scheme [99]. In this configuration, a fraction of the feedback current is sent in the right direction through a series connection of a capacitor and the input coil. Here, the capacitor causes the damping phase change. This scheme basically does not alter any of the noise analysis done before, although it leads to a different total frequency response.

### Experimental possibilities

In general, regarding the noise properties the capacitive input impedance is the most interesting. The compensation of the inductive input impedance allows to reach the lowest possible noise temperature $T_{N0}$ in a big variety of possible measurements. On the downside, one is limiting the bandwidth. Such configurations can for example be used for even more sensitive

magnetometers [59, 64]. The readout of a gravitational wave antenna as shown in section 1.5 on page 16 is another perfect application for this type of measurement.

Regarding the determination of SQUID parameters, the capacitive impedance can be used to fit all important noise contributions. The measurement method described in the end of section 2.5.2 can also be applied in this case. The advantage here is that with a known capacitance $C_L$, the input inductance $m$ can be measured from the resonance frequency with the known influence of the feedback. Although $m$ is not directly present in this section, we did not model an additional inductive part, it can be simply modeled by an increased $L_{IN}$ with a lower coupling factor $k$.

For a known capacitance $C_L$, the measurement of the coupling inductances in FLL can directly be performed in the same way as introduced in the end of section 2.5.1. The simple test for a growing or falling mutual feedback inductance between low frequencies $M_{FB,SQ}$ and frequencies much higher than the resonance frequency $M_{FB,SQ}{}'$ can directly be performed. If the mutual feedback inductance gets smaller above the resonance, the FLL most likely causes instabilities.

To determine the parameters of the SQUID, a measurement on a high quality factor capacitor can be used, see for example reference [20]. In the limit of a high thermal noise, $\omega_R$ can be determined from the peak frequency. In case feedback mechanisms are well characterized, the measured flux noise PSD can be fit to Eqns. (2.56) or (2.58) to determine all parameters.

## 2.6 Conclusions

In a small-signal analysis, we studied the practical frequency response and sensitivity properties of SQUID systems operated in a direct readout and in flux-locked loop operation.

In section 2.1 we introduced our basic assumptions about the SQUID dynamics under the influence of the input circuit. We assume that the small-signal and noise parameters of the SQUID at low frequencies are sufficient to describe the performance. Which mechanism is influencing the SQUID dynamics at the Josephson frequency is ignored at first. This is in contradiction to some publications that postulate new features in the influence of back-action noise [74, 92, 93]. In the following chapter, this assumption will be tested in a numerical experiment on a SQUID operated with a strongly coupled capacitive input circuit.

In section 2.2, we show a small-signal analysis of the SQUID amplifier with a general input impedance connected to its input inductance. We derive expressions for the frequency response and the influence of noise contributions caused by the SQUID amplifier. We included many practical aspects that play a role in typical low-frequency measurements. We incorporate the influence of the small-signal and noise parameters of the SQUID, the loading of the SQUID via a connected output circuit and a possible FLL operation. Furthermore, we include parasitic mutual inductances that can be of importance in a practical measurement.

In section 2.3, we investigate the influence of feedback effects on the input impedance of the amplifier system. These feedback effects are caused by a loading of the amplifier via the connected output circuit or by a possible employed FLL operation. We give a possible explanation for measured resistive parts of the input impedance of SQUIDs operated in direct readout [65, 66]. Here, much higher input resistances were observed than could be

explained by theory. According to our model, the loading of the SQUID by a complex output impedance generates resistive input impedances via the reverse transfer function $G_{JI}$ of the SQUID and possible parasitic mutual inductances. In practice, there are usually much larger time constants connected to an output circuit compared to the timescale of the Josephson oscillations. Therefore, much higher virtual input resistances could be generated. In a two-stage SQUID setup, where the output load of the first stage SQUID is practically purely inductive, even larger virtual input resistances can be generated. Furthermore, we discuss the influence of the FLL on the input impedance. This is especially used in section 2.5.

In section 2.4, we derive a general description of the equivalent input noise temperature of the SQUID amplifier system. Feedback effects, caused by the output loading of the SQUID or the FLL operation, have no influence here. Although these effects change the frequency response of the system and directly inject additional noise of the SQUID in the input circuit, they do not alter the signal-to-noise ratio. We derive the SQUID equivalent input noise temperature and express it in a general form which is independent of the connected input circuit. This forms the basis for our investigations of SQUIDs in chapter 3.

One can define basically three parameters that describe the noise performance. First of all, the additional noise energy resolution $\varepsilon_{VV}$ describes the noise performance if a non-optimum input impedance is connected. If the optimum input impedance is coupled, the minimum noise temperature is expressed by $\varepsilon_0$, see Eqn. (2.24). This, or the effective back-action term $\varepsilon_0{}^2/\varepsilon_{VV} = \varepsilon_{JJ} - \varepsilon_{JV}{}^2/\varepsilon_{VV}$ is the second needed parameter. The optimum input resistance, or quality factor of the input circuit, is expressed by a combination of the two just mentioned parameters. The optimum input reactance is on the other hand influenced by the correlation between back-action and additional noise and by the dynamic inductance of the SQUID. This is expressed by the third term $g_{J\Phi} - \varepsilon_{JV}/\varepsilon_{VV}$. It describes the difference between the optimum input reactance compared to the conjugate complex impedance of the geometric inductance of the SQUID $-\mathrm{j}\omega L_{IN}$.

In the final section 2.5 of this chapter, we investigate the performance of three practical passive input circuits. We derive expressions for the noise temperature for each of the input impedances. The found expressions resemble expressions known from literature. For the capacitive input circuit, we find a new analytical expression for the achievable bandwidth. Here, the *coupled energy resolution* $\varepsilon_{VV}/k^2$ of the SQUID amplifier is of importance for most low-frequency applications. For the readout of MiniGRAIL, a high bandwidth is required and accordingly, the coupled energy resolution will be used as an optimization criterion in our developed SQUID sensors in chapter 5.

Furthermore, we calculate practical measured noise spectra in a direct readout operation as well as in FLL operation of the SQUID amplifier connected to the basic input circuits. This led us to new experimental possibilities. For the case of a variable inductive input circuit, which can be for example achieved by a superconducting Josephson circuit, we present a new approach to determine the three important parameters of the SQUID as mentioned above.

For the resistive and capacitive input circuit, we develop a measurement technique to characterize the parasitic mutual inductance between the feedback coil and the input circuit. This coupling is present in most SQUID layouts and has an influence on the frequency response of SQUIDs operated in FLL. The stability with a capacitive input circuit is discussed under this perspective.

The exact measurement of this parasitic mutual inductance is therefore important for the readout of MiniGRAIL with the capacitive transducer, see section 1.5. In chapter 5, we therefore designed SQUIDs with a special layout that suppresses the parasitic coupling between the feedback and the signal coil. Furthermore, we used the mentioned measurement technique to determine the value of the geometric input inductance of one of our SQUID sensors.

The derived expressions for the measured noise spectra with a strongly coupled capacitance could, in combination with the introduced characterization of the parasitic mutual inductance, be used to determine the noise temperature of SQUID amplifiers in the sense of experiments from references [20, 98, 98, 100].

The basis for the analysis presented in this chapter were the small-signal and noise parameters of the SQUID. In the following chapter 3, we will numerically investigate these properties with the focus on an optimized SQUID design and operation.

# Chapter 3

# Numerical optimization of dc-SQUID amplifiers

In this chapter, we will investigate the properties of dc-SQUIDs in more detail. The analysis shown in chapter 2 is based on the small-signal and noise parameters of the SQUID. For a given set of these parameters, we investigated the frequency response and the signal-to-noise ratio of a SQUID-based system for the readout of an arbitrary input circuit.

The purpose of this chapter is to quantitatively study the achievable performance in the design and operation of SQUID amplifiers. We therefore focus on the one hand on an optimization regarding the minimum achievable additional noise of the amplifier, which is represented by the *additional energy resolution* $\varepsilon_{VV}$. This is of importance in most practical applications. On the other hand, we investigate the minimum achievable equivalent input noise temperature, which is represented by $\varepsilon_0$. This can be of importance in some applications, see for example the capacitive input circuit treated in section 2.5.3 on page 34. There are two studies available in literature that investigate the complete noise properties, including the back-action contribution, of the standard SQUID amplifier. Tesche et al. numerically determined these properties for the case of a standard SQUID with a screening parameter $\beta_L = 1$ [63]. In the now almost forgotten work of Danilov et al. [16, 59] the SQUID dynamics were calculated by analytical approximations in two opposing ranges $\beta_L \ll 1$ and $\beta_L \gg 1$. We here investigate the properties of the standard SQUID in more detail and we will furthermore extend our investigations to other types of SQUIDs.

In section 3.1, we introduce our approach for simulating the performance of the SQUID models. On the basis of the circuit simulator JSIM, we developed a system for the characterization of SQUID amplifiers. Here, the behavior of the SQUID is simulated and all interesting properties can be extracted in the sense of a numerical experiment. In the rest of this chapter, we use the flexibility of the system to characterize a few basic models of SQUIDs. Furthermore, this will be used in chapter 5 to simulate the behavior of models of practical SQUIDs.

In section 3.2, we investigate the performance of typical SQUID designs in the limit of an overdamped Josephson junction. On the one hand we characterize standard SQUIDs and on the other hand SQUIDs with a resistively shunted inductance. The main parameters that

are varied are the screening parameter $\beta_L$ and the working point of the SQUID. First we discuss characteristics, small-signal and noise parameters of a few exemplary SQUIDs. For each of these SQUIDs, we determine the working points exhibiting the best sensitivity in the sense of the minimum additional noise $\varepsilon_{VV}$ and the minimum achievable noise temperature $\varepsilon_0$ as mentioned above. The broad range of extracted properties is, where possible, compared with numerical and analytical results known from literature. Here, we usually find a good agreement.

Then we summarize the interesting properties in the optimum points of sensitivity for all the simulations with varying values of $\beta_L$. The results give a very broad insight into the practical performance. First of all, the optimum working range is of importance. We show that there can be large differences between the working ranges that show the best additional noise $\varepsilon_{VV}$ and the points that show the minimum achievable noise temperature, represented by $\varepsilon_0$. The latter is hard to determine in an experiment, the results of our simulations give an overview of working ranges one should choose. Secondly, the optimum input impedance to achieve the best noise temperature is of interest. As we showed in chapter 2, see especially section 2.4 on page 25, the optimum imaginary and real part of the connected input impedance is dependent on the small-signal and noise parameters of the SQUID in a given working point. This gives information on for example the optimum quality factor of a coupled capacitive impedance or the frequency where the optimum noise temperature is reached. Thirdly, we compare the reachable sensitivity for the variety of SQUID sensors and values of $\beta_L$.

In the last part of section 3.2, we discuss the practical optimization of a SQUID design regarding the choice of the screening parameter $\beta_L$. Under circumstances given by the type of the SQUID design or the fabrication technology, the Stewart-McCumber parameter $\beta_C$ is qualitatively included in the optimization of the SQUID design.

In section 3.3, we focus on washer type SQUIDs with an integrated coil in the limit of a large total length of the windings. Here, the fundamental resonance of the coil lies below the Josephson frequency, the frequency of the SQUID dynamics. This is the practical case for many SQUID designs that require a much larger input inductance compared to the SQUID inductance. Also the SQUIDs that will be shown in chapter 5 are of this type.

First we give an overview of the electromagnetic properties of the washer structure with an integrated coil. In the limit of a long coil, the SQUID inductance is effectively lowered at the Josephson frequency. This is used in a simplified model to study important properties in this configuration. First we investigate new features in the characteristics. This includes hysteretic working ranges that cannot be avoided and have to be taken into account for both the design and the operation of practical SQUIDs with a long integrated coil. Furthermore, we present a similar numerical study as presented in section 3.2. Again we vary the screening parameter $\beta_L$, only this time with a lowered effective inductance at the Josephson frequency. The results are compared to the performance of the standard SQUIDs as presented in section 3.2. The simplified model of the washer type SQUID with a long integrated coil shows differences especially in the optimum working range and in the reachable sensitivity. This fact gives important information on the expected performance of real devices as the ones shown in chapter 5. We conclude with a discussion on the practical implications of the gained insights on both the design and the operation of such sensors.

In the last section 3.4 of this chapter, we perform a numerical experiment on a standard SQUID operated with a strongly coupled capacitive impedance. This turns out to be very

similar to the SQUID with a long integrated input coil. Also here, the SQUID inductance is effectively lowered at the Josephson frequency. For some exemplary SQUIDs, we determine the voltage noise spectra in their working point of minimum reachable noise temperature. The spectra are compared with theoretical expressions from chapter 2 using the properties of the SQUIDs from section 3.3. By varying the quality factors of the capacitive input circuit, we change the influence of both additional noise and back-action noise of the SQUID amplifier. The simulated spectra are well approximated by the analytical expressions and we therefore conclude that the basic assumptions of chapter 2 are applicable.

## 3.1 Numerical characterization of SQUIDs using JSIM

A standard SQUID within the RCSJ model is described by the Langevin Eqns. (1.13) as shown on page 7. Typically, this system of nonlinear differential equations is directly integrated numerically [57, 61, 63]. In this chapter as well as in chapter 5, we investigate the dynamics of SQUID models with increasing complexity. We therefore chose software that is dedicated for the simulation of electrical circuits. This approach is more flexible regarding the investigated model and allows simplifications in the determination of the extracted parameters for our quantitative study.

The approach can be understood as conducting numerical experiments on the SQUID model under investigation. In this experiment, we excite the SQUID with a small varying external flux. The effect of this excitation on the output voltage $V$ and the circulating current $J$ is used to determine the small signal parameters $G_{V\Phi}$ and $G_{J\Phi}$, see Eqn. (1.15) on page 9. Furthermore, we extract the noise PSD of both the output voltage of the SQUID $S_{VV}$ and the circulating current $S_{JJ}$ as well as their cross spectral density $S_{JV}$, see Eqn. (1.18) on page 9. These properties can be used to characterize the sensitivity of the SQUID amplifier with an arbitrary connected input circuit, see section 2.4 on page 25. Details on the simulation approach are given in the current section.

We used the software JSIM [45], a SPICE-based circuit simulator including the RCSJ model of Josephson junctions. The extension with noise sources [46] allows to model the thermal noise of resistances. The setup used to characterize SQUIDs within JSIM is schematically shown in Fig. 3.1. The SQUID is biased at the desired bias current $I$ and external flux $\Phi_E$. Noise sources are used on the one hand to model the Nyquist noise of the shunt resistances and on the other hand to generate the small random excitation of the external flux, as will be explained in more detail below.

The voltage $V$ and the circulating current $J$ are low-pass filtered using auxiliary circuits as indicated in Fig. 3.1. All low-pass filters have the same corner frequency $f_{\mathrm{Out}}$. They restrict the signal to the low frequency white noise spectrum, see Fig. 1.5 on page 10. To achieve this, the time constant of the readout is chosen larger than the largest time constant of the sensor. The value of $f_{\mathrm{Out}}$ is a tradeoff between the minimum Josephson frequency of a SQUID one can characterize and the required calculation time. If the SQUID is oscillating at a frequency $V/\Phi_0 \lesssim f_{\mathrm{Out}}$, the low-pass filter measures the oscillation of the SQUID in addition to the white noise spectrum. All noise characteristics shown later are connected to working points that had a voltage $V$ with $V > 10\, f_{\mathrm{Out}}\, \Phi_0$. Working points with voltages below this value were considered to give a inaccurate approximation of the white noise spectrum and were therefore excluded. To give an example, for a standard SQUID a cutoff frequency

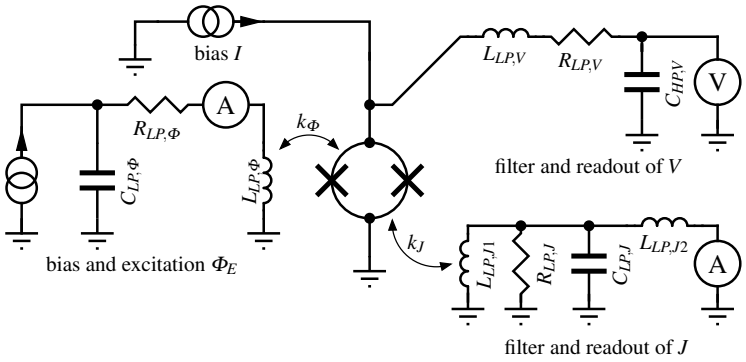


**Figure 3.1:** Schematic of the circuit simulated in JSIM for characterizing a SQUID. No noise sources are attached to the resistances shown here, which are only used to reduce the quality factors of the low-pass filters to 1. The left most current source also generates white noise, which is low-pass filtered with a cutoff frequency $f_{\mathrm{Exct}}$ to generate a random excitation flux. The circulating current of the SQUID $J$ is measured by a symmetrically coupled inductive network. Both $J$ and the voltage across the SQUID $V$ are low-pass filtered with the same corner frequency $f_{\mathrm{Out}}$. The corner frequency of the output low-pass filters $f_{\mathrm{Out}}$ is chosen higher than the one of the excitation: $f_{\mathrm{Out}} = 10\, f_{\mathrm{Exct}}$. All auxiliary circuits are heavily mismatched to the SQUID: $k_\Phi \lll 1$, $k_J \lll 1$, $L_{LP,V} \ggg L_{SQ}$, $R_{LP,V} \ggg R$.

of $f_{\mathrm{Out}} \lesssim I_0 R/(100\,\Phi_0)$ proved to be practical. Here, $I_0 R$ is the characteristic voltage of the Josephson junction, see section 1.2.4 on page 5.

The measurement of the output data begins after a safe delay accounting for the time constants of the low-pass filters and the much faster transients of the SQUID sensor settling the desired bias point. To exclude an influence of the auxiliary circuits on the SQUID sensor, their elements are chosen such that there is no serious impedance matching with the SQUID at any frequency up to the Josephson frequency.

The variance of the low-pass filtered voltage $\mathrm{cov}\,(V,V)$ and the circulating current $\mathrm{cov}\,(J,J)$ is directly related to the effective bandwidth of the filter $B_{\mathrm{Out}}$ and the respective white noise level. The same holds for the cross correlation spectrum $S_{JV}$ and the covariance $\mathrm{cov}\,(J,V)$. The covariance of two equally large sets of discrete samples $x_i$ and $y_i$ is given by:

$$\mathrm{cov}\,(x,y) = \frac{1}{N}\sum_{i=1}^{N}\left(x_i - \langle x\rangle\right)\left(y_i - \langle y\rangle\right) \tag{3.1}$$

Here, $N$ is the number of the samples and $\langle x\rangle$ and $\langle y\rangle$ are the respective mean values. Naturally, $\mathrm{cov}\,(x,x)$ represents the variance of $x$.

From the transfer function $H(f)$ at a frequency $f$, the effective bandwidth of the low-pass filter can be calculated by $B_{\mathrm{Out}} = \int_0^\infty |H(f)|^2\,\mathrm{d}f$. This yields $B_{\mathrm{Out}} = \frac{\pi}{2} f_{\mathrm{Out}}$ for the output low-pass filters shown in Fig. 3.1. Accordingly, the white noise PSDs $S_{VV}{}'$ and $S_{JJ}{}'$ and the white correlation spectral density $S_{JV}{}'$ are calculated by:

$$S_{VV}{}' = \frac{\mathrm{cov}\,(V,V)}{B_{\mathrm{Out}}} \qquad S_{JJ}{}' = \frac{\mathrm{cov}\,(J,J)}{B_{\mathrm{Out}}} \qquad S_{JV}{}' = \frac{\mathrm{cov}\,(J,V)}{B_{\mathrm{Out}}} \tag{3.2}$$

One advantage of this approach is that one directly reduces the amount of data that has to be post-processed. In case of the direct solution of the Langevin equations [57, 61, 63], a

large number of Josephson oscillations is recorded, Fourier transformed and then the white spectrum is extracted. In our approach, the spectrum is reduced within the simulation and one only needs to calculate the covariance of an already reduced amount of data.

The determination of the small-signal parameters is no trivial problem. There are large differences in the magnitude of these small signal parameters of different SQUIDs and working points. To minimize the needed simulation time, we chose for an approach inspired by experimental techniques. A random Gaussian flux excitation with a variance $\mathrm{cov}(\Phi_E, \Phi_E)$ around the working point also causes a change in the output variables. The correlation of the excitation signal and the measured voltage $V$ and circulating current $J$ contains information about the small signal parameters. The excitation is continuously applied during the simulation and measured by the left ammeter as indicated in Fig. 3.1. From its correlation to the output variables, the value of the small-signal transfer functions are then given by:

$$G_{V\Phi} = \frac{\mathrm{cov}(V, \Phi_E)}{\mathrm{cov}(\Phi_E, \Phi_E)} \qquad G_{J\Phi} = \frac{\mathrm{cov}(J, \Phi_E)}{\mathrm{cov}(\Phi_E, \Phi_E)} \tag{3.3}$$

Here, the statistical independence of the noise sources in the SQUID and the excitation was used. Furthermore, we assume that the excitation flux stays within a linear regime of the flux–voltage and the flux–circulating current characteristics around the working point. To assure that the total power of the applied excitation also shows an effect at the output of the SQUID, the bandwidth of the excitation is chosen an order of magnitude smaller than the bandwidth of the output low-pass filter. Because the excitation flux is known and statistically independent from the SQUID noise, its influence on the covariances of the output variables $\mathrm{cov}(V,V)$, $\mathrm{cov}(J,J)$ and $\mathrm{cov}(J,V)$ can be eliminated. The pure noise of the SQUID reads:

$$S_{VV} = S_{VV}{}' - \frac{\mathrm{cov}(\Phi_E, \Phi_E)\, G_{V\Phi}{}^2}{B_{\mathrm{Out}}} = \frac{\mathrm{cov}(V,V)}{B_{\mathrm{Out}}} - \frac{\mathrm{cov}(V, \Phi_E)^2}{B_{\mathrm{Out}}\, \mathrm{cov}(\Phi_E, \Phi_E)} \tag{3.4}$$

$$S_{JJ} = S_{JJ}{}' - \frac{\mathrm{cov}(\Phi_E, \Phi_E)\, G_{J,\Phi}{}^2}{B_{\mathrm{Out}}} = \frac{\mathrm{cov}(J,J)}{B_{\mathrm{Out}}} - \frac{\mathrm{cov}(J, \Phi_E)^2}{B_{\mathrm{Out}}\, \mathrm{cov}(\Phi_E, \Phi_E)} \tag{3.5}$$

$$S_{JV} = S_{JV}{}' - \frac{\mathrm{cov}(\Phi_E, \Phi_E)\, G_{J,\Phi}\, G_{V\Phi}}{B_{\mathrm{Out}}} = \frac{\mathrm{cov}(J,V)}{B_{\mathrm{Out}}} - \frac{\mathrm{cov}(J, \Phi_E)\, \mathrm{cov}(V, \Phi_E)}{B_{\mathrm{Out}}\, \mathrm{cov}(\Phi_E, \Phi_E)} \tag{3.6}$$

The additional flux noise $S_{\Phi,VV}$ and energy resolution $\varepsilon_{VV}$ can now be calculated using Eqns. (1.19)–(1.22), see page 9.

The variance of the excitation flux has to be chosen well. In case it is too big, the characteristics of the SQUID can be degraded and in case it is too small, one needs a long simulation time to reach a good estimate for the small signal parameters. To account for this, we performed two simulation steps. In the first simulation step, we estimate an appropriate variance of the excitation and in the second step, we estimate the sensitivity and small signal parameters with this adapted excitation. In the first simulation step, the standard deviation of the external flux $\sqrt{\mathrm{cov}(\Phi_E, \Phi_E)}$ is chosen to $0.005\,\Phi_0$. This value is small enough not to exceed the small-signal regime of typical working points.

In case the resulting mean value of the voltage $V$ was smaller than $10\, f_{\mathrm{Out}}\, \Phi_0$, we did not perform the second simulation step. This occurs when the SQUID is either superconducting or biased close to the superconducting state. As mentioned above, the white noise spectrum in such working points cannot be measured within the observed bandwidth. The spectra

cannot be considered white over the bandwidth of the output low-pass filter. In this case, we only recorded the mean values of $V$ and $J$. All later shown noise characteristics are at working points above this voltage threshold. We chose a sufficiently low cutoff frequency of the low-pass filter to capture working points of the SQUID with the best sensitivity.

In case the mean value of the voltage $V$ was larger than $10\,\Phi_0\,f_{\mathrm{Out}}$, we considered the spectrum of the SQUID noise in the output low-pass filters as white and we performed a second simulation step to estimate the small-signal and noise parameters with a higher precision. From the first simulation run, we estimated the SQUID noise $S_{VV}$, $S_{JJ}$ and the small-signal parameters $G_{J\Phi}$ and $G_{V\Phi}$ using Eqns. (3.3)–(3.5). The flux excitation was adapted such that the artificially added noise power, see the subtracted terms in Eqns. (3.4) and (3.5), does not exceed the estimated intrinsic SQUID noise. The introduced noise on both $J$ or $V$ has to be considered and therefore, the variance of the excitation flux is chosen on the basis of the output parameter with the comparably larger artificially introduced noise. Expressed in an equation, the adapted variance of the excitation flux for the second simulation run reads:

$$\mathrm{cov}\left(\Phi_E,\Phi_E\right)\Big|_{\text{used during 2nd run}} = B_{\mathrm{Out}}\,\min\left(\frac{S_{VV}}{{G_{V\Phi}}^2}\,,\,\frac{S_{JJ}}{{G_{J\Phi}}^2}\right)\Big|_{\text{estimate 1st run}} \tag{3.7}$$

Here, $\min(a,b)$ is the minimum of the two variables $a$ and $b$. The resulting excitation level can be higher or lower than the start value. For safety, we additionally forced a fixed maximum of $\sqrt{\mathrm{cov}\left(\Phi_E,\Phi_E\right)} \leq 0.04\,\Phi_0$.

In summary, the variance of the artificially introduced flux excitation has at most the same magnitude as the variance of the voltage $S_{VV}\,B_{\mathrm{Out}}$ or the circulating current $S_{VV}\,B_{\mathrm{Out}}$ of the intrinsic SQUID noise. Here, the bandwidth $B_{\mathrm{Out}}$ is much smaller than the Josephson frequency. In practice, this leads to self-adapted flux excitation that does not degrade the characteristics of the SQUID and accounts for differences in the small-signal parameters $G_{V\Phi}$ and $G_{J\Phi}$ of different working points.

Besides its flexibility, a big advantage of JSIM is speed. The calculation of one SQUID from Fig. 3.4 included about $10^9$ plasma oscillations of the Josephson junctions and took 20 hours on a Pentium 4 with 3 GHz. In all simulations, the maximum time step in the simulation is chosen a factor of 25 smaller [45] than a period of the plasma frequency $f_P = \sqrt{I_0/(2\pi\,\Phi_0\,C)}$ of the Josephson junction. Noise sources induce Gaussian distributed random currents at the same rate of the maximum time steps.

At this point, we want to name some problems we encountered using JSIM. First of all, the simulation sometimes randomly crashes and has to be repeated. Nevertheless, we never had the impression that this apparent bug in the software leads to wrong results. Furthermore, the model of the Josephson junction in JSIM is of the RCSJ type and one has to choose a finite capacitance. To model an overdamped Josephson junction, we typically chose a Stewart-McCumber parameter $\beta_C = 0.1$, see Eqn. (1.12) on page 5, in the most cases. This value is low enough not to have an influence, see the discussion in section 1.3.2 on page 9 or Fig. 3.2. Nevertheless, compared to a model of a Josephson junction without the capacitance this leads to longer time for the calculation, because the maximum time steps in the simulation are connected to the plasma oscillations.

To test our simulation approach, we reproduced the characteristics, small-signal parameters and noise parameters of some published simulations from references [2, 58, 63–

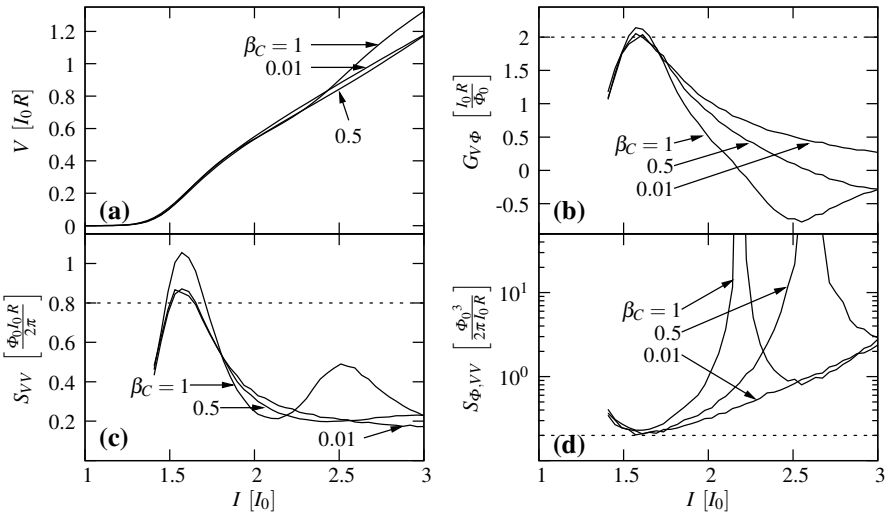


**Figure 3.2:** A simulation is shown for three standard SQUIDs, see the schematic in Fig. 1.3 on page 7, with varying $\beta_C$ at one external flux $\Phi_E = 0.25\,\Phi_0$ with changing bias current $I$. $\beta_L$ was set to 1 and the noise parameter $\Gamma$ was set to 0.05. **(a)** SQUID voltage. **(b)** Flux-to-voltage transfer. **(c)** Voltage noise PSD. **(d)** Additional flux noise PSD. The output low-pass filter was set to $f_{\mathrm{Out}} = I_0 R/(300\,\Phi_0)$. The effective observation time for each of the 50 working points of each SQUID was $1.3{\cdot}10^4/f_{\mathrm{Out}}$. The maximum excitation of the external flux $\sqrt{\mathrm{cov}(\Phi_E,\Phi_E)}$ was set to $0.01\,\Phi_0$.
The dashed lines indicate values calculated from Eqns. (1.23)–(1.27). For comparison, see page 55 in "The SQUID Handbook Vol. I" edited by J. Clarke and A. I. Braginski [2].

65, 67, 80, 101, 102]. In general, we found a good agreement. For demonstration purposes, in Fig. 3.2 we show a simulation that can be found in reference [2]. The original simulation is reproduced well. In the same figure, we also plotted the standard approximation formulas Eqns. (1.23)–(1.27) for SQUIDs with overdamped Josephson junctions, see page 11. They are well fulfilled at the points of optimal sensitivity. The value of minimum additional flux noise $S_{\Phi,VV}$ for the underdamped SQUID with $\beta_C = 1$ is close to the overdamped approximation. The peak in flux noise that can be seen for $\beta_C = 1$ and 0.5 in Fig. 3.2(d) corresponds to working points, where the SQUID inductance $L_{SQ}$ resonates with the effective capacitance of the Josephson junctions $\approx C/2$ [70, 71].

The units shown in Fig. 3.2 and throughout this chapter are normalized. This is based on the Langevin Eqns. (1.13), see page 7. Accordingly, currents are normalized to the critical current $I_0$ of one Josephson junction, voltages to the characteristic voltage $I_0 R$, magnetic flux to the flux quantum $\Phi_0$ and the time to $\Phi_0/(2\pi I_0 R)$. Using these basic units, the voltage noise PSD $S_{VV}$ is normalized to $\Phi_0 I_0 R/(2\pi)$ and the flux noise PSD $S_{\Phi,VV}$ to ${\Phi_0}^3/(2\pi I_0 R)$.

## 3.2 Optimization of typical dc-SQUIDs

In this section we present a numerical characterization of dc-SQUIDs based on the simulation technique presented in the last section. Here, we concentrate on the one hand on standard SQUIDs according to the schematic shown in Fig. 1.3 on page 7. On the other hand, we

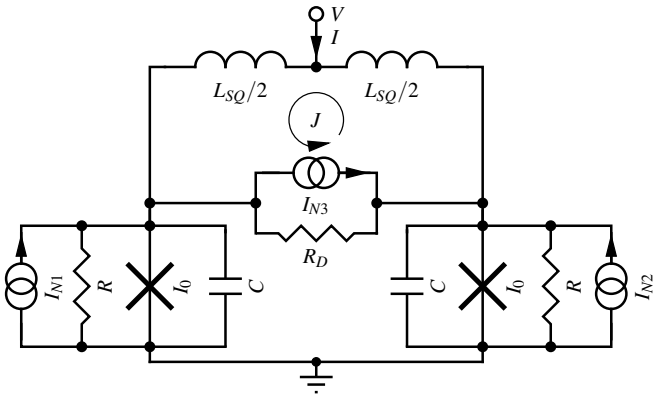


**Figure 3.3:** Basic schematic of a dc-SQUID with resistively shunted inductance. The parameter $\gamma = R/R_D$ describes the value of the chosen damping resistance. The noise source $I_{N3}$ injects the thermal noise current of the damping resistance $R_D$ with a PSD of $4\,k_B\,T\,\gamma/R$. The junctions are usually overdamped throughout this chapter, $\beta_C \ll 1$. For $\gamma = 0$, one gets a standard SQUID without the resistive shunt.

also included SQUID with a resistively shunted inductance [85–87], which is often used in practice, see section 1.4.1 on page 12. Both cases can be described by the schematic shown in Fig. 3.3, where a damping resistance of size $R_D = R/\gamma$ and the corresponding thermal noise current source are connected in parallel to the SQUID inductance.

### 3.2.1 Varied parameters of the investigated SQUIDs

The variable input parameters of the model are the inductance of the SQUID, represented by the screening parameter $\beta_L$, Eqn. (1.14) on page 7, the damping resistance $R_D$, the Stewart-McCumber parameter $\beta_C$, Eqn. (1.12) on page 5, the working point of the SQUID $I$ and $\Phi_E$ as well as its its operation temperature. The latter is represented by the noise parameter $\Gamma$, see Eqn. (1.8) on page 5. The variation of all these parameters is hardly possible and we therefore restrict ourselves to some practical limits.

First of all, we will here only investigate balanced SQUIDs. That means that the critical current $I_0$, capacitance $C$ and shunt resistance $R$ of both Josephson junctions are equal. Furthermore, the SQUID inductance $L_{SQ}$ is distributed evenly over the two branches.

Secondly, we investigate the overdamped regime $\beta_C \ll 1$. Here, the capacitance of the Josephson junction has no influence. We model this in JSIM by setting the value of $\beta_C$ to 0.1 in most of the cases. As already pointed out in section 1.3.2 on page 9, a variation towards the limit $\beta_C \sim 1$ usually does not introduce big differences compared to a modeling with the RSJ model without the capacitance of the junction.

Thirdly, we performed one series of simulations without the damping resistance ($\gamma = 0$) and one with the optimum value $\gamma = 0.5$ given in literature [86, 102].

Furthermore, we have to restrict the investigated working range. In other simulations reported in literature [2, 57, 61, 63, 67], the external flux $\Phi_E$ is chosen at a few discrete values. The bias current $I$ of the SQUID is changed in many more steps. We will first only use $\Phi_E = 0.25\,\Phi_0$ for simplicity. This indeed captures the most sensitive working ranges of most of the SQUIDs. In section 3.2.5 we will show one more flux point that captures

another low noise working point in the range of a low screening parameter $\beta_L \ll 1$. The bias current $I$ was varied in 40 working points between roughly the critical current of the SQUID, which depends on $\beta_L$, and a value of typically $2.2\,I_0$. This range includes typical low noise operation regimes.

We performed simulations on SQUIDs with a varying screening parameter $\beta_L = 0.01$ to 10. To ensure that the noise properties of the SQUID are proportional to the temperature, we chose $\Gamma$ to a comparably low value of 0.005. The reason for choosing this lower value is that the SQUID noise is only proportional to the temperature under the condition that both $\Gamma \ll 1$ and $\Gamma\beta_L \ll 1$ [2]. For a Josephson junction with a critical current of 15 µA, this corresponds to a temperature of 1.8 K. The chosen value for $\Gamma$ is not too low regarding the *MiniGRAIL* project, see section 1.5 on page 16, and the experiments in chapter 5.

In the chosen temperature range, the noise parameters of the SQUID are approximately proportional to the temperature. Therefore, it is convenient to divide the noise terms by $\Gamma$. This leads to the normalization terms $k_B T R$ for the voltage noise PSD $S_{VV}$, $k_B T/R$ for the current noise PSD $S_{JJ}$ and $k_B T {\Phi_0}^2/({I_0}^2 R)$ for the additional flux noise PSD $S_{\Phi,VV}$. It is convenient to use the screening parameter $\beta_L = 1$ to define a normalized inductance. This leads to a normalization term for the different energy resolutions, see Eqns. (1.20) to (1.22) on page 11, of $k_B T \Phi_0/(I_0 R)$. This can be interpreted as the thermal noise energy distributed evenly over the whole bandwidth up to the characteristic frequency of the Josephson junctions.

The corner frequency of the output low-pass filter was set to $f_{\mathrm{Out}} = I_0 R/(600\,\Phi_0)$ in each case and the effective observation time for the second simulation step on the sensitivity was $6.5{\cdot}10^3/f_{\mathrm{Out}}$ per working point. The excitation of the external flux $\sqrt{\mathrm{cov}(\Phi_E, \Phi_E)}$ was restricted to a maximum value of $0.04\,\Phi_0$, which was only reached for some insensitive working points of SQUIDs with $\beta_L > 1$. The automatically adapted standard deviation of the excitation flux stayed mostly below $0.01\,\Phi_0$. In general, the extracted quantities were in good agreement with published results from literature [2, 58, 63–65, 67, 80, 102]. We conclude that the automatically adapter flux excitation does not influence the behavior of the SQUID. Here, we had to mainly rely on published data on the additional noise $\varepsilon_{VV}$ which was investigated more frequently. Comparisons to published results will be pointed out below.

For the SQUIDs with a damping resistance $\gamma = 0.5$ and $\beta_L > 1$, new features in the SQUID dynamics emerge. Here, the optimum operation range shifts towards higher bias currents and voltages [102]. Therefore, we simulated these few particular SQUIDs up to higher bias currents $2.8\,I_0$. Furthermore, we here had to decrease $\beta_C$ to an even lower value of 0.01. This had to be done to exclude resonance effects between the SQUID inductance and the capacitance of the Josephson junctions in the optimum working range. These simulations took a longer time because of the higher plasma frequency.

### 3.2.2 Investigated properties

One of the conclusions in chapter 2 was that the noise temperature of a SQUID amplifier connected to an arbitrary input impedance $\bar{z}_L = \bar{Z}_L/(\omega L_{IN})$ can be described with three parameters, see Eqns. (2.25)–(2.27) in combination with Fig. 2.3 on page 28.

First of all, the additional noise term $\varepsilon_{VV}$ describes the increase in noise for an unmatched input impedance $\bar{z}_L \neq \bar{z}_{L0}$. Secondly, $\varepsilon_0$ defines the minimum reachable noise temperature for

$\bar{z}_L = \bar{z}_{L0}$. The actual value of the optimum input impedance $\bar{z}_{L0}$ is leading to the third term $G_{J\Phi} L_{SQ} - \varepsilon_{JV}/\varepsilon_{VV} = -(\Im[\bar{z}_{L0}] + 1)/k^2$. It describes the difference between the optimum input reactance compared to the conjugate complex impedance of the geometric inductance of the SQUID $-\mathrm{j}\omega L_{IN}$. Here, the coupling efficiency $k^2$ between the input inductance $L_{IN}$ and the SQUID inductance $L_{SQ}$ is used. The real part of the optimum input impedance is given by a combination of the first two parameters $\Re[\bar{z}_{L0}] = k^2 \varepsilon_0/\varepsilon_{VV}$.

These three parameters are dependent on the working point of a given SQUID. On the other hand, they suffice to describe the general performance of a SQUID when its coupling efficiency $k^2$ is given. This is of special interest in applications, where the back-action of the amplifier plays a role. Based on the mentioned three parameters, one can for example estimate the optimum quality factor of a capacitive impedance, see Eqn. (2.50) on page 34, or the achievable bandwidth, see Eqn. (2.53). In the following figures, we will therefore include these three parameters.

Another important result of chapter 2 was that feedback effects do not influence the noise performance. These effects can be altered or compensated during the operation of the SQUID and will be therefore ignored here. Accordingly, the output small-signal parameters $G_{JI}$ and $G_{VI}$ are of secondary importance and will not be investigated further.

Furthermore, we will give the characteristics $J$ and $V$ and the two remaining small signal parameters, the flux-to-voltage transfer $G_{V\Phi}$ and the normalized dynamic SQUID inductance $G_{J\Phi} L_{SQ}$, see Eqn. (1.15) on page 9.

### 3.2.3 Results of the simulation series

To allow a compact overview of the large amount of data and varied parameters, it is convenient to show all data in two graphs, see Figs. 3.4 and 3.5. This makes a comparison of different properties easier. Here, we want to give a short introduction on how to read these two graphs.

In Fig. 3.4, we show the data of all working points of a few exemplary SQUIDs. The shared horizontal axis is given by the bias current $I$. Within each of the sub-figures, we plotted different properties of the six SQUIDs, a combination of three exemplary screening parameters $\beta_L = 0.1, 1, 10$ as well as the two values of the damping resistance $\gamma$. The SQUIDs without a damping resistance ($\gamma = 0$) are shown as solid lines and the ones with damping resistance $\gamma = 0.5$ are shown as dashed lines. This is also indicated in the legend on the top right of the figure.

In each of the lines shown in Fig. 3.4, we also indicate the points of best sensitivity. The squares (■, □) indicate the points of the minimum additional flux noise $S_{\Phi,VV}$ or the respective energy resolution $\varepsilon_{VV}$, see Fig. 3.4(h). The circles (●,○) indicate the points of minimum achievable noise temperature, represented by $\varepsilon_0$ which is shown in Fig. 3.4(j). The symbols used can also be seen in the legend on the top right. Accordingly, Fig. 3.4 can be used to compare the performance of different working points of the six exemplary SQUIDs.

A comparison of the SQUIDs without the damping resistance ($\gamma = 0$) and the SQUIDs with the damping resistance $\gamma = 0.5$ reveals that for $\beta_L = 0.1$, there is practically no difference. Therefore, the solid and dashed lines for $\beta_L = 0.1$ are almost identical all over Fig. 3.4. For the SQUIDs with higher screening parameter $\beta_L = 1$ and 10, the resistive shunt influences the behavior of the SQUID. As mentioned above, the optimum operation range of SQUIDs with $\beta_L > 1$ and the attached damping resistance $\gamma = 0.5$ shifts towards higher bias currents

and voltages [102]. These SQUIDs were therefore simulated up to higher bias currents $2.8\,I_0$. In Fig. 3.4, this is indicated by putting the markers for the optimum working points (□, ○) of the SQUID with $\beta_L = 10$ and $\gamma = 0.5$ on the upper limit of the current axis. The actual results in these optimum working ranges are not far off the indicated values. The exact values for all SQUIDs are shown in the following Fig. 3.5.

Several important properties of the SQUIDs in their optimum working points of sensitivity are now summarized in Fig. 3.5. Here, the shared horizontal axis is the varied screening parameter $\beta_L$. The legend is indicated on the top right of the graph, the symbols and line styles are identical to Fig. 3.4 which shows the characteristics of the exemplary SQUIDs.

Accordingly, one can here compare the properties of all different SQUIDs in their working point of minimum $\varepsilon_{VV}$ and in their working point of minimum $\varepsilon_0$. For the latter, it is important to know at which optimum input impedance $\bar{z}_{L0}$ the minimum noise temperature is achieved. Both the imaginary and the real part of $\bar{z}_{L0}$ in the working points of optimum achievable noise temperature are plotted in Fig. 3.5(d).

To make a comparison of the SQUIDs more straightforward, it is convenient to interpret the varying screening parameter $\beta_L$ as a changing inductance $L_{SQ}$ with fixed junction parameters $I_0$ and $R$. Also in the simulation, the SQUID inductance $L_{SQ}$ was the only changed parameter to vary the screening parameter $\beta_L$. In section 3.2.5, we will qualitatively include $I_0$ and $R$ into the optimization process.

To give an overview of the, from our point of view, most important effects, we will first summarize the properties in the three ranges $\beta_L < 1$, $\beta_L \approx 1$ and $\beta_L > 1$, represented by the exemplary SQUID characteristics shown in Fig. 3.4. In section 3.2.3, we will then globally summarize the results.

**Low inductance SQUID $\beta_L < 1$**

The most obvious consequence of a changing $\beta_L$ is the difference in the critical current of the SQUID. In Fig. 3.4(a), one can see that the exemplary SQUID in the low-inductance range with a screening parameter $\beta_L = 0.1$ has the lowest critical current, the current where the voltage state is reached. We find the expected [57] value of $\approx 1.4\,I_0$ for the applied external flux of $\Phi_E = 0.25\,\Phi_0$. The critical current of all simulated SQUIDs was found at the expected values [57].

If one takes a look at the markers for the working ranges of the best sensitivity, see Fig. 3.4(a) for $\beta_L = 0.1$, it becomes obvious that there are two completely different working ranges. The best additional noise $\varepsilon_{VV}$ (marker ■) is found close to the superconducting state $V \approx 0.15\,I_0\,R$. The minimum reachable noise temperature (marker ●), on the other hand is found at much higher voltages $V \sim 0.6\,I_0\,R$. In the overview Fig. 3.5(a), one can clearly see this separation for all SQUIDs with a screening parameter $\beta_L$ smaller than $\sim 1$.

This is a somewhat surprising result. In practice, one could be tempted to search for the working range that shows the minimum additional flux noise $S_{\Phi,VV}$ and guess that this also leads to the best signal-to-noise ratio. This working range is also close to the point of the observed maximum flux-to-voltage transfer function $G_{V\Phi}$, see the marker ■ for $\beta_L = 0.1$ in Fig. 3.4(f).

In applications where the back-action becomes important, this can lead to a degraded sensitivity. As one can see from Fig. 3.4(i), the noise on the circulating current $S_{JJ}$ is

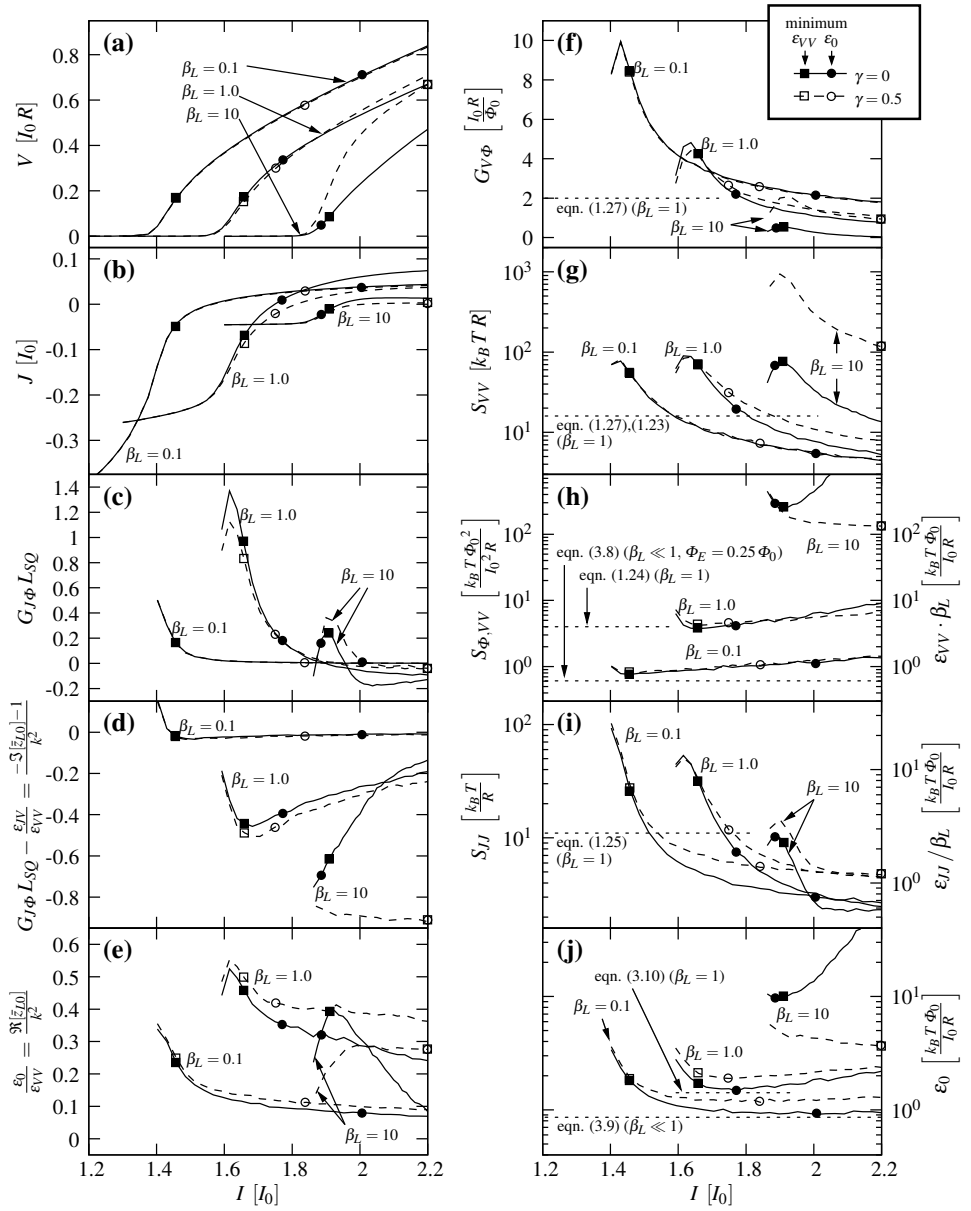


**Figure 3.4:** Simulation of six SQUIDs with varying $\beta_L$ and $\gamma$, see the legend in the top right corner. All simulations are shown versus the bias current $I$. $\Phi_E = 0.25\,\Phi_0$, $\Gamma = 0.005$. We plotted a choice of important parameters in normalized units. **(a)** SQUID voltage. **(b)** Circulating current. **(c)** Normalized dynamic inductance. **(d)** Shift in optimum normalized input reactance. **(e)** Optimum normalized input resistance. **(f)** Flux-to-voltage transfer. **(g)** White noise PSD of the output voltage. **(h)** Additional flux noise and energy resolution. **(i)** White noise PSD of the circulating current and the corresponding energy resolution. **(j)** $\varepsilon_0$, which is proportional to the minimum possible noise temperature when the optimum input impedance $\omega L_{IN} \bar{z}_{L0}$ is connected, see (d),(e).
The working points with minimum additional noise $\varepsilon_{VV}$ are marked with squares, the ones with the minimum possible noise temperature with circles. For $\beta_L$ and $\gamma = 0.5$, the optimum working range is above the range shown here. Also see the figure on the right.

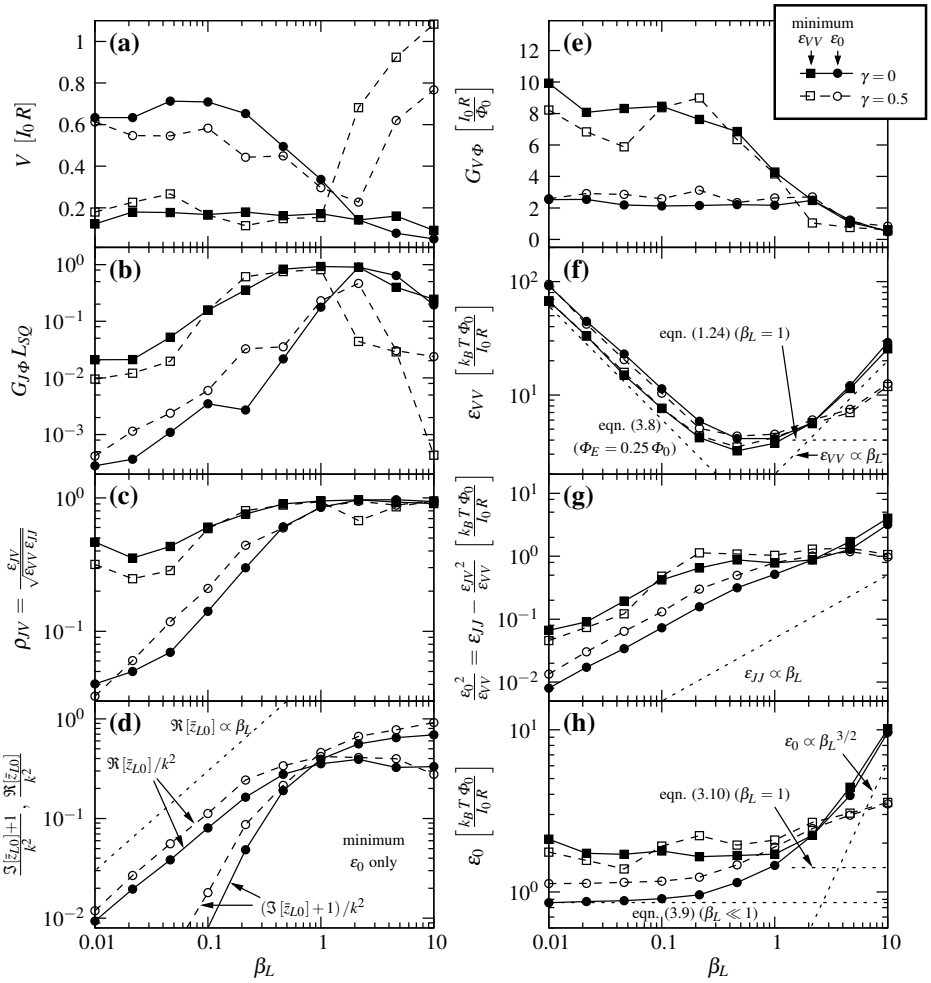


**Figure 3.5:** A choice of properties at the best points of sensitivity, the minimum additional noise (■, □) and the minimum reachable noise temperature (●,○) of all simulated SQUIDs. See the legend in the top right corner. **(a)** SQUID voltage. **(b)** Normalized dynamic inductance. **(c)** Correlation coefficient between the current noise on $J$ and the measured flux $V/G_{V\Phi}$. **(d)** Optimum input impedance. **(e)** Flux-to-voltage transfer. **(f)** Additional noise. **(g)** Effective back-action noise. **(h)** $\varepsilon_0$. See text for details.

decreased for the higher bias currents. Therefore, the SQUID has to be biased there to reach the optimum point of sensitivity.

In the work of Danilov et al. [16, 59], one can find analytical expressions for the performance of standard SQUIDs with a low inductance. They calculated the SQUID characteristics, small-signal parameters and the sensitivity in case of a negligibly small SQUID inductance $2\pi\beta_L \ll 1$.

According to theory, the minimum reachable additional noise is found close to the superconducting state $V \to 0$. Its magnitude is described by [59]:

$$\varepsilon_{VV,\min,\beta_L \ll 1} = \frac{12}{(2\pi)^2 \beta_L \sin^2\left(\pi\Phi_E/\Phi_0\right)} \frac{k_B T \Phi_0}{I_0 R} \qquad (2\pi\beta_L \ll 1, V \to 0) \qquad (3.8)$$

Note that a similar expression has been derived in another analytical work [103]. Equation (3.8) is plotted in Fig. 3.5(f) and shows a good agreement with the simulation. The same holds for simulations on the SQUIDs with $\beta_L < 1$ shown in references [57, 58]. The energy resolution $\varepsilon_{VV}$ scales inversely proportional with the inductance $\varepsilon_{VV} = S_{\Phi,VV}/(2L_{SQ})$, see Eqn. (1.20). Therefore, the screening parameter can be found in the denominator in Eqn. (3.8). For a fixed characteristic voltage $I_0R$, the overall minimum additional flux noise $S_{\Phi,VV}$ can be found for $\beta_L \ll 1$ [59]. This can be seen for the exemplary SQUID with $\beta_L = 0.1$ in Fig. 3.4(h), where we plotted the additional flux noise PSD $S_{\Phi,VV}$.

According to Eqn. (3.8), the global minimum achievable additional flux noise is $S_{\Phi,VV} \approx 0.3\,k_B T {\Phi_0}^2/({I_0}^2 R)$, which can be found at $\Phi_E \to 0.5\,\Phi_0$. Note that this quantity is, according to reference [16], not affected by quantum mechanical effects. Due to our chosen flux bias of $\Phi_E = 0.25\,\Phi_0$, the global minimum in the additional flux noise PSD $S_{\Phi,VV}$ is missed by a factor of two, see Eqn. (3.8). For simplicity, we will ignore this at the moment and add another simulation series with $\Phi_E \to 0.5\,\Phi_0$ in section 3.2.5.

The minimum $\varepsilon_0$ is according to theory indeed found at $\Phi_E \approx 0.25\,\Phi_0$, but at a higher operation voltage V $\approx 0.65\,I_0R$ [16, 59]:

$$\varepsilon_{0,\min} \approx \frac{5.4}{2\pi}\frac{k_B T\,\Phi_0}{I_0 R} \qquad (2\pi\beta_L \ll 1,\ \Phi_E \approx 0.25\,\Phi_0,\ V \approx 0.65\,I_0R) \tag{3.9}$$

This corresponds to the global minimum of the minimum achievable noise temperature in dc-SQUIDs and it is indeed affected by zero point fluctuations [16]. The theoretical minimum for $\varepsilon_{0,\min}$ is $\hbar/2$ [16, 17]. Note the much higher operation voltage compared to the range of minimum additional noise $\varepsilon_{VV}$. The value and working range given in Eqn. (3.9) fit our results well, see the data of the lower range of $\beta_L$ in Figs. 3.5(a) and (h).

Another effect noted in theory [59] can also be seen in the simulations. For the symmetric low-inductance SQUID, both the correlation between the additional and the back-action noise, represented by $\varepsilon_{JV}$, and the normalized dynamic inductance $g_{J\Phi} = G_{J\Phi} L_{SQ}$ vanish. This can be especially seen for the working points of minimum noise temperature in Figs. 3.5(b) and (c) for $\beta_L \ll 1$.

For the SQUIDs with $\beta_L \lesssim 1$ the connected damping resistance with $\gamma = 0.5$ does not alter the SQUID dynamics significantly and the noise terms are increased only slightly. This can be seen for the exemplary SQUID with $\beta_L = 0.1$ in Fig. 3.4 by comparing the solid and the dashed lines in all sub-figures.

**Intermediate inductance SQUID $\beta_L \approx 1$**

For the higher inductance SQUIDs $\beta_L \gtrsim 1$, all low noise working points are found at $\Phi_E \approx 0.25\,\Phi_0$ [2, 57, 60, 67], which we also verified in test simulations.

The reached minimum additional flux noise $S_{\Phi,VV}$ for the SQUID with $\beta_L = 1$ fits the standard SQUID approximation well, see Eqn. (1.24) on page 11. This can be seen in Fig. 3.4(h) for the SQUID with $\beta_L = 1$ in the region marked with ■.

For the SQUID at $\beta_L = 1$, the minimum achievable noise temperature, see Eqns. (1.24)–(1.26) on page 11, was determined by numerical simulations to [57, 58, 63]:

$$\varepsilon_{0,\min,\beta_L=1} \approx 1.4\,\frac{k_B T\,\Phi_0}{I_0 R} \qquad (\beta_L = 1) \tag{3.10}$$

Also here, a good agreement with our simulation was found, as one can see from Figs. 3.4(j) and 3.5(h). The corresponding working range shifts, compared to $\beta_L \ll 1$, to lower voltages. The value from Eqn. (3.10) is only about 60% higher than the overall minimum which is achieved for $\beta_L \ll 1$, see Eqn. (3.9). Nevertheless, there is another big difference. Both the correlation between the additional and the back-action noise, represented by $\varepsilon_{JV}$, and the normalized dynamic inductance $G_{J\Phi} L_{SQ}$ become larger, see Figs. 3.4(c) and (d). This has an influence on the optimum input reactance at which the minimum noise temperature is reached.

As mentioned before, the connected damping resistance with $\gamma = 0.5$ does not alter the SQUID dynamics significantly for the SQUIDs with $\beta_L \lesssim 1$. This can also be seen for the SQUID with $\beta_L = 1$ in Fig. 3.4 by comparing the solid and the dashed lines in all sub-figures. The damping resistance degrades the reachable sensitivity only slightly.

Here, we want to point out some temperature-dependent differences especially in the voltage noise PSD $S_{VV}$, see Fig. 3.4(f), and the flux-to-voltage transfer $G_{V\Phi}$, see Fig. 3.4(g). The simulations shown in Fig. 3.4 were done at a ten times higher temperature compared to the simulations shown in Fig. 3.2. In both cases, the standard SQUID approximation formulas for the additional flux noise PSD $S_{\Phi,VV}$ of a SQUID with $\beta_L = 1$, see Eqn. (1.23) on page 11, fit very well, compare Fig. 3.2(d) with Fig. 3.4(h). As expected, the additional flux noise scales linear with the temperature. On the other hand, the flux-to-voltage transfer $G_{V\Phi}$ increases about a factor of two at the lower temperature compared to Eqn. (1.27), compare the marker ■ for $\beta_L = 1$ and the dotted line in Fig. 3.4(f). Accordingly, the voltage noise PSD $S_{VV}$ also does not scale linearly with temperature, compare Figs. 3.2(c) and 3.4(g) with respect to the there shown dotted lines. This behavior is caused by noise rounding at higher thermal energy. Also see the simulations in references [57, 102] with varying temperature, which show a similar behavior. If the product $\Gamma \beta_L$ gets even larger, also the flux noise PSD $S_{\Phi,VV}$ cannot be expected to scale linearly with the temperature anymore [2, 57, 61].

**High inductance SQUID $\beta_L > 1$**

In the range of $\beta_L > 1$, the additional flux noise $S_{\Phi,VV}$ and the minimum achievable noise temperature, represented by $\varepsilon_0$, of standard SQUIDs increase rapidly. This can be seen by comparing the solid lines in Figs. 3.4(h) and (j). This is accompanied by a decreased flux-to-voltage transfer, see Fig. 3.4(f). The optimum working points here can be found for both the additional noise and the minimum noise temperature close to the superconducting state [16, 59]. The minimum reachable additional energy resolution $\varepsilon_{VV}$ is, according to the analytic theory in the high-inductance range $2\pi\beta_L \gg 1$, found close to the superconducting state $V \to 0$ [16, 59]. The theoretical value reads:

$$\varepsilon_{VV,\min,\beta_L \gg 1} = \frac{3}{2}\beta_L \frac{k_B T \Phi_0}{I_0 R} \qquad (2\pi\beta_L \gg 1, V \to 0) \tag{3.11}$$

The result of our simulations for $\beta_L = 10$ is about a factor of two higher than the value predicted by Eqn. (3.11). For $\varepsilon_0$ the result of our simulation is about a factor of 7 larger than the theoretical expression from reference [59]. The reason for this discrepancy is unknown. Nevertheless, the published data on the additional energy resolution $\varepsilon_{VV}$ in references [57, 58] for the SQUIDs with $\beta_L > 1$ show a good agreement with our result. In Figs. 3.5(d) and (i)

we plotted the predicted dependence of $\varepsilon_{VV} \propto \beta_L$ and $\varepsilon_0 \propto {\beta_L}^{-3/2}$ for $2\pi\beta_L \gg 1$ [59]. The slope fits the results of our simulation, as well as the optimum working range $V \to 0$ for both noise parameters, see the solid lines for $\beta_L > 1$ in Fig. 3.5(a).

For high values of $\beta_L$, the added damping resistance $\gamma = 0.5$ significantly changes the behavior. The first effect is an increased flux-to-voltage transfer and voltage noise in the usual low voltage working range, compare the solid and the dashed line for the exemplary SQUID with $\beta_L = 10$ in Figs. 3.4(f) and (g). Nevertheless, the optimum working range of both additional noise and minimum noise temperature is found at much higher voltages [85–87], see the dashed line in the range $\beta_L > 1$ of Fig. 3.5(a). Here, the flux-to-voltage transfer is comparable with the unshunted case, see Fig. 3.5(e).

As already pointed out, the SQUIDs with damping resistance $\gamma = 0.5$ and $\beta_L > 1$ had to be simulated at higher bias currents up to $2.8\,I_0$. To also exclude an influence of the capacitance, we had to choose a lower value of $\beta_C$ of 0.01. In the range $\beta_L > 1$ and $\beta_C \ll 1$ the additional noise and the minimum noise temperature are improved for the shunted SQUID, see Figs. 3.5(f) and (h). The overall agreement with the published data from reference [102] is good. Although the resonance between the capacitance and the inductance is suppressed by the resistive shunt [85], one can still expect an influence of this resonance on the noise properties. Because of the higher operation voltage of this design, the noise in the optimum working range of the shunted SQUID might be degraded compared to the non-shunted SQUID with the same $\beta_L$ and $\beta_C$. Nevertheless, for high inductance SQUIDs $\beta_L > 1$ a damping resistance in the order of $\gamma = 0.5$ can be recommended [86].

Another effect of the damping resistance is pointed out in reference [87]. The normalized dynamic inductance $G_{J\Phi}\,L_{SQ}$ of the SQUID with a resistively shunted inductance is suppressed significantly, especially in the optimum working range at high voltages $V$. This can be seen in Fig. 3.5(b) by comparing the solid and the dashed line for $\beta_L > 1$. Accordingly, the input inductance of the SQUID operated in direct readout is altered by the damping resistance. Nevertheless, the correlation between the circulating current and the voltage noise stays at high values, see Fig. 3.5(c). The optimum input impedance $\bar{z}_{L0}$ is therefore nearly unaffected by the resistive shunt, see Fig. 3.5(d).

For both the shunted ($\gamma = 0.5$) and the unshunted ($\gamma = 0$) case, the optimum input reactance is shifted far away from the conjugate complex value of the impedance of the SQUID input inductance $-\mathrm{j}\omega L_{IN}$, see the range $\beta_L > 1$ in Fig. 3.5(d).

**Summary**

The working range of the optimum additional noise $\varepsilon_{VV}$ can, except for the SQUID with the resistively shunted inductance $\gamma = 0.5$ with high values of the screening parameter $\beta_L > 1$, be found close to the maximum flux-to-voltage transfer function $G_{V\Phi}$, see the markers ■ in Fig. 3.4(f). The corresponding voltage $V$ is $\approx 0.2\,I_0 R$, see the markers ■ in Fig. 3.5(a). This is close to the usual approximation of $V \approx 0.3\,I_0 R$ [60]. The global minimum additional noise $\varepsilon_{VV}$ can be found at $\beta_L \approx 0.5$ [59], see Fig. 3.5(f). This only holds for a fixed characteristic voltage $I_0 R$, which will be discussed in more detail below.

The working range of the minimum reachable noise temperature, represented by $\varepsilon_0$, can for all SQUIDs with a screening parameter $\beta_L \lesssim 1$ be found close to moderate values of the flux-to-voltage transfer $G_{V\Phi} \approx 2$ to $3\,I_0 R/\Phi_0$, see the markers ● and ○ in Fig. 3.5(e). This corresponds to a working range with higher voltages $\approx 0.7\,I_0 R$ at lower values of

$\beta_L \lesssim 1$ [16, 59], as can be seen for the markers ● and ○ in Fig. 3.5(a). In the range $\beta_L \ll 1$, the global minimum noise temperature is attained, see Eqn. (3.9).

Both the minimum additional noise and noise temperature increase with higher values of $\beta_L > 1$. This effect can be alleviated by shunting the SQUID inductance with a damping resistance. For SQUIDs at very small values of $\beta_L \lesssim 0.1$, the dynamics practically do not change anymore. Here, the coupled energy resolution $\varepsilon_{VV}/k^2$ scales inversely linearly with $\beta_L$, see Fig. 3.5(f), the definition of the energy resolution, Eqn. (1.20) on page 11, and Eqn. (3.8). Decreasing the SQUID inductance $L_{SQ}$ such that the screening parameter $\beta_L$ is further decreased below a value of $\sim 0.1$ has the same effect on the total noise properties as decreasing the coupling efficiency $k^2$. Also see Figs. 3.5(g) and (h), which illustrate the dependency of the effective back-action noise and the minimum noise temperature.

Because the additional noise $\varepsilon_{VV}$ is also a part of $\varepsilon_0$, see Eqn. (2.24) on page 27, one could be tempted think that a minimized $\varepsilon_{VV}$ also leads to the minimum noise temperature. This is about true for SQUIDs with $\beta_L \gtrsim 1$, as one can see from Figs. 3.5(a), (f) and (h). For the lower range of the screening parameter $\beta_L < 1$, there are two completely different optimum working ranges. Here, the search for the additional noise at low voltages leads to a significant increase of the minimum reachable noise temperature, compare the markers ●○ with ■□ in Fig. 3.5(h). This is caused by an increased back-action in the working points showing the minimum additional noise, see Fig. 3.5(g).

To reach the minimum noise temperature, the optimum input impedance $\bar{z}_{L0}$ has to be connected. The magnitude of the real and the imaginary part of this optimum impedance can be seen in Fig. 3.5(d). The imaginary part of the optimum input impedance $\Im\left[\bar{z}_{L0}\right]$ is determined by the normalized dynamic inductance of the SQUID $G_{J\Phi}\,L_{SQ}$ and the correlation between the back-action and the additional noise, see Eqn. (2.26) on page 27. The correlation coefficient $\rho_{JV}$ between the measured flux $V/G_{V\Phi}$ and the circulating current $J$ shows for all SQUIDs and working points a positive sign, see Fig. 3.5(c). This supports the qualitative model [63] that the correlation is mainly caused by noise currents $J$ that generate an apparent external flux, which in turn causes a noise on the voltage $V$ via the flux-to-voltage transfer $G_{V\Phi}$. Note that we verified in simulations that $\varepsilon_{JV}$ is also axially symmetric about $\Phi_E = 0$. The same holds for the normalized dynamic impedance of the SQUID $G_{J\Phi}\,L_{SQ}$. Therefore, also the optimum input impedance $\bar{z}_{L0}$ is symmetric about $\Phi_E = 0$, $\bar{z}_{L0}(\Phi_E) = \bar{z}_{L0}(-\Phi_E)$. Furthermore, the optimum input impedance is capacitive in all working points.

With the data from Figs. 3.5(d), (f) and (h) and the analysis presented in chapter 2, one can derive the performance of the SQUID for an arbitrary connected input impedance, for example a resistive source or a pickup coil. Below, we want to briefly discuss the case of a connected capacitive input circuit.

### 3.2.4 Discussion on the performance with a capacitive input circuit

The quality factor of the optimum capacitive input circuit $Q_{L0}$ can be determined from Eqn. (2.50) on page 34 and the real part of the optimum input impedance, see Fig. 3.5(d). The optimum quality factor $Q_{L0}$ can be expressed as $Q_{L0} \approx \Re\left[\bar{z}_{L0}\right]^{-1}$, where we neglected the shift in the optimum frequency $\omega_0 \approx \omega_L$. From Fig. 3.5(d) we determine $k^2\,Q_{L0}$ for all SQUIDs with a screening parameter $\beta_L \gtrsim 1$ to about 3. $k^2\,Q_{L0}$ increases for lower values of the screening parameter $\beta_L < 1$. At $\beta_L = 0.1$ the optimum quality factor is $Q_{L0} \approx 10/k^2$.

The optimum noise temperature $T_{N0} = \omega_0 \varepsilon_0 / k_B$ can be observed at the optimum frequency $\omega_0$, see Eqns. (2.49) and (2.50) on page 34. The frequency of the optimum noise temperature $\omega_0$ can be expressed as $\omega_0 = \omega_L \left(-\Im\left[\bar{z}_{L0}\right]\right)^{-1/2}$. The magnitude of the shift compared to the passive resonance frequency of the input circuit $\omega_L$ can therefore be determined from the shift in optimum load reactance $\left(\Im\left[\bar{z}_{L0}\right]+1\right)/k^2$. This value is shown in Fig. 3.5(d). For all values of the screening parameter $\beta_L$, the optimum frequency $\omega_0$ is shifted above the passive resonance frequency $\omega_L$. This can be understood by the effective screening of the circulating current noise in the SQUID via the input circuit above the resonance.

The magnitude of the frequency shift between the passive resonance frequency $\omega_L$ and the frequency of the minimum noise temperature $\omega_0$ is dependent on the coupling factor $k^2$ as well as on the screening parameter $\beta_L$. For $\beta_L \lesssim 0.5$, this shift is negligible, whereas for large values of the screening parameter $\beta_L \gtrsim 0.5$ and large values of the coupling efficiency $k^2 \to 1$ the shift can be large.

Naturally, for a high coupling efficiency $k^2$, the SQUID inductance will be screened by the capacitance and this will change the dynamics, especially for SQUIDs with $\beta_L \gtrsim 1$. This will be treated later in this chapter.

### 3.2.5 Optimization of the SQUID design

In practice, the SQUID inductance $L_{SQ}$ is usually related to the requirements of the intended application and therefore has to be considered fixed. This leaves the parameters $I_0$, $R$ and $C$ of the Josephson junction that can be either varied or are determined by the technology. In Figs. 3.6(a) and (c) we plotted the minimum achievable noise parameters from the simulation results presented in the last section. The horizontal axis is given by $\beta_L$, which is accordingly varied with the critical current of the Josephson junction $I_0$. The vertical axis in Figs. 3.6(a) and (c) should be read for a fixed characteristic voltage $I_0 R$, where $R$ is accordingly adapted.

According to theory [59], we missed another working point of minimum additional noise for the low-inductance SQUIDs $\beta_L \lesssim 1$, see Eqn. (3.8) and the subsequent paragraph. We therefore performed another simulation series at $\Phi_E = 0.4\,\Phi_0$ to determine the minimum possible additional noise $\varepsilon_{VV}$ in this range. The results are plotted in Fig. 3.6(a). Here, the optimum operation voltage is even lower $V \approx 0.1\, I_0 R$. The agreement with Eqn. (3.8) is again good for $\beta_L \ll 1$. The minimum reachable noise temperature, represented by $\varepsilon_0$, is degraded at these working points [59].

From Fig. 3.6(a) we determine a minimum reachable additional energy resolution of:

$$\varepsilon_{VV,min} \approx 2.8\, \frac{k_B T\, \Phi_0}{I_0 R} \qquad (\beta_L \approx 0.5) \tag{3.12}$$

These results are surprising because the commonly given value for the optimum screening parameter $\beta_L$ is 1, see for example references [2, 57, 60, 67]. Nevertheless, in the work of Danilov and Likharev [16, 59], the same optimum values are given for an analysis neglecting the capacitance of the Josephson junctions. Also see reference [104] for a similar numerical result. The minimum $\varepsilon_0$ is given by Eqn. (3.9) and occurs for $\beta_L \ll 1$. The added damping resistance $\gamma = 0.5$ slightly increases the noise for $\beta_L \lesssim 1$ [102].

From the axis of Figs. 3.6(a) and (c) it follows that a maximum characteristic voltage $I_0 R$ should be chosen to reach minimum noise parameters. If one assumes typical externally

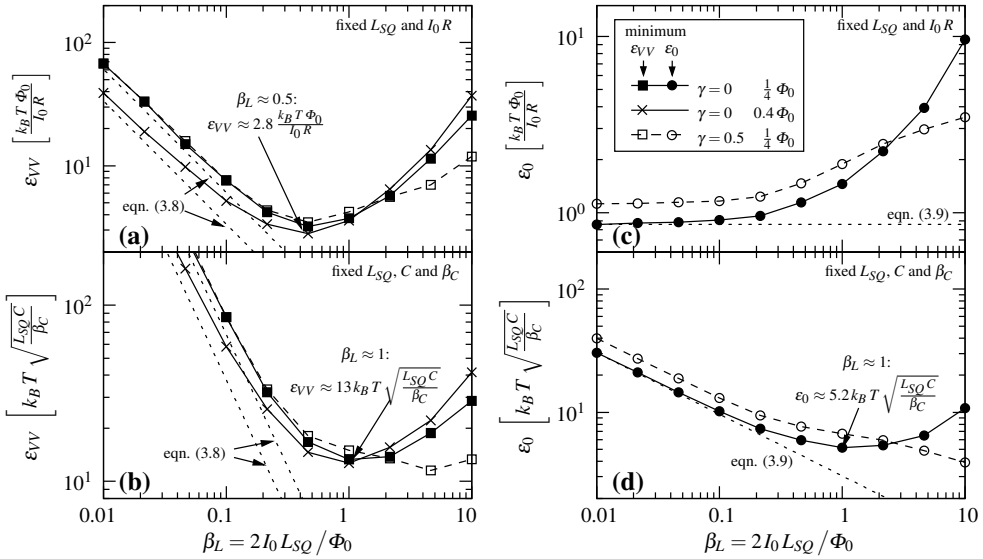


**Figure 3.6:** The two most important noise parameters for a fixed SQUID inductance $L_{SQ}$. The screening parameter $\beta_L$ (horizontal axis) is varied via the critical current $I_0$. **(a)**,**(b)** The minimum additional noise $\varepsilon_{VV}$. **(c)**,**(d)** The minimum $\varepsilon_0$ from the simulation shown in Fig. 3.5. Another simulation series was added for $\gamma = 0$ and $\Phi_E = 0.4\,\Phi_0$. See the legend in (c).
**(a)**,**(c)** correspond to the minimum expected noise parameters if $R$ is chosen to keep $I_0 R$ constant and **(b)**,**(d)** if $R$ is chosen to keep $\beta_C$ constant with a fixed capacitance of the Josephson junction $C$. For the latter case, we applied $I_0 R = \Phi_0 \sqrt{\beta_C \beta_L / (4\pi L_{SQ} C)}$ to transform the data from (a),(c) to (b),(d). See text for details.

shunted low-$T_c$ Josephson junctions within the RCSJ model, there are mainly three restrictions which limit the chosen $I_0 R$.

First, the Josephson junctions have to be non-hysteretic. This is related to the Stewart-McCumber parameter $\beta_C$. As discussed in section 1.2.4 on page 5, the noise-free characteristics become hysteretic above $\beta_C \approx 0.7$. The influence of hysteresis on the operation of the SQUID is a function of $\beta_C$, $\Gamma$, $\beta_L$ and $\Phi_E$ [67]. In an optimized SQUID design, one should choose the highest possible value for $\beta_C$, which still stays below the hysteretic limit. We did not investigate the optimum here, it is usually given by $\beta_C \approx 1$ to 2 for $\beta_L \approx 1$ to 2 [67]. For $\beta_L \ll 1$ and $\Phi_E \approx 0.4$, higher values of $\beta_C$ in the order of 2 to 6 can lead to an improvement [104]. With the fixed SQUID inductance and a fixed capacitance of the Josephson junction, one can use the definitions of $\beta_L$ and $\beta_C$ to express the chosen $I_0 R$ as $\Phi_0 \sqrt{\beta_C \beta_L / (4\pi L_{SQ} C)}$. We used this expression to calculate the expected sensitivity for a fixed value of $\beta_C$, see Figs. 3.6(b) and (d). In conservative designs, typically chosen values for $\beta_C$ are $< 1$. For this case, the found minima for the unshunted SQUIDs ($\gamma = 0$) are:

$$\varepsilon_{VV,min} \approx 13\, k_B T \sqrt{\frac{L_{SQ} C}{\beta_C}} \qquad (\beta_L \approx 1,\ \gamma = 0,\ \Phi_E = 0.25 \text{ to } 0.4\,\Phi_0) \tag{3.13}$$

$$\varepsilon_{0,min} \approx 5.2\, k_B T \sqrt{\frac{L_{SQ} C}{\beta_C}} \qquad (\beta_L \approx 1,\ \gamma = 0,\ \Phi_E = 0.25\,\Phi_0) \tag{3.14}$$

The found minimum additional noise $\varepsilon_{VV}$ is close to the results of simulations in the intermediate damped limit [67]. Here, for a SQUID with a screening parameter of $\beta_L \approx 1$ to 2 and $\beta_C \approx 1$ to 2 a minimum additional noise $\varepsilon_{VV} \approx 12 k_B T \sqrt{L_{SQ} C}$ was estimated. According to Figs. 3.6(b) and (d), the optimum value of $\beta_L$ is now found at about 1. Here, both the minimum additional noise and the minimum possible noise temperature are reached. If the minimum noise temperature is of importance for the intended application, one might consider to optimize for a smaller value of $\beta_L = 0.1$ to 1. The dependence is not very strong $\varepsilon_0 \propto {\beta_L}^{-1/2}$ at low values of $\beta_L < 1$, see Fig. 3.6(d). In case a capacitive impedance has to be read out, a decrease in $\beta_L$ below 1 would shift the frequency of the minimum noise temperature $\omega_0$ closer to the passive resonance frequency $\omega_L$ of the input capacitance and the SQUID input inductance, see the discussion above.

From Figs. 3.6(b) and (d) one might conclude that using a shunt $\gamma = 0.5$ across the SQUID inductance and using higher values of $\beta_L$ leads to even better sensitivities. This conclusion should only be valid for $\beta_C \ll 1$, because of the second limit.

The second limit on the chosen $I_0 R$ is related to the resonance of the SQUID inductance $L_{SQ}$ and the capacitance of the Josephson junctions $C/2$ [70, 71]. The frequency of this resonance should be far away from the operation regime. By using the definition of $\beta_L$ and $\beta_C$, the operation voltage of the SQUID where this resonance occurs can be expressed as $I_0 R \sqrt{2/(\pi \beta_L \beta_C)}$. Because of the low operation voltages this is usually not a problem for the SQUIDs without the resistive shunt, see Fig. 3.5(a). For the high-inductance SQUIDs with the damping resistance $\gamma = 0.5$, the resonant regime can easily come close to such high operation voltages. Although the resonance between the capacitance and the inductance is suppressed in the characteristics [85], one can still expect an influence of this resonance on the noise properties [105]. Therefore, the suggested minimum noise for the SQUIDs with shunted inductance $\gamma = 0.5$ in Figs. 3.6(b) and (d) cannot be considered realistic. In this regime, a detailed analysis for values of $\beta_C \sim 1$ is missing. Also note that high values of $\beta_L$ increase the $1/f$ noise [106], which might cause problems in some applications. Nevertheless, for SQUIDs with $\beta_L > 1$, a damping resistance can be recommended.

In the case of a technology with a fixed critical current density where only the area $A_J$ of the Josephson junction is varied, both the capacitance $C$ and the critical current $I_0$ can be considered proportional to $A_J$. In this case $\beta_C$ is proportional to ${A_J}^2$. Accordingly, $I_0 R$ is proportional to the chosen $\beta_C$ and Figs. 3.6(a) and (c) should be used for the optimization.

The third limit occurs for SQUIDs with integrated input coils. Resonances occur within the structure of the two coupled inductances [80, 82]. The corresponding voltages should be shifted far away from the optimum operation regime. In this case, $I_0 R$ is fixed to a value dependent on the geometry and the electromagnetic properties of the coupling inductances. This can lead to the underdamped Josephson junction regime $\beta_C \ll 1$. In this case Figs. 3.6(a) and (c) should be used for an optimization.

## 3.3 Washer type SQUIDs with a long integrated input coil

In the last section we numerically simulated typical standard SQUIDs, including properties that become important when an input circuit is coupled to the SQUID. The actual coupling of a connected impedance is done via an input coil. In this section we will treat SQUIDs with a tightly coupled input coil.

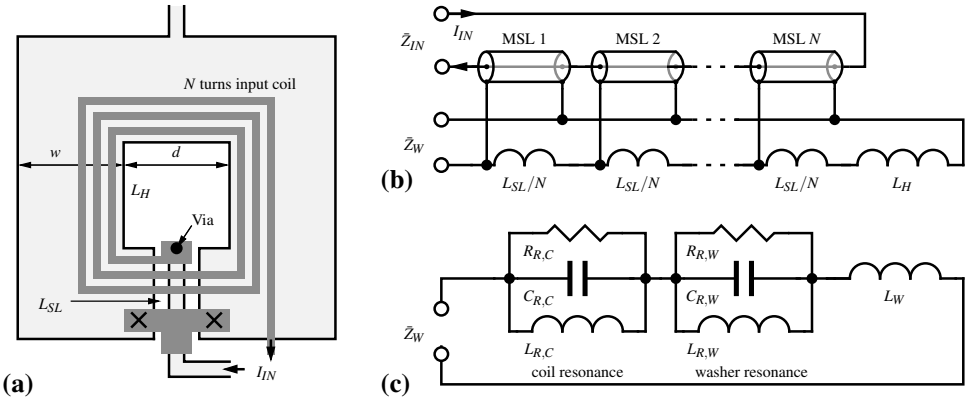


**Figure 3.7: (a)** Schematic of a typical washer type SQUID with integrated input coil. The Josephson junctions are indicated on the bottom part. **(b)** The complete model for the description of the washer impedance $\bar{Z}_W$ at low and RF frequencies. The $N$ windings of the coil are formed by the upper conductors of microstrip lines. These are represented by transmission lines which are connected to the distributed slit inductance $L_{SL}$ and the hole inductance $L_H$ as indicated. **(c)** Simplified lumped circuit element used for fitting the two fundamental resonances, the *coil resonance* ($L_{R,C}$, $C_{R,C}$) and the *washer resonance* ($L_{R,W}$, $C_{R,W}$).

In case a high coupling efficiency $k^2 \rightarrow 1$ is desired, one should integrate the coil directly on the SQUID chip. This is typically done by integrating a coil on a so-called *washer* structure [76], which forms the SQUID inductance.

A basic SQUID design with an integrated input coil based on this washer structure is shown in Fig. 3.7(a). The two inductors are formed in two superconducting layers. The inductances are magnetically coupled mainly via the hole in the washer structure. In case a square washer is used and the width of the outer conductor $w$ is larger than the hole dimension $d$, the low frequency inductance of the washer $L_W$ can be expressed as [76]:

$$L_H = 1.25\,\mu_0\,d \qquad (w > d) \tag{3.15}$$

$$L_W = L_H + L_{SL} \tag{3.16}$$

Here, $L_H$ is the inductance of the hole and $L_{SL}$ is the inductance connected to the slit, see the lower part in Fig. 3.7(a). $\mu_0$ is the permeability of vacuum. The distributed slit inductance is usually approximated by $\approx 0.3$ pH/µm [107]. The low-frequency inductance of the input coil $L_{IN}$ and the mutual inductance $M$ or coupling factor $k_W$ between the washer and the coil inductances are [107]:

$$L_{IN} = N^2\left(L_H + \tfrac{1}{3}L_{SL}\right) + L'_{ST}\,l_C \tag{3.17}$$

$$M = N\left(L_H + \tfrac{1}{2}L_{SL}\right) \tag{3.18}$$

$$k_W = M/\sqrt{L_W\,L_{IN}} \tag{3.19}$$

Here, $N$ is the number of windings of the input coil and $L'_{ST}$ is the distributed inductance of the strip line formed by the windings of the coil and the washer. The total length of the coil $l_C$ is $4N\,(d + (N+1)\,s_C + N\,w_C)$, where $s_C$ is the spacing between the windings of the coil and $w_C$ is the width of the coil conductor.

### 3.3.1 Radio frequency impedance of a washer with an integrated coil

Because a SQUID operates at high frequencies, the radio frequency (RF) properties of the washer structure are of particular importance. Here, the microstrip line (MSL) formed by the washer and the windings of the coil is causing deviations from the purely inductive low frequency behavior.

The distributed inductance $L'_{ST}$ and capacitance $C'_{ST}$ of a superconducting MSL is calculated in reference [108]. Approximate solutions are given by:

$$L'_{ST} \approx \mu_0 \frac{h + 2\lambda_L}{w_C + 2(h + 2\lambda)} \tag{3.20}$$

$$C'_{ST} = \frac{e_0 e_r w_C}{h} K \tag{3.21}$$

Here, the London penetration depth $\lambda_L$ of the superconductors is used. $e_r$ denotes the relative permittivity of the insulator, $h$ its thickness and $e_0$ is the permittivity of vacuum. $K$ is a fringe factor that depends on the geometry, typical values are $K = 1$ to 2 [108].

The behavior of the coupled coil-washer structure can be described by the circuit shown in Fig. 3.7(b) [83, 84]. Each winding of the coil is represented by a MSL, whose upper conductor represents the coil. These MSLs are modeled as lossless transmission lines, as shown in Fig. 3.7(b). The mirrored currents running in the lower lines are connected to the washer inductance at the appropriate place along the distributed slit inductance, the place where the winding crosses the slit in the washer.

In Fig. 3.8, one can see a numerical calculation on a washer structure with an integrated coil of 60 windings. The calculation was performed using the formulas from reference [83]. The plotted impedances $\bar{Z}_{W,O}$ and $\bar{Z}_{IN,O}$ in Fig. 3.8(a) correspond to the washer and the coil impedance. In both cases, the respective other terminal was open.

There are basically two fundamental resonance frequencies [81, 82]. At lower frequencies the so-called *coil resonance* occurs. The coil resonance frequency $f_{R,C}$ is determined by the total length of all windings of the coil $l_C$. If the coil is not shorted to the washer, the length of the coil corresponds to half the wavelength. The fundamental coil resonance frequency $f_{R,C}$ can therefore be approximated by $f_{R,C} \approx \left(2 l_C \sqrt{L'_{ST} C'_{ST}}\right)^{-1}$. The corresponding value is indicated by the left dotted vertical line in each of the plots in Fig. 3.8. The exact value of the fundamental resonance does not fit very well because it is shifted to lower frequencies by the slit inductance $L_{SL}$ [86]. In Fig. 3.8(a) one can also see the harmonics of the coil resonance. Because of the square dependency of the length of the coil on the number of windings $l_C \propto N^2$, $f_{R,C}$ can reach quite low values. With only a few windings, the resonance can easily approach the Josephson frequency of typical SQUIDs. Accordingly, SQUIDs with many-winding coils are usually oscillating far above this resonance. See the upper voltage scale in Fig. 3.8(a).

Above this resonance and its harmonics, the effective impedance of the washer $\bar{Z}_W$ again approaches an inductive behavior [82, 83]:

$$\bar{Z}_{W,RF} \approx \mathrm{j}\omega L_{W,RF} \approx \mathrm{j}\omega \left(1 - {k_W}^2\right) L_W \qquad f_{R,C} \ll f \ll f_{R,W} \tag{3.22}$$

The approximate solution indicates an intuitive model that the coil is effectively shorted above this resonance. In Fig. 3.8(a) we plotted the washer impedance with a shorted coil

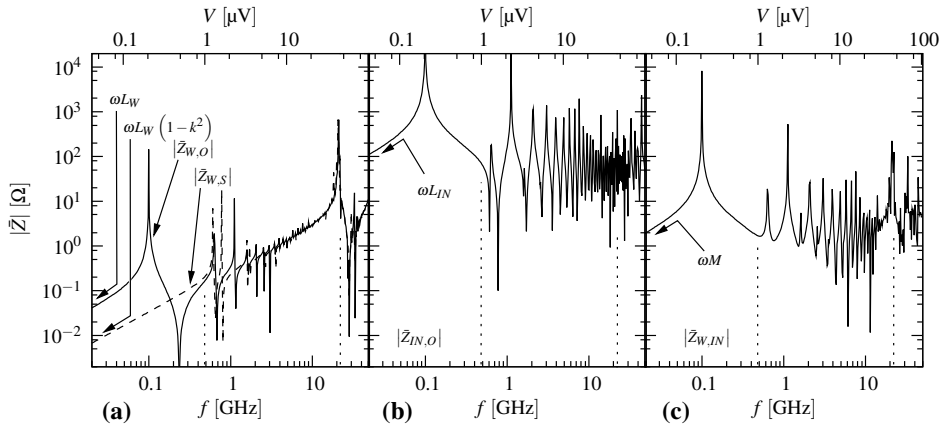


**Figure 3.8:** Characteristic impedances of a washer with an integrated coil ($N = 60$). The low frequency properties of the transformer are $L_W = 320$ pH, $L_C = 0.82$ μH, $k^2 = 0.83$. Characteristic impedances are plotted versus the frequency or voltage, respectively. The pure inductive behavior is indicated at low frequencies. **(a)** Impedance as seen from the terminals of the washer, for an open coil $\bar{Z}_{W,O}$ (solid) and a shorted coil $\bar{Z}_{W,S}$ (dashed). **(b)** Impedance seen from the terminals of the coil $\bar{Z}_{IN,O}$ with open washer. **(c)** Cross impedance $\bar{Z}_{W,IN} = \bar{V}_W/\bar{I}_{IN}$. The parameters are $d = 110$ μm, $N = 60$, $w_C = s_C = 3$ μm, $L'_{SL} = 3.8$ pH/μm, $L'_{ST} = 2.5{\cdot}10^{-7}$ H/m, $C'_{ST} = 3.6{\cdot}10^{-10}$ F/m, $l_C = 11$ cm, $l_{SL} = 0.36$ mm. The dotted vertical lines in (a),(b),(c) indicate the approximate coil resonance (left) and washer resonance (right) frequency, see text.

$\bar{Z}_{W,S}$ as a dashed line. The low frequency inductance of the shorted washer is close to the effective inductance above the coil resonance. Above the coil resonance frequency and its harmonics, the washer impedance is practically independent of a possible loading of the input coil.

The other fundamental resonance, the *washer resonance*, is occurring at much higher frequencies. Here, the coupling coil acts as a ground plane and the corresponding wavelength is determined by the dimensions of the area of the washer covered by the coupling coil. The approximate expression for the washer resonance frequency reads [83]:

$$f_{R,W} \approx \left(8\left(a + \tfrac{4}{3}\, l_{SL}\right)\sqrt{L'_{ST}\, C'_{ST}}\right)^{-1} \tag{3.23}$$

Here, the length of the slit that is covered by the input coil $l_{SL}$ is used. The calculated value for the washer resonance frequency $f_{R,W}$ of the washer shown in Fig. 3.8 is indicated by the right dotted vertical line in each of the plots. The agreement with the respective resonance frequency in the numerically calculated impedance is good.

### 3.3.2 Characteristics of SQUIDs with a long integrated coil

In case a good coupling coefficient $k \to 1$ and a relatively high input inductance are required, in practice one has to use a multi-winding input coil. In this case, the coil resonance frequency is usually located below the Josephson frequency of the SQUID. As shown above, the impedance of the washer structure above the coil resonance frequency is effectively inductive, see Eqn. (3.22). In a practical SQUID design, this effective inductance is increased

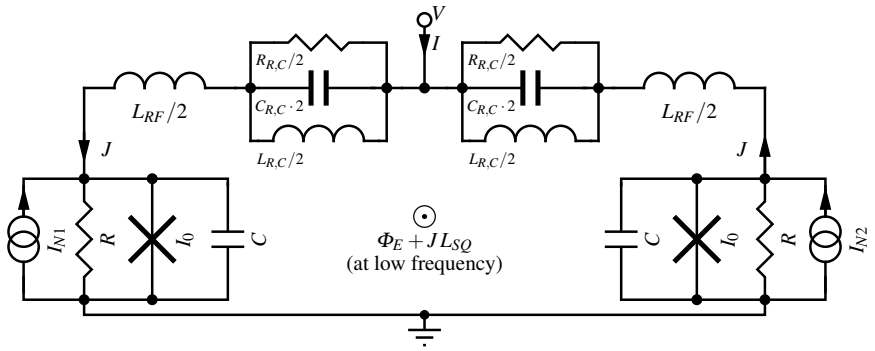


| | | |
|---|---|---|
| Low frequency inductance $L_{SQ}$ | $\beta_L = \frac{2 I_0 L_{SQ}}{\Phi_0}$ | $L_{SQ} = L_{R,C} + L_{RF}$ |
| RF inductance $L_{RF}$ | $\beta_{L,RF} = \frac{2 I_0 L_{RF}}{\Phi_0}$ | $L_{RF} = L_{W,RF} \approx L_W \left(1 - {k_W}^2\right)$ |
| resonating inductance | | $L_{R,C} \approx L_W {k_W}^2$ |

**Figure 3.9:** Simplified schematic of a SQUID with a long integrated coil $f_{R,C} \ll f \ll f_{R,W}$. The resistance $R_{R,C}$ sets the quality factor of the resonance $Q_{R,C} = R_{R,C}\sqrt{C_{R,C}/L_{R,C}}$ which was chosen to 1 in this simplified model. No noise source are attached to this resistance. The table summarizes the frequency dependent effective inductances and the corresponding screening parameters with respect to the washer impedance. The approximated effective RF inductance is given by Eqn. (3.22).

by parasitic inductances, for example associated with the connection of the Josephson junctions. Its integration in a model of the SQUID is of crucial importance [80].

The impedance of the SQUID loop including parasitic capacitances can be modeled by resonance circuits as shown in Fig. 3.7(c), one for the coil resonance and one for the washer resonance. Compared to the complete model description, this simplified approach does not include the harmonics of both fundamental resonances as occurring in the impedances, see Fig. 3.8. If one also neglects the washer resonance and simply distributes the impedance symmetrically over the SQUID, one gets a schematic as shown in Fig. 3.9. A further simplification was done by damping the coil resonance to a quality factor of 1. Furthermore, we assume that there is no noise source connected to the dissipation mechanism that damps the coil resonance. We will discuss these simplifications in section 3.3.4.

The corresponding structure is similar to a double-loop SQUID type, as investigated in the work of Tesche [78]. In case the resonance occurs within the working range, chaotic behavior are found and one can accordingly expect a degraded sensitivity. The optimum sensitivity is found for the case that the coil resonance frequency is far below the Josephson frequency [78]. For this case, the characteristics of the SQUID can be explained by a model presented in reference [78]. In the basic SQUID equations, see Eqn. (1.13) on page 7, the SQUID inductance only occurs in the third equation, the coupling equation of the two Josephson junctions:

$$\frac{\varphi_2(t) - \varphi_1(t)}{2\pi} = \frac{\Phi_E + L_{SQ} J(t)}{\Phi_0} \tag{3.24}$$

Applying the simplified model shown in Fig. 3.9, and assuming that the coil resonance frequency is far below the oscillation frequency of the Josephson junctions, one sees that only the RF inductance $L_{RF}$ has an influence on the dynamics. Its value is smaller than the

total inductance $L_{SQ}$ which is effective at low frequencies. The time dependent circulating current can be divided in two parts $J = J_{DC} + J_{RF}(t)$: the mean value $J_{DC}$ and the RF part caused by the oscillation of the Josephson junctions $J_{RF}(t)$. The equation characterizing the coupling of the two Josephson junctions now reads [78]:

$$\frac{\varphi_2(t) - \varphi_1(t)}{2\pi} = \frac{\Phi_E + L_{RF}\left(J_{DC} + J_{RF}(t)\right) + \left(L_{SQ} - L_{RF}\right) J_{DC}}{\Phi_0} = \frac{\Phi_E^r + L_{RF}\, J(t)}{\Phi_0} \tag{3.25}$$

$$\Phi_E = \Phi_E^r - \left(L_{SQ} - L_{RF}\right) J_{DC} \tag{3.26}$$

With the two equations of the Josephson junctions for the noise-free case $I_{N1} = I_{N2} = 0$, see Eqn. (1.13) on page 7, Eqn. (3.25) describes a *reduced SQUID* with inductance $L_{RF}$ at the same static bias current $I$ and an altered static external flux $\Phi_E^r$. Now let us assume that one knows the dynamics of this reduced SQUID $J(t) = J_{DC} + J_{RF}(t)$, $\varphi_1(t)$ and $\varphi_2(t)$. From $J_{DC}$, one can determine the external flux $\Phi_E$ for the *complete SQUID* with Eqn. (3.26). The total flux through the SQUID loop is the same for both the reduced SQUID and the complete SQUID. The time series $J(t)$, $\varphi_1(t)$ and $\varphi_2(t)$ at RF and low frequencies are unaffected by this transformation and accordingly, both the reduced and the complete SQUID have the same voltage and circulating current. The circulating current $J_{DC}$ and the effective change in inductance $L_{SQ} - L_{RF}$ between the measurement frequency and the frequency of the SQUID operation are thus causing a shift in the observable external flux $\Phi_E$ with respect to the external flux of the reduced SQUID $\Phi_E^r$.

With the differential of the external flux $\mathrm{d}\Phi_E = \mathrm{d}\Phi_E^r \left(1 - \left(L_{SQ} - L_{RF}\right) G_{J\Phi}^r\right)$ the input small-signal parameters of the complete SQUID read [78]:

$$G_{V\Phi}\Big|_{\Phi_E} = \frac{G_{V\Phi}^r}{1 - \left(L_{SQ} - L_{RF}\right) G_{J\Phi}^r}\Bigg|_{\Phi_E^r} \qquad G_{J\Phi}\Big|_{\Phi_E} = \frac{G_{J\Phi}^r}{1 - \left(L_{SQ} - L_{RF}\right) G_{J\Phi}^r}\Bigg|_{\Phi_E^r} \tag{3.27}$$

The change in inductance between high and low frequencies introduces partly hysteretic features in the characteristics of the SQUID [78]. Hysteresis was observed in a number of numerical simulations on SQUIDs with parasitic capacitances [78–80, 109, 110]. In Fig. 3.10 we illustrate the effects for two SQUIDs with an extreme change in inductance $\beta_L/\beta_{L,RF} = L_{SQ}/L_{RF} = 10$. All features in the characteristics for the noise-free case can be explained by the transformation explained above. In Figs. 3.10(c) and (d) we directly simulated two SQUIDs with a low frequency resonance at a corresponding voltage $0.03\, I_0 R$. The quality factor of the resonance was set to 1. Multiple solutions caused by hysteretic effects are generated by determining each shown working point with two different starting points. Before sweeping to the working point of interest, the SQUID was biased with a bias current of $i = 2.1$ and an external flux of $\Phi_E = 0.5\,\Phi_0$ in the one and $0.5\,\Phi_0$ in the other case.

Figure 3.10(a) shows the numerical simulation of a standard SQUID with $\beta_L = 1$. Using this simulation and Eqn. (3.26), we calculated the characteristics of a SQUID with $\beta_L = 10$ and $\beta_{L,RF} = 1$ in Fig. 3.10(b). This can be compared with the direct simulation in Fig. 3.10(c). The characteristics exhibit two types of hysteresis, a voltage hysteresis and a flux hysteresis.

**Voltage hysteresis**

The critical current of a SQUID at one specific external flux $|\Phi_E| > 0$ decreases with decreasing inductance [57]. For a SQUID with a resonating inductance, the transition from

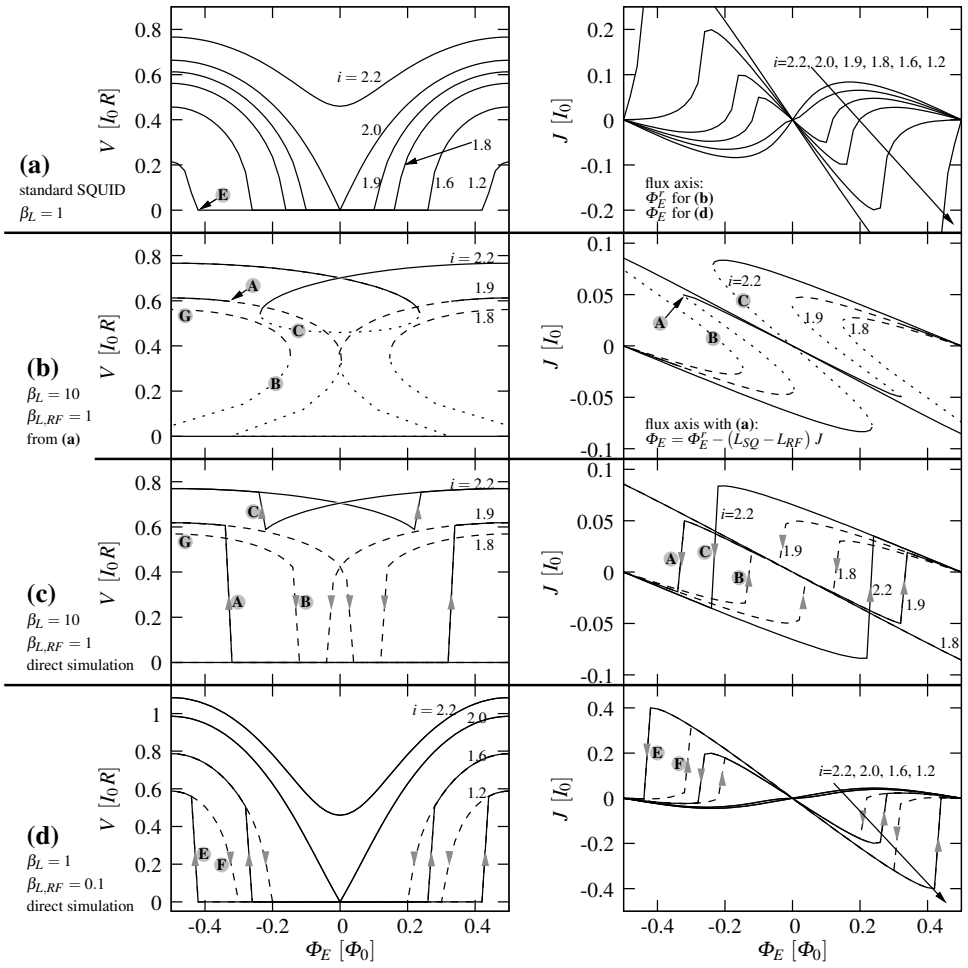


**Figure 3.10:** Illustration of the new features in the characteristics emerging for SQUIDs with a long integrated coil. Mean voltage $V$ and circulating current $J$ characteristics versus external flux for a choice of bias currents $i = I/I_0$. The arrows cross the characteristics with varying bias current $i$ in the indicated order. **(a)** Standard SQUID with $\beta_L = 1$ without resonating inductance, see Fig. 3.9. **(b)** Calculated characteristics for a SQUID with $\beta_L = 10$, $\beta_{L,RF} = 1$ using the data from (a). Unstable solutions (dotted), solutions in voltage state whereas a standard SQUID with $\beta_L = 10$ is superconducting (dashed) and stable solutions where both are in the same state (solid) are indicated. **(c),(d)** Direct simulations of two SQUIDs with $\beta_L/\beta_{L,RF} = L_{SQ}/L_{RF} = 10$. See text for details. $\Gamma = 0$ and $\beta_C = 0.1$ were used in all simulations (a),(c),(d) and no flux excitation was applied.

the superconducting to the voltage state is determined by the total loop inductance $L_{SQ}$ because there is no oscillation of the Josephson junctions in the superconducting state. Once the critical current is reached, the SQUID starts to oscillate at a frequency higher than the resonance frequency $f_{R,C}$. As argued above, the SQUID now behaves like the SQUID with the reduced inductance $L_{RF}$ and the transformed external flux, see Eqn. (3.26). This leads to a transient jump in voltage. The markers Ⓐ and Ⓔ in Fig. 3.10 mark such a transition from the superconducting to the normal state. A comparison of the external fluxes shows that the total SQUID inductance determines the point of this transition. Note that the critical flux

marked with Ⓐ in Fig. 3.10(b) was determined in another simulation not shown here.

Once the SQUID with resonating inductance has switched to the voltage state, it follows the $J$ and $V$ characteristics determined by the reduced SQUID with the lowered effective RF inductance $L_{RF}$. This can be seen by comparing Figs. 3.10(b) and (c). The transition back to the superconducting state is determined by either a direct switching off of the reduced SQUID, see for example the point marked with Ⓕ in Fig. 3.10(d), or by an unstable working range, see the transition marked with Ⓑ in Figs. 3.10(b) and (c). In Fig. 3.10(b) we marked these unstable solutions with a dotted line. These parts of the characteristics cannot be reproduced in the direct simulation in Fig. 3.10(c) and could also not be generated in the simulations in reference [78].

The characteristic marked with Ⓖ in Figs. 3.10(b) and (c) at $i = 1.8$ is in a region below the minimum critical current of a standard SQUID with $\beta_L = 10$. Accordingly, this characteristic could only be reached by first bringing the SQUID into the normal state before lowering the bias current back to $i = 1.8$.

**Flux hysteresis**

For the SQUID with $\beta_L = 10$ and $\beta_{L,RF} = 1$ in the voltage state, the circulating current $J$ is not zero for $\Phi_E = 0$, see Figs. 3.10(b) and (c). This is in contradiction to a symmetric standard SQUID, see Fig. 3.10(a). This unusual behavior is caused on the one hand by the large change in inductance $L_{SQ} - L_{RF}$ and on the other hand by the comparably large values of $J$ for $\beta_L = 1$.

Accordingly, also the flux-to-voltage characteristic does not follow the usual $G_{V\Phi} = 0$ behavior for $\Phi_E = 0$, see Figs. 3.10(b) and (c). The difference between the two observable solutions around $\Phi_E = 0$ is the sign in the external flux of the complete and the reduced SQUID. The transition between the two solutions is accompanied by an unstable solution as already mentioned above. The transition is indicated by the marker Ⓒ shown in Figs. 3.10(b) and (c). Even higher values of $L_{SQ} - L_{RF}$ would lead to more possible solutions [78]. For lower values this type of hysteresis disappears, see Fig. 3.10(d).

**Implications for the operation of a practical device**

Hysteretic parts of both types should be generally avoided for a low noise operation. A sudden switching of the SQUID in direct readout is unacceptable. In flux-locked loop operation, switching events would lead to a pulse in the feedback current before the SQUID reaches the starting working point. The transition event could also be caused by some interference at frequencies higher than the measurement frequency and would occur as excess noise at lower frequencies.

Furthermore, the transitions between the hysteretic points are always accompanied by a jump of the circulating current, see the right column in Fig. 3.10. On the one hand this also leads to an increased back-action noise and on the other hand, resonant states within the coil resonance of a practical device could be excited by the associated transients.

In stable parts of the characteristics with small thermal fluctuations $\Gamma \ll 1$, the voltage $V$ and circulating current $J$ characteristics are also very well explained by the model presented above. Working ranges with multiple solutions will be reduced because of the random flux and bias current [78]. The range of working points showing flux hysteresis, see the exemplary transition marked with Ⓒ in Figs. 3.10(b) and (c), will be effectively reduced further towards

the $\Phi_E = 0$ axis. The range of working points with voltage hysteresis, see the exemplary transition marked with Ⓐ, Ⓑ, Ⓔ and Ⓕ in Figs. 3.10(b), (c) and (d), will be narrowed. In chapter 5, section 5.4.2, we present an experimental observation of the voltage hysteresis in a SQUID. This could only be observed at sub-Kelvin bath temperatures.

### 3.3.3 Numerical optimization of the simplified washer SQUID

In this section we want to present a numerical study on the simplified SQUID with a long integrated coil. Based on the hysteretic characteristics treated in the last section and the standard SQUID behavior presented in section 3.2, one can already see that typical optimum SQUID working points at low voltages will be unstable in a SQUID with changing inductance. The points of optimum sensitivity of standard SQUIDs are usually in the low-voltage region and will therefore be screened by the voltage hysteresis. For low values of $\beta_L$, which is based on the complete low frequency inductance, and external flux $\Phi_E \to 0$, its influence should be smaller because of the decreasing critical current of the complete SQUID in this region. On the other hand, the flux hysteresis becomes important for higher bias currents $i \gtrsim 2$ in the region $\Phi_E \to 0$. For simplicity, we therefore only chose for an optimization at $\Phi_E = 0.25\,\Phi_0$. In this region, the flux hysteresis does not have a big influence, see Figs. 3.10(b) and (c). The SQUID shown there also represents the SQUID with the most extreme values treated in this section: $\beta_L = 10$ and $\beta_{L,RF} = 1$. The bias current $i = I/I_0$ was varied in 31 steps between $i = 1$ and 2.2.

#### Simulation procedure

To make sure that the SQUID is not operating in parts of the characteristics with multiple stable states, we performed two simulations on each working point. This was already done in the simulations shown in Fig. 3.10. First we biased the SQUID above the maximum critical current and at one of two initial flux values of $\Phi_E = \pm 0.5\,\Phi_0$, respectively. After some time the desired working point was adjusted and then we started to collect data. Afterwards we compared the voltage $V$ and circulating current $J$ between the two calculations with different initial flux bias and excluded working points with diverging stable multiple solutions. The excluded working points were indeed only within the voltage hysteretic regime, close to the critical current.

We performed a similar series of simulations as presented in section 3.2. The junctions were overdamped $\beta_C = 0.1$, the temperature was chosen to $\Gamma = 0.005$ and no damping resistance was attached across the SQUID loop, $\gamma = 0$. We performed two simulation series. One for the extreme case of $\beta_L/\beta_{L,RF} = 10$ and a more moderately coupled coil with $\beta_L/\beta_{L,RF} = 4$. The first case can be practically reached by designing a washer with a very large hole inductance $L_H \gg L_{SL}$ and by connecting the junctions with a small additional parasitic inductance. Naturally, the total inductance is available for a coupling of flux at the measurement frequency and therefore $L_{SQ}$ has to be used to normalize the energy resolutions $\varepsilon_{VV}$ and $\varepsilon_{JJ}$.

The resonance frequency of the coil was set at a corresponding voltage of $0.03\,I_0 R$, which is sufficiently small to ensure the idealized behavior in the sense of the simple model described above [78]. The quality factor of the resonance was, for simplicity, again set to 1 to exclude additional effects connected to the resonance.

The simulation system, see Fig. 3.1 and the respective section, was adapted as follows. The frequency of the two low-pass filters $f_{\mathrm{Out}}$ was chosen one order of magnitude below the coil resonance $f_{\mathrm{Out}} = 0.003\, I_0 R/\Phi_0$. We verified in test simulations that a further decrease did not change the results anymore. The effective observation time for each of the sensitive working points was $3.2{\cdot}10^3/f_{\mathrm{Out}}$. The bandwidth of the small flux excitation was chosen one order below the bandwidth of the output low-pass filters $f_{\mathrm{Exct}} = 0.003\, I_0 R/\Phi_0$. The excitation flux was applied only via $L_{RF}$ and the circulating current was also only measured via this part of the inductance. We verified that there is no difference between the current through the resonating inductance $L_{SQ} - L_{RF}$ and the current through the effective RF inductance $L_{RF}$ within the bandwidth of observation $f_{\mathrm{Out}}$. This fits our expectation because at such frequencies the capacitance should not have any influence on the inductances. There should not be a considerable charging current.

**Summary of the results**

The observed characteristics are very well explained by the characteristics for the noise-free case, see Fig. 3.10. Therefore, in Fig. 3.11 we only show the data of the points of best sensitivity. For comparison, the data of a standard SQUID $\beta_L/\beta_{L,RF}$=1 from Fig. 3.5 are shown as well.

The first considerable difference between a standard SQUID and a SQUID with a long integrated coil is the operation voltage. As one can see from Fig. 3.11(a) for intermediate to high values of the screening parameter $\beta_L \gtrsim 1$, the most sensitive operation regime is significantly shifted towards higher voltages $V \approx 0.6\, I_0 R$ compared to the operation range of the standard SQUID. This is caused by the voltage hysteresis. Therefore, the SQUIDs with $\beta_L \gtrsim 1$ have to be biased close to the maximum critical current $I \approx 2\, I_0$. The flux hysteresis was not observed in our chosen parameter range of $\beta_L$ up to 10, $\beta_L/\beta_{L,RF}$ up to 10 and $\Phi_E = 0.25\, \Phi_0$. This fits the expectation from the noise-free characteristics shown in Fig. 3.10.

For low values of the screening parameter $\beta_L < 1$, the influence of the voltage hysteresis also vanishes. Here, the critical current of the complete SQUID decreases and accordingly, there is no discrepancy between the critical currents of the reduced SQUID and the complete SQUID anymore. As can be seen from Fig. 3.11(a) for values $\beta_L$ below 1, the working range of optimum additional noise and the optimum noise temperature approach the values of the standard low inductance SQUID and accordingly diverge between the two optimization criteria of minimum additional noise and minimum noise temperature.

The minimum possible additional flux noise, Eqn. (3.8), and the minimum possible noise temperature, Eqn. (3.8), are reached for all the SQUIDs in the low inductance range $\beta_L \ll 1$, see Figs. 3.11(f) and (h). Here, the change in inductance has no influence, because the SQUID inductance has a vanishing influence on the dynamics for $\beta_L \ll 1$ [59].

For intermediate to large values of the screening parameter $\beta_L \gtrsim 1$, there is no considerable difference between the working range and noise levels in points of optimum additional noise or noise temperature, see Fig. 3.11(f) and (h). The estimated noise parameters of this simplified model are even better compared to the ones of the standard SQUID. As one can see in Fig. 3.11(f), the additional noise is up to a factor of two better than the noise of the conventional SQUID. In reference [78], a simulation is shown on the sensitivity of a similar

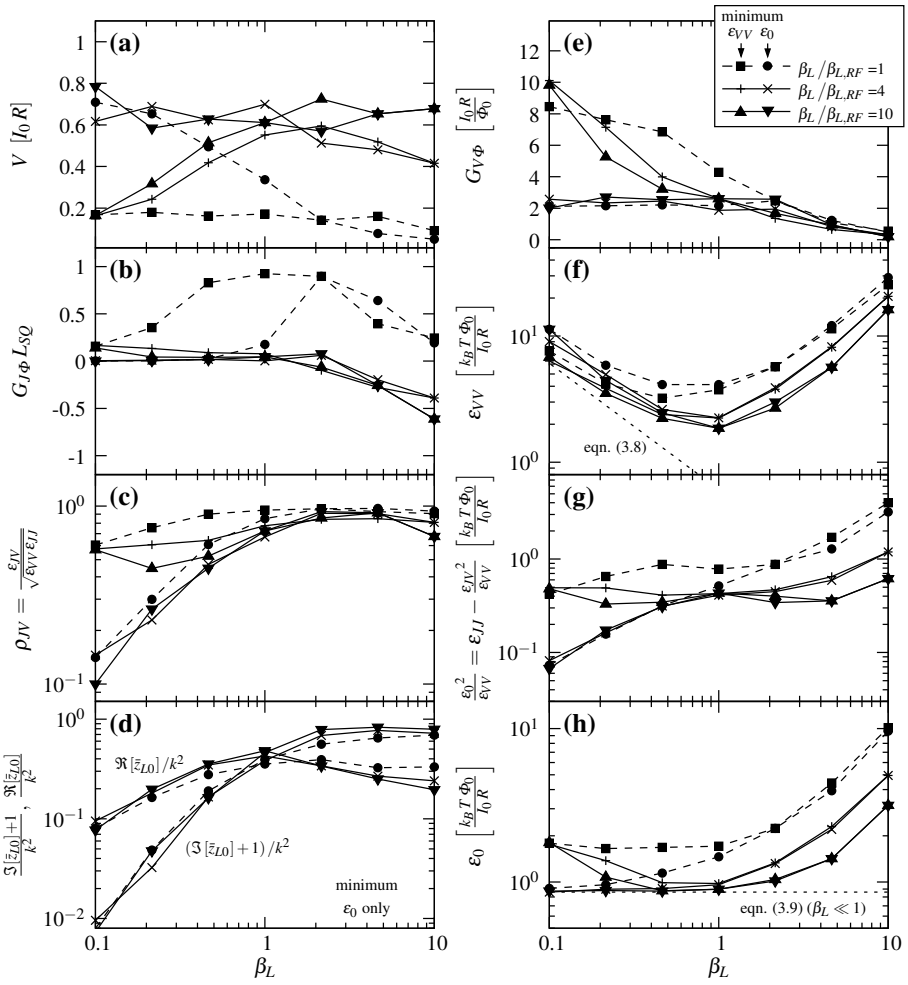


**Figure 3.11:** A choice of properties at the best points of sensitivity, the minimum additional noise (■ ▲ +) and the minimum reachable noise temperature (● ▼ ×) of all simulated SQUIDs. See the legend in (e) and the schematic in Fig. 3.9. Two new simulation series with a different inductance between low frequencies ($\beta_L$) and the voltage state ($\beta_{L,RF}$) of $\beta_L/\beta_{L,RF}$=4 and 10 are shown, respectively. The data for $\beta_L/\beta_{L,RF}$=1, a standard SQUID, were taken from Fig. 3.5. All SQUIDs were varied at $\Phi_E = 0.25\,\Phi_0$. **(a)** SQUID voltage. **(b)** Normalized dynamic inductance. **(c)** Correlation coefficient between the current noise on $J$ and the measured flux $V/G_{V\Phi}$. **(d)** Optimum input impedance. **(e)** Flux-to-voltage transfer. **(f)** Additional noise. **(g)** Effective back-action noise. **(h)** $\varepsilon_0$. See text for details.

SQUID with $\beta_L = 11$ and $\beta_{L,RF} = 1$. Here, a similar resonance frequency but a higher quality factor $Q = 20$ and a noise source connected to the corresponding dissipation were used. The minimum additional flux noise $S_{\Phi,VV} \approx 180 k_B T\, {\Phi_0}^2/({I_0}^2 R)$ was found at a voltage of $\approx 0.6 I_0 R$ [78]. Our result for a SQUID with $\beta_L = 10$ and $\beta_{L,RF} = 1$ is at a similar working point and noise level $S_{\Phi,VV} \approx 170 k_B T\, {\Phi_0}^2/({I_0}^2 R)$.

Compared to the standard SQUID, the changing inductance also improves the minimum reachable noise temperature for $\beta_L \gtrsim 1$, see Fig. 3.11(h). The minimum value for

standard SQUIDs, see Eqn. (3.9), is already reached at about $\beta_L \sim 1$. The optimum input impedance $\bar{z}_{L0}$ shows no considerable differences to a standard SQUID, see Fig. 3.11(d) and the discussion in section 3.2.3.

As one can see in Fig. 3.11(g), the back-action of the SQUIDs with changing inductance and $\beta_L > 1$ is decreased below the noise levels of standard SQUIDs. This was also observed in reference [78]. The results of the simulation series with the intermediate change in effective inductance $\beta_L/\beta_{L,RF} = 4$ lies in all aspects in between the behavior of the standard SQUID with $\beta_L/\beta_{L,RF} = 1$ and the SQUID with a more extreme change in effective inductance $\beta_L/\beta_{L,RF} = 10$. This can be seen for all properties shown in Fig. 3.11.

The noise performance observed in this series of simulations supports the qualitative model for the behavior of the similar double-loop SQUID from reference [78]. Not only the characteristics are determined by a reduced SQUID, as shown in section 3.3.2, the sensitivity is also influenced towards the lower inductance SQUID behavior. This is a positive tendency, but the sensitive points of the reduced SQUID are partly screened by the hysteresis. This drawback is on the other hand again compensated by the much higher coupling inductance $L_{SQ}$ at the low measurement frequency, and the accordingly lower energy resolution $\varepsilon_{VV}$ [78]. As one can see from Eqn. (3.26), the working points of the reduced SQUID are shifted further towards the $\Phi_E = 0$ axis. This suggests that for SQUIDs with $\beta_L \gtrsim 1$, even lower noise levels could be found for $|\Phi_E| < 0.25$ and characteristics without flux hysteresis. Such a behavior was observed for similar SQUIDs in reference [80], see figure 6(f) therein. We will here ignore such working points for simplicity. A direct comparison to the simulations shown in reference [80] is difficult because moderately damped Josephson junctions were used in this case. Nevertheless, the main aspects regarding the characteristics, working ranges and noise levels are consistent with our results.

There is another difference between the standard SQUIDs and SQUIDs with a long integrated coil. A further decrease of the RF inductance $\beta_{L,RF}$ in the presence of a capacitive impedance can be safely excluded. As one can see from Fig. 3.8(c), the coupling between the washer and the coil circuit is degraded above the coil resonance compared to the purely inductive coupling at low frequencies. This coincides with the SQUID showing "parasitic capacitances" mentioned in reference [93]. Accordingly, the assumptions that formed the basis of the small-signal and noise calculations presented in chapter 2 are validated, see the discussion in section 2.1 on page 20. One can assume that a washer SQUID with a long integrated coil will behave as shown in chapter 2. This will be treated in more detail in section 3.4 below.

### 3.3.4 Design and operation of SQUIDs with a long integrated coil

The simulation results shown here are on a simplified model and should be seen as idealized. Nevertheless, the results are useful to better understand the behavior of a real device.

The best performance of the simplified model of a SQUID with a long integrated coil is found at a screening parameter of $\beta_L \approx 1$, see Figs. 3.11(f) and (h). Here, a minimum additional noise $\varepsilon_{VV,min} \approx 2 k_B T \Phi_0 / (I_0 R)$ and approximately the overall minimum reachable noise temperature for SQUIDs, see Eqn. (3.9), are reached. An optimization with respect to $\beta_C$ as applied in section 3.2.5 is doubtful in this case because of the washer resonance. This resonance should be avoided in the operation range, and therefore $I_0 R$ has to be chosen at a fixed value. Even in the case that $\beta_C$ is the limiting factor for maximizing $I_0 R$, one cannot

recommend a too high critical current $I_0$. The larger $\beta_L$ and $\beta_{L,RF}$ are, the more problems are observed with hysteresis and therefore larger differences occur compared to the behavior of the standard SQUID, see for example Figs. 3.10 and 3.11(a).

Obviously, the impedance of the SQUID loop of the complete washer, see Fig. 3.8(a), must have further influence on the SQUID dynamics. This has been studied extensively over the years [78–80, 82, 84, 110–115]. If the SQUID is operated close to a resonance frequency, one typically observes a current-step within the characteristics, the voltage is constant for a particular range of the bias currents. Furthermore, one can observe hysteretic parts of the characteristics or a degraded sensitivity. In the case of the SQUID with a long integrated coil the washer resonance is unavoidable.

A phenomenological approach for the design and operation of SQUID sensors with a long integrated coil, see for example chapter 5 in reference [2], is usually defined as follows. Based on the rule of thumb published in reference [116], one should damp all resonances properly and shift the resonance frequency of the washer $f_{R,W}$ a factor of $\gtrsim 4$ above the Josephson frequency and the coil resonance frequency $f_{R,C}$ a factor of $\gtrsim 4$ below the Josephson frequency. The Josephson frequency is usually approximated by $\approx 0.3\,I_0\,R/\Phi_0$ which is based on simulations on standard SQUIDs [2, 80]:

$$4\,f_{R,C} \lesssim f_{OP} \lesssim f_{R,W}/4 \tag{3.28}$$

$$\text{typical approximation:} \qquad f_{OP} \approx 0.3\,I_0\,R/\Phi_0 \tag{3.29}$$

This leads to an important outcome of the numerical study shown in this section. As one can see in Fig. 3.11(a), the optimum Josephson frequency of such sensors with $\beta_L \gtrsim 1$ is at least double the value given in Eqn. (3.29). One might still be on the safe side with the rule of thumb, Eqn. (3.28), and the standard value of the Josephson frequency, but the danger is that one might also search for the minimum noise in the apparently steepest points at $V \approx 0.3\,I_0\,R$. In a practical measurement, hysteretic working ranges might be smeared out by noise and would appear as the steepest characteristics, whereas the sensitive regions are found at working points with moderate flux-to-voltage transfer $G_{V\Phi}$, see Fig. 3.11(e). We made similar experiences during the characterization of the SQUIDs presented in chapter 5.

The damping of the coil resonance is usually achieved by shunting the input coil with series resistance–capacitance elements. If the parameters are chosen well, this leads to an overdamped resonance and low reachable noise due to the faster decay of the energy stored in the resonant mode $\tau \propto Q/f_{R,C}$ [82, 109, 112, 117]. In a similar approach, damping resistors are directly connected to each of the windings of the input coil [113, 115].

The by means of damping improved noise in the hysteretic parts of the characteristics might still be dominated by non-thermal excess noise [112]. The better approach, especially if one intends to operate the SQUID at sub-Kelvin operation temperatures, is to search for low noise working points at the higher operation voltage $V \approx 0.6\,I_0\,R$, see Fig. 3.11(a). The experimental results from references [112, 116] support this way of argumentation. The behavior of a SQUID with the attached damping elements improves mainly in the low-voltage region, the region of voltage hysteresis.

In our simplified model we properly damped the coil resonance $Q = 1$, but did not include any noise source connected to it. A well chosen series resistance–capacitance element connected in parallel to the input coil will only induce noise over a restricted

bandwidth around the resonance. The induced variance of flux only has a big influence for working points with a small linear flux range, for large values of $G_{V\Phi}$. The optimum points of operation are indeed mainly in the region of moderate flux-to-voltage transfer $G_{V\Phi} \sim 0$ to $3I_0R/\Phi_0$, see Fig. 3.11(e). The noise contribution of the damping of the resonance can often be neglected compared to the shunt resistors, see the discussions in references [78, 112]. We ignore its influence here for simplicity but one should keep in mind that it could degrade the performance compared to our simple model.

Also in the case of the washer resonance, damping is recommended. This typically requires the direct shunting of the SQUID inductance [80, 82, 106], similar to the damping resistor connected in the SQUIDs of the last section, see Fig. 3.3. Because of the quite low washer impedance at the much lower coil resonance frequency, see Fig. 3.8(a), such a damping resistor might not be suitable to damp the coil resonance because $\gamma \gg 1$ would increase the noise of the SQUID considerably [86]. Nevertheless, also this damping helps to improve the overall performance of a real device [106]. Also see the simulations in reference [80], where a damping resistor $\gamma = 1$ only had a small influence at high operation voltages. At low operation voltages, within the hysteretic regime, the damping improved the sensitivity, but the additional flux noise was similar to the undamped SQUID operated at high voltages.

In our simplified model we did not attach a shunt $R_D$ across the total SQUID inductance as shown in Fig. 3.3 because we neglected the washer resonance. Furthermore, the effective inductance at radio frequencies $L_{RF}$ is much smaller in this simulation series. In this case, a moderately chosen damping resistor $\gamma = 0.5$ only has a minor influence on the SQUID dynamics, see Figs. 3.4 and 3.5.

Finally, the effect of capacitive feedback could influence the behavior of a SQUID with an integrated coil [65, 118]. Here, the SQUID voltage directly drives a feedback current through the coil caused by an asymmetry in the coil and materials with a high relative permittivity $e_r$, which are used especially in practical high-$T_c$ SQUIDs [118]. If one assumes on the one hand a symmetric coil layout which is not shorted to the washer and on the other hand small capacitances between the terminals of the input coil and the washer or the part connecting the Josephson junctions, see Fig. 3.7, this effect should be negligible.

## 3.4 Standard SQUID strongly coupled to a capacitance

### 3.4.1 Motivation

In the preceding part of this chapter we analyzed a simplified model of a SQUID with a long integrated coil. One of the conclusions was that because of the missing coupling above the coil resonance frequency, such a SQUID exhibits “capacitive effects” as mentioned in the work of Martinis et al. [93]. The dynamics of the SQUID are dominated by the effective inductance above this frequency. A connected input circuit will not alter the behavior further. The basic assumptions of the analysis presented in chapter 2 are accordingly fulfilled [93] for SQUIDs with a long integrated coil. The known low frequency small-signal and noise parameters at a given working point can directly be applied to calculate the performance of the sensor with different input impedances.

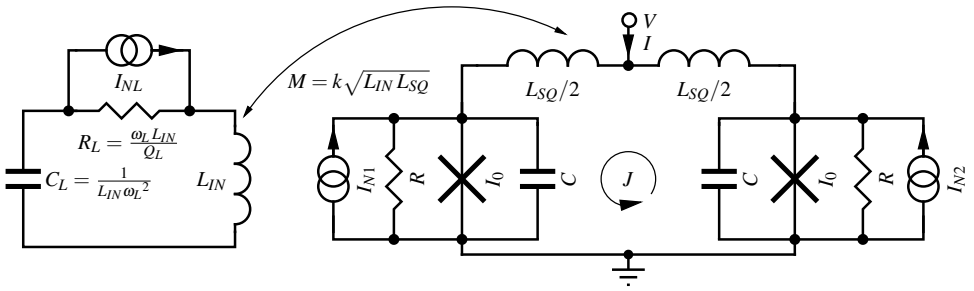


**Figure 3.12:** Standard SQUID strongly coupled to a capacitive input circuit. Here, the input inductance of the SQUID $L_{IN}$ is chosen arbitrarily and $k^2$ is set to 0.9. $\omega_L$ is the passive resonance frequency of the input circuit and $Q_L$ is the corresponding quality factor. $I_{NL}$ is a Nyquist noise current source with a PSD of $4k_B T_L/R_L$ of the resistance in the input circuit.

In the configuration as shown in Fig. 3.12, one has a very similar situation. Here, a capacitive impedance is connected to a standard SQUID amplifier without intrinsic parasitic capacitances. The effective SQUID inductance $L_{SQ}$ is decreased above the resonance frequency $\omega_L = (L_{IN} C_L)^{-1/2}$ of the input circuit. The effective inductance reads $L_{SQ,RF} = L_{SQ}(1-k^2)$ for $\omega \gg \omega_L$. Obviously, the dynamics of the SQUID will change for high values of the coupling efficiency $k^2$.

This problem was treated in several publications [68, 74, 92–94]. In the work of Martinis et al. [93], a model similar to the one described in section 3.3.2 was used to determine the characteristics and the noise of the SQUID coupled to an input circuit. The characteristics of such a system can be explained on the basis of the known characteristics $V$ and $J$ of the *reduced SQUID* with inductance $L_{RF}$ and an external flux $\Phi_E^r$. This leads to the altered flux $\Phi_E$ and small-signal parameters $G_{V\Phi}$ and $G_{J\Phi}$ of the SQUID with a connected input impedance, see Eqns. (3.26) and (3.27). Basically all the publications agree that this transformation correctly predicts the characteristics and small-signal parameters and therefore also the frequency response and effective input impedance of the SQUID [68, 74, 92–94]. Small differences were pointed out to be mistakes in later publications [68, 94]. Accordingly, the characteristics shown in Fig. 3.10 also coincide with the characteristics of the SQUID with a connected capacitive input impedance. Hysteretic working ranges are not mentioned in any of the publications, but they also have to occur in this case. This will be verified below.

It is appealing to also include the noise of the reduced SQUID as a small perturbation in the effective flux [93]. Here, new features in the treatment of the back-action noise appear [74, 92, 93] due to the effective change in SQUID inductance *at* the measurement frequency. The noise on the circulating current $S_{JJ}$ as treated in chapter 2 would therefore also be frequency dependent [74, 92, 93].

This inclusion of the intrinsic noise as a small perturbation on the reduced SQUID seems to be too simple. In the case of thermal fluctuations, the known solutions $\varphi_1(t)$, $\varphi_2(t)$, $J(t)$ of a reduced SQUID at flux $\Phi_E^r$ cannot be used to define a static external flux $\Phi_E$ of the SQUID with a connected capacitive input circuit. The latest publication on the topic by Carroll [68] shows a small-signal analysis of the system as shown in Fig. 3.12, but also includes the equations of the Josephson junctions. It is pointed out that one has to know the noise mixing behavior as well as all input and output small-signal parameters of the reduced SQUID $G^r_{V\Phi}$, $G^r_{J\Phi}$, $G^r_{VI}$ and $G^r_{JI}$ to also perform such a transformation for the noise parameters.

Nevertheless, the calculated effective input, output and correlation noise of the amplifier, see equations (70)-(72) in reference [68], are only determined by the dynamics of the SQUID at the Josephson frequency. The only parameters that determine the low frequency behavior of the amplifier with an arbitrary connected impedance are $L_{SQ}$, $L_{RF}$ and the bias point $\Phi_E$ and $I$. The input circuit has no further influence on the noise performance [68].

The results from reference [68] supports the basic assumption for the analysis presented in chapter 2. The parameters $L_{SQ}$, $\varepsilon_{VV}$, $\varepsilon_{JV}$, $\varepsilon_{JJ}$, $G_{V\Phi}$ and $G_{J\Phi}$ used there represent the effective values at the measurement frequency. How these parameters are determined, which mechanism might influence the SQUID dynamics at the Josephson frequency, was ignored at first. In this section, we will present a numerical experiment to test our calculations of chapter 2 also for the case that the effective SQUID inductance is changing at the measurement frequency.

### 3.4.2 Numerical experiment on the noise temperature

In section 3.3.3 we determined the small-signal and noise parameters of SQUIDs with changing inductance. These parameters were determined well below the resonance causing this change in inductance. In this section we use the data of some exemplary working points to compare theoretical expressions from chapter 2 with the numerically estimated behavior of a SQUID with a strongly coupled capacitive input circuit.

To expose possible additional effects as mentioned above, we therefore concentrate on the extreme case of SQUIDs with a change in inductance of $L_{SQ}/L_{RF} = 10$. This corresponds to a coupling efficiency of $k^2 = 0.9$ in case of the standard SQUID coupled to a capacitive input circuit as shown in Fig. 3.12. The passive (angular) resonance frequency $\omega_L = (L_{IN}\,C_L)^{-1/2}$ of the input circuit was set to a value of $2\pi \cdot 2{\cdot}10^{-3} I_0 R/\Phi_0$, which is much smaller than typical Josephson frequencies.

The quality factor of the input circuit $Q_L$ was set to a value of 100 in many cases. This value is much bigger than the optimum value $Q_{L0}$, see Eqn. (2.50), of each of the shown working points. Therefore, back-action noise will be dominant. This would emphasize mistakes in the theoretical assumptions as pointed out above.

We took several points of minimum additional noise $\varepsilon_{VV}$ and $\varepsilon_0$ from three different SQUIDs with changing $\beta_L$ from the simulation shown in Fig. 3.11. The data of the bias point ($\Phi_E$, $I$), the resulting working point ($V$, $J$), the small-signal parameters and the important noise

**Table 3.1:** Data of exemplary working points and the corresponding results. The data were taken from the simulation shown in Fig. 3.11. In all cases, the external flux is $\Phi_E = 0.25\,\Phi_0$. All working points are the ones showing the minimum $\varepsilon_0$ of each SQUID. The simulations were done with $\beta_C = 0.1$ and $\Gamma = 0.005$.

| | $\beta_L$ | $\beta_{L,RF}$ | $I$ $[I_0]$ | $V$ $[I_0 R]$ | $J$ $[I_0]$ | $G_{V\Phi}$ $\left[\frac{I_0 R}{\Phi_0}\right]$ | $g_{J\Phi}$ | $\varepsilon_{VV}$ $\left[\frac{k_B T \Phi_0}{I_0 R}\right]$ | $\varepsilon_0$ $\left[\frac{k_B T \Phi_0}{I_0 R}\right]$ | $\varepsilon_{JV}/\varepsilon_{VV}$ |
|---|---|---|---|---|---|---|---|---|---|---|
| A | 10 | 1 | 2.0 | 0.62 | 0.03 | 0.23 | −0.59 | 17 | 3.2 | 0.32 |
| B | 1 | 0.1 | 1.8 | 0.61 | 0.03 | 2.6 | 0.05 | 1.9 | 0.9 | 0.51 |
| C | 0.1 | 0.01 | 2.1 | 0.78 | 0.02 | 2.0 | 0.01 | 11 | 0.87 | 0.01 |

parameters are summarized in Table 3.1. The results of the simulations are later used to calculate the theoretical noise spectra.

In the course of the numerical experiments, each SQUID with varying uncoupled screening parameter $\beta_L$ is biased as given in Table 3.1. No initial bias pulses or flux excitation were applied. After some time used for reaching the working point, we started to extract a time series of the SQUID voltage. The low-pass filter for the output voltage as shown in Fig. 3.1 was set to a frequency of $2\pi f_{\mathrm{Out}} = 50\,\omega_L$ and the output voltage was extracted at a three times higher frequency. After collecting $2^{16}$ samples, we performed a Fourier transformation of the output voltage and calculated the output voltage PSD $S_{VV}$. The plotted spectra are normalized to the SQUID parameters and slightly smoothed. Furthermore, we determined the mean circulating current $J$ of the working point.

Here, the SQUID is operated in direct readout. Feedback effects are of no practical influence in the simulation, $\ell_{FB} = 0$. From Eqns. (2.47) and (2.56), see pages 34 and 36, we get the following expression for the equivalent input noise temperature $T_N$ and the measured output voltage PSD $S_{V,M}$ at a given (angular) frequency $\omega$:

$$T_N = \frac{\varepsilon_{VV}\,\omega_L\,Q_L}{2\,k_B\,k^2}\left\{\frac{1}{{Q_L}^2} + \left(\frac{\omega_L}{\omega_0}\right)^2\left(\frac{\omega}{\omega_0} - \frac{\omega_0}{\omega}\right)^2 + k^4\left(\frac{\omega}{\omega_L}\frac{\varepsilon_0}{\varepsilon_{VV}}\right)^2\right\} \tag{3.30}$$

$$S_{V,M} = \frac{4\,k_B\,(T_L + T_N)\,k^2\,L_{SQ}\,{G_{V\Phi}}^2}{\omega_L\,Q_L}\left|\frac{1}{Q_L} + \mathrm{j}\frac{\omega_L}{\omega_R}\left(\frac{\omega}{\omega_R} - \frac{\omega_R}{\omega}\right)\right|^{-2} \tag{3.31}$$

$$\omega_L = \frac{1}{\sqrt{L_{IN}\,C_L}} \qquad \omega_0 = \frac{\omega_L}{\sqrt{1 + k^2 g_{J\Phi} - k^2\frac{\varepsilon_{JV}}{\varepsilon_{VV}}}} \qquad \omega_R = \frac{\omega_L}{\sqrt{1 + k^2 g_{J\Phi}}} \tag{3.32}$$

$$Q_{L0} = \frac{1}{k^2}\frac{\varepsilon_{VV}}{\varepsilon_0}\frac{\omega_L}{\omega_0} \tag{3.33}$$

Here, $\omega_0$ is the frequency where the overall minimum noise temperature with an optimum quality factor $Q_{L0}$ can be observed. $\omega_R$ is the resonance frequency of the capacitance and the screened SQUID inductance. It is therefore dependent on the normalized dynamic inductance $g_{J\Phi} = G_{J\Phi}\,L_{SQ}$ at the given working point. Furthermore, we introduced the temperature $T_L$, which is the thermodynamic temperature of the resistance in the input circuit. $T$ still represents the effective temperature of the shunt resistors of the SQUID.

In Fig. 3.13, we show the simulated spectra for working point "A" from Table 3.1. This corresponds to a SQUID with $\beta_L = 10$ coupled to the capacitive input circuit with a high coupling efficiency $k^2 = 0.9$. The SQUID is biased at the point of best sensitivity. The resulting working point $V$ and $J$ was in very good agreement with the separately simulated values. In Fig. 3.13(a) one can see the spectrum for the case that the input resistance is located at vanishing temperature $T_L = 0$. Accordingly, the SQUID noise determines the whole spectrum. In Fig. 3.13(b), we also included the noise of the resistance in the input circuit. To emphasize the effect, we set the temperature to the double value of the SQUID temperature $T_L = 2\,T$. Note that at frequencies $\omega$ much higher or lower than the resonance frequency $\omega_R$, the thermal noise of the input resistance is not coupling to the SQUID, see Fig. 3.13(b). This is due to the comparably large imaginary impedance for $\omega \neq \omega_R$.

The simulated spectra fit the theoretical expressions in combination with the data from the separate simulation quite well. Small differences here and in the following spectra can be

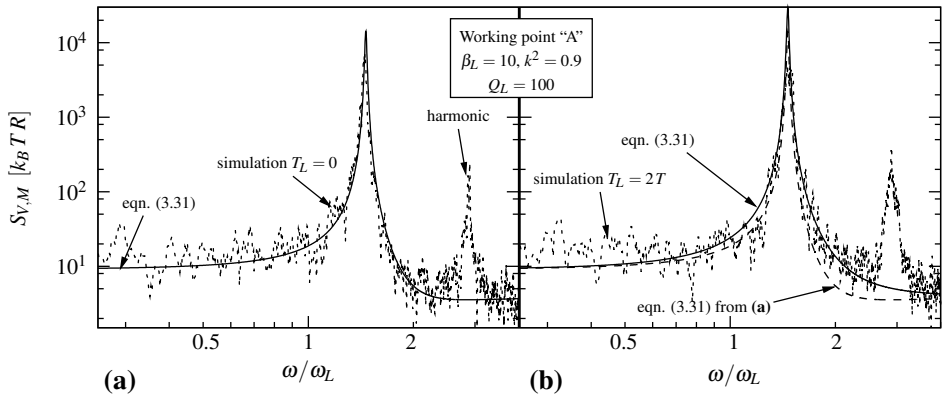


**Figure 3.13:** Simulated voltage PSD $S_{V,M}$ of a standard SQUID with $\beta_L = 10$ coupled to a capacitive input circuit with $Q_L = 100$ (dotted line). The frequency axis is normalized to the passive resonance frequency of the input circuit $\omega_L$. The working point was set to the data "A" from Table 3.1. The theoretical equation (solid line) was calculated with the same data. The temperature of the coupled resonator $T_L$ was set to zero in **(a)** and to $2T$ in **(b)**. In (b), the solid line from (a) is plotted as a dashed line.

explained by small variations $\pm 10\%$ of the noise parameters in Table 3.1. Note that no fitting was applied. The low-frequency additional noise fits quite well for $T_L = 0$, Fig. 3.13(a). The resonance frequency $\omega_R$ is in agreement with the expectation. Because of the negative $g_{J\Phi}$, the effective SQUID input inductance is lower compared to its passive value $L_{IN}$. Therefore, the resonance is shifted above the passive resonance frequency.

The noise close to the resonance is dominated by back-action. This is due to the high quality factor of the input circuit $Q_L \gg Q_{L0}$. For this working point, the optimum quality factor is $Q_{L0} = 2.5$, see Eqn. (3.33). Above the resonance $\omega > \omega_R$, the voltage noise is lowered. Here, the noise running in the SQUID loop is effectively screened. The exact noise at high-frequencies $\omega \gg \omega_R$ in this measurement is also determined by the correlation $\varepsilon_{JV}$ between the additional and the back-action noise. Above the resonance $\omega > \omega_R$, the thermal noise of the resistive parts of the input circuit also shows a contribution, see Fig. 3.13(b). One can clearly see the harmonic of the resonance frequency $\omega_R$. Here, nonlinearities in the SQUID characteristics in combination with generated currents in the input circuit become visible.

The bias point $\Phi_E = 0.25\,\Phi_0$ and $I = 2.0\,I_0$ of the SQUID simulated in Fig. 3.13 is very close to the hysteretic regime. This can be seen in Fig. 3.10(b) and (c). The flux hysteresis does not influence this simulation because a transition would require a large flux pulse from $0.25\,\Phi_0$ to about $-0.25\,\Phi_0$ for example. In contrary, a switching caused by the voltage hysteresis does indeed occur.

To demonstrate this, we biased the same SQUID at a slightly lower bias current $I = 1.85\,I_0$ instead of $2.0\,I_0$. The simulation at this working point is shown in Fig. 3.14. The histogram of the voltages clearly indicates the random switching of the SQUID into the superconducting state, see Fig. 3.10(b) and (c) for a comparison with the characteristics. As expected, the hysteretic behavior treated in section 3.3.2 is also influencing a standard SQUID with a strongly coupled capacitance. The exact behavior close to the hysteretic regime is strongly dependent on the temperature and the quality factor for example.

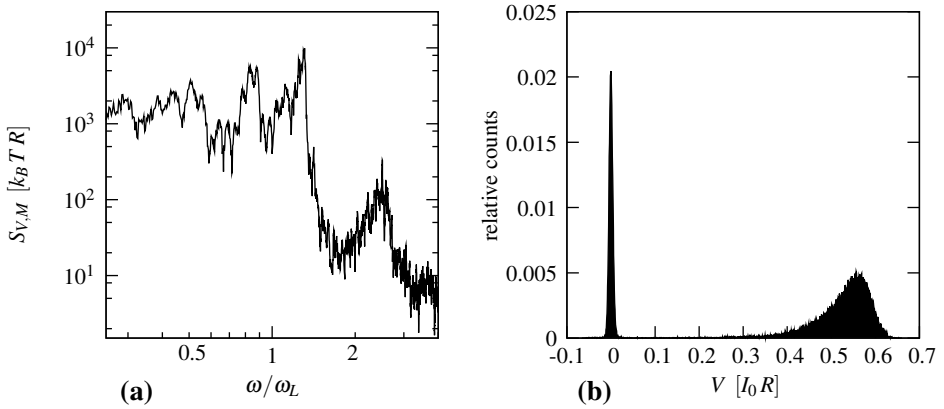


**Figure 3.14:** Same simulation as shown in Fig. 3.13, but with a lower bias current $I = 1.85\,I_0$ instead of $2.0\,I_0$. **(a)** Simulated voltage PSD $S_{V,M}$ and **(b)** the histogram of the voltage. Also compare with Fig. 3.10(b) and (c).

In Fig. 3.15 we show simulations on working point "B" from Table 3.1. Here, a SQUID with $\beta_L = 1$ is biased in the optimum point of sensitivity. The resulting working point $V$ and $J$ was again in good agreement with the expectation. One time we set the quality factor to $Q_L = 100$ and another time we used the optimum value of $Q_L = Q_{L0} = 1.8$.

In Fig. 3.15(b) we also show the equivalent input noise temperature. This was determined from the simulated voltage noise PSD using Eqn. (3.31). This requires the parameters of the capacitive input impedance as well as the small-signal parameters $G_{V\Phi}$ and $g_{J\Phi}$. The latter were taken from the separate simulation, see Table 3.1.

The simulation is again well approximated by the theoretical expression. Note that the resonance frequency is very close to $\omega_L$ in this case, see the peak in Fig. 3.15(a). In contrast,

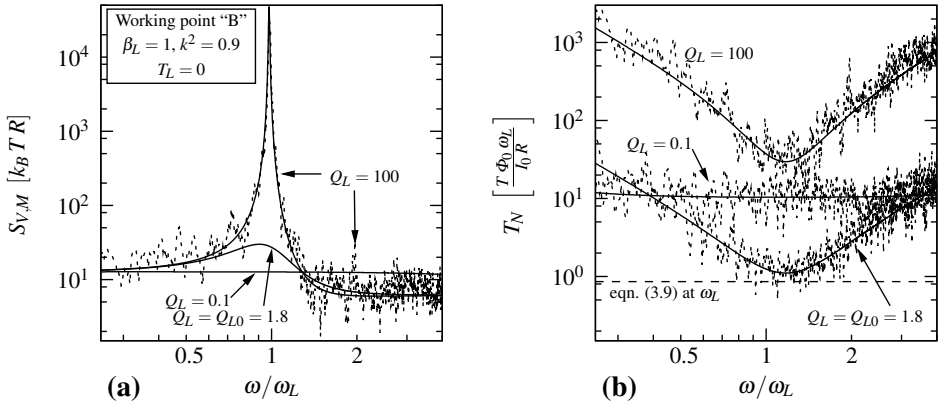


**Figure 3.15: (a)** Voltage PSD $S_{V,M}$ and **(b)** calculated noise temperature $T_N$ of a standard SQUID with $\beta_L = 1$ coupled to a capacitive input impedance. The dotted lines are the respective simulations and the solid lines the theoretical expressions using the data "B" from Table 3.1. Two simulations with varying quality factor are shown. The frequency axis is normalized to the passive resonance frequency of the input circuit $\omega_L$. For clarity we only show one simulated voltage PSD in (a). The temperature of the coupled resonator $T_L$ was set to 0.

the minimum noise temperature is reached at a higher frequency $\omega_R > \omega_L$, see the minima in Fig. 3.15(b).

This SQUID already reaches about the overall minimum noise temperature of SQUIDs, see the dashed line in in Fig. 3.15(b). This would not be possible for a standard SQUID with $\beta_L = 1$ and without a significant change in the RF inductance, compare the solid and the dashed lines at $\beta_L \sim 1$ in Fig. 3.11(h).

The final working point "C", see Table 3.1, is shown in Fig. 3.16. Here, a SQUID with $\beta_L = 0.1$ is biased in the optimum point of sensitivity. In this case, we varied the quality factor over three different values $Q_L = 100$, the optimum value $Q_L = Q_{L0} = 14$ and a lower value $Q_L = Q_{L0} = 1$. Figure 3.16(b) shows the calculated noise temperature.

The simulation is well approximated by the theoretical expression. This SQUID is clearly in the low inductance range. A comparison to Fig. 3.15 shows the most important implications of this. For $Q_L = Q_{L0}$ the overall minimum possible noise temperature is reached in both cases. For the SQUID with $\beta_L = 0.1$, the noise temperature is rapidly increasing for $|\omega - \omega_0| > 0$. The reason is the increased additional noise $\varepsilon_{VV}$ for $\beta_L = 0.1$. In contrary, the back-action noise is decreased, as one can see from the heights of the peaks in Figs. 3.15(a) and 3.16(a). For the case of the low inductance SQUID, the resonance frequency $\omega_R$ and the frequency of optimum noise temperature $\omega_0$ coincide with the passive resonance frequency.

### 3.4.3 Summary

We investigated a very extreme case of $k^2 = 0.9$ and found a reasonably good agreement of the simulations with expressions from the analysis presented in chapter 2. The shown working points are exemplary, but we tested more working points and found similar results if a safe distance to hysteretic ranges was kept. We also varied the temperature to some extent and found a linear dependency of the noise parameters $\varepsilon_{VV}$ and $\varepsilon_0$ of the SQUIDs as shown

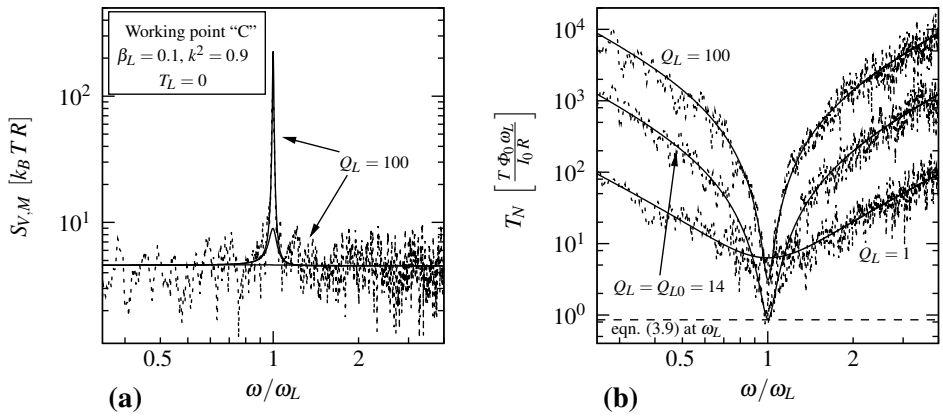


**Figure 3.16: (a)** Voltage PSD $S_{V,M}$ and **(b)** calculated noise temperature $T_N$ of a standard SQUID with $\beta_L = 0.1$ coupled to a capacitive input circuit. The dotted lines are the respective simulations and the solid lines the theoretical expressions using the data "C" from Table 3.1. Three simulations with varying quality factor are shown. The frequency axis is normalized to the passive resonance frequency of the input circuit $\omega_L$. For clarity we only show one simulated voltage PSD in (a). The temperature of the coupled resonator $T_L$ was set to 0.

in Table 3.1. Naturally, the chosen resonance frequency cannot be increased arbitrarily. In case $\omega_R$ approaches the Josephson frequency of the SQUID, the small-signal parameters cannot be considered real-valued anymore. Nevertheless, similar results as presented above were achieved for resonance frequencies $\omega_L$ up to at least $2\pi\,10^{-2}\,I_0 R/\Phi_0$.

We conclude that the performance of a SQUID with a coupled capacitive input circuit is well explained by the low frequency properties of the small-signal and noise parameters as determined far below this resonance. Any additional treatment originating from the change in the SQUID inductance at the measurement frequency, as explained in references [74, 92, 93], is doubtful [68, 94]. We conclude that the assumptions of chapter 2 are justified.

## 3.5 Conclusions

In this chapter, we give a broad overview of the achievable performance of dc-SQUIDs employed for the readout of an arbitrary input impedance.

In section 3.1, we introduced our approach for a quantitative study on the performance of SQUID models. On the basis of the circuit simulator JSIM, we developed a system for the characterization of SQUID amplifiers. Here, the behavior of the SQUID is simulated and all properties of interest can be extracted in the sense of a numerical experiment. In this chapter, we used the flexibility of the system to characterize several models of SQUIDs with increasing complexity. Furthermore, this system will be used in chapter 5 to numerically characterize detailed models of developed devices.

In section 3.2, we give a very detailed overview of the achievable noise parameters of two basic SQUID designs. In the limit of an overdamped Josephson junction, we characterized standard SQUIDs as well as SQUIDs with a resistively shunted inductance. We therefore focused on an optimization regarding the best achievable additional noise of the amplifier, which is represented by $\varepsilon_{VV}$, as well as on the minimum achievable equivalent input noise temperature, which is represented by $\varepsilon_0$. The latter is of importance in applications where the back-action of the amplifier has to be taken into account, see especially the capacitive input impedance treated in chapter 2. The study presented here extends existing results regarding the influence of back-action effects.

All SQUIDs were simulated with a varying working range. The two noise parameters $\varepsilon_{VV}$ and $\varepsilon_0$ were then minimized over the simulated working ranges of all SQUIDs with changing screening parameter $\beta_L = 0.01$ to 10. A choice of characteristics, small-signal and noise parameters at the points of best sensitivity are then summarized in Fig. 3.5. The results are discussed and compared, where possible, to results published in literature. The agreement is good in most of the cases. The two Figs. 3.4 and 3.5 give a very broad insight into the most important properties of practical interest: the working range, small-signal parameters and the sensitivity.

For a constant characteristic voltage $I_0 R$ of the Josephson junction, we find a somehow surprising result. The additional noise $\varepsilon_{VV}$ takes its minimum value at a screening parameter $\beta_L \approx 0.5$. Usually, the optimum screening parameter $\beta_L$ is given by 1 [2, 57, 60, 67]. A literature study showed that two publications [59, 104], both are dated in the 1980s, suggest similar results to ours ($\beta_L \approx 0.5$). In section 3.2.5 we discuss this result with respect to the design of SQUIDs, where the shunt resistance of the Josephson junction $R$ can be chosen

under circumstances and limits given by the fabrication technology and the basic layout. In case the choice in $R$ is restricted by the hysteresis of a Josephson junction of fixed capacitance $C$, the optimization process yields the usually mentioned value of $\beta_L \approx 1$.

Publications on the sensitivity of SQUIDs usually neglect the influence of back-action, and therefore we investigated these properties in more detail here. The few available studies on the complete noise properties of standard SQUIDs [16, 59, 63] are restricted in the choice of the screening parameter $\beta_L$. In the now almost forgotten work of Danilov et al. [16, 59], the SQUID dynamics were calculated by analytical approximations in two opposing ranges $\beta_L \ll 1$ and $\beta_L \gg 1$. It turned out that their expressions for the range $\beta_L \ll 1$ are reproduced well by the simulations. The derived expressions for $\varepsilon_{VV}$ and $\varepsilon_0$ for the range $\beta_L \gg 1$ are not satisfied. Nevertheless, our estimated additional noise $\varepsilon_{VV}$ for $\beta_L > 1$ agrees well with data from other published simulations [57, 58].

Regarding the minimum reachable noise temperature, the range $\beta_L < 1$ shows other interesting properties. For a constant characteristic voltage $I_0 R$, the global minimum achievable noise temperature is reached in this range. The working range and the magnitude of the noise properties for $\beta_L \ll 1$ turn out to be well described by analytical expressions found in the already mentioned work of Danilov et al. [16, 59]. Depending on the fabrication technology and the basic layout, a screening parameter $\beta_L$ of $\approx 1$ might lead to a minimum $\varepsilon_0$, see section 3.2.5.

In case the back-action of the amplifier is of importance for the sensitivity, the operation range is also crucial. The choice of the working point with the minimum additional energy resolution $\varepsilon_{VV}$, which is directly accessible during a measurement, leads to an increased back-action noise for SQUIDs with $\beta_L \lesssim 1$. The shown data give an overview in which region of the characteristics the minimum noise temperature is reachable, see especially Fig. 3.5(a).

If the minimum reachable noise temperature is desired, the optimum input impedance must be known. As we show in chapter 2, see especially section 2.4 on page 25, the optimum imaginary and real part of the connected input impedance is dependent on the small-signal and noise parameters of the SQUID in a given working point. For a capacitive input circuit, this gives information on the optimum quality factor $Q_{L0}$ and the frequency $\omega_0$ where the optimum noise temperature $T_{N0}$ is reached. These parameters can be derived from Fig. 3.5(d). The optimum frequency $\omega_0$ for the readout of an optimum connected capacitance is always located above the passive resonance frequency $\omega_L$, see section 3.2.4. The shown simulation data give insights that are useful for the planning and conduction of this type of measurement, for example for the readout of the capacitive transducers in the gravitational wave antenna MiniGRAIL.

The comparison between the standard SQUID and the resistively shunted SQUID shows that the latter can be of advantage. For small values of the screening parameter, $\beta_L \lesssim 1$, the damping resistance $\gamma = 0.5$ does not significantly change the SQUID dynamics. For SQUIDs with $\beta_L > 1$ the performance of the resistively shunted SQUID improves. Here, the optimum working points are found at much higher Josephson frequencies [102]. Therefore, this improvement might be degraded by the capacitance of the Josephson junctions in a practical device, see section 3.2.3. In difference to the conclusions from reference [87] we do not see a significant enhancement in the matching of the SQUID with an arbitrary input impedance. Although the influence of the dynamic inductance of the SQUID with a resistively shunted inductance is suppressed in its optimum points of sensitivity, the optimum

input reactance does not significantly change. This is caused by the unaffected correlation between the additional and the back-action noise in such sensors, see section 3.2.3.

In section 3.3, we give an overview of the properties of washer type SQUIDs with an integrated coil. We defined a model for the practical case of a SQUID with a long integrated coil. Here, the large total length of the windings shifts the coil resonance frequency below the Josephson frequency of the SQUID. In this case, the effective SQUID inductance at the Josephson frequency is lowered compared to its low frequency value. Based on the characteristics of a standard SQUID, we explain the characteristics of SQUIDs with a long integrated coil. Therefore, we used a model of the similar "double-loop" SQUID type [78]. Parts of the characteristics are found to be hysteretic. In chapter 5 we will present an experimental verification of one type of hysteresis, the "voltage hysteresis". This is caused by the difference in critical current between a standard SQUID with the low-frequency inductance and a standard SQUID with the lowered effective high-frequency inductance. In case of an extreme difference between the low-frequency and the effective high-frequency inductance, we show another type of hysteresis, the "flux hysteresis".

The subsequently presented numerical optimization of the idealized model shows that the voltage hysteresis causes a much higher Josephson frequency compared to standard SQUID sensors. The results of the numerical optimization of this idealized model suggest that the sensitivity can even be enhanced. This can be explained by the qualitative model [78] that characteristics, small-signal and noise parameters of the SQUID with an integrated coil are strongly influenced by its lowered effective inductance at the Josephson frequency. From the point of view of designing and operating such sensors, we discuss degrading effects especially caused by resonances and summarize measures to overcome them, see section 3.3.4.

The insights gained from the simplified model of SQUIDs with a long integrated coil can be useful for the general understanding of the performance of similar SQUIDs and will therefore be used in chapter 5.

In the final section 3.4 of this chapter, we numerically investigated a standard SQUID strongly coupled to a capacitive input impedance. The behavior coincides in many aspects with the idealized model of a SQUID with a long integrated coil. Also here, the SQUID inductance is effectively lowered at the Josephson frequency. We show that one can also observe hysteretic characteristics. For three exemplary SQUIDs, we determine the voltage noise spectra in their working point of minimum reachable noise temperature. The spectra are compared to theoretical expressions from chapter 2 using the properties of the SQUIDs from section 3.3. By varying the quality factors of the capacitive input circuit, we change the influence of both additional noise and back-action noise of the SQUID amplifier. The simulated spectra are well approximated by the analytical expressions and we therefore conclude that the basic assumptions of chapter 2 are applicable. We did not observe additional features in the influence of back-action although the effective SQUID inductance is changing at the measurement frequency, see the discussion in section 3.4.1 on page 73.

All the noise parameters shown throughout this chapter are considered to be proportional to the temperature. This does not hold for quantum mechanical effects, which are not included in the numerical simulations. Quantum mechanics force a fundamental limit on $\varepsilon_0$ and therefore on the minimum reachable noise temperature.

In the following chapter 4, we investigate another limit one typically faces trying to reach the quantum limit by cooling—the hot-electron effect.

# Chapter 4

# Thermal design for sub-Kelvin operation temperatures

The SQUIDs presented in the following chapter 5 are intended for an operation at bath temperatures as low as 20 mK. This suggests a promising reachable sensitivity of the sensor, see Eqn. (1.20) on page 11, but unfortunately there is a practical limit here—the hot-electron effect. Here, the coupling between the electron and the phonon system of a resistive material is weakened. In the presence of dissipated power, this leads to an increased temperature of the electron system and therefore to an increased thermal noise. In this chapter, we study the influence and the suppression of the hot-electron effect.

In section 4.1 we give an overview of a variety of aspects that influence the thermal resistance between the electron system in a resistor and the surrounding bath. We review different theories on the hot-electron effect as well as typical experimental observations. Theoretical predictions and experiments diverge in many cases. The effects of the geometry of the sample are discussed. This essentially affects both the coupling between the electron and the phonon system as well as further thermal resistances one could encounter.

In section 4.2 we investigate the possibility to suppress the hot-electron effect by means of passive cooling. This can be achieved by so-called "cooling fins". Here, an attached volume provides a reservoir for "cold electrons" that exchange with the electrons in the volume of dissipation. This system can be described by electronic thermal transport in the sense of the Wiedemann-Franz law. On the basis of a simplified case of a one-dimensional cooling fin, we demonstrate the properties of such a system.

In section 4.3, we present heating experiments on thin-film resistors made of *PdAu* with possibly connected cooling fins made of *Au*. By means of controlled power dissipation in the resistor combined with noise thermometry, we characterize different configurations. First we show the experimental results on a *PdAu* thin-film resistor without a cooling extension. The possible influence of other effects is investigated and the results are compared to theory. Furthermore, we show measurements on resistors with attached cooling fins. In this case, we compare the results to numerical calculations on the electronic heat transport within the geometry.

We conclude this chapter with a summary of the results and some general design considerations for the shunt resistors of Josephson junctions with respect to a minimum reachable electron temperature.

## 4.1 Thermal resistance of the electrons in thin resistors

An overview of the most effects given here can be found in references [119] and, in the context of "electron-dephasing" experiments, in reference [120]. One has to summarize that the exact behavior of such systems is not very well described by existing theories. In this section we present an overview of the aspects that are important for the thermal resistance of the electron system in a thin-film resistor to the bath at a temperature $T_B$. The resulting effective overheating due to a dissipation $P$ leads to an effective temperature of the electrons $T_E > T_B$ and thus also to a higher effective thermal noise of the resistor.

The typical bath temperature of the experiments shown here are below 500 mK and reached down to 60 mK. The intended operation temperature of our developed SQUIDs is 20 mK, see section 1.5 on page 16. We therefore concentrate on important effects in this temperature range. As a typical dissipation we assume hundreds of picowatt, which is close to the dissipation of our SQUIDs.

### 4.1.1 Hot-electron effect in bulk resistors

For a bulk resistor, several theoretical studies on the low temperatures electron-phonon interaction were done, see for example references [73, 119, 121–124]. The obtained results are described by a formula of the form of:

$$P = \Omega \, \Sigma \, ({T_E}^p - {T_{Ph}}^p) \tag{4.1}$$

Here, $P$ is the dissipated power in the bulk resistor of volume $\Omega$. $\Sigma$ is a constant. The exponent $p$ is dependent on the type and structure of the metal, it is generally determined by the energy relaxation rate between the electron and the phonon system. Because the specific heat capacity of the electron system is proportional to $T_E$, its heat energy is proportional to ${T_E}^2$. Therefore, the energy relaxation rate between the electron and the phonon system is given by [122]:

$${\tau_{EPh}}^{-1} = \alpha \, {T_E}^{p-2} \tag{4.2}$$

The constant $\alpha$ is determined by $\alpha = p\Sigma/\gamma$ [122], where the material dependent Sommerfeld parameter $\gamma$ is used. $\gamma$ determines the heat capacity of the electron gas [125].

The time constant $\tau_{EPh}$ involved here, easily exceed the microsecond range. In experiments, even timescales of milliseconds were observed [126]. Any change in the electron temperature is determined by such slow processes. Because the dynamics of Josephson circuits are several orders of magnitude faster, see for example Eqn. (1.7) on page 4, the electron temperature does not follow the time dependent dissipation connected to the dynamics of a Josephson junction. Accordingly, only the mean dissipation is of importance.

In case the resistor consists of a pure metal, defined by the condition $2\pi \, l_E/\lambda_{Ph} \gg 1$, the *clean limit*, an exponent of $p = 4$ or $p = 5$ was found in theory, depending on the phonon mode that dominantly scatters with the electrons. Here, the electron mean free path $l_E$ and the phonon wavelength $\lambda_{Ph}$ were introduced. In case longitudinal phonons are dominant, the exponent takes a value of $p = 5$ [73, 121–124]. In case the electrons also scatter with transversal phonons, the exponent changes to values of $p = 4$ to 5 [124]. Nevertheless, most experimental results follow Eqn. (4.1) with an exponent of $p = 5$, even for disordered metals.

For a disordered metal, classified by the condition $2\pi l_E/\lambda_{Ph} \ll 1$, the *dirty limit*, theory predicts that the transverse phonons have the dominant contribution to the electron-phonon interaction [120, 124]. The actual exponent $p$ is dependent on the type of disorder. Typical causes of this disorder are for example impurities, non-periodic lattice structures in alloys, defects or the geometric boundaries [125, 127].

In case the dominant scatterer is vibrating with the phonon population, interference further degrades the electron-phonon interaction and the exponent yields $p = 6$ [124]. This case was also observed experimentally [126, 128, 129].

In case the disorder is caused by a scattering potential of static nature, theory predicts an exponent of $p = 4$ [124]. The same result was achieved in another work, where the impurities were assumed to be situated at points shifted from the periodic lattice [130]. The electron-phonon interaction is accordingly enhanced. This behavior was also observed in experiments [131–133].

Mixed situations between the static and the vibrating impurity, as defined in reference [124], lead to an exponent of $p = 4$ to 6 [120, 124].

For all the different cases, the constant $\Sigma$ has a different dependency on the electron mean free path $l_E$ and is thus dependent on the conductivity $\rho^{-1}$ of the metal. Accordingly, $\Sigma$ can vary between different grown films based on the same material(s), depending on the origin of disorder and the fabrication technique and parameters. For a clean metal, theory predicts no such dependency [73]. For a disordered metal, a dependency of $\Sigma$ on the electron mean free path $l_E$ is described in reference [124]. In case of a vibrating disorder ($p = 6$), $\Sigma$ is proportional to $l_E$ and thus also proportional to the conductivity $\rho^{-1}$ of the film. In case of a static disorder ($p = 4$) it is inversely proportional to $l_E$ and $\rho^{-1}$ [120, 124].

As in the case of pure metals, experiments on metals in the dirty limit often showed an exponent $p = 5$ [13, 73, 122, 134]. The results for this are still not understood. Also see the discussion in references [119, 120, 123, 124]. In reference [120, 124], it is argued that actually most experiments were done in an intermediate range between the dirty and the clean limit, in a crossover regime $p = 4$ to 6.

As we will show below, we also observed an exponent $p = 5$ in our experiments. For our employed alloy of *PdAu*, measurements were done on thick film resistors grown with varying resistivity which showed an exponent of $p = 4$ with a $\Sigma \propto \rho^{-1}$ dependency [135]. This case is not explained by any of the existing theories [120]. Another reported measurement [136], also shows an exponent $p = 5$ for a *PdAu* resistor in a range of resistivity and temperature similar to our experiment.

Because of the discrepancy between many measurements and the theory, we will simply assume the exponent $p = 5$ in Eqn. (4.1) which was observed in most experiments on typical thin-film resistors. Here, typical means that no exotic materials were used and no measures were taken to reduce the dimensionality of the electron or phonon system of the resistor or surrounding materials.

### 4.1.2 Influences of the sample geometry and other thermal effects

There exists another thermal resistance that is important in this low temperature range: the *Kapitza resistance*. It is caused by an acoustic mismatch of the phonon systems on interfaces between different materials that the heat flow has to pass on its way to the ambient

bath [137–139]. The Kapitza resistance is described by the following formula:

$$P = K\, A_K \left( {T_{Ph}}^4 - {T_B}^4 \right) \tag{4.3}$$

Here, the area $A_K$ of the interface is introduced. The constant $K$ is dependent on the involved materials. The effect of the Kapitza resistance in combination with the hot-electron effect, see Eqn. (4.1), would also lead to an overheating of the phonon system to temperatures $T_{Ph} > T_B$. At high enough dissipated power this would also increase the temperature of the electron system $T_E$. At high dissipation, the Kapitza resistance is dominant because of the lower exponent 4 in Eqn. (4.3) compared to the typical hot-electron effect dependence.

For thin-film resistors, the Kapitza resistance is usually neglected. One reason is connected to the wavelength of the thermal phonons [125]:

$$\lambda_{Ph} = \frac{h\, v_S}{k_B\, T_{Ph}} \tag{4.4}$$

Here, the speed of sound $v_S$ of the phonon mode was introduced. For typical metals, the speed of sound lies in the range of $v_S \sim 10^3$ m/s. At a phonon temperature $T_{Ph} = 100$ mK, this leads to $\lambda_{Ph} \approx 0.5$ µm, which is bigger than the thickness of typical thin-films. Accordingly, a three-dimensional phonon population cannot exist. Because this is needed for the acoustic mismatch theory of the Kapitza resistance, the temperature of the phonons in the thin-film resistor is usually considered at the same temperature as the phonons of the adjacent substrate [73, 119].

Still, the Kapitza resistance could have an influence on the thermal resistance between the substrate and for example a bath of liquid Helium or a sample holder. In this case the area $A_K$ in Eqn. (4.3) is much bigger compared to the area of the thin-film resistor. Typical coefficients $K$ for most interfaces between dielectric and metal interfaces as well as interfaces between different dielectrics lie in the range of 10 to $10^3$ $\mathrm{W\,m^{-2}\,K^{-4}}$ [138, 140]. As an example, if one assumes a dissipation of $P = 1$ nW on a chip of area $A_K = 10^{-5}$ $\mathrm{m^2}$ with a bath temperature at absolute zero $T_B = 0$, the phonon system would be heated up to only about 50 mK in the worst case. If this power were dissipated in a single thin-film resistor with a volume of $10^{-20}$ $\mathrm{m^3}$ with a typical material constant $\Sigma = 1{\cdot}10^9$ $\mathrm{W\,K^{-5}\,m^{-3}}$, the electrons would according to Eqn. (4.1) heat up to about 2.5 K.

In conclusion, the Kapitza resistance is of negligible influence for a low total on-chip dissipation in thin-film resistors, also see references [13, 73, 122, 140, 141] or the discussion in section II.G in reference [119].

There is another influence of the geometry of the resistor that directly alters the electron-phonon coupling. Also this effect is related to the properties of the acoustic phonon population. In reference [123], the hot-electron effect in resistors made of a clean metal of finite thickness $H$ on a substrate of infinite thickness is theoretically investigated. Because the phonon wavelength is dependent on the temperature, see Eqn. (4.4), the electron-phonon coupling is dependent on the bath temperature. For high temperatures, where $\lambda_{Ph} \ll H$, the resistor can be considered as a bulk resistor and the expected exponent $p = 5$ in Eqn. (4.1) was found. At low temperatures, where $\lambda_{Ph} \gtrsim H$, higher exponents $p > 5$ occur [123]. Theoretical and experimental studies on suspended resistors also show altered electron-phonon interaction compared to bulk resistors [141, 142].

Another possible heat exchange is given by the emission of photons [143, 144]. This is only of importance in resistors of very small total volume. The experiments shown in reference [144] were performed on resistors made of the same alloy as the one we investigated, but were approximately three orders of magnitude smaller in volume.

## 4.2 Cooling fins for the suppression of the hot-electron effect

From Eqn. (4.1) follows that a big volume $\Omega$ of the resistor suppresses the hot-electron effect. The idea of increasing the effective volume by attaching an electrically negligible extension $\Omega_{CF}$ to the resistor was already investigated in references [72, 73, 134, 140, 145]. This attached volume provides a reservoir for "cold electrons" that exchange with the electrons in the volume of dissipation.

The total power conducted to the phonon system in these two parts of the volume is:

$$P = P_R + P_{CF} = (\Omega_R + \Omega_{CF})\,\Sigma\left({T_R}^5 - {T_{Ph}}^5\right) \tag{4.5}$$

Here, we used the volume $\Omega_R$ of the resistor and the temperature of the electrons $T_R$ in the resistor. The effective volume of the cooling fin $\Omega_{CF}$ is a function of $T_R$, as will be shown below. Based on the preceding section, we here assume a dominant hot-electron effect. Therefore, we assume that the phonon temperature $T_{Ph}$ is identical to the bath temperature $T_{Ph} = T_B$. Furthermore, we use the typically observed exponent $p = 5$ in Eqn. (4.1).

A microscopic model for the cooling effect can be found in reference [73]. The characteristic length an electron travels before thermalizing and emitting a phonon is given by the electron-phonon interaction length $l_{EPh}$:

$$l_{EPh} = \sqrt{D\,\tau_{EPh}} \tag{4.6}$$

Here, the time constant of the electron-phonon interaction , $\tau_{EPh}$ is used, see Eqn. (4.2). $D$ is the diffusion constant of the electrons in the metal and is also material dependent. For the assumed exponent $p = 5$, the electron-phonon relaxation rate ${\tau_{EPh}}^{-1}$ scales with ${T_R}^3$. $T_R$ is the electron temperature of the resistive part, the hot-spot with dissipation. Thus, the characteristic length $l_{EPh}$ is proportional to ${T_R}^{-3/2}$. Also note that shot-noise can occur if $l_{EPh}$ exceeds the length of the resistor [146], but we will come back to this below.

On the basis of the temperature dependency of the electron-phonon interaction length, the authors of reference [73] argue that for a non-uniformly heated resistor, there is only a restricted effective volume. If the total power is only dissipated in a small part $\Omega_R$ of a much bigger total volume $\Omega_R + \Omega_{CF}$, hot electrons only effectively thermalize within a volume restricted by either $l_{EPh}$ or the boundary of the cooling volume.

Accordingly, there are basically three regimes [134, 145]. At low temperatures $T_R$, the electron-phonon interaction length $l_{EPh}$ is much bigger than the dimensions of the total volume, so all the volume takes part in the cooling process. The behavior can be described by Eqn. (4.5) with the whole geometric volume of the cooling fin $\Omega_{CF}$.

At high temperatures $T_R$, where the electron-phonon interaction length $l_{EPh}$ is much smaller than the dimension of the volume with dissipation $\Omega_R$, the additional cooling effect vanishes. This effectively leads to $\Omega_{CF} = 0$ in Eqn. (4.5).

At intermediate temperatures, where $l_{EPh}$ is less or similar to the dimensions of the cooling volume, but still bigger than the dimensions of the dissipation volume $\Omega_R$, the effective volume of the cooling fin $\Omega_{CF}$ is proportional to ${l_{EPh}}^{\mathrm{Dim}}$, where "Dim" is the number of dimensions the electrons can travel. If $\Omega_R$ is much smaller than ${l_{EPh}}^{\mathrm{Dim}}$, Eqn. (4.5) effectively follows $P \propto {T_E}^{5-3\,\mathrm{Dim}/2}$ [73]. This reduced exponent was observed for resistors with attached cooling fin in references [73, 134, 145] as well as the measurements we will show below.

Leaving the microscopic model, the thermal transport within the geometry of such a system can be described using the Wiedemann-Franz law. It states that the thermal conductivity via the electron system is proportional to the electrical conductivity [125, 147]. Although this is typically considered to be valid in our temperature range [125, 147], there is another important condition. To speak of a well-defined electron temperature at one point within the volume under consideration, the length scale of the electron-electron interaction has to be small compared to typical geometries and spacial changes of the electron temperature [119]. An estimate for this length scale for our employed *PdAu* alloy is given in reference [148]. At a temperature of 0.1 K, the electron-electron scattering length is below 1 µm. Accordingly, we assume that the electron temperature is spatially well-defined. The total heat balance is then described by, see for example section II.D in reference [119]:

$$\underbrace{\frac{P}{\Omega}}_{\text{dissipation}} - \underbrace{\Sigma\left({T_E}^5 - {T_{Ph}}^5\right)}_{\text{power drained to phonons}} = -\nabla \underbrace{\left(\frac{\mathscr{L}}{\rho} T_E \nabla T_E\right)}_{\text{heat flux electrons}} \tag{4.7}$$

Here, $\nabla$ is the Nabla operator, $P/\Omega$ represents possibly dissipated power in a volume element, $\mathscr{L}$ is the Lorenz number $2.45{\cdot}10^{-8}\ \mathrm{W\,\Omega\,K^{-2}}$ and $\rho$ the specific resistivity of the material. The Lorenz number is derived from the free electron model but in practice, $\mathscr{L}$ can be material- and temperature dependent [125, 147]. We will ignore this fact for simplicity.

For an idealized cooling fin, there exists an analytic solution for Eqn. (4.7). For a negligible phonon temperature $T_{Ph} = 0$ and an infinitely long cooling fin with a constant cross-section, the spatially dependent electron temperature $T_E(x)$ can be expressed as [140]:

$$T_E(x) = T_R\left(1 + \frac{x}{l_T}\right)^{-2/3} \tag{4.8}$$

$$l_T = \sqrt{\frac{14\,\mathscr{L}}{9\,\rho\,\Sigma}\,\frac{1}{T_R^3}} \tag{4.9}$$

As indicated in Fig. 4.1(a), $T_R$ here denotes the electron temperature in the beginning of the cooling fin $x = 0$, which corresponds to the temperature of the electrons in the dissipating resistor. The position is defined as $x \geq 0$. The length-scale of changes is $l_T$, which we call *thermal relaxation length*. Note that $l_T$ shows the same temperature dependence as the electron-phonon relaxation length $l_{EPh}$ from Eqn. (4.6), although the two length scales were estimated on two different bases. In reference [149], a similar thermal relaxation length was defined by comparing the thermal resistance between the electron and the phonon system and the thermal resistance caused by diffusion of the electrons. For our employed *PdAu* layer, see Table 4.1, $l_T$ yields $11\ \mathrm{\mu m\,K^{3/2}} \cdot {T_R}^{-3/2}$.

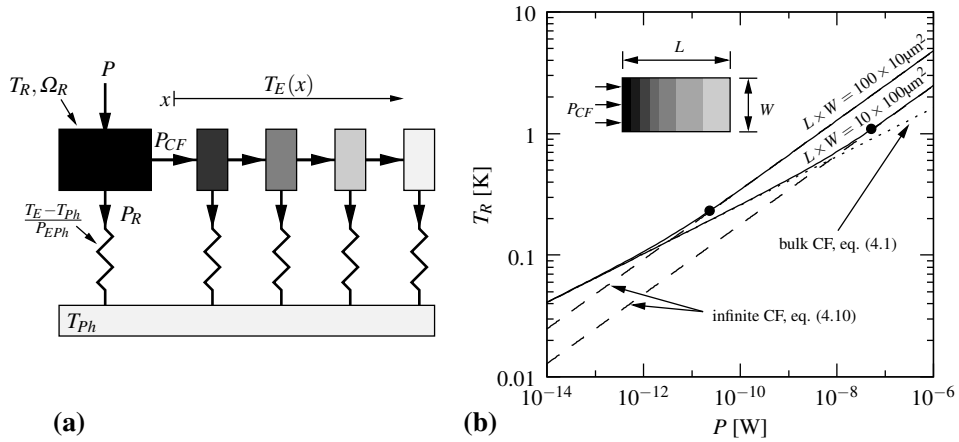


**Figure 4.1:** **(a)** Simplified schematic for a resistor (on the left) with a connected one-dimensional (coordinate $x$) cooling fin. The indicated thermal resistances between the electron and the phonon system are determined by Eqn. (4.1). In **(b)**, the solid lines show numerical calculations of the electron temperature $T_R$ at the beginning of two linear cooling fins in *PdAu* with varying length $L$ and width $W$ at $T_{Ph} = 0$. The height $H$, resistivity $\rho$ and hot electron material constant $\Sigma$ were taken from Table 4.1. The dotted line represents Eqn. (4.1) with $p = 5$ and the total volume of the CFs, which is identical for both CFs. The dashed lines indicate Eqn. (4.10) for an infinitely long cooling fin. The temperature, where the thermal relaxation length $l_T$ is equal to the length $L$ of each CF, see Eqn. (4.9), is indicated by a solid point.

The total power conducted to the phonon system can be obtained from Eqn. (4.8) by estimating the heat flux of the electron system on the beginning of the CF, see Eqn. (4.7):

$$P_{CF} = -A_{CF}\frac{\mathscr{L}}{\rho}T_E(x)\frac{\mathrm{d}T_E(x)}{\mathrm{d}x}\bigg|_{x=0} = A_{CF}\frac{2\mathscr{L}}{3\rho\, l_T}{T_R}^2 = A_{CF}\sqrt{\frac{2\mathscr{L}\Sigma}{7\rho}}{T_R}^{7/2} \qquad (4.10)$$

Here, the area of the cross-section $A_{CF}$ of the cooling fin was used. Note that the same result can be obtained by integrating the power conducted to the phonon system over the infinite length of the CF. In terms of the electron-phonon interaction in a bulk resistor, the same behavior can be modeled using a temperature dependent total volume of $\frac{2}{7} l_T A_{CF}$. Accordingly, the power-temperature dependency $P_{CF} \propto {T_E}^{5-3/2}$ of this idealized case corresponds to the microscopic model mentioned above. Of course, a solution with exponent 5, as mentioned above for the low temperature range, does not directly exist in Eqn. (4.10) because the thermal relaxation length $l_T$ cannot reach boundaries in an infinitely long CF.

In Fig. 4.1(b), we show a numerical calculation of this crossover. We used the finite element method (FEM) based software *Comsol Multiphysics* [150] to solve Eqn. (4.7) on a one dimensional CF with a finite length $L$. At low temperatures, all the volume of the cooling fin is taking part in the cooling behavior, see Eqn. (4.1). At higher temperatures, where $l_T$ becomes smaller than the length of the cooling fin, the behavior is well described by the infinitely long cooling fin. Any volume beyond a distance $l_T$ from the dissipation area does not take part in the cooling behavior.

As already mentioned above for the microscopic model, at high temperatures the power conducted to the cooling fin $P_{CF}$ can become small compared to the thermal power in the

resistor. The reason is the temperature dependency of the thermal relaxation length $l_T$ or the lower exponent in Eqn. (4.10) compared to the exponent of 5. Note that the simple calculation in Eqn. (4.5) only holds as long as the dimensions of the resistor are small compared to $l_T$. In the other case, temperature gradients can also occur within the volume of dissipation.

The idealized cooling fin is useful to gain a qualitative insight into the behavior of attached cooling volumes, but in practice there are two effects that are not included. Naturally, the temperature of the phonon system should be taken into account for the case that the electron system is not completely out of thermal equilibrium. Furthermore, the actual dimension the electrons can travel is of importance.

We also qualitatively studied the two-dimensional case. For this purpose, we numerically calculated the behavior of Eqn. (4.7) in cylindrical coordinates on a cooling fin with radius $r_{CF}$. If the source of dissipation is a point-source in the middle of a cooling fin, the expected power $P \propto {T_R}^2$ behavior is obtained at unpractically high temperatures, where $r_{CF}$ is much bigger than $l_T$, which was of course defined for the one-dimensional case. At such high temperatures, $l_T$ in practice comes close to the dimensions of the hot-spot, for example the width of a thin-film resistor connected to a two-dimensional cooling fin. If the beginning of the cooling fin is modeled as an inner radius $r_I \ll r_{CF}$ in the cylindrical coordinates, a behavior between the linear case $P \propto {T_R}^{7/2}$ and the two-dimensional case $P \propto {T_R}^2$ was found. For similar results, see section II.H in reference [119]. Note that in this work, a very similar thermal relaxation length was defined. As a rule-of-thumb, only the total volume within a distance of a small fraction of the thermal relaxation length $l_T$ from the hot spot participates in the cooling.

In conclusion, the effective cooling behavior of attached reservoirs for "cold electrons" is not trivial, but it can be approximated by a fraction of the thermal relaxation length $l_T$, see Eqn. (4.9). This *cooling radius* is, in agreement with a microscopic model, proportional to $T^{-3/2}$. All the resistive volume within this cooling radius takes part in the thermalization of hot electrons, it forms the volume $\Omega$ as used in Eqn. (4.1).

## 4.3 Heating experiments on resistors with cooling fins

During our first run at the *IPHT Jena* in the "LTS SQUID" process [77], we added cooling fins to the shunt resistors of the SQUIDs. As already pointed out before, this can lower the effective noise of SQUIDs cooled to the mK temperature range [72]. Details on the measurements on the included SQUID sensors will be shown in chapter 5.

To directly study the influence of the hot-electron effect and its suppression in more detail, we added some test structures on the mask of this run. Their layout is shown in Fig. 4.2. Here, a resistor in the standard layer of *PdAu* is contacted by superconducting *Nb* pads. In other cases, there are CFs connected to a resistor of the same layout. The CFs of $80 \times 80$, $80 \times 280$ or $37.5 \times 530$ µm$^2$ area were put in a layer of *Au*. The reason for choosing *Au* was the expected better cooling behavior. The properties of the two layers are listed in Table 4.1. Especially the resistivity is much lower for *Au* which enhances the thermal transport within the cooling fin. The thermal relaxation length $l_T$, see Eqn. (4.9), yields 11 µm K$^{3/2} \cdot {T_R}^{-3/2}$ for *PdAu* and 30 µm K$^{3/2} \cdot {T_R}^{-3/2}$ for *Au*. Accordingly, a bigger cooling volume would be accessible in the *Au* layer.

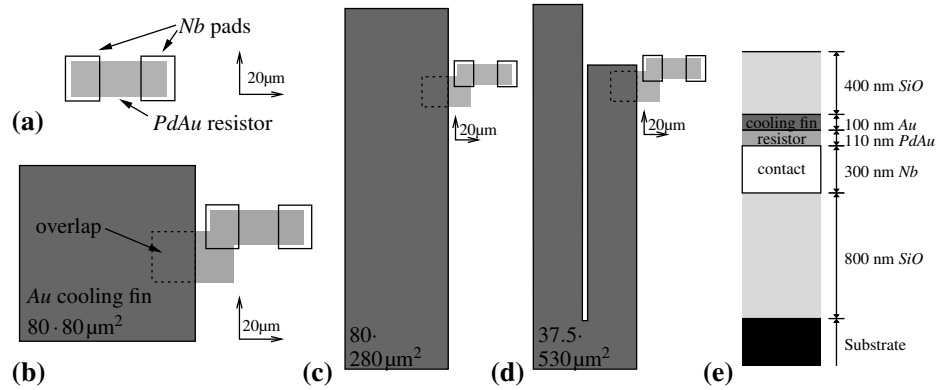


**Figure 4.2:** Layout of the different resistors with possibly connected CFs. **(a)** Bulk resistor in *PdAu* with 15 µm width. The total length is 42.5 µm and the effective length of the resistor, the spacing between the *Nb* contact pads, is 18.5 µm. In **(b)**,**(c)**,**(d)** the same resistor is extended in an electrically unimportant area and overlaps with the CF over an area of $20 \times 22.5$ µm$^2$ in all three cases. Here, electrical contact is made between the *PdAu* and the *Au* layer of the CF. CFs with varying size **(b)** $80 \times 80$, **(c)** $80 \times 280$ and **(d)** $37.5 \times 530$ µm$^2$ are connected. In **(e)**, the vertical dimensions of the involved layers are shown, simplified as if all were stacked. The lower *SiO* layer is present all over the sample, whereas the upper one, a cover layer, was not present in parts of the *Au* cooling fin including the overlap with the *PdAu* layer [77].

### 4.3.1 Description of the measurements

By means of dissipating power in the resistors and performing noise thermometry, as it was done for example in references [13, 72, 145], we studied the thermal behavior of these configurations. In difference to the typical measurement technique [13, 72, 145], we extended the setup by a capacitance that forms a high-pass filter. Its purpose will be explained below. The schematic of the measurement setup is shown in Fig. 4.3. The measurements were performed in collaboration with *Leiden University* using a dilution refrigerator from *Leiden Cryogenics* [151].

The sample with the resistor under investigation was mounted on a printed circuit board within a module made of *Nb*. This module was placed in the mixing chamber of a dilution refrigerator. The same module also contained the SQUID amplifier and a high-pass capacitor, a standard part based on polyester with a room temperature capacitance of 4.7 µF. The

**Table 4.1:** Data of the two involved metal layers.

| | | *PdAu* | *Au* |
|---|---|---|---|
| thickness $H$ | [nm] | 110 [a] | 100 [a] |
| sheet resistance $R_\square$ | [Ω] | 3.5 [b] | |
| specific resistance $\rho = R_\square H$ | [µΩ cm] | 39 | 1.8 [c] |
| material constant hot-electron effect $\Sigma$ for $p = 5$ | [W K$^{-5}$ m$^{-3}$] | $0.79 \cdot 10^9$ [d] | $2.4 \cdot 10^9$ [122] |

[a] fabrication goal
[b] from resistance measurements below 1 K
[c] from the standard technology values $\rho_{Au} = R_\square H = 0.4\ \Omega \cdot 45$ nm [77]
[d] from fit to dissipation measurement, see section 4.3.2

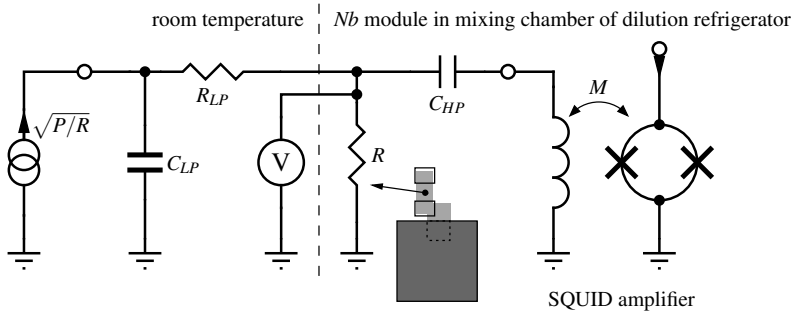


**Figure 4.3:** Measurement setup. A current source at room temperature is used to control the dissipation. The current is low-pass filtered at room temperature ($C_{LP} = 1$ µF, $R_{LP} = 760$ kΩ) with a sub-Hz corner frequency. In the low temperature part, a capacitance $C_{HP} = 4.7$ µF is connected to form a high-pass filter for the noise of the resistor $R$ under study. This noise is measured using the SQUID amplifier presented in section 5.4.2 on page 107. See the text for more details.

capacitance did not drastically change when cooled down to our measurement temperatures. The measured corner frequency of the high-pass filter below 4 K was ≈ 8 kHz.

Furthermore, it was possible to measure the voltage across the resistor by means of a pair of cables connected in a four-point configuration. Below bath temperatures of 1 K, we measured values of the resistors close to 4.4 Ω for all the different characterized resistors. These values were a few percent lower than the values measured at 4.2 K. This corresponds to a sheet resistance of 3.5 Ω, whereas the goal of fabrication was 4 Ω. We do not know if this variation originated from either a changed thickness $H$ of the *PdAu* layer, a difference in the resistivity or a mixed situation. For simplicity, we addressed the comparably small deviation in sheet resistance to a change in resistivity and assumed the goal thickness of the layer of 110 nm as the fabricated thickness, see Table 4.1.

The SQUID used for the readout of the noise was a SQUID with integrated flux transformer [36] which was fabricated on the same wafer. More details can be found in chapter 5. The SQUID was directly coupled to a *Supracon* SQUID-electronics [152] and the noise spectrum was determined in flux-locked loop. The advantage of the employed high-pass scheme is, besides allowing to easily bias the resistor with a constant current, that we could also measure the noise of the readout system in the low frequency region and subtract its noise PSD. A typical noise measurement is depicted in Fig. 4.4(a). Furthermore, we also subtracted the noise PSD of the room temperature low-pass resistor, which is not present in the low frequency range. The effective temperature of the electron system in the shunt resistor was determined by:

$$T_E = \frac{R}{4k_B M^2}\left(S_{\Phi,HF} - S_{\Phi,VV} - \frac{4k_B \cdot 300\ \mathrm{K} \cdot M^2}{R_{LP}}\right) \tag{4.11}$$

Here, $S_{\Phi,HF}$ is the flux noise PSD between 90 and 100 kHz and $S_{\Phi,VV}$ is the effective additional flux noise PSD of the SQUID. $R$ is the measured value of the resistor and $R_{LP} = 760$ kΩ is the value of the room temperature filter resistance. The corresponding schematic is shown in Fig. 4.3. The back-action noise of the SQUID, as introduced in chapter 2, has no influence here due to the comparably large values of the resistor or, in other words, due to the low quality factor $Q \ll 1$. Because we simply used the SQUID

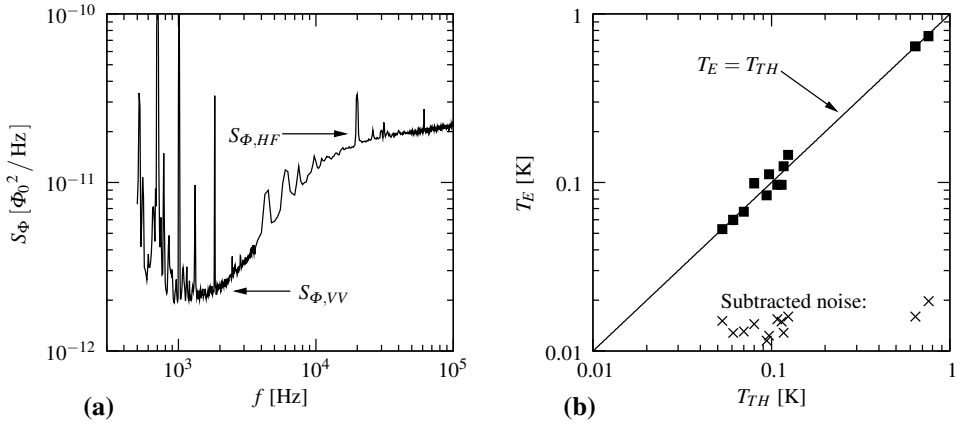


**Figure 4.4:** **(a)** Typically measured SQUID flux-noise spectrum, here at a temperature of 84 mK. The noise peaks at the lower frequencies were mainly caused by mechanical vibrations that could not be damped and the high-frequency peaks were of most probably both mechanical and electromagnetic origin. The two important noise levels are indicated, see Eqn. (4.11). **(b)** Comparison of the measured bath temperatures for the later shown measurement series, determined by either the integrated thermometer or the SQUID. $T_{TH}$ is the temperature determined from an in the dilution refrigerator integrated thermometer. $T_E$ is determined from the measured SQUID spectra without a dissipation with Eqn. (4.11), where the "x" markers show the equivalent temperature of the subtracted noise of the readout system. See the second and third term of Eqn. (4.11), the marker "$S_{\Phi,VV}$" in (a) and the text for more details.

in a single-stage setup, the additional noise of the SQUID of typically 1.5 $\mu\Phi_0/\sqrt{\text{Hz}}$ was dominated by the input voltage noise of the electronics.

During all the measurement series shown below, we first stabilized the temperature of the dilution refrigerator and recorded the value from an integrated thermometer. Then we measured the resistance $R$, using comparably small currents, and measured the noise spectrum of the SQUID to determine the temperature without power dissipation. Then we gradually changed the current through the resistor and recorded the $P - T_E$ characteristics, with $P = RI^2$. In the end of each series we verified that the bath temperature did not change during the measurement.

In Fig. 4.4(b) we show a comparison of the bath temperatures determined by the two different methods. The result suggests that there is no systematic error between the values measured via the SQUID or via the thermometer. The differences mainly originate from a thermal gradient within the mixing chamber, the integrated thermometer was situated about 10 cm away from the *Nb* module that contained the sample. Furthermore, the graph shows that the in Eqn. (4.11) subtracted noise of the readout system is not dominant but of importance for an accurate determination of the electron temperature.

### 4.3.2 Measurement results for the resistor

The results for the resistor without CF are shown in Fig. 4.5. The bath temperatures $T_B$ are the values determined from the SQUID measurement without dissipation. We fitted the measurement data to Eqn. (4.1). Here, we only used the data from the lower range of power dissipation $P$, up to $\approx 1$ nW. The resulting exponent of $p = 5.05$ is in accordance to the

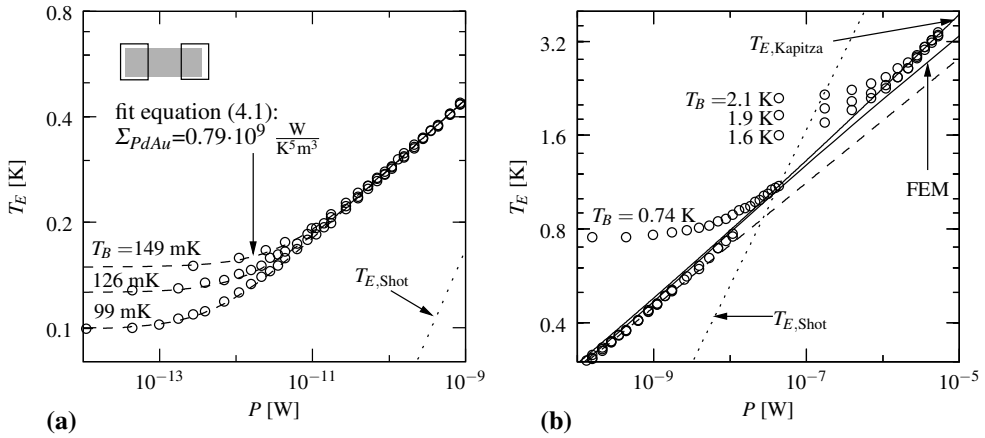


**Figure 4.5:** Measurement on the bulk resistor for different bath temperatures. The dissipated power $P$ is plotted versus the electron temperature $T_E$. **(a)** Measured data to determine the material constant of the hot-electron effect, where the complete volume of the resistor including the parts covered with *Nb* was used. The resulting fit of Eqn. (4.1) is shown as dashed lines. **(b)** All measured data at the higher temperature regime. The three measurements at the highest bath temperatures were performed in a vacuum-pumped $^4He$ bath-cryostat. The fit for the low power regime is also here shown as a dashed line. The apparent temperature due to shot noise $T_{E,\mathrm{Shot}}$ is estimated from Eqn. (4.13) with $F = \sqrt{3}/4$. The solid line marked with "FEM" is the numerical calculation of Eqn. (4.7) with $T_{Ph} = 100$ mK and the data from Table 4.1. The electron temperature with influence of the Kapitza resistance $T_{E,\mathrm{Kapitza}}$ is calculated with Eqn. (4.14) with the total area of the resistor, $T_B = 0$ and $K = 80\,\mathrm{W\,m^{-2}\,K^{-4}}$. $K$ was chosen to fit the data at the highest temperatures.

most experiments on metals in the clean and dirty limit, see section 4.1. The data of another reported measurement [136], also suggests an exponent $p = 5$ for a *PdAu* resistor.

Our sample sample was certainly in the *dirty limit*. In reference [136], we found an estimate for the mean free path of the electrons $l_E \approx 2$ nm. The there investigated *PdAu* layer had a similar resistivity. In reference [153], the speed of sound $v_S$ is estimated to $3.5{\cdot}10^3$ m/s for the longitudinal and $1.3{\cdot}10^3$ m/s for the transverse phonons in *PdAu*, respectively. The expression $2\pi\, l_E/\lambda_{Ph}$ yields with Eqn. (4.4) and the minimum bath temperature of 100 mK a value of $\sim 10^{-3}$, the dirty limit. Accordingly, our observed exponent $p \approx 5$ is another example for experimental results that are in discrepancy with existing theories. See section 4.1 for a more detailed discussion.

Because the resistor is contacted by a superconductor, hot electrons stay within the resistive volume because of Andreev reflection. Due to the superconducting proximity effect, the superconducting volume could be extended into the covered parts of the resistor [119]. This has practically no influence on the resistance because of the comparably long resistor. The dissipative area is not altered significantly. Nevertheless, the by *Nb* covered parts of the resistor, about half of the total area, could become superconducting and would also not participate in the cooling of hot electrons. We will ignore this fact because on the one hand the superconducting proximity effect requires an ideal contact and on the other hand, we observed a thermal conduction through the covered parts. As will be shown below, the connected cooling fins significantly lowered the electron temperature of the resistor at low dissipated power. Because the additional power has to pass the geometry covered by *Nb*, see

Fig. 4.2, we assume that there was no significant proximity effect.

The fit of Eqn. (4.1) with a constant exponent $p = 5$ is shown in Fig. 4.5(a). Using the total volume of the resistor we were able to estimate the hot electron material constant for the *PdAu* layer $\Sigma_{PdAu} = 0.79{\cdot}10^9\ \mathrm{W\,K^{-5}\,m^{-3}}$. Because some of the theories mentioned in section 4.1 predict a dependency of $\Sigma$ on the mean free path $l_E$ [135], the estimate $l_E \approx 2$ nm or the resistivity of 39 µΩ cm should be given with this value.

In reference [153], the Sommerfeld parameter $\gamma$ for a *PdAu* alloy is experimentally determined to $3.88\ \mathrm{mJ\,mol^{-1}\,K^{-2}}$. Using standard values for the density and atom mass, this leads to an electronic heat capacity in *PdAu* of $\approx 400\ \mathrm{J\,m^{-3}\,K^{-2}} \cdot T_E$. With Eqn. (4.2), this allows us to estimate the characteristic electron-phonon scattering time in our experiment to:

$$\tau_{EPh,PdAu} = \frac{\gamma}{5\Sigma} \approx 1{\cdot}10^{-7}\ \mathrm{s\,K^3} \cdot {T_E}^{-3} \tag{4.12}$$

At the minimum observed electron temperatures of about 100 mK, see Fig. 4.5(a). Accordingly, the electrons emitted energy to the phonon system in scattering processes that took place every 0.1 milliseconds in average. See reference [126] for even longer time scales of such processes.

At this point we want to name another possible effect that could influence our experiment, the *hot-electron shot noise* [119, 146, 154, 155]. According to literature, shot noise becomes important when on the one hand the electron-phonon interaction length $l_{EPh}$ exceeds the length of the resistor and on the other hand the energy of electrons becomes larger than the thermal energy $eV \gg k_B T$, $V$ being the voltage across the resistor $V = \sqrt{PR}$.

This shot noise shows a current noise component whose PSD is white at the frequencies accessible in our experiment. The PSD is proportional to the average current through the resistor and is thus also proportional to $\sqrt{P}$. Compared to the hot-electron effect, see Eqn. (4.1), the shot noise would mimic an exponent $p = 2$. In our experiment, the shot noise and Nyquist noise PSDs would add. Accordingly, the shot noise can be modeled by a noise temperature $T_{E,\mathrm{Shot}}$ that adds to the thermodynamic electron temperature $T_E$ [146]:

$$T_{E,\mathrm{Shot}} = F\frac{2e\sqrt{PR}}{4k_B} \tag{4.13}$$

Here, the Fano factor $F$ was introduced. $F$ takes a value of $\sqrt{3}/4$, if the resistor is shorter than $l_{EPh}$ and longer than the electron-electron interaction length [146, 154]. The latter condition was verified in section 4.2, the electron-electron scattering length stays below 1 µm in our experiment. As already pointed out before, $F$ vanishes if the resistor is much longer than $l_{EPh}$.

We also performed measurements at higher bath temperatures. The measurement data of all series in a higher temperature regime are depicted in Fig. 4.5(b). In both Figs. 4.5(a) and 4.5(b), we plotted the theoretically estimated shot noise contribution according to Eqn. (4.13). We have to conclude that we see no dominant influence of shot noise over the whole measurement range. We will now check the conditions for its occurrence in our case.

The electron-phonon interaction length $l_{EPh}$, see Eqn. (4.6), can be estimated with the electron diffusion constant $D$. With the resistivity of our *PdAu* layer and data from reference [135], $D$ yields 16 $\mathrm{cm^2/s}$. This leads with Eqn. (4.12) to an electron-phonon interaction length of $l_{EPh} \approx 13\ \mathrm{\mu m\,K^{3/2}} \cdot {T_E}^{-3/2}$. Accordingly, $l_{EPh}$ exceeds the length of our

resistor below electron temperatures of $\approx 800$ mK. From this point of view, shot noise is likely to occur, see for example Fig. 3 in reference [155].

The comparison of thermal energy and charge energy is not trivial, because of the phonon cooling. The minimum temperatures in our experiment are in the order of 100 mK, and the electrons and phonons stay at the same temperature up to a dissipation in the order of picowatt. Here, the ratio $eV/(k_B T)$ yields about 0.2 and this value grows with higher dissipation. In this intermediate regime, the total noise of the resistor is described best by the Nyquist noise with the spatially averaged electron temperature [119, 154]. The spatial dependent electron temperature is calculated with Eqn. (4.7). In fact Eqn. (4.13) in our assumed limit was derived on the basis of a similar calculation on a thin resistor with negligible phonon cooling in the middle of two well-thermalized resistive contacts with $T_E = T_{PH}$ [146, 154]. In this case, the cooling in the thin resistor is mainly due to electron diffusion towards its edges and accordingly there are large temperature gradients along the resistor. The spatially averaged Nyquist noise leads to Eqn. (4.13) [146, 154].

In our case the contacts of the resistor are of about the same size as the resistor itself and they are thermally isolated due to the superconducting contact pads. Therefore, large temperature gradients cannot occur across the resistor. We expect the electron temperature to be similar to the average temperature in the resistor, even at high dissipated power. This leads us to the conclusion that direct shot noise does not seem to play a role in our experiment. Based on this and the fact that we cannot see any evidence for shot noise in our measurement, we neglect its influence in our analysis. Nevertheless, a minor influence of temperature gradients within the resistor might be of importance and will be calculated below.

At higher dissipated power $P \gg 1$ nW, the exponent $p$ deviates from the low power regime, see Fig. 4.5(b). The measurement at $T_B = 740$ mK follows $p \approx 4.4$. In contrary to the already excluded shot noise, we have two other possible explanations for this deviation.

First of all, the length of the by *Nb* covered parts of the resistor is equal to the thermal relaxation length $l_T$ at $T_E = 1$ K, see Eqn. (4.9). Accordingly, these parts of the volume do not fully participate in the cooling above this temperature. A FEM calculation of Eqn. (4.7) on the real geometry of the resistor is shown in Fig. 4.5(b). For this purpose, we again used the software *Comsol Multiphysics* [150]. We defined the geometry in two dimensions with the data for *PdAu* from Table 4.1. Simulating the real measurement, we only dissipated power in the area $A_R$ between the *Nb* connectors. Then we calculated the average of the electron temperature $T_E(x,y)$ over the area between the connectors $T_R = {A_R}^{-1} \iint T_E(x,y)\,\mathrm{d}x\,\mathrm{d}y$. $T_R$ corresponds to the effective temperature one would observe in a noise measurement. The result for varying power is shown in Fig. 4.5(b) as the solid line marked with "FEM". As one can see, the calculation deviates as expected from the fit for the bulk resistor, which is shown as a dashed line. At much higher temperature, the behavior is described by a solution of Eqn. (4.1) with an exponent $p = 5$ and the volume between the contact pads only. Nevertheless, the deviation at even higher temperatures is not well explained.

Another influence at high power could be given by the the Kapitza resistance. Combining Eqns. (4.1) and (4.3) leads to:

$$T_{E,\mathrm{Kapitza}} = \sqrt[5]{\frac{P}{\Sigma H A_R} + \left(\frac{P}{K A_R} + {T_B}^4\right)^{5/4}} \tag{4.14}$$

We also plotted this noise contribution in Fig. 4.5(b). This model could be an explanation for

the high temperature deviation. At low temperatures, it is of vanishing influence. Furthermore, at low temperatures the existence of a Kapitza resistance at the boundary between the resistor and the surrounding *SiO* substrate is doubtful. As already pointed out in section 4.1.2, a requirement for the Kapitza resistance is that two distinct phonon populations must exist in the adjacent materials. With Eqn. (4.4) and the above given data for the speed of sound in *PdAu*, one can estimate that the wavelength of the phonons $\lambda_{Ph}$ becomes larger than the thickness of the resistive layer at temperatures below 1.5 K for the longitudinal and below 0.6 K for the transversal phonon system, respectively. Thus, in our measurement regime, the phonon population in the resistor should be two-dimensional. The theory on the Kapitza resistance is based on three-dimensional phonon populations.

The phonon dimensionality could have another effect, as mentioned in section 4.1.2. According to reference [123], the exponent $p$ in Eqn. (4.1) changes when the phonon wavelength becomes comparable to the film thickness. In our experiment and in the work presented in reference [136], an exponent $p = 5$ was found in terms of Eqn. (4.1). In both cases, a resistor of the same alloy *PdAu* with reduced phonon dimensionality was investigated. Resistors of the same alloy but with clearly three-dimensional phonons were characterized in reference [135]. Here, an exponent $p = 4$ was observed. We conclude that the electron-phonon coupling in our two-dimensional phonon case could be of $p = 4$ dependence [135] affected by the phonon dimensionality in the sense of the work presented in reference [123].

### 4.3.3 Results on resistors with CFs

We repeated the same experiment on three different configurations of resistors with attached cooling fins, see Fig. 4.2(b), (c) and (d). To compare our measurement data with the theory of the electronic thermal transport, we again performed FEM calculations on Eqn. (4.7) in two dimensions.

In the calculation, the phonon temperature $T_{Ph}$ was assumed to be equal to the bath temperature $T_B$ over the whole geometry and to be independent of the power. Naturally,

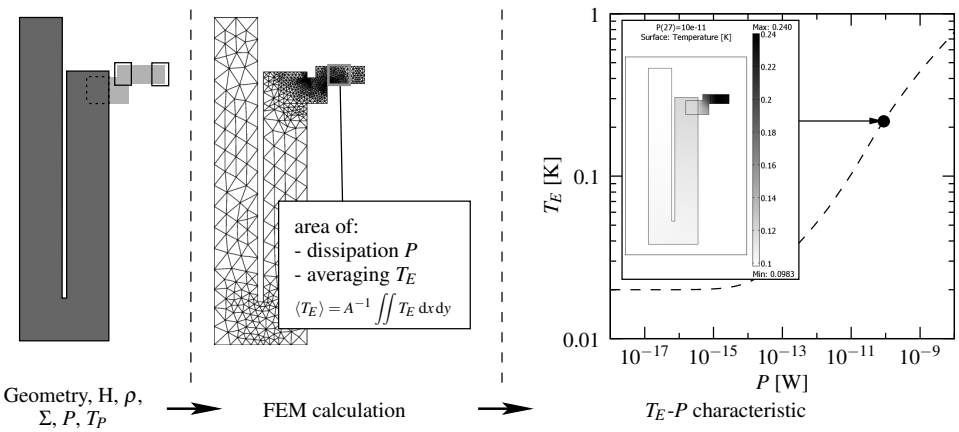


**Figure 4.6:** Illustration of the FEM calculation on Eqn. (4.7). The grey scale in the picture of the FEM calculation shows the electron temperature $T_E$ from 0.1 K (white) to 0.24 K (black). The dissipated power $P$ was 0.1 nW and the bath temperature was $T_B = 20$ mK. See text for details.

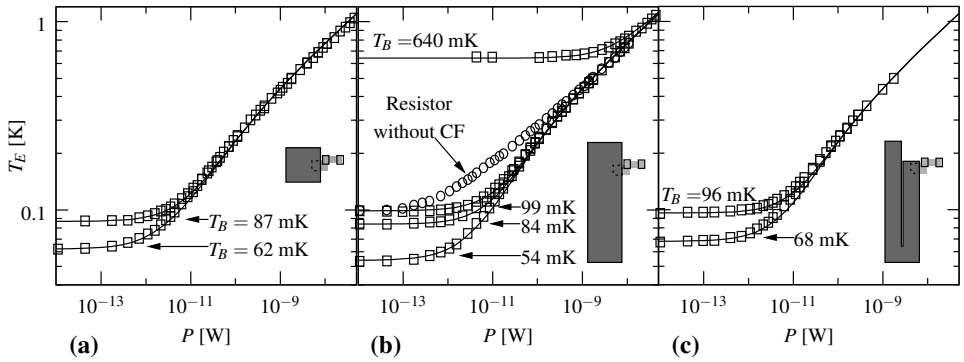


**Figure 4.7: (a),(b),(c)** Measurement data for different bath temperatures $T_B$ on resistors with varying CFs, see Fig. 4.2. The dissipated power $P$ is plotted versus the electron temperature $T_E$. The black lines are the FEM calculation as described above with the accurate geometry of each configuration and the bath temperature derived from the measurement. In (b), we also plotted one measurement series of the stand-alone resistor from Fig. 4.5.

the dissipation term in Eqn. (4.7) was only applied in the area between the contact pads. The respective parts of the geometry were modeled with the values from Table 4.1. In the overlapping area of *PdAu* and *Au*, $d_{Au}\Sigma_{Au} + d_{PdAu}\Sigma_{PdAu}$ and $d_{Au}/\rho_{Au} + d_{PdAu}/\rho_{PdAu}$ were used in the respective terms. To estimate the effective electron temperature of the resistor for each dissipated power, the temperature was averaged in the area between the *Nb* connectors. The calculations are illustrated in Fig. 4.6.

Both the FEM calculations and the measurement data for all three configurations are shown in Fig. 4.7. Note that the only fit used is the one from the last section, the determination of $\Sigma_{PdAu}$. The agreement is very good, which suggests that our experiment is well described by the electronic thermal transport model. Especially the data for the *PdAu* layer seem to be close to the real values. The theoretical Lorenz number $\mathscr{L}$ also seems to be a good approximation.

From Fig. 4.7(b) one can see that the connected cooling fin lowers the temperature as expected. This supports the conclusion that the superconducting proximity effect in the area covered by *Nb* can be neglected, see the last section on the experimental results on the stand-alone resistor. Above a disspated power of $\approx 100$ pW, which is also about the power dissipation of the SQUIDs that were fabricated on the same wafer, the additional cooling effect vanishes.

We performed FEM calculations on the different configurations to make the comparison of the different CFs easier. The result is shown in Fig. 4.8(a). The two CFs of $80 \times 280$ µm$^2$ and $37.5 \times 530$ µm$^2$ area, thus with a comparable volume, show about the same behavior. The smaller CF $80 \times 80$ µm$^2$ shows a slightly smaller cooling power. We have to conclude that we could not clearly see a difference between the different attached cooling fins in *Au*. First we intended to measure differences according to the dimensionality of the *Au* fin. Unfortunately, we underestimated the screening of the weak thermal *PdAu* connection to the CF.

If one approximates this connection to the cooling fin to be a one-dimensional cooling fin, the distance to the beginning of the *Au* cooling fin is roughly 30 µm. The thermal relaxation length, see Eqn. (4.9), becomes smaller than this value at temperatures $T_E \gtrsim 0.5$ K. Above this temperature there is no influence of material connected beyond that distance, see

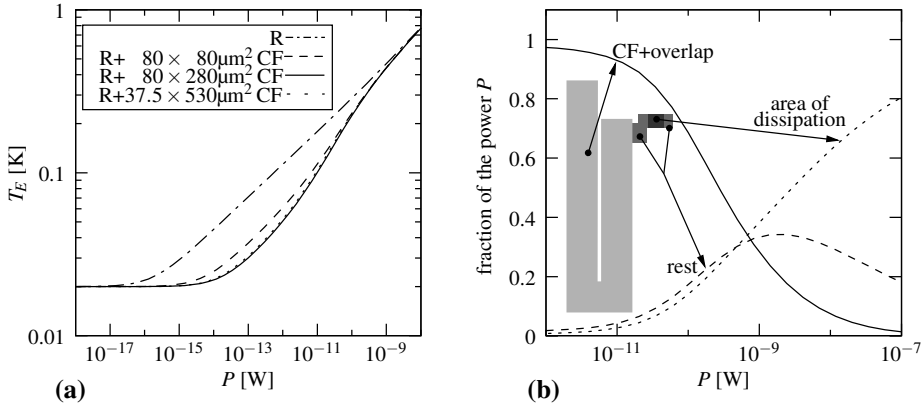


**Figure 4.8:** **(a)** FEM calculations on all the characterized configurations at a bath temperature $T_{Ph}$=20 mK. Note that the solid and the dotted line are almost identical. **(b)** Illustration where within the geometry the largest fraction of the power is drained to the phonon system. This is calculated by $P^{-1} \int H \Sigma \left( {T_E}^5 - {T_P}^5 \right) \mathrm{d}A$ within each of the indicated parts.

section 4.2. A comparison of the calculation of the resistor with and without cooling fins in Fig. 4.8(a) supports this insight.

In Fig. 4.8(b), we show a calculation that indicates in which parts of the geometry the dissipated power is drained to the phonon system. At low dissipated power $P$, the whole volume participates in the cooling. This corresponds to the data for $P \lesssim 10^{-11}$ W in Fig. 4.8(b). Here, the larger fraction of the dissipated power is drained within the cooling fin. This is due to the fact that the cooling fin also covers the largest fraction of the total volume. At intermediate dissipated power, the cooling volume is restricted in the sense of the temperature dependent thermal relaxation length, see Eqn. (4.9). At high dissipation $P \gtrsim 10^{-8}$ W, the largest fraction of the power is drained within the volume of dissipation.

The three regimes as mentioned in section 4.2 are present in the calculation. The intermediate and high power regimes can also be clearly identified in the measurement data, see the comparison of the experimental data on resistors with and without the cooling fin in Fig. 4.7(b). The low power regime, is not accessible at our bath temperatures and other measurements on resistors with attached cooling fins [73, 145].

A fit of the measurement data on the resistors with cooling fins to Eqn. (4.1) in the lower range of power dissipation leads to an apparent lower exponent $p \approx 2.5$. This is in agreement with other measurements on resistors with CFs [73, 145]. According to the simple non-uniform heating model described in reference [73], this is caused by a diffusion of hot electrons into a cooling volume of one till two dimensions. This is a good approximation of our geometry. See section 4.2 for more details.

## 4.4 Conclusions

In this chapter we theoretically and experimentally investigated the hot-electron effect and its suppressions by attaching a reservoir for “cold electrons”, so-called cooling fins.

In section 4.1, the important theories and encountered effects are mentioned. In summary, the hot-electron effect is determined by several concepts that cannot be strictly separated.

First of all, there are different theories on bulk resistors that predict a varying exponent $p$ in the electron temperature to dissipated power function $P \propto {T_E}^p$. This value of the exponent ranges from 4 to 6, depending on the disorder of the sample and the origin of this disorder. Furthermore, the dimensionality of the phonon system in the resistor can alter on the one hand the exponent $p$ and on the other hand it has an influence on a possible thermal resistance of the phonon system in the resistor to adjacent materials.

In section 4.2, we described the behavior of cooling fins attached to a dissipating resistor. One can basically expect three regimes of cooling behavior. At low temperatures, the complete volume of resistor and attached cooling fin participates in the cooling of hot electrons. At intermediate temperatures, the cooling volume is restricted in the sense of the temperature dependent thermal relaxation length. At high temperatures, only the volume of dissipation takes part in the cooling of hot electrons. A temperature dependent thermal relaxation length from the calculation of an idealized one-dimensional cooling is a good approximation for the involved cooling radius. This is demonstrated by a numerical calculation on a finite one-dimensional cooling fin.

In section 4.3, we present heating experiments on thin-film resistors made of *PdAu*. This is achieved by means of controlled power dissipation in the resistor combined with noise thermometry. The noise was measured using a SQUID amplifier. The typical setup for this measurement [13, 73, 145] was extended by a high-pass filter capacitance. This constricts the dissipated power to the resistor of interest and allows the extraction and compensation of the additional noise of the readout system.

In section 4.3.2, we show the experimental results on a thin-film resistor made of *PdAu* without a cooling extension. We found the typically observed exponent $p = 5$. The measurement data do not show an influence of the Kapitza resistance or shot noise. We therefore conclude that we directly measured the energy transfer between the electron and the phonon system. Because our sample is certainly in the dirty limit, the exponent $p = 5$ is in contradiction to theory. A comparison with results reported in literature on resistors of the same alloy [135, 136] but of different thickness led to the conclusion that the exponent $p = 5$ could be influenced by the dimensionality of the phonon population in the shunt resistor [123].

In section 4.3.3 we numerically and experimentally studied configurations of resistors with attached cooling fins. The measured data are well approximated by numerical calculations on the thermal heat conduction within the geometry.

For the investigated layout of resistors with cooling fins, the additional cooling effect vanishes for typical power dissipation of our SQUIDs. To minimize the effective electron temperature in resistors with attached cooling fins we conclude:

1. The volume of the resistor itself has to be maximized. If there is a choice in material, also $\Sigma$ should be maximized. Naturally, this directly lowers the electron temperature of the resistor and of the temperature on the boundary to an adjacent cooling volume. This has the additional effect of an increased thermal relaxation length, see Eqn. (4.9), which in turn makes larger parts of the cooling fin accessible.

2. The largest possible amount of metal should be situated as close as possible to the volume of dissipation. The effective cooling radius is given by the thermal relaxation length.

3. Following from the Wiedemann-Franz law, a material with a lower resistivity further increases this length scale, see Eqn. (4.9).

Furthermore, the employment of bulk resistors could be beneficial. Another approach we want to name here would be an active cooling by means of tunneling effects [119]. Nevertheless, the damping effect of the shunting resistor of the Josephson junction must be maintained. This complicates the implementation of these techniques.

The numerical calculations on the electronic thermal transport turn out to be a useful tool for the thermal design of superconducting electronics. This will be applied in chapter 5.

# Chapter 5

# Design and characterization of dc-SQUID amplifiers

In this chapter we want to summarize the results of our design and characterization process on SQUIDs with a long integrated input coil. The developments are intended for a utilization in the *MiniGRAIL* project, see section 1.5 on page 16. The requirement is a best reachable sensitivity with an input inductance in the order of $L_{IN} \approx 1.5$ µH. Because an operation in the sub-Kelvin temperature range is planned, we attached cooling fins to the shunt resistors of the SQUIDs. Furthermore, the readout of the capacitive transducers of MiniGRAIL has to be achieved with SQUIDs operated in a flux-locked loop (FLL).

There are many parallels to the preceding chapters of this thesis. In chapter 2, we analyze the low noise operation of SQUID sensors. The results give insight into the operation of a SQUID system with a capacitive input circuit and can accordingly be used to define some special requirements for MiniGRAIL. The minimum equivalent input noise temperature is not needed for MiniGRAIL. The achievable values in the kHz frequency regime are in the order of µK [156], which is several orders of magnitude below the intended operation temperature of 20 mK. The more interesting properties for MiniGRAIL are the bandwidth and the stability. From the analysis of chapter 2 follows that an increased bandwidth of the SQUID operated with a high quality factor input circuit requires a minimum coupled energy resolution $\varepsilon_{VV}/k^2$. Furthermore, the stability in FLL requires a minimum coupling between the feedback and the signal coils of the SQUID or further compensation measures. Naturally, the investigation of the properties of a SQUID with a long integrated coil shown in chapter 3 is of importance here. The large required input inductance clearly leads to the long coil limit. In this chapter, several effects also presented in the numerical analysis of chapter 3 will be investigated. In chapter 4, we studied the possibilities to reduce influences of the hot-electron effect by means of passive cooling. The minimum required energy resolution combined with the sub-Kelvin operation temperature led to the work presented there. In this chapter, we will evaluate our SQUID designs from this point of view.

Here, we will first give a brief description of the employed fabrication technology for our SQUID designs and the employed modeling and experimental techniques.

In section 5.4, we will present the design and performance of our first developed SQUID sensors. The observed effects partly led to the work presented in the preceding chapters. On

the one hand, these were unusual characteristics that could not be explained by the standard SQUID theory. On the other hand, we investigated the noise behavior of a SQUID at low temperatures which was dominated by the hot-electron effect.

The gained experience of designing, modeling and characterizing SQUIDs was used in a second design step, which will be presented in section 5.5. We will conclude this chapter with an outlook and recommendations for possible further improvements.

## 5.1 Description of the used fabrication technology

Our SQUID designs include integrated thin-film coils with a 3 µm width of the winding and spacing between the windings. The total length of all windings of the coils reached several centimeters. The stable fabrication required for such structures was the main reason for our decision to make use of a commercial process. All designs were fabricated in the "LTS SQUID" process of the foundry at the *IPHT Jena* [77].

The Josephson junctions are of superconducting-insulating-normalconducting-superconducting $Nb-Al_2O_3-Al-Nb$ type. The layout gives a minimum possible size of the Josephson junctions of $3.5 \times 3.5$ µm$^2$. The Josephson junctions of all the SQUIDs shown in this chapter use this minimum size. The effective size in a fabricated device is given by $3.2 \times 3.2$ µm$^2$ [77]. Therefore, the critical current reads $I_0 = 3.2 \times 3.2$ µm$^2 J_0$. Critical current densities $J_0$ between 10 and 1500 A/cm$^2$ can be fabricated with a global tolerance of about 20 % [77]. Within one chip the tolerance of $J_0$ is given by 5 %. The dimension of all our chips was $2.5 \times 2.5$ mm$^2$. A value of 0.05 pF/µm$^2$ is given for the capacitance of the Josephson junction [77]. We used a value of $C \approx 0.6$ pF based on the defined size of the Josephson junction, which was chosen to the minimum possible area. To reach a non-hysteretic operation of the Josephson junctions, they have to be shunted externally. Therefore, a resistive *PdAu* layer is available, which does not show superconducting properties. The sheet resistance of the standard 115 nm thick *PdAu* layer is 4 Ω. The superconducting structures can be formed in two *Nb* layers. Josephson junctions are put between these two layers, the resistive layer can only be contacted from the top electrode.

The integrated coils are placed in the upper *Nb* layer. As mentioned above, the width of the coil wire and the spacing between different wires is 3 µm. The properties of the strip line formed by the input coil and the washer, which typically defines the SQUID inductance, are of importance for a realistic model of the SQUID. Using the thickness of the insulating *SiO* layer of 800 nm between the upper and the lower *Nb* layer and using a relative permittivity $e_r$ of 6.5, we estimate [108] the distributed inductance $L'_{ST}$ and capacitance $C'_{ST}$ of the coil microstrip line as $2.5 \cdot 10^{-7}$ H/m and $3.6 \cdot 10^{-10}$ F/m, see equations (3.20) and (3.21) on page 62. The fringe factor $K$ reads $\approx 1.7$ [108].

## 5.2 Modeling techniques

For SQUIDs, the most important property of a layout is the inductance of fabricated structures. All our SQUIDs are based on the washer structure [76]. For a detailed description see section 3.3 on page 60. Although the inductive properties of the real washer are known quite well, see Eqns. (3.15)–(3.20) on page 61, there are many uncertainties in a practical layout. The slit inductance $L_{SL}$ can differ from design to design. There are parasitic inductances

associated with connections of multiple washers, the Josephson junctions, its shunt resistors or other damping resistors within the design for example.

A precise prediction of all these properties of the structures in the SQUID is not simple. One would need to determine all self-inductances within each of the branches of a simplified schematic of the SQUID. Furthermore, mutual inductances could play a role. For a precise determination of these properties, numerical field calculations are indispensable [157–160].

We used the numerical inductance calculation software *Fasthenry* [161] with an extension that includes the London equations. It can therefore model superconductors [160]. We did not include the complete SQUID design in these calculations but used it to determine the inductance on simplified test structures. The slit inductance was for example usually determined to about $L_{SL}{}' \approx 0.4$ to 0.5 pH/µm, depending on the width of the washer $w$ and possibly located return paths of the coil within the slit, see Fig. 3.7 on page 61. We also used Fasthenry to estimate the inductances of interconnections between washers or the parasitic inductances of connected damping resistors.

The radio frequency (RF) properties of washer structures are of special importance because of their direct influence on the SQUID dynamics, see section 3.3 on page 60. The modeling process of a washer with integrated coil was summarized in section 3.3.1 on page 62, which is based on the work of Enpuku et al. [82]. The RF properties can be determined numerically using the parameters of the coil microstrip line $L'_{ST}$ and $C'_{ST}$, the length of each of the windings of the coil, the slit inductance $L_{SL}$ and the hole inductance of the washer $L_H$.

Naturally, it is interesting to numerically study the behavior of a SQUID model extracted from the layout. A simulation of a SQUID including the complete model of the washer structure, see Fig. 3.7(b) on page 61, is possible [84]. We used the software JSIM, see section 3.1 on page 43, which also includes the model of a lossless transmission line. Accordingly, the behavior of every single winding of integrated coils could be included in the simulation. Because of our many-turn SQUID designs, this would increase the complexity of the simulation significantly. Therefore, we fitted the impedance $\bar{Z}_W$ of each of the washers of the SQUID designs to a simplified model as shown in Fig. 3.7(c). On the one hand, this simplified model does not include harmonics of the two fundamental resonances, the *coil resonance* and the *washer resonance*. Furthermore, the influence of a connected input circuit cannot be modeled accurately. On the other hand, it is able to fit the resonance frequencies and the most important property, the effective inductance $L_{W,RF}$ above the coil resonance.

## 5.3 Experimental techniques

The experiments shown throughout this chapter were partly performed using our own facilities at the University of Twente. The measurements at sub-Kelvin bath temperatures were done at the Kamerlingh Onnes Laboratory at Leiden University, in collaboration with the MiniGRAIL team.

We used a variety of SQUID electronics. Besides self developed electronics from the University of Twente with an equivalent input voltage noise with an amplitude spectral density of $\approx 1.9$ nV/$\sqrt{\text{Hz}}$, we also employed commercially available SQUID electronics from *Star Cryoelectronics* [162] and *Supracon* [152] with an input voltage noise of $\approx 1.8$ nV/$\sqrt{\text{Hz}}$ and $\approx 0.4$ nV/$\sqrt{\text{Hz}}$, respectively. Naturally, all of the electronics allow the direct readout of the

SQUID sensor. All of them also include a *flux-locked loop* (FLL) setup as shown in Fig. 1.7 on page 15.

Such typical values of the input voltage noise of room temperature electronics would degrade the sensitivity of the SQUID in direct readout, especially for the minimum temperature experiments, see Eqn. (1.31) on page 14. Therefore, we employed a two-stage SQUID setup, see Fig. 1.6(b) on page 14. We typically used an amplifier SQUID with a relatively high mutual inductance $M_2$, and a low bias resistance $R_B$ compared to the output resistance of the first stage SQUID $G_{VI,1\mathrm{st}}$. The resulting high gain originating from the additional amplifier stage $G_{V1,V2}$, see Eqn. (1.32) on page 14, allows the elimination of the noise of the room temperature electronics. On the downside, this typically leads to multiple modulations of the second stage SQUID. This kind of operation is not recommended in a long-term measurement because on the one hand, multiple locking points are possible, and on the other hand, the linear flux-range is reduced. This leads to problems in applications where a high slew-rate [88] is required. Nevertheless, for research on the minimum noise parameters of a given SQUID, it is suitable. One can characterize a large variety of working points, also at low flux-to-voltage transfer $G_{V\Phi,1\mathrm{st}}$. As a practical note we want to point out that it is important to adapt the bandwidth of the FLL to the maximum stable bandwidth [88], see Eqn. (1.35) on page 15 and the subsequent discussion. For working points with high values of $G_{V1,V2}\,G_{V\Phi,1\mathrm{st}}$, one has to lower the gain of the amplifier $G_{AMP}$ or increase the time constant of the integrator $\tau_I$ for example.

For a low noise operation, the SQUID has to be shielded against external interferences. During all the measurements shown here, the SQUIDs were situated within a *Nb* module in combination with an additional ferromagnetic shield. In the electrical connections to the SQUID, passive resistive, inductive and capacitive filter networks were placed. These filter elements were partially situated in the cryogenic environment. To achieve a high bandwidth in FLL operation, see section 1.4.2 on page 13, a more modest filtering has to be used on the readout voltage and feedback lines.

## 5.4 Results from our first designs

### 5.4.1 Overview of the design process

For our first SQUID designs, we joined a fabrication run with a critical current density of $J_0 = 110\ \mathrm{A/cm^2}$. This leads to $I_0 = 11.3\ \mu\mathrm{A}$ for the minimum-sized Josephson junction.

The main optimization criteria were, due to the intended application in MiniGRAIL, a nominal input inductance $L_{IN} = 1.6\ \mu\mathrm{H}$ with the lowest possible energy resolution $\varepsilon_{VV}$, see Eqn. (1.20) on page 11. This design policy was changed during the second design step. According to the analysis presented in chapter 2, the *coupled energy resolution* $\varepsilon_{VV}/k^2 = S_{\Phi,VV}\,L_{IN}/(2M^2)$ is the most important parameter for a low noise operation in most applications. In the case of the readout of the capacitive transducers of MiniGRAIL, a low coupled energy resolution $\varepsilon_{VV}/k^2$ leads to a larger bandwidth around the electrical resonance frequency, see sections 1.5 and 2.5.3 on pages 16 and 34.

The optimization was based on the one hand on the standard formulas for the inductances, see Eqns. (3.15)–(3.20) on page 61. On the other hand, we relied on the standard SQUID approximation, see Eqn. (1.24) on page 11. To avoid hysteresis in the Josephson junctions, we

chose $\beta_C \leq 0.7$. We were well aware that there are resonances in the coil structures. Therefore we calculated the corresponding fundamental resonances and shifted the intended Josephson frequency far away from these resonances. We therefore used the usually given rule-of thumb [116] for this type of sensors, see Eqn. (3.28) on page 72. Compared to Eqn. (3.28) we did not use the safety factor of 4. We believe that the washer resonance frequency can be determined quite well and therefore, we decided to choose a more advantageous factor of 2 instead. The implications will be discussed at the end of this section.

We added a damping resistance $R_D$ of the size of the shunt resistance of the Josephson junction $R_D = R$ in parallel to the SQUID inductance. This might help to damp resonant states within the SQUID design [106], see the discussion in section 3.3.4 on page 71.

Because of the intended operation in the sub-Kelvin temperature range, the additional *Au* layer for the cooling fins was included in the fabrication process. All shunt resistors of our SQUIDs were extended with a cooling fin to reduce the hot-electron effect. The measurements presented in chapter 4 were performed on test-structures that were also located on the same wafers as our first SQUID designs.

### 5.4.2 SQUID with an integrated flux transformer

One design approach for SQUIDs with a high input inductance is the SQUID with an integrated flux transformer [111, 117]. A photograph of a fabricated device as well as a simplified schematic are shown in Fig. 5.1.

The reason for choosing this layout is the large difference between the SQUID inductance and the input inductance. The SQUID inductance $L_{SQ}$ with $\beta_L = 1$ would be $\approx 90$ pH with the given critical current. This is about four orders of magnitude below the intended input inductance of $L_{IN} \approx 1.5$ µH. A direct integration of the large required number of windings on a single-washer SQUID while maintaining the given values of the inductances $L_{SQ}$ and

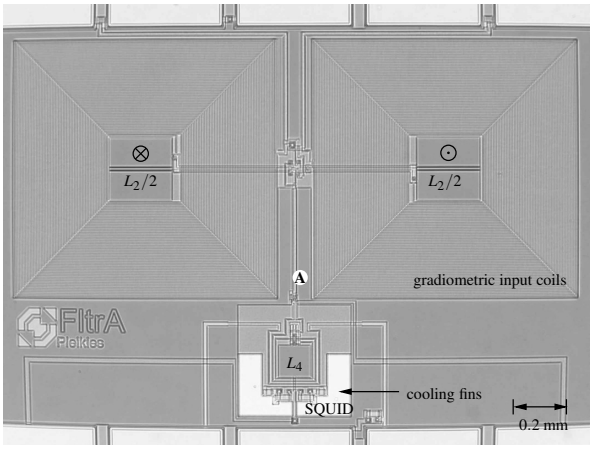


(a)

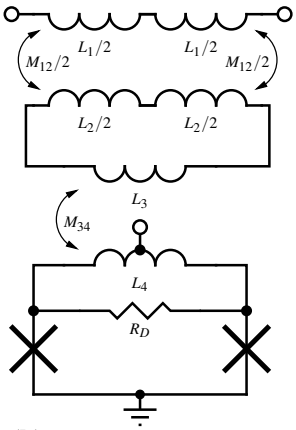


(b)

**Figure 5.1:** **(a)** Photograph of the SQUID with integrated flux transformer. **(b)** Simplified schematic for low frequencies. The transformer loop $L_2$-$L_3$ is on one side coupled to the gradiometric input coil $L_1$ with $N = 60$ turns each. On the other side it is coupled to a SQUID with inductance $L_4$. A feedback line which directly couples to the SQUID inductance $L_4$ is not shown for simplicity.

$L_{IN}$ is not possible with the given technology. This discrepancy can be overcome by using a double transformer as shown in Fig. 5.1(b). The disadvantage of this design is that in practice one ends up with a lowered total coupling efficiency $k^2 \lesssim 0.5$ [117].

Naturally, the effective inductances are altered by the intermediate loop containing $L_2$ and $L_3$. For the configuration as shown in Fig. 5.1(b), the effective low-frequency parameters of the SQUID inductance, input inductance and mutual inductance are given by [111]:

$$L_{SQ} = L_4 - \frac{{M_{34}}^2}{L_2 + L_3} \tag{5.1}$$

$$L_{IN} = L_1 - \frac{{M_{12}}^2}{L_2 + L_3} \tag{5.2}$$

$$M = \frac{M_{12}\, M_{34}}{L_2 + L_3} \tag{5.3}$$

To reduce interference of external signals, we chose for a gradiometric configuration of the pickup inductances $L_1$ and $L_2$. A detailed description of the design will be given below.

### First experimental results

Our first experimental results on this SQUID design [36] were performed in Leiden University. The measurements were performed in a dilution refrigerator using the electronics from *Star Cryoelectronics*. In Fig. 5.2, we show experimental flux–voltage characteristics obtained at two different bath temperatures $T_B = 4.2$ to 0.3 K.

As one can see by comparing the two graphs, the (apparent) flux-to-voltage transfer $G_{V\Phi}$ is getting very high. We estimated values of up to $\approx 800\ \mu V/\Phi_0$ at the lower bath temperature and critical current. This is about an order of magnitude higher than values from the standard approximation formula, see Eqn. (1.27) on page 11.

Measurements on the additional flux noise $\sqrt{S_{\Phi,VV}}$ in a two-stage setup showed a value of 1.4 $\mu\Phi_0/\sqrt{\text{Hz}}$ at a bath temperature of $T_B = 4.2$ K and operation voltages of $\approx 10$ to 20 μV.

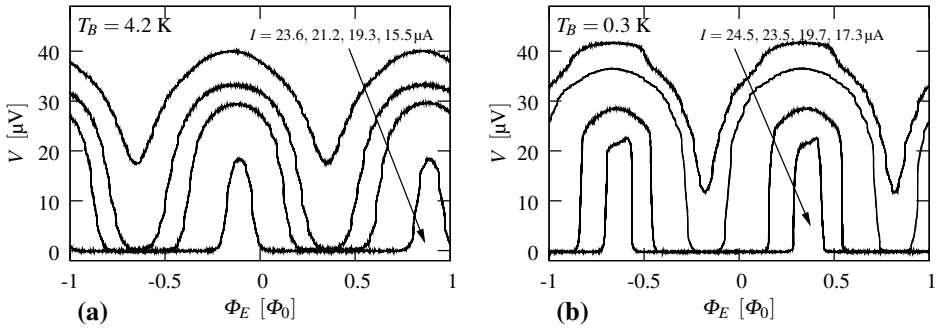


**Figure 5.2:** First experimental examination of the characteristics of the SQUID with integrated flux transformer. We show flux–voltage characteristics with varying bias current $I$ and bath temperature **(a)** $T_B = 4.2$ K and **(b)** $T_B = 0.3$ K. The arrows cross the characteristics with varying bias current $I$ in the indicated order. The input coil was shunted with a series resistance-capacitance element ($30\,\Omega - 1$ nF). The flux axis was determined from the measured current through the feedback line with a fitted mutual inductance $M_{FB,SQ} = 104$ pH. The external flux $\Phi_E$ is shifted by constant magnetic fields that are present in the setup.

Beforehand, the noise was optimized by connecting a series resistance-capacitance element ($30\,\Omega - 1\,\mathrm{nF}$) in parallel to the input coil [112]. At lower bath temperatures, no considerable improvement of the flux noise was found at this bias point. This unusual SQUID behavior was unexpected, so we turned our attention to a more detailed modeling and numerical simulations of the designs [36]. This decision led to the work presented in chapter 3.

### Model of the SQUID

It turned out that the most important property of the SQUID structure is given by the impedance of the washer with the long integrated coil, as depicted in Fig. 5.3(a). Here, one can see the calculated impedance [82] of the pickup washer $L_2/2$ in Fig. 5.1(b). See section 3.3.1 on page 62 for more details on the calculation. The dimension of the square hole of the washer is 235 µm. Accordingly, the hole inductance is 370 pH, see Eqn. (3.15) on page 61. The slit inductance of the covered parts of the washer with a length of 370 µm was estimated to 140 pH. The input coil inductance $L_1$ of the two gradiometric coils in series and their mutual inductance $M_{12}$ were estimated with Eqns. (3.17)–(3.18), see page 61, to 3.1 µH and 53 nH, respectively.

As pointed out in section 3.3.1 on page 62, there are two fundamental resonances. The *coil resonance*, see marker Ⓑ in Fig. 5.3, is located far below typical Josephson frequencies of the SQUID, see the upper axis in Fig. 5.3(a). This is caused by the large total length of the 60 windings of about 0.15 m. The *washer resonance* frequency is close to the expected value of 18 GHz from Eqn. (3.23), see page 63.

To allow a numerical simulation of this configuration, we fitted the impedance of this washer with the lumped circuit element model, see the dashed line in Fig. 5.3(a). In the total model shown in Fig. 5.3(b), the two fitted networks corresponding to the resonances are again marked with Ⓑ and Ⓒ. A residual inductance above the two fundamental resonances

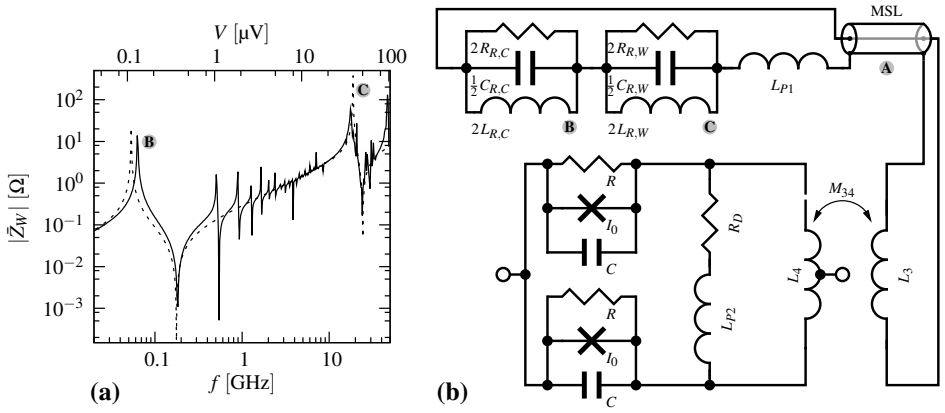


**Figure 5.3: (a)** Impedance of the washer, $L_2/2$ in Fig. 5.1, with the floating and open integrated coil $L_1/2$. Complete model calculation (solid) and fitted lumped circuit model (dotted) with a high quality factor $Q = 1000$. The fitted elements are Ⓑ $L_{R,C} = 470$ pH, $C_{R,C} = 19$ nF and Ⓒ $L_{R,W} = 19$ pH, $C_{R,W} = 3.8$ pF. The upper axis shows the corresponding voltage. **(b)** Model of the SQUID with coupled transformer. Noise sources are not shown for simplicity, they are attached to $R_D$ and the two resistances $R$. The quality factor of the two resonances was set to $Q_{R,C} = R_{R,C}\sqrt{C_{R,C}/L_{R,C}} = 1$ and $Q_{R,W} = R_{R,W}\sqrt{C_{R,W}/L_{R,W}} = 1000$. See the text for details.

is included in $L_{P1}$. Furthermore, $L_{P1}$ also includes the parasitic inductance 50 pH caused by the connecting leads between the two gradiometric washers. This value was estimated using simplified test structures in Fasthenry [160].

The connection of the SQUID and the two gradiometric washers was done in form of a 10 µm wide and 390 µm long microstrip line, see the transmission line marked with Ⓐ in Figs. 5.1(a) and 5.3(b). Its total inductance and capacitance were estimated [108] to 37 pH and 0.36 pF, respectively. The coupling coil to the SQUID has only two windings, the estimated coil inductance is at a frequency higher than the washer resonance frequency of the big coupling washer in the transformer loop. For simplicity, we ignored its influence and modeled the pure inductive behavior only.

The dimension of the square hole in the SQUID washer is 120 µm. Including the estimated parasitic inductances of the slit and the Josephson junctions, the calculated inductance of the uncoupled SQUID $L_4$ is 250 pH. The mutual inductance was calculated to $M_{34} = 400$ pH and the inductance of the coupling coil $L_3$ with two windings to 1010 pH. A parasitic inductance in series with the damping resistor was estimated to $L_{P2} = 60$ pH which is caused by the connecting microstrip line crossing the slit.

All the just mentioned elements have an influence on the corresponding inductances of the total SQUID at low frequencies, see Eqns. (5.1)–(5.3). The resulting properties as well as some important SQUID parameters are summarized in Table 5.1. The value $\beta_{L,RF}$ represents the effective screening parameter above the coil resonance. Furthermore, we show measured data obtained during our first experimental investigation presented above. The measured data for $R$, $I_0$ and $M$ are close to the design values.

**Experimental verification of hysteresis caused by an integrated input coil**

Because of the coil resonance, see marker Ⓑ in Fig. 5.3, the screening parameter is changing from $\beta_L \approx 1.8$ at low frequencies to effectively $\beta_{L,RF} \approx 1.1$ in the voltage state, see Table 5.1. According to the results of section 3.3.2 on page 63, this leads to a *voltage hysteresis*. Because of the relatively small change in inductance, the *flux hysteresis* is not present in this system or any other SQUID presented in this chapter.

During the measurements on the hot-electron effect presented in chapter 4, we used a SQUID of this design as the amplifier for the noise thermometry. The measurements were performed in direct readout and therefore we could specifically search for the phenomenon. In this case, we used the *Supracon* electronics [152].

Figure 5.4(a) depicts the re-examined flux–voltage characteristics which indeed showed a hysteretic behavior. This only became visible at this low bath temperature $T_B = 0.1$ K ($\Gamma = 0.0004$). Note that here, the effective electron temperature is strongly dependent on the

**Table 5.1:** Design and experimental values of the SQUID with integrated flux transformer.

| | $I_0$ [µA] | $R$ [Ω] | $L_{SQ}$ [pH] | $L_{IN}$ [µH] | $M$ [nH] | $k^2$ | $\beta_L$ | $\beta_{L,RF}$ | $C$ [pF] | $\beta_C$ |
|---|---|---|---|---|---|---|---|---|---|---|
| design | 11.3 | 5.7 | 170 | 1.8 | 10 | 0.3 | 1.8 | 1.1 | 0.6 | 0.7 |
| measurement | 12 | 5.0 | | | 8.7 | | 1.9[a] | 1.2[a] | | 0.6[a] |

[a] using the design values of $L_{SQ}$ or $C$

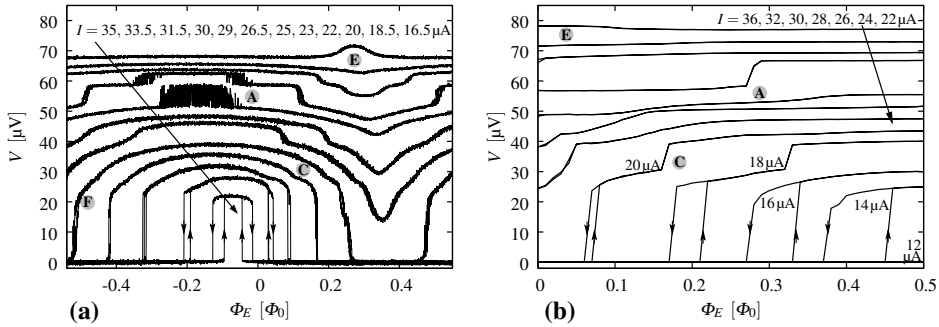


**Figure 5.4:** **(a)** Experimental re-examination of the characteristics of the SQUID with integrated flux transformer at $T_B = 0.1$ K. We show flux–voltage characteristics with varying bias current. Hysteretic transitions are indicated with arrows. The input coil was shunted with a series resistance-capacitance element ($50\,\Omega - 1\,\mathrm{nF}$) as well as the resistor and capacitor as shown in Fig. 4.3 on page 92. **(b)** Numerical simulation of the model shown in Fig. 5.3 at $T = 0.1$ K. The capacitive and inductive properties as given above were used. The experimental $R$ and $I_0$ from Table 5.1 were applied. The quality factors of the two fundamental resonances were set to $Q_{R,C} = 1$ and $Q_{R,W} = 1000$.

state of the SQUID. In the superconducting state it equals the bath temperature $T_B$, whereas in the voltage state it is considerably increased due to the hot-electron effect, see chapter 4.

During the measurement, we changed the external flux via the feedback coil. The frequency of this sweep was in the kHz range. The wideband noise had to be reduced by means of a low-pass filter. The characteristic for each bias current shown in Fig. 5.4(a) was obtained by a whole period of one single sweep of the external flux. Accordingly, the flux is varied in two directions. The transition from superconducting state to the voltage state and back follows the paths as indicated by arrows in Fig. 5.4(a), independent on which slope the preceding transition took place. Also note that the hysteresis is not an artefact originating from a delay of the low-pass filter.

We are not sure why we did not observe the hysteresis during the first measurement, see Fig. 5.2(b). One reason could be the three times lower bath temperature. Furthermore, there could also be an external interference from the lab environment which caused a permanent random switching. It could also be an effect related to the changed readout electronics.

The observed behavior fits the expectations from the results shown in section 3.3.2, especially see Fig. 3.10 on page 66. Once the still superconducting SQUID reaches the critical current, which is dependent on $\beta_L$, it switches to the voltage state. The dynamics in the voltage state are determined by the model of a *reduced SQUID* with the reduced SQUID inductance $L_{SQ,RF}$ and the reduced screening parameter $\beta_{L,RF}$. The point of switching back to the superconducting state is determined as presented in section 3.3.2. Naturally, thermal noise or external interferences can cause a transition between the two states.

This effect was observed in a number of numerical simulations on SQUIDs with parasitic capacitances [78–80, 109, 110], but to our knowledge this is the first experimental observation of such a behavior. As one can see from the results of chapter 3, see especially section 3.3.4 on page 71, this hysteresis cannot be avoided if one needs a SQUID with a comparably large input inductance and a high coupling efficiency $k^2$. Note that although the coil resonance frequency occurs at a corresponding voltage of $V \approx 0.1$ µV, see marker Ⓑ in Fig. 5.3, it still affects the whole voltage range up to $V \approx 20$ µV.

In Fig. 5.4(b), we show a numerical simulation on the model of the SQUID with integrated flux transformer, see Fig. 5.3(b). The simulated characteristics show a very similar hysteretic behavior. The simulation was done similar to the ones shown in Fig. 3.10 on page 66. Each working point was simulated two times, once the SQUID was brought into the working point from the superconducting state and once it was beforehand put in the voltage state. The voltage was low-pass filtered with a corner frequency of 100 MHz and the shown mean voltage was determined by integrating over in total 0.1 µs. The quality factor of the coil resonance $Q_{R,C}$ was reduced in the simulation to suppress initial transients.

Besides the hysteresis, there are other features in the characteristics that might have been identified. In the voltage range 30 to 40 µV one can see a large voltage step in the simulation, see marker Ⓒ in Fig. 5.4(b). This is caused by the washer resonance, see marker Ⓒ in Fig. 5.3(a). In the measurement, see Fig. 5.4(a), the characteristics also show an irregularity at about the same voltage region. Here, the influence seems to be much smaller. This discrepancy could be explained by a much smaller quality factor $Q_{W,R} \ll 1000$ of the resonance in the real device because of dissipative elements in the microstrip line of the coil at such high frequencies.

In the voltage region 50 to 70 µV both the simulation and the measurement show strong irregularities, see marker Ⓐ in Fig. 5.4. Here, the capacitance of the microstrip line marked with Ⓐ in Figs. 5.1(a) and 5.3(b) is resonating with the residual inductances of the coupled transformer loop. Furthermore, the coil resonance of the two-winding coupling coil to the SQUID is situated in the same voltage region. This is not included in the model, but should also have an influence on the experimental characteristics.

The voltage range of the resonance between the capacitance of the Josephson junctions and the residual SQUID inductance, see marker Ⓔ in Fig. 5.4, does not fit very well. This indicates that there are still uncertainties in the model.

The marker Ⓕ in Fig. 5.4(a), indicates the working range we typically used for the measurements shown in chapter 4 or later performed two-stage measurements where this SQUID was used as an amplifier SQUID.

### 5.4.3 The first SQUID with a parallel washer configuration

During the first run we added another design, the SQUID with a parallel washer configuration. It is an adaption of a layout especially created for a reduced mutual inductance between the feedback and the signal coil systems $M_{FB,SQ}$ [163]. According to the discussion in section 2.5.3, see page 37, this decreases problems with stability of the SQUID operated in FLL with a capacitive input circuit. Sensors based on this layout were investigated in detail, see for example references [27, 156, 164]. A coupled energy resolution of $\varepsilon_{VV} = 52\,\hbar$ was reached for a sensor with an input inductance $L_{IN}$ of 1.6 µH [156]. For this design, also the minimum reachable noise temperature, represented by $\varepsilon_0$, was determined. By coupling the sensor to a high quality factor capacitive input circuit, see section 2.5.3 on page 34, and measuring the back-action noise of the SQUID, $\varepsilon_0$ was estimated to 27 $\hbar$ [156].

In Fig. 5.5(a), one can see a photograph of our first adaption of the same basic layout. The design consists of four washers, two with an integrated feedback coil and two with an integrated signal coil. Each of the coils is in a gradiometric configuration to its counterpart. The balanced layout of the washers reduces the parasitic mutual inductance $M_{FB,SQ}$ to nominally zero [163]. As one can see from the simplified schematic in Fig. 5.5(b), one

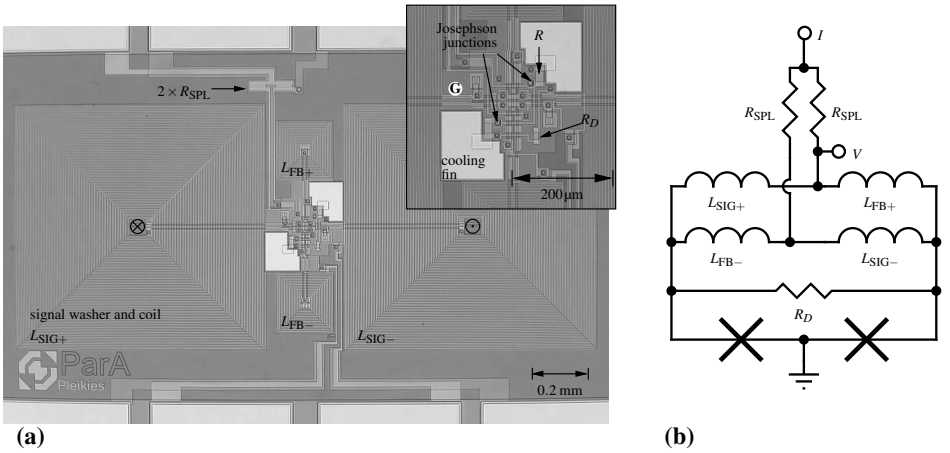


**Figure 5.5: (a)** Photograph of the first SQUID with a parallel washer configuration. The inset shows a magnification of the middle part. **(b)** Simplified schematic for low frequencies. The four gradiometric coupling coils are not shown for simplicity.

feedback and one signal washer are connected in series. The two gradiometric branches are then connected in parallel to the Josephson junctions. The bias current is symmetrically fed into the SQUID via two resistor $R_{\mathrm{SPL}}$ that are integrated on the chip. This is in difference to the original design, where this symmetrical splitting typically has to be done on an external printed circuit board. We also added a contact that allows a direct readout of the SQUID voltage $V$ without a constant offset $\frac{1}{2} R_{\mathrm{SPL}} I$ caused by the bias current.

Because of the parallel connection of the two identical branches, the effective SQUID inductance is $L_{SQ} = \frac{1}{2}(L_{\mathrm{SIG}} + L_{\mathrm{FB}})$. The two coupling coils $L_{IN,\mathrm{SIG}}$, which are not shown in Fig. 5.5(b), are connected in series. Accordingly, the effective input inductance of the design reads $L_{IN} = 2 L_{IN,\mathrm{SIG}}$. The effective mutual inductance is the value of a single washer $M = M_{SIG}$.

In contrast to the original design, we implemented the series connection of the two signal coils and the two feedback coils on-chip. This can be seen in the magnified photograph of the middle part of the chip shown in Fig. 5.5(a). Also in this design we attached cooling fins to the shunt resistors and added a resistive shunt $R_D = R$ across the effective SQUID inductance to damp possible resonant states.

### Model of the SQUID

In analogy to the behavior of the SQUID with integrated flux transformer, we observed unexpected effects during the measurement [36]. This will be shown below. Accordingly, we also re-examined the layout of this SQUID to create a more detailed model. Again we calculated the radio frequency impedance of the two integrated washers. The result is shown in Fig. 5.6(a). We show the direct calculation of the signal washer with the integrated coil (solid line) as well as the fitted impedance (dotted line). The series connection of the fitted impedances of the feedback and the signal washer are shown as a dashed line.

The coil integrated on the signal washer consists of 70 windings around the square hole of 60 µm dimension. The total length of the coil was estimated to 0.14 m. Accordingly, the

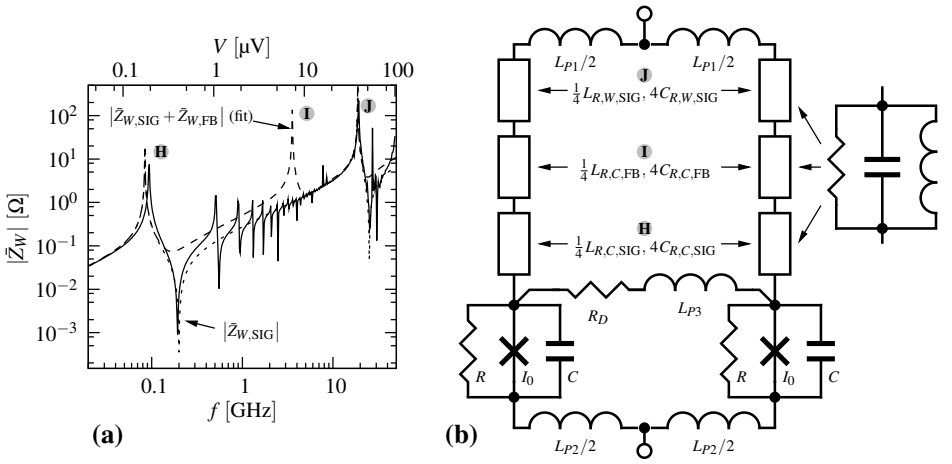


**Figure 5.6: (a)** Impedance of the signal and the feedback washer with the floating and open integrated coil. Complete model calculation for the signal washer (solid), its fitted lumped circuit model (dotted) and the fitted series impedance of both washers (dashed) with a high quality factor $Q = 1000$. The fitted elements are Ⓗ $L_{R,C,\mathrm{SIG}} = 210$ pH, $C_{R,C,\mathrm{SIG}} = 17$ nF, Ⓙ $L_{R,W,\mathrm{SIG}} = 20$ pH, $C_{R,W,\mathrm{SIG}} = 3.6$ pF and Ⓘ $L_{R,C,\mathrm{FB}} = 40$ pH, $C_{R,C,\mathrm{FB}} = 50$ pF. The residual inductance of both washers above the resonances was fit to 50 pH. The upper axis shows the corresponding voltage. **(b)** Model of the SQUID. The factor of $\frac{1}{4}$ of the fitted washer inductance accounts for the parallel connection of two identical branches with one signal and one feedback washer connected in parallel, see Fig. 5.5(b), and for the balanced distribution over the two branches of the SQUID in the model. Noise sources are not shown for simplicity, they are attached to $R_D$ and the two resistances $R$. The bias splitting network was neglected for simplicity. The quality factor $Q_R = R_R\sqrt{C_R/L_R}$ of the three resonances was set to 1 (Ⓗ), 1000 (Ⓘ) and 1000 (Ⓙ), respectively. See the text for details.

coil resonance frequency of the signal washer, marked with Ⓗ in Fig. 5.6(a), is located at very low frequencies compared to the Josephson frequency of the SQUID. The estimated slit inductance $L_{SL}$ of this washer was determined to 165 pH.

The feedback washer has an integrated coil consisting of 15 windings around a small hole. The effective low frequency inductance was estimated to $L_H + L_{SL} = 16$ pH $+ 49$ pH. The coil resonance frequency of this configuration was estimated to be at a corresponding voltage of 8 μV, see marker Ⓘ in Fig. 5.6.

To create a simplified model including all these resonances, we assumed that the effective impedance of the SQUID consists of the parallel connection of two identical branches, see Fig. 5.5(b), each of them consisting of a series connection of one feedback and one signal washer. The impedance of this series connection is shown as a dashed line in Fig. 5.6(a). The parallel connection of the two identical branches is now incorporated into a SQUID model, see Fig. 5.6(b). Here, the bias splitting resistors $R_{\mathrm{SPL}}$ with a design value of 0.5 Ω have been neglected. As pointed out before, this is not expected to influence the dynamics of the SQUID because of the high estimated parasitic inductance of 0.3 nH of this branch.

The parasitic inductance $L_{P1} = 85$ pH shown in Fig. 5.6(b) accounts on the one hand for the residual washer inductance of $\frac{1}{2}$ 50 pH above all resonances Ⓗ, Ⓘ and Ⓙ of both washers. On the other hand, it also accounts for the estimated parasitic inductance 60 pH originating from the connecting parts in the middle of the chip. This is caused by the inductance of the slit containing the two connecting wires of the coils.

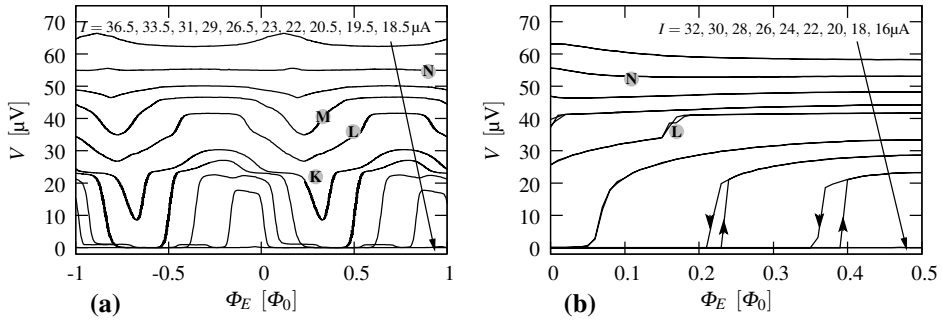


**Figure 5.7: (a)** Experimental characteristics of the SQUID with a parallel washer configuration at a bath temperature $T_B = 0.6$ K. We show flux–voltage characteristics with varying bias current. The input coil was shunted with a series resistance-capacitance element ($50\,\Omega - 1\,\mathrm{nF}$). **(b)** Numerical simulation of the model shown in Fig. 5.6 at $T = 0.6$ K. Hysteretic transitions are indicated with arrows. The capacitive and inductive properties as given in the text and Fig. 5.6 as well as the experimental $R$ and $I_0$ from Table 5.2 were used.

Furthermore, we estimated two parasitic inductances $L_{P2} = 50$ pH and $L_{P3} = 50$ pH accounting for the inductance of microstrip lines connecting the Josephson junctions as well as the damping resistor $R_D = R$ in the middle of the SQUID, see Fig. 5.5(a). This includes parasitic inductances of the crossing of these microstrip lines over the two triple-slit structures in the middle of the design.

The effective SQUID parameters according to this model are given in Table 5.2. The screening parameter $\beta_L$ takes a quite high value of 2.9 in this case. This is caused by the relatively high critical current density for a design with such a high input inductance $L_{IN}$ of the SQUID. We also give a value for the effective screening parameter at the Josephson frequency $\beta_{L,RF}$ above the two coil resonances, between marker Ⓘ and Ⓙ in Fig. 5.6(a).

### Experimental characteristics

In Fig. 5.7(a) we show the measured flux–voltage characteristics of the parallel washer with a parallel washer configuration. The measurements were done using *Star Cryoelectronics* [162] electronics. The bath temperature $T_B = 0.6$ K was reached by a dilution refrigerator. The voltage was measured using the connector $V$ in Fig. 5.5(b). In Table 5.2 we show experimental values for $R$ and $I_0$, determined from the current–voltage characteristics, and $M$, determined from the direct modulation via the input coil. The agreement is good.

In Fig. 5.7(b) we show a simulation of the model presented above, see Fig. 5.6(b). This simulation was done at the same temperature. Again, each working point was calculated

**Table 5.2:** Design and experimental values of the first SQUID in a parallel washer configuration.

| | $I_0$ [µA] | $R$ [Ω] | $L_{SQ}$ [pH] | $L_{IN}$ [µH] | $M$ [nH] | $k^2$ | $\beta_L$ | $\beta_{L,RF}$ | $C$ [pF] | $\beta_C$ |
|---|---|---|---|---|---|---|---|---|---|---|
| design | 11.3 | 5.6 | 270 | 1.5 | 12.4 | 0.4 | 2.9 | 1.6 | 0.6 | 0.65 |
| measurement | 11 | 4.9 | | | 11.2 | | 2.8[a] | 1.6[a] | | 0.5[a] |

[a] using the design values of $L_{SQ}$ or $C$

two times with a different initial state. Once, we started from the superconducting state and once from the voltage state before sweeping to the working point. The voltage was low-pass filtered with a corner frequency of 300 MHz and the shown mean voltage was determined by integrating over in total 1 µs.

During this measurement, we did not see the hysteresis, although it appears in the simulation. The characterization was done in the same setup as the first experimental investigation of the characteristics of the SQUID with integrated flux transformer, see section 5.4.2. Possible explanations are external interferences which lead to a random switching of the hysteretic state or effects in the SQUID electronics. We did not re-investigate the hysteretic behavior of this SQUID closer at such low temperatures. Nevertheless, we are sure that also in this case the hysteresis is present in the lower voltage range. Compared to the measurements at higher temperatures, the characteristics again became very steep. Also during the sensitivity measurements, no low noise working points were found in this range.

At voltages of about 25 µV there is a strong irregularity in the characteristics, see marker Ⓚ in Fig. 5.7. This effect is not present in the simulation. One possible explanation is that here a harmonic of the coil resonance of the feedback washer is excited, see marker Ⓘ in Fig. 5.6(a). In the simulation, its fundamental resonance cannot be seen because it is located within the hysteretic working range. Another explanation would be that the determined coil resonance frequency is wrong. Nevertheless, the most plausible explanation is a cross-talk between the washers. In this design, we tried to reduce the inductance by covering the slits of the connecting parts of the washers with small strips in the upper *Nb* layer, see marker Ⓖ in Fig. 5.5(a).

The washer resonance of the signal washer leads again to very strong distortions in the simulated characteristics, see marker Ⓛ in Fig. 5.7(b). This is caused by the high quality factor of 1000. In the measurement, one can see much smaller irregularities in the range of 30 to 40 µV, which we address to the washer resonance of the signal washer. In accordance to the SQUID shown in the last section, the quality factor of this resonance could be reduced in the real device. Such irregularities are hard to spot in the characteristics, but also the measured sensitivity was degraded in this voltage range.

The point of the resonance between the residual SQUID inductance and the capacitance of the Josephson junctions is in good agreement between the measurement and the simulation, see marker Ⓝ in Fig. 5.7.

**Experimentally reached sensitivity**

To determine the sensitivity, we used a two-stage setup, see Fig. 1.6(b) on page 14. As the second stage SQUID, we used the SQUID with integrated flux transformer presented above. Because of the relatively large mutual inductance $M = 8.7$ nH of the second stage SQUID, we had to use another filter inductance in series with the input coil of the second stage. We used the connector *I* in Fig. 5.5(b) and a bias resistor $R_B$ of 0.5 Ω. The two-stage SQUID setup was put in a shielding *Nb* module within the mixing chamber of the dilution refrigerator.

The general performance was similar to the SQUID with integrated flux transformer. First we optimized the noise of the SQUID in the lower voltage range at a temperature of 4.2 K by means of damping elements attached to the input coil. After cooling down, it again turned out that the noise behavior was of non-thermal origin. Some low noise points could

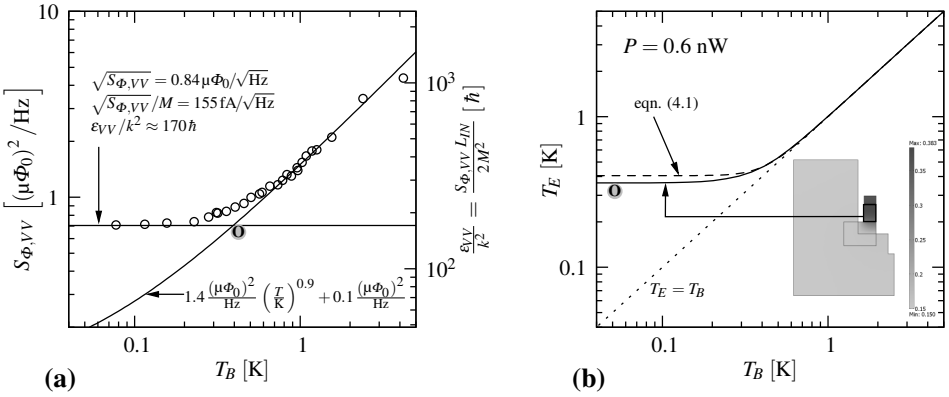


**Figure 5.8: (a)** Measured flux noise of the SQUID with a parallel washer configuration with changing bath temperature. The working point was close to marker Ⓜ in Fig. 5.7(a). The input coil was shunted with a series resistance-capacitance element ($50\,\Omega - 1\,\mathrm{nF}$). The minimum noise and a fitting curve of the data between 800 mK and 3 K are shown as indicated. The axis with the coupled energy resolution $\varepsilon_{VV}/k^2$ was calculated with the experimental value of $M$ and the design value of $L_{IN}$, see Table 5.2. **(b)** Determined effective electron temperature $T_E$ versus the bath temperature $T_B$ in the shunt resistor for a power dissipation $P$=0.6 nW. This was determined by a FEM calculation (solid line). The data from Table 4.1 on page 91 as well as the layout of the shunt resistor were used. The dashed line shows a direct calculation with Eqn. (4.1) on page 84 using $p = 5$ and the area of the resistor between the *Nb* contact pads of $21 \times 15\ \mu\mathrm{m}^2$.

partly not even be operated in FLL after lowering the temperature. We now know that we tried to measure the noise in the hysteretic regime of the characteristics.

Nevertheless, in the case of the SQUID with a parallel washer configuration, we found a stable working point in the region of the characteristics marked with Ⓜ in Fig. 5.7(a). In Fig. 5.8, we show the measured flux noise at this working point. Each of the points was taken by first stabilizing the bath temperature and then measuring the white flux noise above 1 kHz in FLL operation. The bath temperature was determined similar to the experiments presented in chapter 4. By switching off the first stage SQUID, one can determine the Nyquist noise of the resistors $\frac{1}{2}R_{\mathrm{SPL}} + R_B$ in the input loop of the second stage SQUID. This noise was, similar to the experiments shown in chapter 4, used to determine the temperature in the SQUID module. Note that we found one more stable working point at even higher voltages, but here the sensitivity was slightly worse.

As the fit indicates, the noise scaled almost linearly in a temperature regime down to a bath temperature of $\approx 0.6$ K. For an unknown reason, this fit does not scale perfectly to the highest bath temperature of 4.2 K. Here, a flux noise of 2.1 $\mu\Phi_0/\sqrt{\mathrm{Hz}}$ was measured. Furthermore, the fit indicates a comparably small excess noise. One possible explanation for this is the input noise of the room temperature electronics, which we estimated to be in this range. The typically achieved gain $G_{V1,V2}$ of the two-stage setup, see Eqn. (1.32) on page 14, was in the order of 20.

Below bath temperatures $T_B$ of 0.2 K, the noise of the SQUID did not improve further. Here, the measured flux noise was 0.84 $\mu\Phi_0/\sqrt{\mathrm{Hz}}$. This corresponds to an equivalent input noise current of $\sqrt{S_{\Phi,VV}}/M = 155$ fA$/\sqrt{\mathrm{Hz}}$. Using the experimental value of $M$ and the design value of $L_{IN}$, see Table 5.2, the coupled energy resolution $\varepsilon_{VV}/k^2$ reads 170 $\hbar$.

The minimum effective temperature $T_E \approx 0.4$ K is determined as indicated with marker Ⓞ in Fig. 5.8(a). This crossover temperature coincides with the determined minimum effective electron temperature in Fig. 5.8(b). Here, we calculated the influence of the hot-electron effect on the temperature in the shunt resistors. The dissipated power was estimated from the working point at $I \approx 30$ µA and $V \approx 40$ µV, see marker Ⓜ in Fig. 5.7(a). Assuming that all the power is dissipated in the two shunt resistors and not in the damping resistor $R_D$ leads to $P = 0.6$ nW. Because the measurements shown in chapter 4 were performed on a sample from the same wafer, we believe that the used data on the thermal properties are correct.

The minimum noise level could in big parts be determined by the splitting network for the bias current. This effectively shunts the SQUID inductance with a comparably low resistance $2R_{\mathrm{SPL}} = 1\ \Omega$, see Fig. 5.5(b). As argued before, the comparably high parasitic inductance attached to this branch, we estimate $\approx 300$ pH, will exclude an influence of the noise of this resistor at the Josephson frequency. Nevertheless, it will also induce some noise at the measurement frequency. Note that also here some dissipation takes place, we estimate a similar minimum electron temperature of this resistor of $\approx 0.3$ K at the same working point. The additional flux noise originating from this bias resistor cannot be calculated easily because it also involves the dynamic inductance of the SQUID $G_{J\Phi}$ and is accordingly dependent on the working point.

As mentioned before, this resistor might also have a positive damping influence especially on the coil resonance of the signal washer. Nevertheless, if one looks at the massive coils integrated on this SQUID, one can conclude that the reached sensitivity is comparatively good.

### 5.4.4 Conclusions drawn from the first design step

Although there are uncertainties in the models used here, we think that the most degrading effects could be identified. The most important effect, the voltage hysteresis, covers the whole voltage range up to $\approx 0.4 I_0 R$. This could be directly observed in an experiment. We could also clearly see an influence of the hysteresis on the sensitivity of both SQUIDs.

The noise characterization of the SQUID with integrated flux transformer at a bath temperature of 4.2 K was done in the hysteretic range. Here, the damping resistors attached to the coil helped to improve the additional flux noise to $\sqrt{S_{\Phi,VV}} = 1.4\ \mu\Phi_0/\sqrt{\mathrm{Hz}}$. With the measured mutual inductance $M = 8.7$ nH this corresponds to an equivalent input noise current of 330 fA/$\sqrt{\mathrm{Hz}}$. Using the design value of the input inductance $L_{IN}$, the measured value of $M$, we estimate a coupled energy resolution $\varepsilon_{VV}/k^2 = S_{\Phi,VV} L_{IN} / \left(2M^2\right) \approx 1000\,\hbar$ at a temperature of 4.2 K. Unfortunately, cooling down did not further improve the noise. In retrospect, we understand that we were measuring excess noise caused by a switching within the hysteretic regime. Although the damping improved the noise at a higher temperature, further cooling revealed that the noise was determined by the lifetime of resonant states in the input coil with accompanied random switching between the hysteretic states [112].

During the measurement at lower temperatures, we also searched for other low noise working points. This did not lead to an improvement of the sensitivity beyond the mentioned value. The reason were different points in the characteristics with apparent resonances. Due to our optimistic guess of the working range of both sensors during the design process, the washer resonance of the coupling coils of both SQUIDs is situated just above the hysteretic voltage range.

The SQUID with a parallel washer configuration showed a stable low noise working point at lower temperatures. At a temperature of 4.2 K, we measured a similar coupled energy resolution of $\approx 1100\,\hbar$. This decreased to $\approx 170\,\hbar$ for bath temperatures below 0.2 K. The minimum sensitivity is mainly determined by the hot-electron effect. The exact noise level might be influenced by the employed resistance network for the symmetrical splitting of the bias currents needed for this design.

Some points of resonances originated from introduced parasitic capacitances that could have been avoided. For the SQUID with integrated flux transformer, this was for example a microstrip line within the transformer loop. For the SQUID with a parallel washer design, the shielding of slits might have caused additional resonances. Furthermore, the coil resonance of the comparably unimportant feedback coil was dangerously close to the working regime.

## 5.5 The second design step

We were able to join another run on the "LTS SQUID" process of the foundry of the *IPHT Jena* [77], see section 5.1. The design value of the critical current density was $J_0 = 120\ \mathrm{A/cm^2}$. This leads to $I_0 = 12.3\ \mu\mathrm{A}$ for the minimum-sized Josephson junction.

We adapted our design process based on the experiences gained during the evaluation of the performance of the sensors from the first design step. One adapted policy was to reduce unnecessary parasitic capacitances within the designs. We did not use microstrip lines for connections and did not use shielding pads over slits within the SQUID design.

From the observed hysteresis, we concluded that we had to assume a much higher operation voltage. This was also one conclusion of chapter 3, see section 3.3.4 on page 71.

Regarding the experiments on the hot-electron effect, we chose for shunt resistors of a much larger area. The results of one of our SQUIDs, see Fig. 5.8, suggest that the effective electron temperature $T_E$ was about 0.4 K. The cooling fins practically did not improve the electron temperature. Therefore, we followed our conclusions of chapter 4 and chose for much bigger shunt resistors.

The shunt resistors cannot be chosen arbitrarily big. The limit is related to the electrodynamic properties of this shunt resistor. A wide and long shunt resistor also exhibits a distributed inductance in series with the resistor and a distributed capacitance in parallel to the Josephson junction. For very big resistors, this can lead to an ineffective damping. To have a fall-back solution, we accordingly made two versions of our SQUIDs. In the one case, we made the shunt resistors 30 µm wide, in the other case 60 µm wide. The length of the shunt resistor was about the same as the width with the chosen value of the resistance. During the first design step, the shunt resistors were 15 µm wide. Accordingly, we increased the volume $\Omega$ of the shunt resistors by a factor of 4 and 16, respectively. With Eqn. (4.1) on page 84, one can expect $T_E \propto \Omega^{-1/5}$. One can thus only expect a small decrease of the electron temperature to $\approx 0.6\,T_E$ for the larger version of the shunt resistors and a SQUID with the same power dissipation. Also in the new design we attached cooling fins. Nevertheless, from the results presented in chapter 4, we learned that they can only have a minor influence in the typical dissipation range of the SQUIDs presented here. We abandoned the additional *Au* layer for the cooling fin because this would have led to only marginal improvements.

There is another important difference in our general design policy. This time, we used the coupled energy resolution $\varepsilon_{VV}/k^2$ as a design criterion. The design process was done in three

stages. First, we chose the basic layout and estimated parasitic inductances one could expect outside of the washer structures.

In the second stage, we varied the hole size and the number of turns of the washer. This led to the effective SQUID parameters $L_{SQ}$, $L_{IN}$ and $k^2$. Here, $L_{IN}$ is fixed by the requirement for MiniGRAIL $L_{IN} \approx 1.5$ µH. From the simple SQUID approximation, see Eqn. (1.24) on page 11, we estimated the sensitivity of the SQUID. The therefore needed shunt resistance $R$ was here chosen such that the washer resonance frequency $f_{R,W}$ was far above the intended operation range ($f_{R,W}\,\Phi_0 = 1.2\,I_0\,R$), see Eqn. (3.28) on page 72. Accordingly, the dimensions of the integrated coil are included in the optimization process, see Eqn. (3.23) on page 63 and section 3.3 on page 60 for more details on the needed properties of the washer. From the second design stage, we chose a hole size and number of integrated turns for the washer that about minimizes the coupled energy resolution $\varepsilon_{VV}/k^2$.

In the last stage of the design process, we extended the model of the SQUID with the RF impedance of the washer. On the basis of simulations, we chose the value of the shunt resistance such that there was a margin of $0.4\,I_0\,R$ between the hysteretic voltage range and the voltage range where the washer resonance is of influence.

### 5.5.1 The second SQUID with a parallel washer configuration

The advantage of the SQUID with a parallel washer design compared to the SQUID with integrated flux transformer is that one can achieve a higher coupling efficiency $k^2$. Furthermore, one can expect an easier operation with a capacitive input impedance, regarding the stability. We therefore concentrated on this layout.

A photograph of the re-designed SQUID is shown in Fig. 5.9(a). The first change becomes clear if one compares the layout of the core part of the design with the one of the first sensor, see Fig. 5.5(a). In the new design we did not realize the series connection of the two gradiometric feedback and signal coils on-chip. This has to be done externally, as in

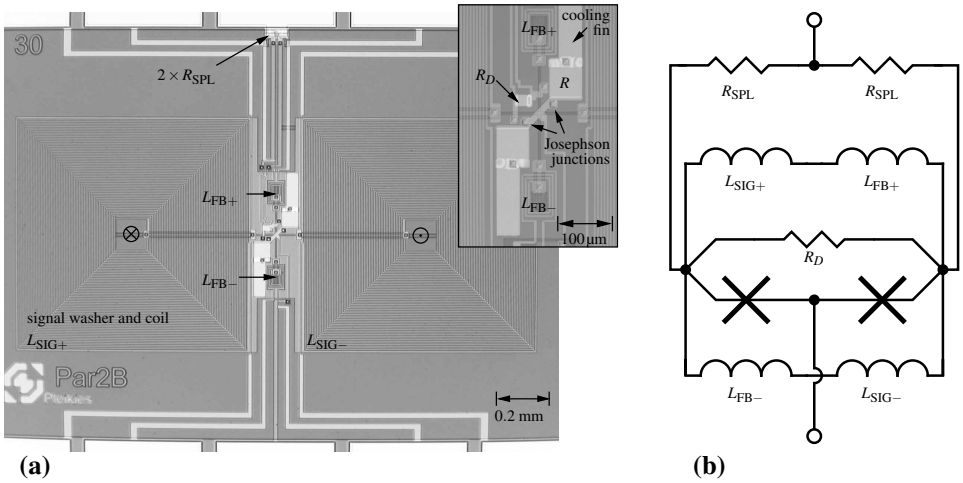


**(a)** **(b)**

**Figure 5.9: (a)** Photograph of the second SQUID with a parallel washer configuration. The inset shows a magnification of the middle part. **(b)** Simplified schematic for low frequencies. For simplicity, the four gradiometric coupling coils are not shown.

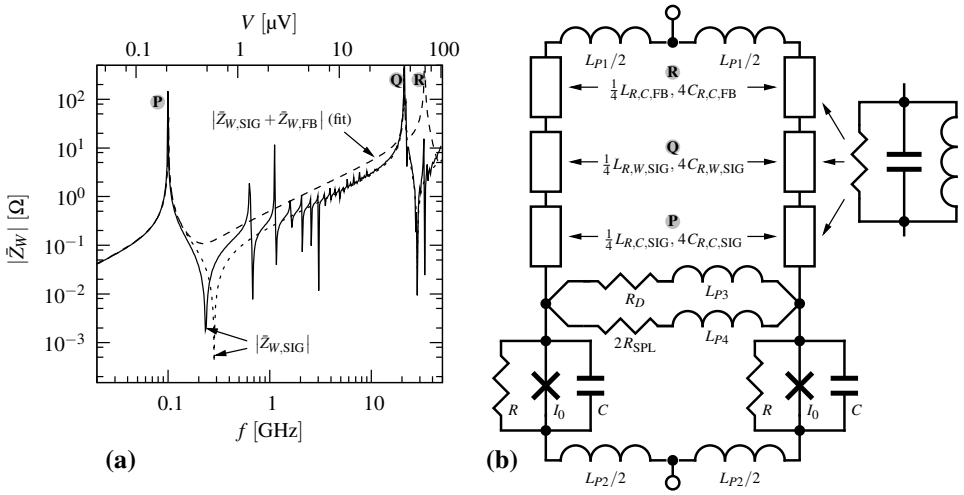


**Figure 5.10: (a)** Impedance of the signal and the feedback washer with the floating and open integrated coil. Complete model calculation for the signal washer (solid), its fitted lumped circuit model (dotted) and the fitted series impedance of both washers (dashed) with a high quality factor $Q = 1000$. The coil and coupling impedance of the signal washer can be seen in Fig. 3.8 on page 63. The fitted elements are Ⓟ $L_{R,C,\mathrm{SIG}} = 276$ pH, $C_{R,C,\mathrm{SIG}} = 9$ nF, Ⓠ $L_{R,W,\mathrm{SIG}} = 18$ pH, $C_{R,W,\mathrm{SIG}} = 3.2$ pF and Ⓡ $L_{R,C,\mathrm{FB}} = 36$ pH, $C_{R,C,\mathrm{FM}} = 0.63$ pF. The residual inductance of both washers above the resonances was fit to 57 pH. The upper axis shows the corresponding voltage. **(b)** Model of the SQUID. The factor of $\frac{1}{4}$ of the fitted washer inductance accounts for the parallel connection of two identical branches with one signal and one feedback washer connected in series on the one hand, see Fig. 5.9, and for the balanced distribution over the two branches of the SQUID in the model on the other hand. Noise sources are not shown for simplicity, they are attached to $R_D = R$, the two $R$ and $R_{\mathrm{SPL}} = 0.4R$. The quality factor $Q_R = R_R\sqrt{C_R/L_R}$ of the three resonances was set to 1 (Ⓟ), 1000 (Ⓠ) and 1000 (Ⓡ), respectively. See the text for details.

case of the original design [163]. This leads to considerable simplifications. The parasitic inductances are of smaller magnitude and easier to estimate.

The resistive network for the splitting of the bias current, see Fig. 5.9(b), is now connected slightly differently, this is not expected to have any considerable influence. The sensitivity of the last design might have been degraded because of the noise of this splitting network. We therefore increased $R_{\mathrm{SPL}}$ from $\approx 0.1R$ to $\approx 0.4R$. The direct voltage noise of the effective resistance $\frac{1}{2}R_{\mathrm{SPL}}$ in series to the SQUID has no significant influence. Nevertheless, this time we included the noise current of the effective resistance $2R_{\mathrm{SPL}}$ in the model of the SQUID.

The design process introduced above led to a signal washer with an integrated coil with 60 windings around a hole of 110 μm dimension. The inductance of the slit $L_{SL}$ of this washer was estimated to 140 pH. The feedback coupling system was dimensioned such that the corresponding coil resonance was far above the expected washer resonance of the signal washer. This was not the case in our last design. At the same time, we tried to minimize its effective washer inductance because this has no influence on the sensitivity of the SQUID. A too big value would unnecessarily decrease the effective coupling factor of the SQUID $k$. The feedback washer has a hole of 30 μm dimension with an integrated coil with 3 windings. The slit inductance estimated for this case is 24 pH.

In Fig. 5.10(a), one can see the estimated SQUID impedance of the two washers at RF

frequencies. Again, the large length of the signal coil of 0.11 m leads to a very low coil resonance frequency, see marker Ⓟ. In the same figure we also show the total fitted RF impedance of the feedback and the signal washer in series. The washer resonance of the signal washer is compared to the fist version of this design at about the same frequency, see marker Ⓙ in Fig. 5.6 and Ⓠ in Fig. 5.10. The coil resonance of the feedback coil, see marker Ⓡ in Fig. 5.10, is now shifted far away from typical Josephson frequencies.

In Fig. 5.10(b), one can see the corresponding model of the SQUID. The inductance of the connection of the four washers in the middle of the SQUID was estimated to 20 pH. This is gathered with the residual inductance of the fitted washer impedances above all resonances in the inductance $L_{P1} = 49$ pH. For the connection of the Josephson junctions and the washer damping resistor $R_D$, we also estimate parasitic inductances of $L_{P2} = L_{P3} = 20$ pH, respectively. The value of the damping resistor was again chosen to $R_D = R$. The inductance of the bias splitting network was estimated to $L_{P4} = 350$ pH. The capacitance $C$ of the Josephson junction not only includes its intrinsic value of 0.6 pF. We also added half of the total capacitance of the large version of the shunt resistor to the ground plane. This is based on a rule-of-thumb from chapter 5 of reference [2]. The area of this resistor was $60 \times 53\ \mu\text{m}^2$.

On the basis of simulations, we now chose the bias resistor such that there was a margin of $\approx 0.4 I_0 R$ between the two expected voltage ranges with degraded sensitivity. On the lower end, this is the hysteretic regime which indirectly caused by the coil resonance, see marker Ⓟ in Fig. 5.10(a). On the upper end this is the washer resonance, see marker Ⓠ in the same figure. The similar simulation on the fabricated device will be shown below.

The resulting properties of the design are listed in Table 5.3. The expected sensitivity on the basis of the simulation was $\varepsilon_{VV}/k^2 \approx 100\ \hbar/\text{K}$. The minimum noise temperature is represented by $\varepsilon_0$, see Eqn. (2.25) on page 27. Based on the simulation we estimated $\varepsilon_0 \approx 20\ \hbar/\text{K}$. About one third of this noise is caused by the splitting resistor network ($R_{\text{SPL}} = 0.4R$), which was determined by test simulations. We find this acceptable, especially if one considers a possible damping effect on for example harmonics of the signal coil.

We now want to compare the properties of the first and the second design of the SQUID with a parallel washer configuration, see Tables 5.2 and 5.3. The SQUID inductance is smaller in the second design and the coupling efficiency increased considerably. On the one hand this originated from the simplifications in the layout and on the other hand from the now used coupled energy resolution as an optimization criterion. The value of the shunt resistance $R$ is now chosen at a considerably smaller value. This is a consequence of the more careful chosen working range between the hysteretic range, which scales with $I_0 R$, and the washer resonance frequency.

The dissipated power in the planned optimum operation regime was $\approx 0.6$ nW per shunt resistor. Here we estimated a minimum reachable temperature of $\approx 0.25$ K.

**Table 5.3:** Design and experimental values of the second SQUID in a parallel washer configuration.

| | $I_0$ [μA] | $R$ [Ω] | $L_{SQ}$ [pH] | $L_{IN}$ [μH] | $M$ [nH] | $k^2$ | $\beta_L$ | $\beta_{L,RF}$ | $C$ [pF] | $\beta_C$ |
|---|---|---|---|---|---|---|---|---|---|---|
| design | 12.3 | 3.5 | 234 | 1.6 | 15 | 0.6 | 2.8 | 1.1 | 0.77 | 0.3 |
| measurement | 18 | 3.2 | | 1.5 | 13 | | 4.1[a] | 1.6[a] | | 0.4[a] |

[a] using the design values of $L_{SQ}$ or $C$

### 5.5.2 Experimental results

The fabricated SQUID showed a considerably increased critical current $I_0 = 18$ µA compared to the design value of 12.3 µA. The resistive layer was slightly below the design values. This results in an increase in $\beta_L$ of 50% and in $I_0 R$ of 30%, see Table 5.3. The resistance of the bias splitting network $\frac{1}{2} R_{\mathrm{SPL}}$ was determined from the current–voltage characteristics below the critical current of the SQUID to 0.66 Ω. The offset voltage $\frac{1}{2} R_{\mathrm{SPL}} I$ originating from this series resistance was subtracted in all the graphs shown in this section.

#### Characteristics

In Fig. 5.11(a), we show the experimental characteristics of the SQUID sensor. This measurement was performed in a bath of liquid $^4He$, $T_B = 4.2$ K, using self developed electronics from Twente University. No damping element was attached to the input coil. In Fig. 5.11(b), we show the simulation of the model shown in Fig. 5.10(b) with the experimental values for $I_0$, $R$ and $R_{\mathrm{SPL}}$, see Table 5.3. The damping resistance $R_D$ was scaled proportionally with $R$. The simulation was performed as described in section 3.1 on page 43. No excitation flux was applied. The corner frequency of the voltage low-pass filter was chosen to $f_{\mathrm{Out}} = 10$ MHz. Each working point had to be observed for a comparably long time of 20 µs to get a stable result in the hysteretic low-voltage regime. We reduced the quality factor of the signal coil resonance to 1 to shorten the simulation time.

Figure 5.11 nicely illustrates the false assumption we followed during the characterization of our first SQUIDs. One could think that the steep characteristics up to about 30 µV ($0.5 I_0 R$) are also the most sensitive. This voltage range is also the typical sensitive region for standard SQUIDs without a long integrated coil. Here, the characteristics just appear steep in consequence of the hysteresis covered by thermal noise, see the results on our first designs, the discussion in section 3.3.4 on page 71 and the voltage regions of best sensitivity

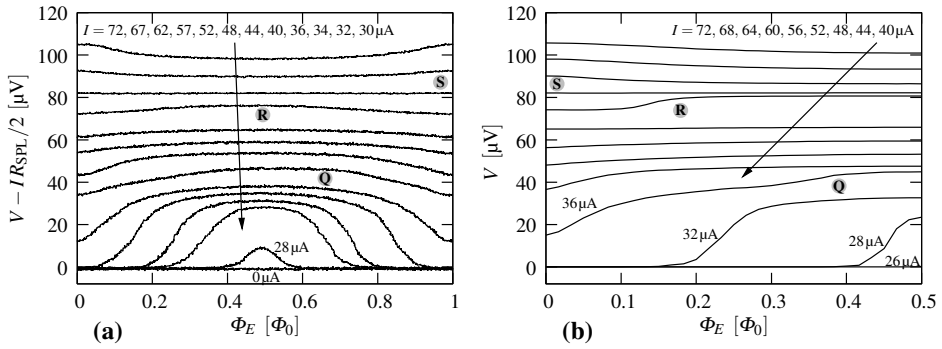


**Figure 5.11:** **(a)** Experimental characteristics of the SQUID with a parallel washer configuration with the large 60 µm wide shunt resistor at a bath temperature $T_B = 4.2$ K. We show flux–voltage characteristics with varying bias current. The offset voltage caused by the bias splitting network and the static magnetic flux were subtracted. The input coil was not shunted. **(b)** Numerical simulation of the model shown in Fig. 5.10(b) at $T = 4.2$ K. The capacitive and inductive properties as given in the text and Fig. 5.10 as well as the experimental $R$ and $I_0$ from Table 5.3 were used. The quality factors of the modeled resonances were set to $Q_{R,C} = 1$ for the coil resonance of the signal coil and 1000 for the other two resonances.

shown in Fig. 3.11(a) on page 70.

The agreement between the experimental and simulated characteristics is very good. The bias currents $I$ fit well, which indicates that the total SQUID inductance of the model is close to the inductance of the fabricated device. The voltage range marked with Ⓠ in Fig. 5.11(b) corresponds to the washer resonance of the signal washer, see marker Ⓠ in Fig. 5.10. Also in the experimental characteristics there are similar irregularities at about the same voltage. We believe these are caused by the washer resonance. In the sensitivity measurement that will be shown below, we also found degradations in this voltage region. In consequence of the increased $I_0 R$ in the fabricated SQUID, this resonance is located closer to the hysteretic regime than originally intended.

In the same voltage region, asymmetries in the flux–voltage characteristics become visible. We address this to an unbalanced layout of the damping resistor $R_D$, see Fig. 5.9(a).

The voltage range marked with Ⓡ in figure Fig. 5.11(b) corresponds to the coil resonance of the feedback washer, see marker Ⓡ in Fig. 5.10. Here, both the simulation and the experimental characteristics exhibit irregularities. Nevertheless, in the measurement this could also be caused by a harmonic of the washer resonance of the signal washer Ⓠ.

The effective resonance between the capacitance of the Josephson junctions and the residual SQUID inductance, marked with Ⓢ in Fig. 5.11 is at about the same voltage in both the simulation and the experiment. This is another indication that the model is a good representation of the real device.

**Coupling inductances**

For this device we performed a detailed measurement of the inductive properties. First, we measured the mutual inductance between the signal coil and the SQUID $M$ by directly modulating with the input coil. The experimental value $M = 13.2$ nH is 15% smaller than the design value, but still in good agreement, see Table 5.3.

We then performed a characterization of the input coil inductance as described above Eqn. (2.34) on page 31. We shunted the SQUID input inductance $L_{IN}$ by bonding wires, naturally both gradiometric signal coils were connected in series in the right direction. From the flux noise of 721 $\mu\Phi_0/\sqrt{\text{Hz}}$, measured in FLL at very low frequencies, we estimated the value of the effective shunt resistance of $R_S = 18$ mΩ formed by the bonding wires. From the $-3$ dB corner frequency $f_S$ of 2.18 kHz of the flux noise, we estimated the effective input inductance $L_{IN}{}' = 1.32$ μH in FLL.

Then we characterized the inductive coupling between the feedback and the signal inductances $M_{FB,SQ}$. By modulating the SQUID in open loop via the feedback coil, once at a low frequency $f \ll f_S$ and once at a high frequency $f \gg f_S$, we estimated the two mutual inductances $M_{FB,SQ} = 164$ pH and $M_{FB,SQ}{}' = 146$ pH. $M_{FB,SQ}$ corresponds to the usually observed direct mutual inductance, as in Fig. 5.11(a). $M_{FB,SQ}{}'$ also includes a component of coupling from the feedback coil to the input circuit and then to the SQUID. From Eqn. (2.34) we estimate $k\, k_{FB,IN}/k_{FB,SQ} = 0.11$. Note that large positive values of this term can cause instabilities for a FLL operated SQUID with a coupled capacitive input circuit [94], see section 2.5.3 on page 37. For standard SQUIDs, where the feedback and the signal coil are coupling to the same hole, $k\, k_{FB,IN}/k_{FB,SQ}$ usually takes positive nonzero values. Also note that the measured value for $k\, k_{FB,IN}/k_{FB,SQ}$ is not intrinsic in the SQUID design. If one connects the four coils via leads that are routed far away from the SQUID, the value can be

reduced towards zero because of the symmetric layout [163]. During this measurement, we connected all coils by bonding wires directly across the chip which of course also couple to the hole of the signal washer for example.

From Eqn. (2.35) on page 31 one can see that the input inductance $L_{IN}{}'$ as determined in FLL is in fact $L_{IN}{}' = L_{IN} M_{FB,SQ}{}' / M_{FB,SQ}$. The geometric input inductance of the SQUID $L_{IN}$ accordingly reads 1.48 µH. This is slightly smaller than the design value, see Table 5.3.

**Sensitivity**

To determine the sensitivity of this SQUID, we performed a measurement in a two-stage SQUID setup, see Fig. 1.6(b) on page 14. As second stage SQUID, we used the SQUID with integrated flux transformer, see section 5.4.2. The bias resistance $R_B$ shunting the first stage SQUID was 0.5 Ω. Again we inserted a filter inductance in series with $R_B$. This had to be done because of the relatively high mutual inductance of the second stage $M$. The second stage SQUID would otherwise be degraded by the output noise of the first stage.

By means of a four-point measurement, we were able to determine the voltage across the bias resistor $R_B$ and the SQUID as well as the total bias current $I_1$ of the first stage. From these data and the experimentally determined bias resistance $R_B$ and bias splitting resistance $R_{\mathrm{SPL}}$, we can calculate the effective SQUID voltage in each working point without the additional offset caused by $R_{\mathrm{SPL}}$.

From the characterization of our first SQUIDs, we saw that attached damping elements on the input coil can lead to low noise working points that turn out to be less sensitive when the SQUID is cooled down. Although such damping networks are generally recommended, we decided to characterize the SQUID without it.

By varying the bias current of the first stage $I_1$ and locking the SQUID at different flux points, we characterized the SQUID over large parts of the characteristics. By means of vacuum pumping, we reduced the bath temperature from $T_B = 4.2$ K to 1.5 K. This temperature was determined by the noise of the resistance $R_B + \frac{1}{2} R_{\mathrm{SPL}}$ in the input loop of the second stage for $I_1 = 0$.

In Fig. 5.12(b), we show a choice of lower noise working points for a variety of effective voltages of the SQUID. Each point corresponds to the white noise measured in FLL at frequencies above 10 Hz. Note that the noise is normalized to the bath temperature $T_B$. In the same figure, we show the simulated sensitivity of the model at a temperature of 1 K ($\Gamma = 0.002$). This time, a small excitation flux was applied as described in section 3.1 on page 43. Furthermore, each working point was simulated two times with a different initial starting point. Hysteretic points were then excluded in the shown sensitivity. The corner frequency of the voltage low-pass was again chosen to $f_{\mathrm{Out}} = 10$ MHz. Each working point was observed for 10 µs. We reduced the quality factor of the signal coil resonance to 1 to shorten the simulation time.

The agreement of the simulated and the experimental sensitivity is good in many aspects. At the lower voltages, within the hysteretic regime, the sensitivity did not considerably improve at the lower bath temperature $T_B = 1.5$ K. In the range of the washer resonance of the signal washer Ⓠ, also see Figs. 5.10 and 5.11, a low noise working point was only found at the higher bath temperature $T_B = 4.2$ K. Above this washer resonance, see marker Ⓣ in Fig. 5.12(b), a linear temperature dependence was observed. The observed noise is also close

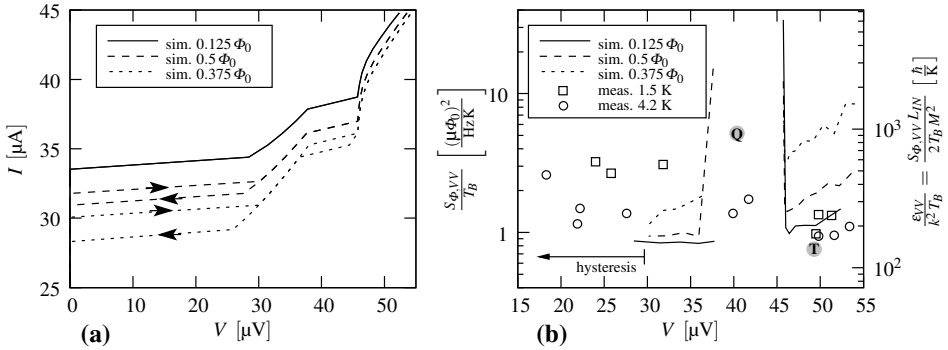


**Figure 5.12:** **(a)** Numerically simulated current–voltage characteristics of the model shown in Fig. 5.10 at $T = 1$ K for three different values of flux $\Phi_E$. Hysteretic paths are indicated by arrows. The capacitive and inductive properties as given in the text and Fig. 5.10 as well as the experimental $R$ and $I_0$ from Table 5.3 were used. The quality factors of the modeled resonances were set to $Q_{R,C} = 1$ for the coil resonance of the signal coil and 1000 for the other two resonances. The additional noise is shown in (b), where the hysteretic regions are excluded. **(b)** Experimental and simulated additional flux noise $S_{\Phi,VV}$ of the second SQUID with a parallel washer configuration. The noise is normalized to the temperature, $T_B = 4.2$ K and 1.5 K in the measurement. The input coil was not shunted. The right axis shows the corresponding coupled energy resolution using experimental values from Table 5.3.

to the simulated sensitivity. In the restricted low noise working region below the washer resonance, which is shown in the simulation, we were not able to reach a good sensitivity.

The minimum reached additional flux noise $\sqrt{S_{\Phi,VV}}$, see marker Ⓣ in Fig. 5.12 was 2.0 $\mu\Phi_0/\sqrt{\text{Hz}}$ and 1.2 $\mu\Phi_0/\sqrt{\text{Hz}}$ at a bath temperature of $T_B = 4.2$ K and 1.5 K, respectively. This corresponds to an equivalent input current noise of $\sqrt{S_{\Phi,VV}}/M = 320\ \text{fA}/\sqrt{\text{Hz}}$ and 190 $\text{fA}/\sqrt{\text{Hz}}$, respectively. The measurements were performed on the SQUID with the large, 60 μm wide, shunt resistors. Accordingly, we do not expect problems originating from the increased volume of the shunt resistors.

The normalized coupled energy resolution $\varepsilon_{VV}/(k^2 T)$ reads 170 $\hbar$/K. This is about a factor of two worse than the simulated design value. We believe that the main reason for this discrepancy are the increased values of $\beta_L$ and $I_0 R$ of the fabricated device with respect to the design. Nevertheless, the estimated normalized coupled energy resolution $\varepsilon_{VV}/(k^2 T)$ takes about 60% of the value estimated for the first design. Furthermore, we expect an improvement of the minimum reachable temperature.

Another effect should be mentioned here. From the simulation shown in Fig. 5.12(b), one can see that the sensitivity is improving for smaller values of external flux $\Phi_E \to 0$. This corresponds to our observation during this measurement and the measurement shown in section 5.4.3. It fits a quantitative understanding of the behavior of SQUIDs with a long integrated coil. Not only the characteristics are determined by the *reduced SQUID* with the effective RF screening parameter $\beta_{L,RF}$, also the sensitivity, see the discussion in section 3.3.3 on page 69. The points of best sensitivity of a standard SQUID are usually found at $\Phi_E = 0.25\,\Phi_0$, see for example section 3.2.5 on page 58. Accordingly, the points of sensitivity of the SQUID with the long integrated coil would be found at a smaller external flux, see the transformation in Eqn. (3.26) on page 65. The results of the optimization of the simplified model, see Fig. 3.11 on page 70, could accordingly be further improved for values of external flux $\Phi_E$ smaller than 0.25 $\Phi_0$.

### 5.5.3 Outlook

We estimate an electron temperature at the working point marked with Ⓣ in Fig. 5.12 of about $\approx 0.3$ K. This suggests that a coupled energy resolution of about 50 $\hbar$ is possible. This is close to the optimum performance achieved for the original design [156].

Simulations suggest that in the same working point, a low noise temperature is achievable. The corresponding energy resolution $\varepsilon_0$ yields $\approx 10\,\hbar$. Nevertheless, a re-fabricated sensor with the working range clearly shifted away from the washer resonance, would be an even more promising option.

Furthermore, an evaluation of the exact influence of damping elements within the SQUID design, namely $R_D$ and $R_{\mathrm{SPL}}$, would possibly give more room for optimization.

## 5.6 Conclusions

In this chapter, we present the design, modeling and characterization of SQUIDs developed for the gravitational wave antenna MiniGRAIL. The main requirement is given by a large input inductance $L_{IN} \approx 1.5$ µH with a minimum additional coupled energy resolution $\varepsilon_{VV}/k^2$ at the aimed operation temperature of 20 mK. To reach a good coupling efficiency $k^2$, the input coil has to be integrated on the SQUID design. This turns out to introduce many effects that are not present in standard SQUIDs.

During the characterization of our developed SQUIDs, we could clearly identify hysteretic working ranges. After having observed the effect in numerical simulations, we experimentally re-examined the characteristics of one of our SQUIDs at a bath temperature of $T_B = 0.1$ K. We indeed directly observed the expected behavior, see section 5.4.2. To our knowledge this is the first experimental evidence for this effect.

Measurements on the sensitivity of all presented SQUID sensors exhibited a degrading effect originating in hysteresis. Low noise working points were located above the hysteretic voltage range. The performance within the hysteretic regime could be partly improved by means of series resistive-capacitive damping elements connected across the input coil, see sections 5.4.2 and 5.4.3. Nevertheless, such working points turned out to show mainly non-thermal noise. The sensitivity did not considerably improve by decreasing the bath temperature. For the measurement shown in section 5.5.2 we did not attach any damping element to the coil to exclude similar misleading results at higher temperatures.

In chapter 3, we studied a simplified model of SQUIDs with a long integrated coil. Here, the resonance frequency of the integrated coil is located below the Josephson frequency of the SQUID. This is the case for all of our developed SQUIDs shown in this chapter. Also the simplified model includes hysteretic working ranges, see section 3.3.2. We argued that the voltage hysteresis has to be taken into account while designing and operating SQUIDs with a long integrated coil, see for example section 3.3.4 on page 71. The experimental results shown in this chapter strongly support this insight. We conclude that the simplified model of SQUIDs with a long integrated coil is applicable to explain the basic behavior of real devices.

To numerically study the performance of our developed SQUIDs in more detail, we derived the most important properties for the operation from the layout. These properties were extracted by numerical inductance calculation on simplified test structures on the one hand

and by calculating the RF impedance of the washer structures with integrated coils on the other hand. Simplified models of the SQUIDs were simulated and compared to the characteristics of all our developed sensors. In general, the agreement was good. Although there are uncertainties in the models used here, we think that many degrading effects could be identified. These include the already mentioned hysteresis as well as several unavoidable and avoidable resonances within the structures of the SQUIDs. Also a simulation on the sensitivity, see section 5.5.2, showed a good agreement with the measurements.

The comparison of the experimental and the numerically determined characteristics and sensitivity presented in section 5.5.2 shows a very good agreement. To our knowledge, this has never been achieved in such detail for SQUIDs with integrated coils. Therefore, we conclude that the performance of this type of SQUIDs is more controllable and predictable than is usually assumed.

The numerical characterization of detailed models was incorporated into the design process of the second SQUID with a parallel washer configuration, see section 5.5. The measured normalized coupled energy resolution $\varepsilon_{VV}/(k^2 T)$ is 170 $\hbar$/K. This is about a factor of two higher than the simulated design value. The main reason for this discrepancy are the increased values of $\beta_L$ and $I_0 R$ of the fabricated device. Nevertheless, the coupled energy resolution improved to about 60% of the value obtained for the first design. For a SQUID with an integrated coil of $L_{IN} = 1.5$ µH inductance, such a sensitivity is good. Using an experimental approach discussed in chapter 2, we estimated the geometric input inductance excluding a screening caused by the FLL operation.

For the first SQUID with a parallel washer configuration, a minimum coupled energy resolution of 170 $\hbar$ was measured at bath temperatures below 0.2 K, see section 5.4.3. This was found to be mainly determined by the hot-electron effect which led to an effective minimum reachable temperature of $\approx 0.4$ K. In the re-designed sensor, we therefore used shunt resistors of a larger size, see the conclusions of chapter 4. The measurements suggest that the by one order of magnitude increased volume of the resistors does not introduce degrading effects which could possibly be caused by a degraded damping of the Josephson junction. We therefore expect an improvement in the minimum reachable electron temperature $T_E$ of the characterized second SQUID with a parallel washer configuration to $\approx 0.3$ K. The overall performance is expected to be good, see section 5.5.3.

As one can see from the results of chapter 3, see section 3.3.4 on page 71, a screening parameter $\beta_L$ close to 1 would lead to an improvement in sensitivity. This would require a re-fabrication of the same design. A possible investigation of smaller damping within the SQUID sensor, could lead to further improvements. We believe that with the same fabrication technology and the requirements of the MiniGRAIL project, a coupled energy resolution $\varepsilon_{VV}/k^2$ in the order of 10 $\hbar$ is realizable. Furthermore, minimum reachable noise temperatures of an order of magnitude above the quantum limit seem feasible.

The most crucial factor for SQUIDs with a long integrated coil from the point of view of the fabrication technology is the spacing and width within the coil. Smaller dimensions effectively lead to a higher washer resonance frequency, see section 3.3.1 on page 62 in chapter 3. Therefore, SQUIDs fabricated in a sub-micron technology would make even further improvements [20] possible.

# References


[1] D. J. V. Harlingen, R. H. Koch, and J. Clarke, "Superconducting quantum interference device with very low magnetic flux noise energy," *Appl. Phys. Lett.*, vol. 41, no. 2, pp. 197–199, 1982.

[2] J. Clarke and A. Braginski, *The SQUID Handbook Vol. 1*. Wiley-VCH, 2006.

[3] J. Clarke and A. Braginski, *The SQUID Handbook Vol. 2*. Wiley-VCH, 2006.

[4] R. C. Jaklevic, J. Lambe, A. H. Silver, and J. E. Mercereau, "Quantum Interference Effects in Josephson Tunneling," *Phys. Rev. Lett.*, vol. 12, no. 7, pp. 159–160, 1964.

[5] H. Ter Brake, J. Flokstra, W. Jaszczuk, R. Stammis, G. van Ancum, A. Martinez, and H. Rogalla, "The UT 19-channel DC SQUID based neuromagnetometer," *Clin. Phys. Physiol. Meas.*, vol. 12, pp. 45–50, 1991.

[6] J. Wikswo Jr, "SQUID magnetometers for biomagnetism and nondestructive testing: important questions and initial answers," *IEEE Trans. Appl. Supercond.*, vol. 5, no. 2 Part 1, pp. 74–120, 1995.

[7] M. Peters, J. Stinstra, S. Van Den Broek, J. Huirne, H. Quartero, H. Ter Brake, and H. Rogalla, "On the fetal magnetocardiogram," *Bioelectrochem. Bioenerg.*, vol. 47, no. 2, pp. 273–281, 1998.

[8] R. Hohmann, M. Maus, D. Lomparski, M. Gruneklee, Y. Zhang, H. Krause, H. Bousack, and A. Braginski, "Aircraft wheel testing with machine-cooled HTS SQUID gradiometersystem," *IEEE Trans. Appl. Supercond.*, vol. 9, no. 2 Part 3, pp. 3801–3804, 1999.

[9] S. Linzen, A. Chwala, V. Schultze, M. Schulz, T. Schuler, R. Stolz, N. Bondarenko, and H. Meyer, "A LTS-SQUID System for Archaeological Prospection and Its Practical Test in Peru," *IEEE Trans. Appl. Supercond.*, vol. 17, no. 2 Part 1, pp. 750–755, 2007.

[10] A. Zięba, "Image and sample geometry effects in SQUID magnetometers," *Rev. Sci. Instrum.*, vol. 64, p. 3357, 1993.

[11] J. Kirtley, M. Ketchen, K. Stawiasz, J. Sun, W. Gallagher, S. Blanton, and S. Wind, "High-resolution scanning SQUID microscope," *Appl. Phys. Lett.*, vol. 66, p. 1138, 1995.

[12] Y. Greenberg, "Application of superconducting quantum interference devices to nuclear magnetic resonance," *Rev. Mod. Phys.*, vol. 70, no. 1, pp. 175–222, 1998.

[13] M. Roukes, M. Freeman, R. Germain, R. Richardson, and M. Ketchen, "Hot electrons and energy transport in metals at millikelvin temperatures," *Phys. Rev. Lett.*, vol. 55, no. 4, pp. 422–425, 1985.

[14] C. Lusher, J. Li, V. Maidanov, M. Digby, H. Dyball, A. Casey, J. Nyeki, V. Dmitriev, B. Cowan, and J. Saunders, "Current sensing noise thermometry using a low Tc DC SQUID preamplifier," *Meas. Sci. Technol.*, vol. 12, no. 1, pp. 1–15, 2001.

[15] J. Pleikies, O. Usenko, G. Frossati, and J. Flokstra, "SQUID current amplifiers for sub-kelvin operation temperatures," *Cryogenics*, vol. In Press, 2009.

[16] V. Danilov, K. Likharev, and A. Zorin, "Quantum noise in SQUIDs," *IEEE Trans. Magn.*, vol. 19, no. 3, pp. 572–575, 1983.

[17] R. Koch, D. Van Harlingen, and J. Clarke, "Quantum noise theory for the dc SQUID," *Appl. Phys. Lett.*, vol. 38, p. 380, 1981.

[18] D. Awschalom, J. Rozen, M. Ketchen, W. Gallagher, A. Kleinsasser, R. Sandstrom, and B. Bumble, "Low-noise modular microsusceptometer using nearly quantum limited dc SQUIDs," *Appl. Phys. Lett.*, vol. 53, p. 2108, 1988.

[19] M. Mück, J. Kycia, and J. Clarke, "Superconducting quantum interference device as a near-quantum-limited amplifier at 0.5 GHz," *Appl. Phys. Lett.*, vol. 78, p. 967, 2001.

[20] P. Falferi, M. Bonaldi, M. Cerdonio, R. Mezzena, G. A. Prodi, A. Vinante, and S. Vitale, "10 $\hbar$ superconducting quantum interference device amplifier for acoustic gravitational wave detectors," *Appl. Phys. Lett.*, vol. 93, no. 17, p. 172506, 2008.

[21] V. Polushkin, D. Drung, and H. Koch, "A broadband picovoltmeter based on the direct current superconducting quantum interference device with additional positive feedback," *Rev. Sci. Instrum.*, vol. 65, p. 3005, 1994.

[22] J. Sese, E. Bartolome, A. Camon, J. Flokstra, G. Rietveld, and C. Rillo, "Simplified calculus for the design of a cryogenic current comparator," *IEEE Trans. Instrum. Meas.*, vol. 52, no. 2, pp. 612–616, 2003.

[23] C. Rillo, J. Sese, E. Bartolome, J. Flokstra, A. Camon, and G. Rietveld, "On the sensitivity of cryogenic current comparators: theory and experiments," *Metrologia*, vol. 40, no. 2, pp. 51–56, 2003.

[24] N. Booth and D. Goldie, "Superconducting particle detectors," *Supercond. Sci. Technol.*, vol. 9, no. 7, pp. 493–516, 1996.

[25] M. Frank, C. Mears, S. Labov, F. Azgui, M. Lindeman, L. Hiller, H. Netel, and A. Barfknecht, "High-resolution X-ray detectors with high-speed SQUID readout of superconducting tunnel junctions," *Nucl. Instrum. Methods Phys. Res. Sect. A*, vol. 370, no. 1, pp. 41–43, 1996.

[26] G. Harry, I. Jin, H. Paik, T. Stevenson, and F. Wellstood, "Two-stage superconducting-quantum-interference-device amplifier in a high-Q gravitational wave transducer," *Appl. Phys. Lett.*, vol. 76, p. 1446, 2000.

[27] A. Vinante, R. Mezzena, G. Prodi, S. Vitale, M. Cerdonio, P. Falferi, and M. Bonaldi, "Dc superconducting quantum interference device amplifier for gravitational wave detectors with a true noise temperature of 16 $\mu$K," *Appl. Phys. Lett.*, vol. 79, p. 2597, 2001.

[28] M. Podt, L. Gottardi, A. Waard, G. Frossati, and J. Flokstra, "A spherical gravitational wave detector readout by nearly quantum limited SQUIDs," *Supercond. Sci. Technol.*, vol. 16, no. 12, pp. 1531–1535, 2003.

[29] M. Podt, L. Gottardi, A. de Waard, G. Frossati, and J. Flokstra, "Development of a SQUID readout system for the MiniGRAIL," *IEEE Trans. Appl. Supercond.*, vol. 15, no. 2 Part 1, pp. 785–788, 2005.

[30] A. de Waard, L. Gottardi, J. van Houwelingen, A. Shumack, and G. Frossati, "MiniGRAIL, the first spherical detector," *Class. Quantum Gravity*, vol. 20, no. 10, pp. 143–152, 2003.

[31] L. Gottardi, *Transducers and low noise two-stage SQUID amplifiers for the spherical gravitational wave antenna MiniGRAIL*. PhD thesis, Leiden University, The Netherlands, 2004.

[32] A. de Waard, M. Bassan, Y. Benzaim, V. Fafone, J. Flokstra, G. Frossati, L. Gottardi, C. Herbschleb, A. Karbalai-Sadegh, K. Kuit, *et al.*, "Preparing for science run 1 of MiniGRAIL," *Class. Quantum Gravity*, vol. 23, no. 8, pp. 79–84, 2006.

[33] L. Gottardi, A. de Waard, O. Usenko, G. Frossati, M. Podt, J. Flokstra, M. Bassan, V. Fafone, Y. Minenkov, and A. Rocchi, "Sensitivity of the spherical gravitational wave detector MiniGRAIL operating at 5 K," *Phys. Rev. D*, vol. 76, no. 10, p. 102005, 2007.

[34] J. Pleikies, O. Usenko, G. Frossati, and J. Flokstra, "Optimization of a low-Tc dc SQUID amplifier with tightly coupled input coils," *IEEE Trans. Appl. Supercond.*, 2009. In press.

[35] J. Pleikies, O. Usenko, and J. Flokstra, "Numerical studies on dc-SQUID sensors with tightly coupled input coil," *J. Phys.: Conf. Ser.*, vol. 97, p. 012254 (6pp), 2008.

[36] J. Pleikies, O. Usenko, K. Kuit, J. Flokstra, A. de Waard, and G. Frossati, "SQUID Developments for the Gravitational Wave Antenna MiniGRAIL," *IEEE Trans. Appl. Supercond.*, vol. 17, no. 2, pp. 764–767, 2007.

[37] M. Tinkham, *Introduction to Superconductivity*. Courier Dover Publications, 2004.

[38] J. Bardeen, L. Cooper, and J. Schrieffer, "Theory of Superconductivity," *Physical Review*, vol. 108, no. 5, pp. 1175–1204, 1957.

[39] L. Solymar, *Superconductive Tunnelling and Applications*. John Wiley & Sons, 1972.

[40] K. Likharev, *Dynamics of Josephson Junctions and Circuits*. CRC Press, 1986.

[41] B. Josephson, "Possible new effects in superconductive tunnelling," *Phys. Lett.*, vol. 1, no. 7, pp. 251–253, 1962.

[42] K. Likharev, "Superconducting weak links," *Rev. Mod. Phys.*, vol. 51, no. 1, pp. 101–159, 1979.

[43] D. E. McCumber, "Effect of ac Impedance on dc Voltage-Current Characteristics of Superconductor Weak-Link Junctions," *J. Appl. Phys.*, vol. 39, no. 7, pp. 3113–3118, 1968.

[44] W. C. Stewart, "Current-voltage characteristics of superconducting tunnel junctions," *J. Appl. Phys.*, vol. 45, no. 1, pp. 452–456, 1974.

[45] E. Fang and T. Van Duzer, "A Josephson integrated circuit simulator JSIM for superconductive electronics application," in *Extended Abstracts of 1989 Int. Superconductive Electronics Conf*, pp. 407–410, 1989.

[46] J. Satchell, "Stochastic simulation of SFQ logic," *IEEE Trans. Appl. Supercond.*, vol. 7, no. 2, pp. 3315–3318, 1997.

[47] R. Kautz and J. Martinis, "Noise-affected I-V curves in small hysteretic Josephson junctions," *Phys. Rev. B*, vol. 42, no. 16, pp. 9903–9937, 1990.

[48] J. F. L. Vernon and R. J. Pedersen, "Relaxation Oscillations in Josephson Junctions," *J. Appl. Phys.*, vol. 39, no. 6, pp. 2661–2664, 1968.

[49] D. Adelerhof, H. Nijstad, J. Flokstra, and H. Rogalla, "(Double) relaxation oscillation SQUIDs with high flux-to-voltage transfer: Simulations and experiments," *J. Appl. Phys.*, vol. 76, p. 3875, 1994.

[50] M. Van Duuren, G. Brons, D. Adelerhof, J. Flokstra, and H. Rogalla, "Double relaxation oscillation superconducting quantum interference devices with gradiometric layout," *J. Appl. Phys.*, vol. 82, p. 3598, 1997.

[51] A. Hamster, M. Van Duuren, G. Brons, J. Flokstra, and H. Rogalla, "A 1-MHz low noise preamplifier based on double relaxation oscillation SQUIDs," *IEEE Trans. Appl. Supercond.*, vol. 9, no. 2 Part 3, pp. 2915–2918, 1999.

[52] R. Welty and J. Martinis, "A series array of DC SQUIDs," *IEEE Trans. Magn.*, vol. 27, no. 2, pp. 2924–2926, 1991.

[53] M. Van Duuren, G. Brons, J. Flokstra, and H. Rogalia, "Smart SQUIDs based on relaxation oscillation SQUIDs," *IEEE Trans. Appl. Supercond.*, vol. 9, no. 2 Part 3, pp. 2919–2922, 1999.

[54] M. Podt, A. Mieog, J. Flokstra, and H. Rogalla, "Design of a fast digital double relaxation oscillation SQUID," *IEEE Trans. Appl. Supercond.*, vol. 11, no. 1 Part 1, pp. 1235–1238, 2001.

[55] T. Reich, T. Ortlepp, F. Uhlmann, and P. Febvre, "Experimental analysis of a digital SQUID device at 4.2 K," *Supercond. Sci. Technol.*, vol. 18, no. 8, pp. 1077–1081, 2005.

[56] D. Drung, R. Cantor, M. Peters, H. Scheer, and H. Koch, "Low-noise high-speed dc superconducting quantum interference device magnetometer with simplified feedback electronics," *Appl. Phys. Lett.*, vol. 57, p. 406, 1990.

[57] C. Tesche and J. Clarke, "dc SQUID: Noise and optimization," *J. Low Temp. Phys.*, vol. 29, no. 3, pp. 301–331, 1977.

[58] J. Bruines, V. Waal, and J. Mooij, "Comment on: Dc SQUID: Noise and optimization by Tesche and Clarke," *J. Low Temp. Phys.*, vol. 46, no. 3, pp. 383–386, 1982.

[59] V. Danilov, K. Likharev, and O. Snigirev, "Signal and noise parameters of SQUIDs," in *SQUID'80* (H. Hahlbohm and H. Lübbig, eds.), pp. 473–507, Walter de Gruyter, Berlin, 1980.

[60] T. Ryhänen, H. Seppä, R. Ilmoniemi, and J. Knuutila, "SQUID magnetometers for low-frequency applications," *J. Low Temp. Phys.*, vol. 76, no. 5, pp. 287–386, 1989.

[61] D. Koelle, R. Kleiner, F. Ludwig, E. Dantsker, and J. Clarke, "High-transition-temperature superconducting quantum interference devices," *Rev. Mod. Phys.*, vol. 71, no. 3, pp. 631–686, 1999.

[62] P. Lynn, *An Introduction to the Analysis and Processing of Signals*. Palgrave Macmillan, 1989.

[63] C. Tesche and J. Clarke, "dc SQUID: Current noise," *J. Low Temp. Phys.*, vol. 37, no. 3, pp. 397–403, 1979.

[64] J. Clarke, C. Tesche, and R. Giffard, "Optimization of dc SQUID voltmeter and magnetometer circuits," *J. Low Temp. Phys.*, vol. 37, no. 3, pp. 405–420, 1979.

[65] C. Hilbert and J. Clarke, "Measurements of the dynamic input impedance of a dc SQUID," *J. Low Temp. Phys.*, vol. 61, no. 3, pp. 237–262, 1985.

[66] P. Falferi, R. Mezzena, S. Vitale, and M. Cerdonio, "Measurement of the dynamic input impedance of a dc superconducting quantum interference device at audio frequencies," *Appl. Phys. Lett.*, vol. 71, p. 956, 1997.

[67] V. Waal, P. Schrijner, and R. Llurba, "Simulation and optimization of a dc SQUID with finite capacitance," *J. Low Temp. Phys.*, vol. 54, no. 3, pp. 215–232, 1984.

[68] K. Carroll, "DC SQUID small signal analysis," *IEEE Trans. Magn.*, vol. 27, no. 2, pp. 3017–3020, 1991.

[69] J. Martinis and J. Clarke, "Current noise measured in the dc SQUID," *J. Low Temp. Phys.*, vol. 65, pp. 459–468, 1986.

[70] H. Zappe and B. Landman, "Analysis of resonance phenomena in Josephson interferometer devices," *J. Appl. Phys.*, vol. 49, p. 344, 1978.

[71] H. Zappe and B. Landman, "Experimental investigation of resonances in low-Q Josephson interferometer devices," *J. Appl. Phys.*, vol. 49, p. 4149, 1978.

[72] F. C. Wellstood, C. Urbina, and J. Clarke, "Hot-electron limitation to the sensitivity of the dc superconducting quantum interference device," *Appl. Phys. Lett.*, vol. 54, no. 25, pp. 2599–2601, 1989.

[73] F. Wellstood, C. Urbina, and J. Clarke, "Hot-electron effects in metals," *Phys. Rev. B*, vol. 49, no. 9, pp. 5942–5955, 1994.

[74] C. Tesche, "Optimization of dc SQUID linear amplifiers and the quantum noise limit," *Appl. Phys. Lett.*, vol. 41, p. 490, 1982.

[75] C. Caves, "Quantum limits on noise in linear amplifiers," *Phys. Rev. D*, vol. 26, no. 8, pp. 1817–1839, 1982.

[76] J. Jaycox and M. Ketchen, "Planar coupling scheme for ultra low noise DC SQUIDs," *IEEE Trans. Magn.*, vol. 17, no. 1, pp. 400–403, 1981.

[77] IPHT Jena e.V., Department of Quantum Electronics, Postfach 100239, 07702 Jena, Germany, *Correspondence and Design Rules LTS SQUID process*, 2008. Online available at http://www.ipht-jena.de/uploads/media/a13_ipht_squid_1_4_04.pdf.

[78] C. Tesche, "Analysis of a double-loop dc SQUID," *J. Low Temp. Phys.*, vol. 47, no. 5, pp. 385–410, 1982.

[79] D. Drung and W. Jutzi, "Hysteretic Noise Simulation of dc SQUIDs with Input Coil," in *SQUID'85* (H. Hahlbohm and H. Lübbig, eds.), pp. 807–812, Walter de Gruyter, Berlin, 1985.

[80] T. Ryhänen, H. Seppä, and R. Cantor, "Effect of parasitic capacitance and inductance on the dynamics and noise of dc superconducting quantum interference devices," *J. Appl. Phys.*, vol. 71, no. 12, pp. 6150–6166, 1992.

[81] K. Enpuku and K. Yoshida, "Modeling the dc superconducting quantum interference device coupled to the multiturn input coil," *J. Appl. Phys.*, vol. 69, no. 10, pp. 7295–7300, 1991.

[82] K. Enpuku, R. Cantor, and H. Koch, "Modeling the direct current superconducting quantum interference device coupled to the multiturn input coil. II," *J. Appl. Phys.*, vol. 71, no. 5, pp. 2338–2346, 1992.

[83] K. Enpuku, R. Cantor, and H. Koch, "Modeling the dc superconducting quantum interference device coupled to the multiturn input coil. III," *J. Appl. Phys.*, vol. 72, no. 3, pp. 1000–1006, 1992.

[84] G. Hildebrandt, F. Uhlmann, G. Daalmans, and F. Bommel, "A novel approach in calculating V-I curves of a DC-SQUID coupled to a planar input coil," *IEEE Trans. Appl. Supercond.*, vol. 6, no. 1, pp. 19–23, 1996.

[85] K. Enpuku, K. Sueoka, K. Yoshida, and F. Irie, "Effect of damping resistance on voltage versus flux relation of a dc SQUID with large inductance and critical current," *J. Appl. Phys.*, vol. 57, no. 5, pp. 1691–1697, 1985.

[86] K. Enpuku, K. Yoshida, and S. Kohjiro, "Noise characteristics of a dc SQUID with a resistively shunted inductance. II. Optimum damping," *J. Appl. Phys.*, vol. 60, p. 4218, 1986.

[87] K. Enpuku and K. Yoshida, "Resistively shunted dc SQUID coupled to an input coil," *J. Appl. Phys.*, vol. 59, no. 5, pp. 1714–1719, 1986.

[88] D. Drung, "High-$T_c$ and low-$T_c$ dc SQUID electronics," *Supercond. Sci. Technol.*, vol. 16, no. 12, pp. 1320–1336, 2003.

[89] V. Foglietti, M. Giannini, and G. Petrocco, "A double DC-SQUID device for flux locked loop operation," *IEEE Trans. Magn.*, vol. 27, no. 2, pp. 2989–2992, 1991.

[90] M. Podt, M. van Duuren, A. Hamster, J. Flokstra, and H. Rogalla, "Two-stage amplifier based on a double relaxation oscillation superconducting quantum interference device," *Appl. Phys. Lett.*, vol. 75, p. 2316, 1999.

[91] J. Clarke, W. Goubau, and M. Ketchen, "Tunnel junction dc SQUID: Fabrication, operation, and performance," *J. Low Temp. Phys.*, vol. 25, no. 1, pp. 99–144, 1976.

[92] C. Tesche, "Analysis of strong inductive coupling on SQUID systems," *IEEE Trans. Magn.*, vol. 19, no. 3, pp. 458–460, 1983.

[93] J. Martinis and J. Clarke, "Signal and noise theory for a dc SQUID amplifier," *J. Low Temp. Phys.*, vol. 61, no. 3, pp. 227–236, 1985.

[94] W. Folkner, M. Moody, J. Richard, K. Carroll, and C. Tesche, "Instrumentation of a resonant gravitational radiation detector with a planar thin-film dc SQUID," *J. Appl. Phys.*, vol. 65, p. 5190, 1989.

[95] S. Maas, *Noise In Linear And Nonlinear Circuits*. Artech House, 2005.

[96] M. Simmonds, W. Fertig, and R. Giffard, "Performance of a resonant input SQUID amplifier system," *IEEE Trans. Magn.*, vol. 15, no. 1, pp. 478–481, 1979.

[97] C. Hilbert and J. Clarke, "DC SQUIDs as radiofrequency amplifiers," *J. Low Temp. Phys.*, vol. 61, no. 3, pp. 263–280, 1985.

[98] P. Falferi, M. Bonaldi, M. Cerdonio, M. Mück, A. Vinante, R. Mezzena, G. Prodi, and S. Vitale, "Characterization of the Input Noise Sources of a dc SQUID," *J. Low Temp. Phys.*, vol. 123, no. 5, pp. 275–302, 2001.

[99] A. Vinante, M. Bonaldi, P. Falferi, M. Cerdonio, R. Mezzena, G. Prodi, and S. Vitale, "Stabilization and optimization of a two-stage dc SQUID coupled to a high Q resonator," *Physica C*, vol. 368, no. 1-4, pp. 176–180, 2002.

[100] P. Falferi, M. Bonaldi, M. Cerdonio, A. Vinante, and S. Vitale, "Back action of a low noise dc SQUID," *Appl. Phys. Lett.*, vol. 73, p. 3589, 1998.

[101] R. Voss, "Noise characteristics of an ideal shunted Josephson junction," *J. Low Temp. Phys.*, vol. 42, no. 1, pp. 151–163, 1981.

[102] K. Enpuku, T. Muta, K. Yoshida, and F. Irie, "Noise characteristics of a dc SQUID with a resistively shunted inductance," *J. Appl. Phys.*, vol. 58, no. 5, pp. 1916–1923, 1985.

[103] B. Chesca, "Analytical Theory of DC SQUIDS Operating in the Presence of Thermal Fluctuations," *J. Low Temp. Phys.*, vol. 111, no. 1, pp. 165–196, 1998.

[104] D. Drung and W. Jutzi, "Hysteretic noise in dc SQUIDs," *IEEE Trans. Magn.*, vol. 21, no. 2, pp. 430–433, 1985.

[105] G. Testa, S. Pagano, E. Sarnelli, C. Calidonna, and M. Furnari, "Improved superconducting quantum interference devices by resistance asymmetry," *Appl. Phys. Lett.*, vol. 79, p. 2943, 2001.

[106] V. Foglietti, W. Gallagher, M. Ketchen, A. Kleinsasser, R. Koch, and R. Sandstrom, "Performance of dc SQUIDs with resistively shunted inductance," *Appl. Phys. Lett.*, vol. 55, p. 1451, 1989.

[107] M. Ketchen, "Design considerations for DC SQUIDs fabricated in deep sub-microntechnology," *IEEE Trans. Magn.*, vol. 27, no. 2 Part 4, pp. 2916–2919, 1991.

[108] W. H. Chang, "The inductance of a superconducting strip transmission line," *J. Appl. Phys.*, vol. 50, no. 12, pp. 8129–8134, 1979.

[109] H. Seppä and T. Ryhänen, "Influence of the signal coil on DC-SQUID dynamics," *IEEE Trans. Magn.*, vol. 23, no. 2, pp. 1083–1086, 1987.

[110] R. Leoni, P. Carelli, and V. Foglietti, "Stray capacitance effect in superconducting quantum interferometers," *J. Appl. Phys.*, vol. 64, p. 2527, 1988.

[111] B. Muhlfelder, W. Johnson, and M. Cromar, "Double transformer coupling to a very low noise SQUID," *IEEE Trans. Magn.*, vol. 19, no. 3, pp. 303–307, 1983.

[112] J. Knuutila, A. Ahonen, and C. Tesche, "Effects on dc SQUID characteristics of damping of input coil resonances," *J. Low Temp. Phys.*, vol. 68, no. 3, pp. 269–284, 1987.

[113] R. Ono, J. Koch, A. Steinbach, M. Huber, and M. Cromar, "Tightly coupled dc SQUIDs with resonance damping," *IEEE Trans. Appl. Supercond.*, vol. 7, no. 2 Part 3, pp. 2538–2541, 1997.

[114] J. Schambach, H. Meyer, L. Warzemann, P. Weber, K. Bluthner, G. Daalmans, F. Bommel, and D. Uhl, "Analytical calculation of the I-V characteristics of SQUIDs with parasitic elements," *Supercond. Sci. Technol.*, vol. 9, no. 8, pp. 617–621, 1996.

[115] M. Huber, A. Steinbach, and R. Ono, "Resonance damping in tightly coupled dc SQUIDs via intra-coil resistors," *Physica C*, vol. 351, no. 2, pp. 85–90, 2001.

[116] R. Cantor, T. Ryhanen, D. Drung, H. Koch, and H. Seppa, "Design and optimization of DC SQUIDs fabricated using a simplified four-level process," *IEEE Trans. Magn.*, vol. 27, no. 2 Part 4, pp. 2927–2931, 1991.

[117] J. Knuutila, M. Kajola, H. Seppä, R. Mutikainen, and J. Salmi, "Design, optimization, and construction of a dc SQUID with complete flux transformer circuits," *J. Low Temp. Phys.*, vol. 71, no. 5, pp. 369–392, 1988.

[118] T. Minotani, K. Enpuku, and Y. Kuroki, "Effect of capacitive feedback on the characteristics of direct current superconducting quantum interference device coupled to a multiturn input coil," *J. Appl. Phys.*, vol. 82, p. 457, 1997.

[119] F. Giazotto, T. T. Heikkilä, A. Luukanen, A. M. Savin, and J. P. Pekola, "Opportunities for mesoscopics in thermometry and refrigeration: Physics and applications," *Rev. Mod. Phys.*, vol. 78, no. 1, p. 217, 2006.

[120] J. J. Lin and J. P. Bird, "Recent experimental studies of electron dephasing in metal and semiconductor mesoscopic structures," *J. Phys.-Condes. Matter*, vol. 14, no. 18, pp. 501–624, 2002.

[121] V. Gantmakher, "Experimental Study of Electron-Phonon Scattering in Metals," *Rep. Progress Physics*, vol. 37, no. 3, pp. 317–362, 1974.

[122] P. Echternach, M. Thoman, C. Gould, and H. Bozler, "Electron-phonon scattering rates in disordered metallic films below 1 K," *Phys. Rev. B*, vol. 46, no. 16, pp. 10339–10344, 1992.

[123] S. Qu, A. Cleland, and M. Geller, "Hot electrons in low-dimensional phonon systems," *Phys. Rev. B*, vol. 72, no. 22, p. 224301, 2005.

[124] A. Sergeev and V. Mitin, "Electron-phonon interaction in disordered conductors: Static and vibrating scattering potentials," *Phys. Rev. B*, vol. 61, no. 9, pp. 6041–6047, 2000.

[125] C. Kittel, *Introduction to Solid State Physics 7th edn*. John Wiley & Sons, New York, 1996.

[126] M. Gershenson, D. Gong, T. Sato, B. Karasik, and A. Sergeev, "Millisecond electron–phonon relaxation in ultrathin disordered metal films at millikelvin temperatures," *Appl. Phys. Lett.*, vol. 79, p. 2049, 2001.

[127] N. Ashcroft and N. Mermin, *Solid state physics*. New York, 1976.

[128] L. Taskinen and I. Maasilta, "Improving the performance of hot-electron bolometers and solid state coolers with disordered alloys," *Appl. Phys. Lett.*, vol. 89, p. 143511, 2006.

[129] J. Karvonen, L. Taskinen, and I. Maasilta, "Influence of Temperature Gradients on Tunnel Junction Thermometry below 1 K: Cooling and Electron–Phonon Coupling," *J. Low Temp. Phys.*, vol. 149, no. 1, pp. 121–135, 2007.

[130] W. Jan, G. Wu, and H. Wei, "Electron–Lattice Interaction in Impure Metals," *Phys. Scr.*, vol. 71, no. 5, pp. 552–555, 2005.

[131] G. Bergmann, W. Wei, Y. Zou, and R. Mueller, "Nonequilibrium in metallic microstructures in the presence of high current density," *Phys. Rev. B*, vol. 41, no. 11, pp. 7386–7396, 1990.

[132] J. DiTusa, K. Lin, M. Park, M. Isaacson, and J. Parpia, "Role of phonon dimensionality on electron-phonon scattering rates," *Phys. Rev. Lett.*, vol. 68, no. 8, pp. 1156–1159, 1992.

[133] C. Wu, W. Jian, and J. Lin, "Electron-phonon scattering times in crystalline disordered titanium alloys between 3 and 15 K," *Phys. Rev. B*, vol. 57, no. 18, pp. 11232–11241, 1998.

[134] P. Falferi, R. Mezzena, M. Mück, and A. Vinante, "Cooling fins to limit the hot-electron effect in dc SQUIDs," *J. Phys.: Conf. Ser.*, vol. 97, p. 012092, 2008.

[135] Y. Zhong and J. Lin, "Observation of a Linear Mean-Free-Path Dependence of the Electron-Phonon Scattering Rate in Thick AuPd Films," *Phys. Rev. Lett.*, vol. 80, no. 3, pp. 588–591, 1998.

[136] M. Kanskar and M. Wybourne, "Crossover between Dissipative and Nondissipative Electron Transport in Metal Wires," *Phys. Rev. Lett.*, vol. 73, no. 15, pp. 2123–2126, 1994.

[137] G. Pollack, "Kapitza Resistance," *Rev. Mod. Phys.*, vol. 41, no. 1, pp. 48–81, 1969.

[138] O. Lounasmaa, *Experimental principles and methods below 1K*. Academic Press New York, 1974.

[139] E. Swartz and R. Pohl, "Thermal boundary resistance," *Rev. Mod. Phys.*, vol. 61, no. 3, pp. 605–668, 1989.

[140] A. Savin, J. Pekola, D. Averin, and V. Semenov, "Thermal budget of superconducting digital circuits at subkelvin temperatures," *J. Appl. Phys.*, vol. 99, p. 084501, 2006.

[141] J. Karvonen and I. Maasilta, "Influence of Phonon Dimensionality on Electron Energy Relaxation," *Phys. Rev. Lett.*, vol. 99, no. 14, p. 145503, 2007.

[142] F. Hekking, A. Niskanen, and J. Pekola, "Electron-phonon coupling and longitudinal mechanical-mode cooling in a metallic nanowire," *Phys. Rev. B*, vol. 77, no. 3, p. 33401, 2008.

[143] D. Schmidt, R. Schoelkopf, and A. Cleland, "Photon-Mediated Thermal Relaxation of Electrons in Nanostructures," *Phys. Rev. Lett.*, vol. 93, no. 4, p. 45901, 2004.

[144] M. Meschke, W. Guichard, and J. P. Pekola, "Single-mode heat conduction by photons," *Nature*, vol. 444, no. 7116, pp. 187–190, 2006.

[145] A. Vinante, P. Falferi, R. Mezzena, and M. Mück, "Hot-electron effect in palladium thin films," *Phys. Rev. B*, vol. 75, no. 10, p. 104303, 2007.

[146] A. Steinbach, J. Martinis, and M. Devoret, "Observation of Hot-Electron Shot Noise in a Metallic Resistor," *Phys. Rev. Lett.*, vol. 76, no. 20, pp. 3806–3809, 1996.

[147] A. Anderson and R. Peterson, "The thermal resistance between electrons and phonons in copper," *Phys. Lett. A*, vol. 38, no. 7, pp. 519–520, 1972.

[148] J. Lin and N. Giordano, "Localization and electron-electron interaction effects in thin Au-Pd films and wires," *Phys. Rev. B*, vol. 35, no. 2, pp. 545–556, 1987.

[149] S. Intiso, J. Pekola, A. Savin, Y. Devyatov, and A. Kidiyarova-Shevchenko, "Rapid single-flux-quantum circuits for low noise mK operation," *Supercond. Sci. Technol.*, vol. 19, no. 5, p. 335, 2006.

[150] "Comsol Multiphysics Version 3.3." FEM software, Comsol Inc., Stockholm, Sweden, 2007.

[151] Leiden Cryogenics B.V., Galgewater 21, 2311 VZ Leiden, The Netherlands.

[152] Supracon AG, Wildenbruchstr. 15, 07745 Jena, Germany.

[153] S. Yeh, J. Lin, J. Xiunian, and Z. Dianlin, "Electron-phonon-impurity interference effect in disordered $Au_{56}Pd_{44}$ and $IrO_2$ thick films," *Phys. Rev. B*, vol. 72, no. 2, p. 24204, 2005.

[154] K. Nagaev, "Influence of electron-electron scattering on shot noise in diffusive contacts," *Phys. Rev. B*, vol. 52, no. 7, pp. 4740–4743, 1995.

[155] Y. Naveh, D. Averin, and K. Likharev, "Shot noise in diffusive conductors: A quantitative analysis of electron-phonon interaction effects," *Phys. Rev. B*, vol. 58, no. 23, pp. 15371–15374, 1998.

[156] P. Falferi, M. Bonaldi, M. Cerdonio, A. Vinante, R. Mezzena, G. Prodi, and S. Vitale, "27 $\hbar$ SQUID amplifier operating with high-Q resonant input load," *Appl. Phys. Lett.*, vol. 88, p. 062505, 2006.

[157] G. Hildebrandt and F. Uhlmann, "Inductance calculation for integrated superconducting structures by minimizing free energy," *IEEE Trans. Appl. Supercond.*, vol. 5, no. 2 Part 3, pp. 2766–2769, 1995.

[158] G. Hildebrandt and F. Uhlmann, "Magnetic field computation in superconducting thin film structuresby a volume integral equation method," *IEEE Trans. Magn.*, vol. 32, no. 3 Part 1, pp. 690–693, 1996.

[159] M. Khapaev, A. Kidiyarova-Shevchenko, P. Magnelind, and M. Kupriyanov, "3D-MLSI: software package for inductance calculation in multilayersuperconducting integrated circuits," *IEEE Trans. Appl. Supercond.*, vol. 11, no. 1 Part 1, pp. 1090–1093, 2001.

[160] "Inductance calculation software FastHenry 3.0wr," 2001. Whiteley Research Inc., 456 Flora Vista Avenue, Sunnyvale, CA 94086, U.S.A.; Code available at http://www.wrcad.com/.

[161] M. Kamon, M. Tsuk, and J. White, "FASTHENRY: A multipole-accelerated 3-D inductance extraction program," *IEEE Trans. Microw. Theory Tech.*, vol. 42, no. 9 Part 1, pp. 1750–1758, 1994.

[162] STAR Cryoelectronics, 25-A Bisbee Court, Santa Fe, NM 87508-1412, USA.

[163] M. B. Simmonds, "High symmetry dc SQUID system." US Patent 5053834, 1991.

[164] R. Mezzena, A. Vinante, P. Falferi, S. Vitale, M. Bonaldi, G. Prodi, M. Cerdonio, and M. Simmonds, "Sensitivity enhancement of Quantum Design dc superconducting quantum interference devices in two-stage configuration," *Rev. Sci. Instrum.*, vol. 72, p. 3694, 2001.

# Summary

The dc Superconducting Quantum Interference Device (dc-SQUID) is one of the most sensitive magnetic field sensors available. In this thesis, we concentrate on its application as an amplifier. The developed sensors are intended for the utilization in the first spherical resonant mass gravitational wave antenna MiniGRAIL. Therefore, minimum noise SQUID amplifiers are required. This thesis covers topics related to the optimized design and operation of SQUID amplifiers.

In chapter 2, we investigate requirements and optimization criteria for practical SQUID amplifier based systems with different connected input circuits. We therefore concentrate on typical measurement frequencies far below the Josephson frequency of the SQUID, the frequency of its intrinsic oscillation. This is done on the basis of a small-signal analysis of the SQUID and typical elements present in a measurement system. On the one hand, we include a standard flux-locked loop (FLL) operation. This is used in typical SQUID measurements to linearize the response of the SQUID by applying a negative feedback flux via a feedback coil. On the other hand, we include the loading of the SQUID amplifier via a connected output impedance, which is given by the next amplifier stage.

In the first part of chapter 2, we discuss the influence of these external circuits on the input impedance of the SQUID amplifier. At low frequencies, this impedance is purely inductive. In case of a flux-locked loop operation or a possible loading of the SQUID via a connected output circuit, both negative and positive resistive input impedances can be generated. Based on this, we give a possible explanation for published measurements on the input impedance of SQUID amplifiers. The derived expressions are later used to explain the frequency response of the SQUID amplifier with some basic connected input impedances. This is useful for the design and characterization of the respective measurement system and helps to understand observed spectra in a practical measurement.

In the second part of chapter 2, we present an analysis on the signal-to-noise ratio. Here, the FLL operation and a possible loading of the SQUID via a connected output circuit turn out to be without influence. We performed the analysis including both the voltage noise of the SQUID, which represents an *additional noise* of the amplifier, as well as the noise on the circulating current in the SQUID loop. The latter represents the *back-action noise* of the amplifier, because it can directly influence a connected input impedance. We derive a general description of the equivalent input noise temperature of the SQUID amplifier with an arbitrary connected input impedance. This forms the basis for our investigations of SQUIDs in chapter 3.

In the final part of chapter 2, we investigate the performance of three practical passive input circuits. We derive expressions for the noise temperature for each of the input

impedances. For the capacitive input circuit, we find an analytical expression for the achievable bandwidth. This is an important criterion for the readout of MiniGRAIL. Furthermore, we calculate practical measured noise spectra in a direct readout operation as well as in FLL operation of the SQUID amplifier with the basic input circuits. Experimental possibilities for characterizing the noise properties as well as the stability of the SQUID amplifier with a capacitive input circuit are discussed.

In chapter 3, we numerically investigate the optimized design and operation of dc-SQUIDs incorporating the results obtained in chapter 2. Based on a circuit simulator, we developed a feasible system for numerically characterizing SQUIDs. This is used to investigate the properties of SQUIDs of varying configuration.

In the first part of chapter 3, we give a detailed overview of the achievable noise parameters of two basic SQUID designs. We therefore focused on an optimization regarding the best achievable additional noise of the amplifier as well as on the minimum achievable equivalent input noise temperature. The presented study is compared to published results and extends them especially regarding the influence of back-action effects. We give a very broad insight into the most important properties of practical interest: the working range, small-signal parameters and the sensitivity. The optimization of the SQUID design and the operation of the amplifier is discussed. This includes the choice of the screening parameter $\beta_L$ of the SQUID as well as the choice in working ranges of optimum sensitivity. In applications where the back-action noise is of importance, the results allow to derive information about the matching of input circuits and the expected performance.

In the second part of chapter 3, we give an overview of the properties of washer type SQUIDs with an integrated coil. This wide-spread layout for thin-film SQUID sensors is typically chosen when a high coupling efficiency to a connected input impedance is required. The integration of the input coil is attended by introduced parasitic capacitances. These elements can influence the impedance of the SQUID loop at the Josephson frequency and therefore alter the dynamics of the sensor.

We defined a model for the practical case of a SQUID with a long integrated coil. Here, the large total length of the windings shifts the coil resonance frequency below the Josephson frequency of the SQUID. In this case, the effective SQUID inductance at the Josephson frequency is lowered compared to its low frequency value. Based on the characteristics of a standard SQUID, we explain the characteristics of SQUIDs with a long integrated coil. Parts of the characteristics are found to be hysteretic. The subsequently presented numerical optimization of the idealized model shows that the hysteresis forces one to operate the SQUID at much higher Josephson frequencies compared to standard SQUID sensors. This is an important insight for both the design and the operation of such sensors. The results of the numerical optimization of this idealized model suggest that the sensitivity can even be enhanced. This can be qualitatively understood by the fact that characteristics, small-signal and noise parameters of the SQUID with an integrated coil are strongly influenced by the lowered effective inductance at the Josephson frequency. The insights gained from the simplified model of SQUIDs with a long integrated coil can be useful for the general understanding of the performance of similar SQUIDs. The practical performance of such sensors is discussed also with respect to effects that are not included in the idealized model.

In the final part of chapter 3, we numerically studied a standard SQUID strongly coupled to a capacitive input impedance. The behavior coincides in many aspects with the idealized

model of a SQUID with a long integrated coil. Also here, the SQUID inductance is effectively lowered at the Josephson frequency. Accordingly, this configuration also exhibits hysteretic characteristics. Some published studies on the performance of this configuration predict additional features in the influence of back-action noise due to an effective screening of the SQUID inductance *at* the measurement frequency. These effects are questionable and were therefore not included in the analysis presented in chapter 2. For three exemplary SQUIDs, we determine the voltage noise spectra in their working point of minimum reachable noise temperature. The spectra are compared with theoretical expressions from chapter 2 and show a good agreement. We conclude that the assumptions of chapter 2 are applicable.

In chapter 4, we investigate the hot-electron effect and its suppression. This effect imposes a practical limit on the cooling behavior of SQUID sensors and therefore on the minimum reachable sensitivity. Here, the coupling between the electron and the phonon system of a resistive material is weakened. Due to the dissipated power in the SQUID, this leads to an increased temperature of the electron system in the shunt resistors of the Josephson junction and therefore to an increased thermal noise.

In the first part of chapter 4, we give an overview of theories on the hot-electron effect and other aspects that influence the effective thermal resistance between the electron system of a thin-film resistor and the surrounding bath. Furthermore, we described the behavior of *cooling fins* attached to dissipating resistors. Heat is transported to these cooling reservoirs via electronic heat conduction and therefore, the effective cooling volume is increased. This is demonstrated by a numerical calculation on a finite one-dimensional cooling fin.

In the second part of chapter 4, we present heating experiments on thin-film resistors made of *PdAu*. Here, power is dissipated in the resistor and the electron temperature is determined by noise thermometry. The noise was measured using a SQUID amplifier. The experimental results on a thin-film resistor without a cooling extension yield a relation $P \propto {T_E}^5$. Here, $P$ is the dissipated power and $T_E$ is the temperature of the electrons in the thin-film resistor. A detailed analysis of the measurement data led to the conclusion that we directly measured the energy transfer between the electron and the phonon system. Because our sample is certainly in the dirty limit, the observed exponent 5 is in contradiction with theory. This discrepancy is not unusual, there is a variety of experiments that contradicts with existing theories. A comparison with results reported in literature on resistors of the same alloy but of different thickness suggests that the electron-phonon coupling could be influenced by the dimensionality of the phonon population in the shunt resistor.

Furthermore, we numerically and experimentally studied configurations of resistors with attached cooling fins. The measured data are well approximated by numerical calculations on the thermal heat conduction within the geometry. The numerical calculations on the electronic thermal transport turn out to be a useful tool for the thermal design of superconducting electronics. We discuss some general measures to reduce an influence of the hot-electron effect by means of passive cooling.

In chapter 5, we present the design, modeling and characterization of SQUIDs developed for the gravitational wave antenna MiniGRAIL. The main requirements are given by a large input inductance $L_{IN} \approx 1.5$ µH with a minimum additional coupled energy resolution $\varepsilon_{VV}/k^2$ at the aimed operation temperature of 20 mK. Our designs were fabricated in the low-$T_c$ SQUID process of the foundry at the *IPHT Jena*. Many aspects related to the design and operation of these sensors coincide with the topics presented in the preceding chapters.

Because of the required high coupling efficiency $k^2$, the input coil has to be integrated on the SQUID design. Together with the large required input inductance, this leads to SQUIDs with a long integrated coil, as treated in chapter 3. During the characterization of our developed SQUIDs, we could clearly identify hysteretic working ranges. We directly observed the expected behavior for one of our sensors. This is to our knowledge the first direct experimental evidence for this effect. As argued in chapter 3, this is of importance for both the design and operation of such sensors. The hysteresis is usually not directly observable at a bath temperature of 4 K. Nevertheless, the sensitivity is also degraded in this case. This has to be taken into account for both the design and the operation of such sensors. The optimum operation voltage is often much larger compared to standard SQUIDs. The hysteretic working range typically appear as steep flux–voltage characteristics, which might mislead a user to operate the SQUID in these parts of the characteristics. Measurements on the sensitivity of all presented SQUID sensors exhibited a degrading effect originating from hysteresis. The performance within the hysteretic working range could be partly improved by means of series resistive-capacitive damping elements connected across the input coil. Nevertheless, such working points turned out to show mainly non-thermal noise which could not be considerably improved by cooling.

To numerically study the performance of our developed SQUIDs in more detail, we derived the most important properties for the operation from the layout. These properties were extracted by numerical inductance calculation on simplified test structures on the one hand and by calculating the RF impedance of the washer structures with integrated coils on the other hand. Simplified models of the SQUIDs were simulated and compared to the characteristics of all our developed sensors. In general, the agreement was good. We think that many degrading effects could be identified. This includes the already mentioned hysteresis as well as several unavoidable and avoidable resonances within the structures of the SQUIDs. Also the numerically determined sensitivity of one of our sensors showed a good agreement with measurements. To our knowledge, this has never been achieved in such a detail for SQUIDs with integrated coils. Therefore, we conclude that the performance of this type of SQUIDs is more controllable and predictable than is usually assumed.

We especially concentrated on the layout of a SQUID with a parallel washer configuration. Here, parasitic coupling between the feedback coils and the signal coils is minimized. This helps to improve the stability of the readout system with the capacitive transducers of MiniGRAIL. For the first developed sensor, a minimum coupled energy resolution of 170 $\hbar$ was measured at bath temperatures below 0.2 K. This was found to be mainly determined by the hot-electron effect which led to an effective minimum reachable temperature of about 0.4 K. The numerical characterization of detailed models was incorporated into the design process of the second sensor. The measured normalized coupled energy resolution $\varepsilon_{VV}/(k^2 T)$ is 170 $\hbar$/K at bath temperatures above 1 K. This is about a factor of two higher than the simulated design value. The main reason for this discrepancy are the increased values of $\beta_L$ and $I_0 R$ of the fabricated device. Nevertheless, the coupled energy resolution improved to about 60% of the value obtained for the first design at higher bath temperatures. In the redesigned sensor, we used shunt resistors of a larger size. The measurements suggest that the increase in volume of an order of magnitude does not introduce degrading effects. We therefore expect an improvement of the minimum reachable electron temperature to about 0.3 K.

# Samenvatting

## (Summary in dutch)

Het dc Superconducting Quantum Interference Device (dc-SQUID) is een van de meest gevoelige magneetveldsensoren die beschikbaar zijn. In dit proefschrift concentreren we ons op het gebruik daarvan als versterker. De ontwikkelde sensoren zijn bedoeld voor gebruik in de eerste sferische resonante massa gravitatie golf antenne MiniGRAIL. Hiervoor zijn SQUID versterkers met minimale ruis nodig. Dit proefschrift behandelt onderwerpen die gerelateerd zijn aan het optimale ontwerp en werking van SQUID versterkers.

In hoofdstuk 2 onderzoeken we de eisen en optimalisatiecriteria voor op praktische SQUID versterker gebaseerde systemen verbonden aan verschillende ingangsnetwerken. We concentreren ons daarom op typische meetfrequenties die ver beneden de Josephsonfrequentie van het SQUID, zijn intrinsieke oscillatie frequentie, liggen. Dit wordt gedaan op basis van zwakke-signalen analyse van het SQUID en typische elementen van het meetsysteem. Eenerzijds includeren we de standaard flux-locked loop (FLL) werking. Deze wordt gebruikt in typische SQUID metingen om het gedrag te lineariseren door het aanbrengen van een negatief teruggekoppelde flux via een terugkoppelspoel. Anderzijds includeren we de belasting van SQUID versterkers via een aangesloten uitgangsimpedantie, bijvoorbeeld de volgende versterkertrap.

In het eerste deel van hoofdstuk 2 wordt de invloed van deze externe schakelingen op de ingangsimpedantie van de SQUID versterker besproken. Bij lage frequenties is deze impedantie puur inductief. In geval van een flux-locked loop configuratie of een eventuele belasting van het SQUID via een aangesloten uitgangsnetwerk kunnen zowel negatieve als positieve impedanties gegenereerd worden. Op basis hiervan geven we mogelijke verklaringen voor gepubliceerde metingen over de ingangsimpedantie van SQUID versterkers. Wij gebruiken die afgeleide uitdrukkingen later om het frequentiegedrag van de SQUID versterker te verklaren waarbij simpele ingangsimpedanties aangesloten zijn. Dit helpt om het meetsysteem te ontwerpen en te karakteriseren alsmede de geobserveerde spectra in praktische metingen te begrijpen.

In het tweede deel van hoofdstuk 2 presenteren we een analyse van de signaal-ruis verhouding. Hier blijken de FLL configuratie en een mogelijke belasting van het SQUID via een aangesloten uitgangsnetwerk geen invloed te hebben. We hebben een analyse uitgevoerd waar zowel de spanningsruis van het SQUID, welke gerepresenteerd wordt door een additionele ruis van de versterker, en de ruis van de rondgaande stroom in het SQUID ring, in beschouwing wordt genomen. De laatste representeert de back-action-ruis van de versterker, omdat het direct invloed kan hebben op de aangesloten ingangsimpedantie. We leiden een algemene beschrijving van de equivalente ingangsruistemperatuur af met een willekeurig aangesloten ingangsimpedantie. Deze vormen de basis van ons onderzoek van

SQUIDs in hoofdstuk 3.

In het laatste deel van hoofdstuk 2 onderzoeken we de prestaties van drie praktische ingangsnetwerken. We leiden een uitdrukking af voor de ruistemperatuur van elk van de ingangsimpedanties. Voor het capacitieve ingangsnetwerk vinden we een analytische uitdrukking voor de haalbare bandbreedte. Dit is een belangrijk criterium voor de uitlezing van MiniGRAIL. Verder berekenen we de praktisch gemeten ruisspectra bij een directe uitlezing en in een FLL configuratie van de SQUID versterker die aangesloten is aan de elementaire ingangsnetwerken. Experimentele mogelijkheden voor de karakterisatie van de ruiseigenschappen van de SQUID versterkers en de stabiliteit van de SQUID versterkers met een capacitief ingangsnetwerk worden besproken.

In hoofdstuk 3 onderzoeken we numeriek het optimale ontwerp en de optimale utilisatie van dc-SQUIDs met de resultaten verkregen in hoofdstuk 2. Op basis van een netwerksimulator hebben we een werkbaar systeem om numeriek SQUIDs te karakteriseren ontwikkeld. Dit wordt gebruikt om eigenschappen van SQUIDs in verschillende configuraties te onderzoeken.

In het eerste deel van hoofdstuk 3 geven we een gedetailleerd overzicht van haalbare ruis parameters van de twee basis SQUID ontwerpen. Het focus ligt daarom op een optimalisatie voor wat betreft de best haalbare additionele ruis van de versterker alsmede van de minimaal haalbare equivalente ingangsruistemperatuur. De gepresenteerde studie is vergeleken met gepubliceerde resultaten en breidt deze uit vooral voor wat betreft de invloed van back-action effecten. We geven een zeer breed inzicht in de meest belangrijke eigenschappen van praktische aard: het werkgebied, zwakke-signalen parameters en gevoeligheid. De optimalisatie van het SQUID ontwerp en de utilisatie van de versterker worden behandeld. Dit omvat de keuze in de screening parameter $\beta_L$ van het SQUID alsmede de keuze in het werkgebied van de optimale gevoeligheid. In toepassingen waar de back-action-ruis belangrijk is geven de resultaten informatie over het koppelen van ingangsnetwerken en de verwachte prestatie.

In het tweede deel van hoofdstuk 3 geven we een overzicht van de eigenschappen van washer-type SQUIDs met een geïntegreerde spoel. Deze wijdverspreide layout voor dunne-film SQUID sensoren wordt typisch gekozen als een hoge koppelefficiëntie aan een aangesloten ingangsimpedantie nodig is. De integratie van de ingangsspoel wordt vergezeld door de introductie van parasitaire capaciteiten. Deze elementen kunnen de impedantie van de SQUID ring bij de Josepshon frequentie beïnvloeden en daardoor verandert het dynamische gedrag van de sensor.

We hebben een model gedefinieerd voor het praktische geval van een SQUID met een lange geïntegreerde spoel. Hier wordt door de totale lengte van de windingen de resonantiefrequentie van de spoel verschoven tot onder de Josephsonfrequentie van het SQUID. In dit geval wordt de effectieve inductie van het SQUID bij de Josephsonfrequentie verlaagd in vergelijking met zijn lage frequentie waarde. Gebaseerd op de karakteristieken van een standaard SQUID leggen we uit wat de karakteristieken van SQUIDs met lange geïntegreerde spoelen zijn. Delen van de karakteristiek blijken hysteretisch te zijn. De daarna gepresenteerde numerieke optimalisatie van hetgeïdealiseerde model laat zien dat de SQUID door deze hysterese bij hogere Josephsonfrequenties gebruikt dienen te worden dan standaard SQUID sensoren. De resultaten van de numerieke optimalisatie van dit geïdealiseerde model suggereert dat de gevoeligheid zelfs verbeterd kan worden. Kwalitatief kan dit begrepen worden door het feit dat de karakteristieken, zwakke signalen- en ruisparameters van het

SQUID met een geïntegreerde spoel sterk beïnvloed worden door zijn verlaagde effectieve inductie bij de Josephsonfrequentie. Het inzicht verkregen van het versimpelde model van SQUIDs met een lange geïntegreerde spoel kan zinvol zijn voor het algemene begrip van de prestaties van soortgelijke SQUIDs. De praktische prestaties van dergelijke sensoren wordt besproken, ook met het oog op effecten die niet worden meegenomen in het geïdealiseerde model.

In het laatste deel van hoofdstuk 3 onderzoeken we numeriek een standaard SQUID die sterk gekoppeld is aan een capacitieve ingangsimpedantie. Het gedrag komt in veel aspecten overheen met het geïdealiseerde model van een SQUID met een lange geïntegreerde spoel. Ook hier is de SQUID inductie effectief verlaagd bij de Josephsonfrequentie. Deze configuratie laat eveneens hysteretische karakteristieken zien. Een deel van de gepubliceerde studies over de prestaties van deze configuratie voorspelt additionele eigenschappen aangaande de invloed van back-action-ruis door de effectieve afscherming van het SQUID inductie *bij* de meetfrequentie. Deze effecten zijn discutabel en zijn daarom niet meegenomen in de analyse die gepresenteerd is in hoofdstuk 2. Voor drie voorbeeld SQUIDs zijn de spanningsruis spectra bepaald in het werkpunt van de minimaal haalbare ruistemperatuur. De spectra zijn vergeleken met de theoretische uitdrukkingen van hoofdstuk 2 en laten een goede overeenkomst zien. We concluderen dat de aannames van hoofdstuk 2 toepasbaar zijn.

In hoofdstuk 4 onderzoeken we het hot-elektron effect en de onderdrukking daarvan. Dit effect stelt een praktische limiet aan het koelgedrag van SQUID sensoren en daardoor aan hun minimaal haalbare gevoeligheid. Hier wordt de koppeling tussen de elektronen en het phonon systeem van een resistief materiaal verzwakt. Door het gedissiperde vermogen in het SQUID leidt dit tot een verhoogde temperatuur van het elektron systeem in de shunt-weerstanden van de Josephson juncties en daardoor tot een verhoging van de thermische ruis.

In het eerste deel van hoofdstuk 4 geven we een overzicht van de bestaande theorieën van het hot-elektron effect en andere aspecten die van invloed zijn op de effectieve thermische weerstand tussen het elektron systeem van een dunne-filmweerstand en het bad waarin het zich bevindt. Verder beschouwen we het gedrag van koelvinnen die bevestigd zijn aan de dissiperende weerstand. Warmte wordt naar deze koelreservoirs getransporteerd via elektronische warmtegeleiding en daardoor wordt het effectieve koelvolume vergroot. Dit wordt gedemonstreerd aan de hand van een numerieke berekening in een eindige eendimensionale koelvin.

In het tweede deel van hoofdstuk 4 presenteren we opwarmingsexperimenten aan dunne-filmweerstanden gemaakt van *PdAu*. Hierin wordt vermogen gedissipeerd en de elektrontemperatuur wordt bepaald door ruisthermometrie. De ruis werd gemeten met een SQUID versterker. We laten de experimentele resultaten zien van een dunne-filmweerstand zonder koelvin uitbreiding. We vonden een relatie van $P \propto {T_E}^5$. Hier is $P$ het gedissipeerde vermogen en $T_E$ de temperatuur van de electronen in de dunne-filmweerstand. Een gedetailleerde analyse van de gemeten data leidt tot de conclusie dat we direct de energie overdracht tussen de elektronen en het phonon systeem gemeten hebben. Omdat het onderzochte metaal zich zeker in de *dirty limit* bevindt is de geobserveerde exponent 5 in tegenspraak met de theorie. Deze discrepantie is niet ongebruikelijk, er zijn een aantal experimenten die de bestaande theorieën tegenspreken. Een vergelijking van gepubliceerde resultaten over weerstanden van dezelfde legering maar met een andere dikte suggereert dat de elektron-phonon koppeling beïnvloed zou kunnen worden door het aantal dimensies van de phonon populatie in de

shunt-weerstand.

Verder hebben we numeriek en experimenteel de configuraties van de weerstanden verbonden met koelvinnen bestudeerd. De gemeten data wordt goed benaderd door de numerieke berekeningen van de thermische warmtegeleiding in de geometrie. Deze berekeningen van het elektro-thermische transport blijkt een bruikbaar gereedschap te zijn voor het thermisch ontwerp van supergeleidende elektronica. We bespreken enkele algemene maatregelen om de invloed van het hot-elektron effect door passieve koeling te verminderen.

In hoofdstuk 5 presenteren we het ontwerp, de modelvorming en de karakterisatie van ontwikkelde SQUIDs voor de gravitatie golf antenne MiniGRAIL. De belangrijkste vereisten worden gegeven door de grote ingangsimpedantie $L_{IN} \approx 1.5$ µH met een minimale additionele gekoppelde energie resolutie $\varepsilon_{VV}/k^2$ bij de gewenste werktemperatuur van 20 mK. Onze ontwerpen zijn gefabriceerd in het lage-$T_c$ SQUID proces van de foundry op de IPHT Jena. Veel aspecten gerelateerd aan het ontwerp en de werking van deze sensoren overlappen met de onderwerpen die gepresenteerd zijn in de voorgaande hoofdstukken.

Vanwege de vereiste hoge koppelefficiëntie $k^2$ moet de inkoppelspoel geïntegreerd worden in het SQUID ontwerp. Samen met de vereiste hoge ingangsinductie leidt dit tot een SQUID met een lange geïntegreerde spoel zoals behandeld in hoofdstuk 3. Tijdens de karakterisatie van de door ons ontwikkelde SQUIDs konden we duidelijk de hysteretische werkgebieden identificeren. Dit is naar ons idee het eerste direkte experimentele bewijs voor dit effect. Zoals besproken in hoofdstuk 3 is dit belangrijk voor zowel het ontwerp als het utilisatie van dergelijke sensoren. De hysterese is doorgaans niet direct zichtbaar bij een badtemperatuur van 4 K. Desalniettemin is de gevoeligheid ook verslechterd in die gevallen. Hiermee moet rekening gehouden worden voor zowel het ontwerp als de utilisatie van dergelijke sensoren. De optimale werkspanning is vaak veel groter in vergelijking met standaard SQUIDs. Het hysteretische werkgebied wordt typisch zichtbaar als een steile flux versus spanningskarakteristiek welke een gebruiker zou kunnen misleiden om het SQUID in deze gebieden van de karakteristiek in te stellen. Metingen van de gevoeligheid van alle gepresenteerde SQUID sensoren vertonen een nadelig effect veroorzaakt door hysterese. De prestatie binnen het hysteretische regime zou deels verbeterd kunnen worden door een serieel weerstand-capaciteit demp element verbonden aan de ingangsspoel. Desalniettemin lieten dergelijke werkpunten niet-thermische ruis zien die door koeling niet verbeterd kon worden.

Om numeriek de prestatie van de door ons ontwikkelde SQUIDs in meer detail te kunnen bestuderen hebben we voor de werking belangrijke eigenschappen afgeleid van de layout. Deze eigenschappen werden enerzijds verkregen door numerieke inductieberekeningen van versimpelde teststructuren en anderzijds door berekeningen van de radiofrequentieimpedantie van de washer structuur met geïntegreerde spoel. Versimpelde modellen van de SQUIDs werden gesimuleerd en vergeleken met de karakteristieken van alle andere door ons ontwikkelde sensoren. In het algemeen was de overeenkomst goed. We denken dat veel degraderende effecten geïdentificeerd zouden kunnen worden. Dit omvat de al genoemde hysterese alsmede verschillende onvermijdbare en vermijdbare resonanties binnen de layout van de SQUIDs. Ook de numeriek bepaalde gevoeligheid van een van onze sensoren liet een goede overeenkomst zien met de metingen. Naar ons idee is dit nog nooit zo nauwkeurig bereikt voor SQUIDs met een geïntegreerde spoel. Daarom concluderen wij dat in het algemeen de prestatie van dit type SQUIDs beter controleerbaar en voorspelbaar is dan veelal wordt aangenomen.

We hebben ons in het bijzonder geconcentreerd op een layout van een SQUID met een parallelle washer configuratie. Hier is de parasitaire koppeling tussen de terugkoppelspoelen en de signaalspoelen geminimaliseerd. Dit helpt de stabiliteit van het uitleessysteem met de capacitieve transducer van MiniGRAIL te verbeteren. Voor de eerst ontwikkelde sensor is een minimaal gekoppelde energie resolutie van $170\hbar$ gemeten voor badtemperaturen beneden 0.2 K. Dit werd grotendeels bepaald door het hot-elektron effect dat leidt tot een effectieve minimaal haalbare temperatuur van $\approx 0.4$ K. De numerieke karakterisatie van gedetailleerde modellen werd verwerkt in het ontwerpproces van de tweede sensor. De gemeten genormaliseerde gekoppelde energie resolutie $\varepsilon_{VV}/(k^2 T)$ is $170\hbar/\mathrm{K}$ bij badtemperaturen boven 1 K. Dit is ongeveer een factor 2 hoger dan de gesimuleerde ontwerpwaarde. De belangrijkste reden voor deze discrepantie zijn de verhoogde waarde van $\beta_L$ en $I_0 R$ van het gefabriceerde device. Desalniettemin is de gekoppelde energie resolutie verbeterd met ongeveer 60% ten opzichte de waarde verkregen bij het eerste ontwerp bij hogere badtemperaturen. In de nieuw ontworpen sensor hebben we grotere shunt-weerstanden gebruikt. De metingen suggereren dat de toename van ongeveer een orde van grootte van het volume geen negatieve effecten introduceert. We verwachten daarom een verbetering van de minimaal haalbare elektrontemperatuur tot ongeveer 0.3 K.

# Acknowledgements

Conducting research and writing a Ph.D. thesis are enduring and slow processes which are hardly manageable without the support of numerous people. Here, I would like to thank all of you who were there for me over the past years. I sincerely hope that I did not forget to name somebody here.

First of all, I would like to mention my supervisors Horst Rogalla and Jaap Flokstra. As usual, I do not know if I should speak in German, Dutch or English to Horst, so I will just stick to the latter. Thank you for giving me the opportunity to conduct my Ph.D. research at the Low Temperature division of the University of Twente and for the useful discussions. The numerous and excessive sessions with Jaap helped me to understand the way of scientific work, organization and the needed physics—thank you for all the guidance, support, trust, freedom and patience while correcting this thesis.

Without the MiniGRAIL team from Leiden University the presented work would not have been possible. In this respect, I especially want to name Giorgio Frossati, Oleksandr "Sasha" Usenko, Arlette de Waard and Tjerk Oosterkamp. Thanks for the nice working atmosphere, technical support, useful discussions and the always warm welcome. It has always been a pleasure working with you. The scientific exchange with Paolo Falferi and Andrea Vinante, from AURIGA is highly appreciated. You habe always been valuable partners in discussing the strange effects in SQUID systems.

The fabrication of SQUID sensors as presented in chapter 5 of this thesis is no simple task. The IPHT Jena realiably helped us solving this problem. I especially want to thank Hans-Georg Meyer, Viatcheslav Zakosarenko, Jürgen Kuhnert and Ronny Stolz for the opportunity to fabricate the presented SQUIDs, the support and the useful discussions.

Furthermore, I would like to thank the supervisors of my master thesis Prof. Uhlmann and Thomas Ortlepp from the Ilmenau University of Technology. Your educational skills helped me to understand the basics needed for the work presented in this thesis. Moreover, your trust gave me the opportunity to start my work at the Low Temperature division of the University of Twente.

Ik ben blij dat ik na mijn afstuderen in de Sensor vakgroep terecht gekomen ben. Mijn kamergenoot Martin, dat was hij tenminste voor het grootste deel van de tijd, is over de jaren een echte vriend geworden – ik ben blij dat wij samen konden werken, elkaar van het werk afleiden, discussiëren, feesten, selfs soms sporten, culturele evenementen bezoeken en veel meer. Het was een groot plezier, wij zullen elkaar nog vaker zien! Mijn vervolg-kamergenoot Kris wil ik bedanken voor zijn typisch Nederlandse gezelligheid die ik in de kroeg vaak kon waarderen. Ons vakantietje in de Verenigde Staten was echt leuk! En bedankt voor jouw bezorgdheid over mijn gezondheid – tijdens mijn rookpauzes moest ik vaker aan je denken.

Reinder, onze grote Fries, dank je voor het leuke gezelschap, jouw speciale humor en de ondersteuning bij vragen over Linux. Mijn voorganger Martin Podt wil ik voor de goede achtergelaten basis en de nuttige discussies bedanken. Verder wil ik Imdat voor zijn hulp en gezelschap, vooral tijdens de lange meet-sessies aan de kust, bedanken. Het was altijd een groot plezier met jou te werken.

Over Kees Verwijs, het laatste lid van onze lunch-groep, kan ik niets dan positiefs zeggen. Jouw jong gebleven karakter heeft erg geholpen de soms opgelopen frustratie weer kwijt te raken. Ik heb van de vele discussies over onze vaak tegengestelde smaak met films en muziek genoten. Es war übercool mit dir!!! Succes met jouw verdediging!

De “Low Temperature division” is een leuke vakgroep om te werken. Aico, Aleksandar, Alexander, Ans, Ariando, Dick, Frank, Gerard, Hans, Harry, Hendrie, Inke, Jeroen, Joost, Joska, Maarten, Mark, Martin S., Pieter, Sasha . . . , bedankt voor de gezelligheid, typisch Nederlandse activiteiten als zeilen en Grolsch drinken, jullie inzet mij het Nederlands te leren en de ondersteuning in het dagelijkse werk. Het was vooral tijdens de grote voetbal-toernooien grappig tussen “Holländern” te leven, wonen en werken.

Leider konnte ich im Laufe meiner Zeit in Holland immer weniger bei meiner Familie sein, was auch für mich nicht immer leicht war. Trotz der geografischen Distanz wart ihr immer für mich da. Liebe Oma, Eltern und meine Schwester Anne, ich möchte das nicht als selbstverständlich hinnehmen und euch herzlich dafür danken. Natürlich werde ich auch Opa immer dankbar für seine Unterstützung und seinen Einfluss auf meine Person sein, auch wenn ich ihm das nicht mehr persönlich sagen kann.

Im Besonderen möchte ich die Unterstützung durch meine Freundin Nadine nennen. Vor allem in den letzten Zügen des Schreibens der vorliegenden Arbeit hast du mir sehr geholfen mich besser zu organisieren und mit dem Stress zurechtzukommen. Du warst mir eine große und unglaublich liebe Hilfe. Danke, dass du bei mir bist.

Also my friends here in Enschede are of importance for both myself and the work presented in this thesis. Thanks to Marco, Espen, Hasan, Jordi, Rajeev, Anne R., Davide and my friends from “Witbreuksweg 399”—Ivo, Antti, Sabine, Giorgos, Ruben, Sebastian, Ruth just to name a few. Knowing you broadened my horizons and provided the basis for killing stress and forgetting the strange world of physics for some time.

Furthermore, I would like to thank the people who helped me to improve the quality of this thesis. Jaap, Horst, Anne, Martin, Kees, Paolo, Alexander and Sasha, I highly appreciate your efforts.

I wish everyone health, success, luck and all the best for the future.

*Johannes*

# Propositions

accompanying the thesis

STRONGLY COUPLED, LOW NOISE DC-SQUID AMPLIFIERS

1. The usually neglected back-action noise is of significant influence when a strongly coupled impedance takes absolute values of up to roughly the absolute value of the input impedance of a typical SQUID amplifier.
   *Chapter 2 and 3 of this thesis*

2. The qualitative behavior of a SQUID amplifier at low measurement frequencies can be modeled independently of the mechanism which determines the SQUID dynamics at the much higher Josephson frequency.
   *Chapter 3 of this thesis*

3. The noise of superconducting electronics can be decreased by cooling and consequently quieting the system. This measure directly limits itself, as one can see in the hot-electron effect.
   *Chapter 4 of this thesis*

4. Optimizing the design of SQUIDs with an integrated coil is no trivial task. The same holds for an optimized operation of such sensors.
   *Chapter 3 and 5 of this thesis*

5. Simulations on detailed models of physical systems give insights that can be hardly achieved in a measurement. This is especially important for superconducting electronics whose complex dynamics are easily affected in an experimental environment.
   *Chapter 5 of this thesis*

6. The wide coverage of the campus with wireless network is certainly convenient. This advantage does not justify the problems caused in sensitive experiments.

7. The actual economic crisis was only possible because many people blindly followed the rules of accounting instead of common sense. In analogy, the evaluation of scientific efforts should not only be determined by numbers of publications, citations and impact factors.

8. One main difference between a physicist and an engineer is that the physicist tends to think in logarithmic scale while the engineer tends to think in linear scale. Only a combination of both can lead to sustainable achievements.

9. The amount of hair gel used by the average Dutchman is only beaten by his milk consumption.

10. The only thing proven by “theories” like *Intelligent design* or the related *Creationism* is that people can behave very irrationally when their view of the world is questioned.

Johannes Pleikies
Enschede, 10 June 2009


# Propositions

accompanying the thesis

STRONGLY COUPLED, LOW NOISE DC-SQUID AMPLIFIERS

1. The usually neglected back-action noise is of significant influence when a strongly coupled impedance takes absolute values of up to roughly the absolute value of the input impedance of a typical SQUID amplifier.
   *Chapter 2 and 3 of this thesis*

2. The qualitative behavior of a SQUID amplifier at low measurement frequencies can be modeled independently of the mechanism which determines the SQUID dynamics at the much higher Josephson frequency.
   *Chapter 3 of this thesis*

3. The noise of superconducting electronics can be decreased by cooling and consequently quieting the system. This measure directly limits itself, as one can see in the hot-electron effect.
   *Chapter 4 of this thesis*

4. Optimizing the design of SQUIDs with an integrated coil is no trivial task. The same holds for an optimized operation of such sensors.
   *Chapter 3 and 5 of this thesis*

5. Simulations on detailed models of physical systems give insights that can be hardly achieved in a measurement. This is especially important for superconducting electronics whose complex dynamics are easily affected in an experimental environment.
   *Chapter 5 of this thesis*

6. The wide coverage of the campus with wireless network is certainly convenient. This advantage does not justify the problems caused in sensitive experiments.

7. The actual economic crisis was only possible because many people blindly followed the rules of accounting instead of common sense. In analogy, the evaluation of scientific efforts should not only be determined by numbers of publications, citations and impact factors.

8. One main difference between a physicist and an engineer is that the physicist tends to think in logarithmic scale while the engineer tends to think in linear scale. Only a combination of both can lead to sustainable achievements.

9. The amount of hair gel used by the average Dutchman is only beaten by his milk consumption.

10. The only thing proven by “theories” like *Intelligent design* or the related *Creationism* is that people can behave very irrationally when their view of the world is questioned.

Johannes Pleikies
Enschede, 10 June 2009